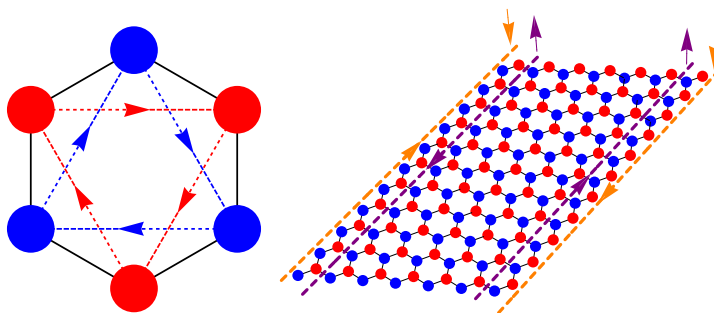




UNIVERSIDAD AUTÓNOMA DE MADRID
Departamento de Física de la Materia Condensada

LATTICE DEFORMATIONS AND SPIN-ORBIT EFFECTS IN TWO-DIMENSIONAL MATERIALS

Tesis doctoral presentada por
HÉCTOR OCHOA DE EGUILOR ROMILLO



Director:

PROF. FRANCISCO GUINEA LÓPEZ

Tutor:

PROF. GUILLERMO GÓMEZ SANTOS

MADRID, ABRIL 2014

*But then again pristine isolation might not be the best idea
It's not good trying to immortalize yourself*

Lou Reed. From *Begining of a great adventure*,
included in *New York* (Sire Records, 1989)

Agradecimientos

Es conocido que la felicidad no radica tanto en los resultados como en las expectativas. Por eso cuando uno acaba un proyecto suele sentir más un vacío interno que una sensación de júbilo. El júbilo, sin embargo, sobreviene en el proceso, cuando se van ajustando las expectativas a las condiciones reales del terreno, y paulatinamente se van logrando resultados. En fin, Ítaca y los famosos versos de Cavafis... no voy a extenderme en esto.

Cuando uno empieza un proyecto como una tesis doctoral sus expectativas no son precisamente económicas sino más bien de trascendencia. El ego es el carburante que alimenta la ambición. Está bien ambicionar, pero tratar de inmortalizarse a través de las obras necesariamente conduce al aislamiento, y así no hay forma de avanzar en las obras, y al final uno se queda solo y triste, con sus expectativas insatisfechas, y lo que es peor, las cosas a medio acabar.

Por eso la lección más valiosa que he aprendido en estos años es que para avanzar en cualquier proyecto hay que dejar de lado la soberbia, sin renunciar a la ambición ni la autoestima. Y eso lo he aprendido de la gente que me ha acompañado durante la elaboración de esta tesis.

Del primero que he aprendido esto es de mi director. Paco es una persona excepcional en todos los sentidos. Un científico de una intuición enorme, y una modestia que le está a la par. Afortunadamente, en estos últimos años le han venido por fin los reconocimientos, merecidísimos. Sólo tengo palabras de admiración y agradecimiento para él, no sólo por lo que he aprendido trabajando juntos, sino por todo lo que ha hecho por mí al margen de lo científico, procurando siempre que tenga el mejor porvenir profesional.

El ambiente que he encontrado en el ICMM ha sido excepcional en lo científico y sencillamente inmejorable en lo humano. El primero al que debo un reconocimiento es a Eduardo Castro, con el que trabajé al comienzo de mi tesis y del que tanto me he aprovechado: de su talento natural para la Física y de su insuperable capacidad de trabajo. Eduardo ha sido todo un referente y su impronta está presente en todo lo bueno que esta tesis pueda tener. Trabajar con Rafa Roldán ha sido también todo un lujo. Mi interés (algo tardío) sobre los dicalcogenuros se debe precisamente a él. Discutir con Rafa es siempre muy enriquecedor, es el mejor ejemplo de honestidad intelectual que conozco.

Siento admiración por muchas de las personas con las que he compartido mesa y discusiones casi a diario: Alberto, Ángel, Mauricio, Yago, también Fernando aunque hayamos coincidido menos. No puedo olvidarme del frente spaghetti formado por

Laura, Luca y Vincenzo, y por supuesto Emmanuele, con el que tan buenos momentos pasé en Santa Bárbara. Jose y Lucía, durante su estancia en Madrid y la época del master respectivamente, me enseñaron que detrás de los cálculos DFT hay también seres humanos. Y siempre tendré un recuerdo muy especial de Fito y Bruno, con los que he compartido meriendas y muchísimas discusiones.

La calidad de la investigación que se hace en este departamento junto al hecho de que sus miembros estén siempre tan abiertos a la discusión es el mejor acicate para alguien que empieza una carrera científica y apenas sabe de qué va esto: Pilar, con la que siempre es tan divertido hablar, y por supuesto Ramón, que ha ampliado mis horizontes científicos y musicales; Belén, Leni y María José, que tanto se han esforzado siempre en la divulgación, y que junto a Ramón organizaron además una serie de cursos fabulosos; Pablo y Elsa, a los que entre otras cosas les debo mis conocimientos (nunca suficientes) de *Mathematica*.

Mención especial merece Geli, por haber dedicado tanto tiempo en orientarme y discutir críticamente mi trabajo (incluida la redacción de esta memoria). La puerta de su despacho siempre ha estado abierta para mí, y se lo agradezco muchísimo, pues ha influido mucho y para bien en mi formación científica.

I want to express my gratitude and admiration to all the outstanding collaborators with whom I had the luck to work during these years: Misha Katsnelson, Antonio Castro Neto, who has helped me a lot, and specially Volodya Fal'ko, who has been my host in Lancaster. I really enjoyed these so productive stays and I learnt a lot from him. Miguel Ángel Cazalilla se ha portado extraordinariamente bien conmigo y he disfrutado mucho trabajando con él. Y por último, el grupo de Rodolfo Miranda y Amadeo López de Parga, en especial Fabián Calleja, que ha sido tan generoso al permitirme usar una de sus figuras en esta memoria.

Aprovecho la oportunidad para agradecer a Guillermo Gómez su accesibilidad durante estos años.

Y no puedo olvidarme de aquellos que me han acompañado fuera del trabajo: de los chicos del equipo de balonmano, que son los que más han sufrido mi mala leche; de Yu Kyoung, la tía más cachonda del mundo; de mi familia, en especial mis padres Jesús y Estela, que entre otras cosas han sido la principal agencia financiadora durante los años de mi formación y una fuente de inspiración y orgullo constante; y finalmente, y por encima de todo, por todas las cosas que ella sabe y que nunca me perdonaría decir en público, de Ana. Lov u a lot.

Gracias a todos. De verdad que he sido muy feliz haciendo esta tesis.

A mis chicas, Ana, Estela, Mishi y Yuki

Abstract

This thesis deals with the interplay between structural and electronic properties of two-dimensional materials such as graphene, and the novel and very interesting phenomena, both from the point of view of fundamental Physics and potential applications, which emerge when lattice distortions such as strains or superlattice modulations are combined with the dynamics of the electrons confined in two spatial dimensions. The main microscopic ingredient which is behind all these phenomena is the spin-orbit interaction. On the one hand, we analyze in detail how the spin-orbit interaction modifies the electronic structure of these materials, and on the other, how structural changes affect the spin-orbit interaction suffered by the electrons of the solid, then modifying its electronic response in a very peculiar manner due to the entanglement of the spin and orbital degrees of freedom.

The contents of the thesis are divided in three blocks. The first part is devoted to study the effect of out-of-plane (flexural) vibration modes on the electronic properties of graphene. We examine in detail the influence of the electron-phonon coupling on the mobilities of suspended graphene samples, and we compare our findings with transport experiments, revealing that scattering by these phonon modes constitute the main intrinsic limitation to electron mobilities. Then, we study how flexural phonons contribute to enhance the spin-orbit coupling in graphene, which is in principle very weak due to the lightness of carbon.

In the second part we analyze in detail different spin relaxation mechanisms mediated by the spin-orbit interaction. We focus on the standard Elliot-Yafet and D'yakonov-Perel' mechanisms, and how such conventional theories are modified when spatially varying spin-orbit fields are considered due to the presence of impurities or curvature.

In the last part we propose novel platforms for engineering topological states of matter based on the interplay between strain and superlattice perturbations in combination with the spin-orbit interaction. Our first proposal relies on the application of shear strain in monolayers of transition metal dichalcogenides in order to create spin-polarized pseudo-Landau levels. The resulting system resembles a time reversal invariant version of the quantum Hall effect. We also study a system consisting on graphene grown on iridium with some monolayers of lead intercalated between them. The experiments show that the local density of states develops a sequence of regularly spaced sharp resonances due to the presence of the lead. These resonances are attributed to the confinement due to spatially modulated spin-orbit fields created by lead, which mimic the effect of a magnetic field.

Resumen

Esta tesis trata de la interacción entre las propiedades estructurales y electrónicas de materiales bidimensionales como el grafeno, y los fenómenos que emergen cuando deformaciones de la red como las tensiones elásticas o las modulaciones producidas por super-redes se combinan con la dinámica de los electrones confinados en dos dimensiones espaciales, muy interesantes tanto desde el punto de vista de la Física fundamental como del de las aplicaciones. El ingrediente microscópico esencial que está detrás de esta fenomenología es la interacción espín-órbita. Por un lado, analizamos en detalle cómo la interacción espín-órbita modifica la estructura electrónica de estos materiales, y por otro, cómo los cambios estructurales afectan a la interacción espín-órbita experimentada por los electrones del sólido, modificando su respuesta electrónica de una manera muy peculiar debido al entrelazamiento de los grados de libertad orbitales y de espín.

Los contenidos de esta tesis están divididos en tres bloques. El primero está dedicado al estudio del efecto de las vibraciones fuera del plano (flexurales) en las propiedades electrónicas del grafeno. Examinamos en detalle la influencia del acoplo electrón-fonón en las movilidades de las muestras de grafeno suspendido, y comparamos nuestros hallazgos con experimentos de transporte que revelan que la dispersión debida a estos modos de fonones constituye la principal limitación intrínseca de las movilidades electrónicas. Estudiamos entonces cómo estos modos de fonones flexurales contribuyen al aumento del acoplo espín-órbita en grafeno, que es en principio muy débil debido al bajo número atómico del carbono.

En la segunda parte analizamos en detalle diferentes mecanismos de relajación de espín mediados por la interacción espín-órbita. Nos centramos en los mecanismos convencionales de Elliot-Yafet y D'yakonov-Perel', y cómo éstos se modifican cuando se incluye el efecto de campos espín-órbita que varían en el espacio debido a la presencia de impurezas o curvatura.

En la última parte proponemos nuevas plataformas para el diseño de estados topológicos de la materia basados en la combinación de tensiones y perturbaciones debido a super-redes con la interacción espín-órbita. Nuestra primera propuesta se basa en la aplicación de tensiones de cizalladura en monocapas de dicalcogenuros de metales de transición con el objeto de crear pseudo-niveles de Landau polarizados en espín. El sistema resultante recuerda a una versión invariante bajo inversión temporal del efecto Hall cuántico. También estudiamos el sistema formado por grafeno crecido sobre iridio con algunas monocapas de plomo intercaladas entre ambos. Los experimentos muestran que la densidad local de estados desarrolla una secuencia de resonancias muy nítidas y regularmente espaciadas debidas a la presencia del

plomo. Estas resonancias se atribuyen al confinamiento debido a la modulación espacial de campos espín-órbita creados por el plomo que imitan el efecto de un campo magnético.

Contents

List of Figures	xvii
List of Acronyms	xxiii
Part 0: Preliminaries	1
1 Introduction	3
2 Model Hamiltonians for SOC and connection with QSHE state	13
2.1 Introduction	13
2.2 Basic electronic properties	14
2.2.1 Graphene	14
2.2.2 Bilayer graphene	19
2.2.3 Graphene multilayers	23
2.2.4 MX_2	26
2.3 SOC in 2D hexagonal crystals	33
2.3.1 Graphene materials	34
2.3.2 MX_2	42
2.3.3 Heavy adatoms	47
2.4 Topological aspects	49
2.4.1 Haldane model	49
2.4.2 QSHE in graphene	51
Part 1: Flexural phonons and SOC	53
3 Electron-phonon coupling and electron mobility in suspended graphene	55
3.1 Introduction	55
3.2 Phonon modes in graphene	56
3.2.1 In-plane modes	57
3.2.2 Out-of-plane (flexural) modes	60
3.3 Electron-phonon coupling	63
3.4 Variational approach to semi-classical transport	67

3.5	Phonon limited resistivity	69
3.5.1	In-plane phonons	71
3.5.2	Flexural phonons	74
3.5.3	Asymptotic behaviors	82
3.6	Comparison with experiments	83
3.7	Conclusions	88
4	Effect of flexural phonons on SOC	89
4.1	Introduction	89
4.2	Spin-phonon coupling in graphene	90
4.3	Tight-binding estimation	92
4.3.1	Phonons at Γ	92
4.3.2	Phonons at K_{\pm}	95
4.4	Kane-Mele gap enhancement	97
4.5	Conclusions	100
	Part 2: Spin relaxation	101
5	SOC-mediated spin relaxation	103
5.1	Introduction	103
5.2	EY and DP mechanisms in graphene and MX_2	106
5.2.1	Mori-Kawasaki formula	107
5.2.2	Graphene	110
5.2.3	MX_2	111
5.3	Beyond EY mechanism in graphene: SOC scatterers	115
5.4	Conclusions	122
6	Spin-lattice relaxation	123
6.1	Introduction	123
6.2	Spin-lattice coupling: geometrical perspective	125
6.3	Spin-lattice relaxation	127
6.3.1	Static wrinkles	129
6.3.2	Flexural phonons	131
6.4	Conclusions	134
	Part 3: New platforms for topological phases	137
7	QSHE in MX_2 monolayers	139
7.1	Introduction	139
7.2	QSHE created by strain	140
7.2.1	Strain in MX_2 monolayers	141
7.2.2	Realization of the Bernevig-Zhang model	142

7.2.3	Experimental consequences	145
7.3	Alternative route: superlattice potentials	146
7.4	Conclusions	150
8	Electronic confinement in graphene due to spatially varying SOC	153
8.1	Introduction	153
8.2	STM/STS experiments on graphene on Ir(111) with intercalated Pb . .	154
8.3	Phenomenological model	158
8.4	Tight-binding simulation	161
8.4.1	Two-bands tight-binding model	161
8.4.2	Scheme of calculation	164
8.4.3	Results	164
8.5	Interpretation	167
8.6	Conclusions	168
	Conclusions	173
	Conclusiones	175
	Appendix	175
A	Point groups	177
A.1	C_{6v}	179
A.2	D_{3d}	182
A.3	D_{3h}	183
B	Collision integral for scattering by phonons	187
C	Electronic structure of graphene commensurate with a Pb monolayer	195
	Bibliography	199
	List of publications	221

List of Figures

2.1	Honeycomb lattice (A sublattice in blue, B sublattice in red) and graphene BZ.	14
2.2	Left: Bilayer graphene lattice, continuum line represents top layer, dashed line bottom layer. Blue sites correspond to A sublattice, red sites to B sublattice. Right: 4 atoms unit cell of bilayer graphene and a few neighboring sites. The continuum black line represents the intra-layer hopping parameter γ_0 . The dashed lines represents inter-layer hopping parameters $\gamma_{i=1,3,4}$ (γ_1 in black, γ_3 in blue, γ_4 in red).	20
2.3	Top: Hexagonal unit cell and electronic bands around \mathbf{K}_\pm points of trilayer graphene in the Bernal stacking. Bottom: The same for rhombohedral stacking. The notation is the same in both cases: in red and blue the atoms of the top and bottom layer, in black atoms of the intermediate layer. Squares correspond to A sites, and circles to B sites. The bands are computed within the tight-binding described through the text with $\gamma_0 = 3.16$ eV, $\gamma_1 = 0.381$ eV.	24
2.4	Top view of the lattice in real space of MX_2 monolayers.	26
2.5	Hopping integrals considered in the tight-binding model.	30
2.6	Bands calculated within the tight-binding model described in the text. The model is only valid around \mathbf{K}_τ points (highlighted in the figure). We take the values summarized in Tab. 2.5 for MoS_2	30
2.7	Electronic bands deduced from the tight-binding model of Eq. (2.18). The values of the Slater-Koster parameters are summarized in Tab. 2.7.	36
2.8	Sketch of the microscopic processes which lead to the effective SOC terms discussed in the text. (a) First-order processes which lead to the splitting of the valence band. (b) Second-order processes associated to the splitting of the conduction band. (c) Second-order processes which lead to a Bychkov-Rashba coupling when σ_h symmetry is broken.	45

2.9	Top: Electronic bands of a graphene strip with a 20 unit cells width and armchair edges. Left: Only nearest neighbors hopping t . Middle: Staggered potential $M = 0.6\sqrt{3}t$. Right: Haldane second nearest neighbors hopping $t' = 0.2t$, $\phi = \pi/2$. Bottom: On the left, graphene unit cell where the arrows mark the directions of positive phase hopping. On the right, sketches of the edge states in the QHE and QSHE phases. . .	50
3.1	Kinematics of electron scattering by: (a) in-plane phonons, (b) non-strained flexural and (c) strained flexural phonons.	70
3.2	Resistivity due to scattering by in-plane phonons as a function of temperature (in blue, monolayer graphene, in red, bilayer). In both cases $n = 10^{12} \text{ cm}^{-2}$ and we take $g = 3 \text{ eV}$ and $\beta = 3$	73
3.3	Resistivity due to scattering by out-of-plane phonons as a function of temperature (in blue, monolayer graphene, in red, bilayer). The logarithmic factor in Eq. (3.79) is dropped. Dashed lines show resistivity due to in-plane phonons, previously discussed. In both cases $n = 10^{12} \text{ cm}^{-2}$ and we take $g = 3 \text{ eV}$ and $\beta = 3$	77
3.4	Different asymptotic behaviors of resistivity in the absence (left) and at the presence of non-negligible (right) strain. Dashed blue line represents T_{BG} for in-plane phonons, and dashed blue line corresponds to T_c in both cases.	83
3.5	(a) Electron transport in suspended graphene. Graphene resistivity $\varrho = R(w/l)$ as a function of gate-induced concentration n for $T = 5, 10, 25, 50, 100, 150$ and 200 K . (b) Examples of $\mu(T)$. The T range was limited by broadening of the peak beyond the accessible range of n . The inset shows a scanning electron micrograph of one of our suspended device. The darker nearly vertical stripe is graphene suspended below Au contacts. The scale is given by graphene width of about $1 \mu\text{m}$ for this particular device.	84
3.6	First order self-energy diagrams. The dashed line represents the phonon propagator, and the straight line the 4-point vertex. Note that the first diagram is 0 since the $\mathbf{q} = 0$ component of the vertex is integrated out.	85
3.7	The infrared cutoff q_c as a function of the applied strain u for monolayer (in red dashed line) and bilayer graphene (in blue). In both cases $T = 300 \text{ K}$	86
4.1	a) Definition of the angle ϕ . b) Sketch for the calculation of the new hoppings between p_z and p_i orbitals.	93

4.2	Effective Kane-Mele mass induced by the coupling with flexural phonons. In red (lower curve) the estimation neglecting the acoustic branch and the dispersion of the optical one. In blue (upper curve) the calculation within the model described in Appendix B.	97
4.3	Dispersion of flexural phonons computed within the nearest-neighbor force model described in the text with $\alpha = 8.5$ eV. In red (upper curve) the dispersion for the optical branch, in blue (lower curve) the acoustic branch.	99
5.1	In-plane spin lifetimes as a function of the carrier concentration. Left: Electron doping. Right: Hole doping. Dashed black line corresponds to $\Gamma = 0.001$ eV, dotted blue to $\Gamma = 0.01$ eV, and solid red $\Gamma = 0.1$ eV. Inset: In-plane spin lifetimes for electron concentrations in double logarithmic scale. Notice the different time scale in the top and bottom panels.	112
5.2	Out-of-plane spin lifetimes as a function of the carrier concentration. In black (dashed) $\Gamma = 0.001$ eV, in blue (dotted) $\Gamma = 0.01$ eV, in red $\Gamma = 0.1$ eV. In all the cases $\Delta_{BR} = 10^{-2}\lambda$. Inset: Spin lifetime for hole concentrations where the correction given by Eq. (5.37).	113
5.3	Geometry of the scattering problem.	117
5.4	Scattering cross section as a function of the carrier concentration.	120
5.5	Spin-flip cross section for out-of-plane spin polarization as a function of carrier concentration.	121
5.6	Spin-flip cross section for in-plane spin polarization as a function of carrier concentration.	121
6.1	Two different situations for spin relaxation in the presence of a non-uniform SOC. When $\ell \ll \mathcal{L}$, the situation resembles the conventional DP mechanism, whereas for $\ell \gg \mathcal{L}$ the same scaling as for the EY mechanism is obtained.	124
6.2	The three diagrams which contribute to Π operator to the lowest order in the spin-lattice coupling.	128
6.3	Schematic behavior of spin relaxation induced by wrinkles of typical size q^{-1} and height $\sqrt{\langle h^2 \rangle}$. The top and bottom lines correspond to $q\ell > 1$ and $q\ell < 1$, respectively. The experimental situation ^[235–237, 253] for electrons and holes in MoS ₂ is denoted by a dot and a star, respectively.	130
6.4	Spin relaxation induced by flexural phonons for different regimes of temperature and disorder. Red dashed line represents T_ℓ	133

7.1	(a) Low-energy spectrum of a semiconducting transition metal dicalcogenide around the \mathbf{K}_{\pm} points of the BZ described by the continuum-limit Hamiltonian in Eq. (7.8). The inset shows the orientation of the stress tensor field discussed through the text with respect to the lattice. (b) Schematic representation of the Landau Levels (LLs) induced in the valence band when strain is applied.	143
7.2	Sketch of the effect of the BZ in a superlattice, and states mixed by the superlattice potential.	148
8.1	Left: 9.3×9.3 moiré structure formed by graphene grown directly on Ir(111). Right: Original moiré unit cell in the intercalated region where the atoms in yellow correspond to the Pb atoms.	155
8.2	Courtesy of Fabián Calleja. A) STM topograph over a graphene/Pb/Ir area located next to a monoatomic step of the Ir(111) substrate. B) Schematic model of the atomic arrangement on the Pb intercalated island. C) Differential conductivity of graphene/Pb/Ir(111) (in red) and graphene/Ir(111) (in blue) at the points indicated by the crosses in panel A. The dI/dV intensity map recorded along the highlighted line in panel A is shown between the spectra at the extremes. D) Energy positions of the peaks as a function of the assigned quantum number n	157
8.3	Unit cells of the hexagonal (C_{6v}) graphene crystal and rectangular (orthorhombic, C_{2v}) substrate of Pb atoms.	159
8.4	Hopping terms which lead to \mathbf{A} at the $\pm\mathbf{K}$ points.	162
8.5	Hopping terms which lead to Δ_{KM} (left) and A_0 (right) at the $\pm\mathbf{K}$ points.	162
8.6	Translation invariance in the zig-zag direction is assumed. The problem for each k_x can be mapped to a 1 dimensional tight-binding chain with 2 atoms per unit cell. A finite chain (the region where the SOC changes) is connected to two semi-infinite leads (where the SOC is taken as a constant). The effect of the semi-infinite leads is incorporated to the Green operator of the chain by means of a self-energy, which is computed from the solution of the Dyson equation for the leads.	164

8.7	(a) Spatial evolution of the SOC across the border of the Pb intercalated regions. The non-uniform SOC profile follows an error function spread in 60 unit cells of graphene along the armchair direction, and the results shown in (b) correspond to the LDOS in the middle. The inset shows a Pb island with its physical edge in black, and the in-plane spin-polarized counter-propagating modes expected at the edges of the region where the SOC changes. The color of the arrows indicates opposite in-plane spin polarizations. (b) LDOS calculated for gr/Pb/Ir(111). A non-uniform SOC with a maximum strength of $\lambda_1 = \lambda_2 = 0.5t$ is assumed. The parameters correspond to $A_x(y) = 2\lambda(y)/at$, $A_y = 0$, and we assume $A_0 = 0.06\sqrt{3}t$ (≈ 0.3 eV). Here t is the first neighbor hopping parameter of graphene (3 eV) and a is the distance between carbon atoms.	165
8.8	LDOS when only the gauge potential \hat{A} is considered (λ_1 and λ_2 hoppings). The values in the legend refer to the maximum value at the center of the Pb islands.	166
8.9	Left: LDOS when both the gauge \hat{A} and scalar \hat{A}_0 potentials are considered. The profile is the same in both cases. The maximum values of the couplings are $\lambda_1 = \lambda_2 = 0.5t$, $\lambda_0 = 0.02t$. Right: LDOS for different values of a non-uniform Kane-Mele coupling.	166
C.1	Left: Real space lattice of graphene on an commensurate Pb monolayer. The unit cell of the system is highlighted within dashed lines. The blue circles represent the Pb atoms. Right: Original hexagonal BZ of graphene and the reduced BZ of graphene commensurate with Pb. The dots represent the folding of high symmetry points of the original BZ.	196
C.2	New hopping terms within the 8 atoms unit cell generated after the integration of the Pb orbitals.	197

List of Acronyms

BZ	Brillouin zone
CVD	Chemical vapour deposition
DFT	Density functional theory
DP	D'yakonov-Perel'
EY	Elliot-Yafet
FQHE	Fractional quantum Hall effect
IQHE	Integer quantum Hall effect
Ir	Iridium
Irrep	Irreducible representation
LEED	Low Energy Electron Diffraction
LL	Landau level
Pb	Lead
LDOS	Local density of states
QFT	Quantum field theory
QHE	Quantum Hall effect
RG	Renormalization group
SOC	Spin-orbit coupling
STM	Scanning tunnel microscopy
STS	Scanning tunnel spectroscopy
TRI	Time reversal invariant
ZA	Flexural acoustic

ZO Flexural optical

PART 0:
PRELIMINARIES

1

Introduction

By two-dimensional (2D) crystals we denote a wide family of novel materials^[1] among which graphene^[2] is the paradigm. Since the 70's and thanks to the ultra-high vacuum technology it has been possible to grow very thin crystals, even one atom thick. However, these solids were metastable in the best scenario, which means, essentially, that only could survive on the metallic substrate where they grew. Of course, this prevented any potential application, and even a careful characterization. The discovery of graphene in 2004,^[3] a single layer of carbon atoms arranged in a honeycomb lattice, constituted a complete revolution in this research line and a milestone in Solid State Physics.

Two different families are usually distinguished among the allotropes of carbon: diamond, unique and very hard, which is a band insulator, and graphite, a semiconductor with multiple applications which goes from pencils to nuclear reactors. Graphite is composed of graphene layers weakly coupled by Van der Waals forces. Geim and Novoselov and their collaborators in the University of Manchester were able to exfoliate graphite down to a single layer. This single layer is mechanically stable and can be transferred to different substrates. Moreover, its transport properties improve when part of the substrate is removed and a portion of the graphene sample remains suspended.^[4]

The graphene-like materials do not end with the single layer, and also bilayer graphene,^[5]

trilayer graphene, *etcetera*, can be exfoliated. These graphene materials can be grown not only by mechanical methods but also by Chemical Vapor Deposition (CVD) techniques,^[6] what allows a good control on the number of layers. As we will see, their electronic properties depend not only on the number of layers, but also on the stacking.

The family of atomically thin 2D crystals goes beyond the allotropes of carbon and already includes materials as silicene^[7,8] (like graphene but made of silicon), graphane C_2H_2 ,^[9] germanane Ge_2H_2 ,^[10] monolayers of hexagonal boron nitride hBN,^[11] or bilayers of gallium chalcogenides Ga_2X_2 .^[12] This thesis deals with transition metal dichalcogenides.^[13] Bulk transition metal dichalcogenides are composed of X-M-X layers stacked on top of each other and also coupled by Van der Waals forces. Like graphite, these materials can be exfoliated down to a single layer.^[14] The transition metal atoms (M) are arranged in a triangular lattice and each one is bonded to six chalcogen atoms (X). From now on we denote these materials by its stoichiometric formula, MX_2 .

In spite of their different chemical composition, these crystals share honeycomb-like lattice and several features in their electronic properties. As we will see, graphene is a multivalley semiconductor: the Fermi level crosses the bands at the two inequivalent corners of the hexagonal Brillouin Zone (BZ). These two points are connected by a very important discrete symmetry, *time reversal symmetry*, which expresses the invariance of the equations of the theory under the inversion of time $t \rightarrow -t$. This fact allows several physical mechanisms to break time reversal symmetry fictitiously within each valley, leading to novel and very interesting phenomena. In the case of MX_2 we must distinguish between the materials with an odd number of electrons per unit cell, such as Niobium or Tantalum compounds, which are metallic and whose Fermi surface is very unstable due to the strong electronic correlations associated to the orbital character of the bands crossed by the Fermi level,^[15] and those with an even number of electrons per unit cell, such as Molybdenum or Tungsten compounds, which are semiconductors where, as in the case of graphene, the Fermi level lies around the two inequivalent corners of the BZ. We focus on the semiconducting compounds.

Despite the similarities just described, there are important differences between graphene and MX_2 regarding the SOC. In order to understand such differences, it is important to keep the origin of the spin-orbit interaction in mind. In non-relativistic quantum mechanics, the spin is introduced as an internal angular momentum that particles possess as an intrinsic property. In some sense, it was introduced *ad hoc* in order to understand some experiments in the early stages of quantum mechanics,^[16] but it was not fully understood until the fusion of quantum mechanics and special relativity, what we know as quantum field theory (QFT). Then, the spin emerges as a property which reflects the invariance of the underlying theory under Lorentz trans-

formations of special relativity. The Lie group associated to such transformations is called the Lorentz group. An electron, which is a spin 1/2 particle, must be described by a mathematical object which transforms non-trivially under this group. This is precisely a spinor ψ , which transforms according to the spinorial representation of the Lorentz group. In such representation the generators of the group are given by the commutators of the gamma matrices γ_μ , which are elements of a Clifford algebra. In 3 spatial dimensions, the simplest representation of the Clifford algebra is in terms of 4×4 matrices, so ψ is a 4-component object. The equation of motion deduced from a relativistic action for ψ is the Dirac equation,^[17]

$$(i\hbar\gamma^\mu\partial_\mu - mc^2)\psi = 0, \quad (1.1)$$

where c is the velocity of light and m is the mass of the particle, an electron in our case. If we assume a dependence on time as $\psi = e^{-iEt/\hbar} \begin{pmatrix} \chi \\ \phi \end{pmatrix}$, where χ , ϕ are 2-component objects, the stationary version of this equation reads

$$\begin{aligned} \mathcal{H}_0 \begin{pmatrix} \chi \\ \phi \end{pmatrix} &= E \begin{pmatrix} \chi \\ \phi \end{pmatrix}, \text{ with} \\ \mathcal{H}_0 &= \begin{pmatrix} mc^2 & c\sigma_i\hat{p}_j \\ c\sigma_i\hat{p}_i & -mc^2 \end{pmatrix}. \end{aligned} \quad (1.2)$$

We have chosen the Dirac representation of γ_μ matrices, so σ_i are Pauli matrices. Let's assume that the electronic dynamics is also affected by a static potential V , so the complete Hamiltonian reads $\mathcal{H}_0 + V$. Then, the spin-orbit interaction arises as a relativistic correction to the electronic dynamics within the potential V . Our aim is to rewrite Eq. (1.2) for the positive energy (particle) sector as a Schrodinger equation. From Eq. (1.2) is clear that χ satisfies the equation

$$(mc^2 - E + V)\chi + c^2\sigma_i\hat{p}_i [E + mc^2 - V]^{-1}\sigma_j\hat{p}_j\chi = 0. \quad (1.3)$$

We define $\epsilon \equiv E - mc^2$, which can be interpreted as the energy of the electron in the non-relativistic limit. Then, Eq. (1.3) can be cast as $(\mathcal{H}_S + V)\chi = \epsilon\chi$ where

$$\mathcal{H}_S = c^2\sigma_i\hat{p}_i [\epsilon + 2mc^2 - V]^{-1}\sigma_j\hat{p}_j.$$

The next step is to expand $[\epsilon + 2mc^2 - V]^{-1}$ in powers of $(\epsilon - V)/2mc^2$ (equivalently, in powers of v^2/c^2 , where v is the velocity of the electron defined as $\sqrt{2m(\epsilon - V)}$):

$$[\epsilon + 2mc^2 - V]^{-1} \approx \frac{1}{2mc^2} \left(1 - \frac{\epsilon - V}{2mc^2} \right) + O(v^4/c^4).$$

After a straightforward calculation \mathcal{H}_S reads

$$\mathcal{H}_S \approx \frac{|\hat{\mathbf{p}}|^2}{2m} + V - \frac{1}{4mc^2} (\epsilon - V) |\hat{\mathbf{p}}|^2 - \frac{[V, \hat{\mathbf{p}}] \cdot \hat{\mathbf{p}}}{4m^2c^2} - \frac{i}{2\hbar m^2c^2} ([V, \hat{\mathbf{p}}] \times \mathbf{p}) \cdot \mathbf{s}. \quad (1.4)$$

The first two terms build the conventional Schrodinger-like Hamiltonian that we would write in order to describe the dynamics of the electron in a non-relativistic theory. The third and fourth terms are relativistic corrections to the kinetic and potential energies that arise to the lowest order in v^2/c^2 . The last one, however, is a purely relativistic term, in the sense that it is non-diagonal in the internal degrees of freedom of the spinor χ . An angular momentum operator $s_i = \hbar\sigma_i/2$ can be defined. This is the electron spin angular momentum, and it is coupled with the orbital degrees of freedom. By expanding the conmutator we get

$$\mathcal{H}_{SO} = \frac{1}{2m^2c^2} (\nabla V \times \mathbf{p}) \cdot \mathbf{s}. \quad (1.5)$$

The electron in a solid suffers in general such relativistic interaction, where V represents the potential created by the crystalline surrounding. If we model V as an hydrogen-like potential of the form $V(r) = -Z/r$, where Z is proportional to the mass of the atomic species of the solid, then we have

$$\mathcal{H}_{SO} = \frac{Z}{2m^2c^2r^3} \mathbf{L} \cdot \mathbf{s}, \quad (1.6)$$

where \mathbf{L} is the orbital angular momentum operator. This last equation tells us that, in general, the spin-orbit effects increase with the mass of the atomic species of the crystal, and its effect is lower for higher orbitals. Furthermore, since in a given atomic orbital the typical distance between the electron and the nucleus of the atom is measured in units of the Bohr radius, which is inversely proportional to Z , we conclude that the strength of the spin-orbit interaction scales approximately as Z^4 .

This fact explains the main difference regarding the SOC between graphene and MX_2 . Carbon is a light material, and therefore, the SOC in graphene is expected to be weak. This opens the door to many potential applications. Spintronics^[18] takes the advantage of the intrinsic spin degree of freedom of the electron in order to encrypt and spread information, as the conventional electronics makes with the electron charge. A good solid-state platform must allow the possibility of manipulating the electron spin at will. The weakness of the SOC and the near absence of C^{13} atoms (with non-vanishing nuclear spin which may lead to electron spin relaxation through the hyperfine interaction) makes graphene an ideal candidate for spintronics devices.

On the other hand, transition metals are heavy atoms, so the SOC in MX_2 is expected to be strong. However, the 2D nature of these materials, together with the lack of

a center of inversion, makes them even more interesting from the point of view of spintronics since the out-of-plane spin polarization is protected precisely by the SOC. The absence of a center of inversion implies that the two out-of-plane spin polarizations are energetically separated around the BZ corners. Time reversal symmetry imposes that this energy difference has opposite sign at each valley. In other words, by tuning the Fermi level conveniently one can populate only one spin polarization in one valley and the opposite one in the other. Such identification between the valley and spin degrees of freedoms is the basis of very interesting phenomena,^[19–22] some of them will be described in detail in this thesis.

The SOC has deeper consequences on the band structure of some solids, something which is in connection with a concept very common in the terminology of Condensed Matter Physics nowadays: *topological order*.^[23] Landau's Fermi liquid and symmetry-breaking theories are the traditional frameworks within which most of the phenomena in Condensed Matter Physics and many-body theory are described. The concept of order is introduced to characterize different states of matter. The definition of order involves phase transitions. Two states have the same order if we can smoothly change from one into the other without passing by a phase transition. Traditionally, different orders are associated to different symmetries. Ginzburg-Landau theory,^[24] the standard theory for phase transitions, is based on this relation, introducing order parameters associated to symmetries.

However, there are some systems whose description goes beyond this picture. The quantum Hall effect (QHE) both in the integer (IQHE)^[25] and fractional (FQHE)^[26] versions are examples of systems where the Landau's theories paradigm breaks down. Therefore, new ways of characterizing order are required. The concept of topological order^[27] arises in order to fill this gap in the theoretical description of phase transitions.

In QFT, topological order is introduced associated to the topology of the fields seen as continuous mappings between topological spaces.^[28] Two fields are topologically equivalent if one can be continuously deformed into the other. This amounts the existence of a continuous mapping (homotopy) between them which defines an equivalence relation. The set of all topological equivalent classes of fields viewed as mappings forms the homotopy group. Then, each field can be uniquely assigned to a certain homotopy class, and consequently, the functional integration defining the theory can be organized as a sum over different topological sectors. The action for each topological sector contains a topological term which depends only on the topological class of the fields (topological charge). There exist different types of topological actions, such as θ -terms or Chern-Simons theories,^[29] which correspond to effective low energy descriptions of the QHE liquid, as Ginzburg-Landau theory corresponds to a continuum description of symmetry-broken phases.

In band theory of solids, the band structure defines a mapping from the crystal momentum \mathbf{k} defined on a torus, the BZ, to the space of Bloch Hamiltonians $\mathcal{H}(\mathbf{k})$. Then, topological order can be introduced for gapped band structures by considering the equivalent classes of $\mathcal{H}(\mathbf{k})$ that can be continuously deformed into another without closing the energy gap. Such topological information is not encrypted in the eigenvalues but in the eigenvectors. It is then necessary to introduce the concept of Berry phase,^[30] a phase picked up by the Bloch wave function $|u_n(\mathbf{k})\rangle$ along an adiabatic evolution path on the parameter space, the BZ in this case,

$$\gamma_n = \int_{\mathcal{C}} d\mathbf{k} \cdot \mathbf{A}_n(\mathbf{k}), \text{ with } \mathbf{A}_n = i \langle u_n(\mathbf{k}) | \nabla_{\mathbf{k}} | u_n(\mathbf{k}) \rangle. \quad (1.7)$$

Here n labels the band. The Berry connection $\mathbf{A}_n(\mathbf{k})$ is gauge dependent, however, for a closed path \mathcal{C} , the Berry phase only can change by an integer multiple of 2π under a gauge transformation in order to ensure that the Bloch wave function is single valued. In that situation, Stokes theorem allows to write

$$\gamma_n = \oint_{\mathcal{C}} d\mathbf{k} \cdot \mathbf{A}_n(\mathbf{k}) = \int_S d^2\mathbf{k} \nabla \times \mathbf{A}_n(\mathbf{k})|_z. \quad (1.8)$$

The Berry curvature $\Omega_n(\mathbf{k}) = \nabla \times \mathbf{A}_n(\mathbf{k})|_z$ can be defined as a truly *local* (not associated to paths), gauge invariant property of the band which characterizes its topological nature. This is more clear if we observe that the integration of the Berry curvature over the entire BZ is an integer multiple of 2π ,

$$C_n = \frac{1}{2\pi} \int_{BZ} d^2\mathbf{k} \Omega_n(\mathbf{k}) \in \mathbb{Z}, \quad (1.9)$$

given that $\Omega_n(\mathbf{k})$ is a 2-form and the BZ is a compact manifold. This integer index C_n , the Chern number, is the topological charge associated to the band n .

The IQHE can be understood from this perspective. Although the original translational invariance is lost due to the presence of the magnetic field and the spectrum is reorganized in Landau levels (LLs), if a new unit cell enclosing a magnetic flux quantum is defined, then the invariance under translations of this new *magnetic lattice* is restored.^[31] Therefore, the eigenstates can still be labeled by a crystal momentum \mathbf{k} in a folded BZ, and the previous discussion is applicable. The origin of the quantized transverse conductivity does not reside in the formation of LL, but in their non-trivial topological character. Furthermore, starting with the Kubo formula^[32] one may see that the transverse conductivity can be written as^[33–36]

$$\sigma_{xy} = \frac{e^2}{\hbar} \sum_n \int_{BZ} \frac{d^2\mathbf{k}}{(2\pi)^2} f_n \Omega_n(\mathbf{k}), \quad (1.10)$$

where f_n is the occupation function of band n . At zero temperature σ_{xy} is quantized in units of e^2/h . The robustness of such quantization is implicit in the topological nature of the Chern number, since it does not change when the Hamiltonian varies smoothly.

It is clear that the breaking of time reversal symmetry plays a crucial role in the QHE physics. Note that in the presence of time reversal symmetry we have $\Omega_n(\mathbf{k}) = -\Omega_n(-\mathbf{k})$ and then $C_n = 0$. It is then when the SOC arises as a fundamental microscopic ingredient in order to generate other non-trivial insulating phases essentially different from the QHE in the sense that time-reversal symmetry is not broken. Let's imagine two fermionic species connected by time reversal symmetry, for instance, the two spin polarizations, and an interaction which acts as an effective magnetic field for each one but with opposite sign in order to preserve time reversal symmetry. The SOC may play the role of such magnetic field. Under certain circumstances, we may have a QHE for each partner. In that situation, we will have a zero Hall conductivity, but non-zero quantized responses are still possible. In the example of spin, it is clear that $\sigma_{xy} = \sigma_{xy}^\uparrow + \sigma_{xy}^\downarrow = 0$, but the spin Hall conductivity defined as $\sigma_{SH} = (\hbar/2e) (\sigma_{xy}^\uparrow - \sigma_{xy}^\downarrow)$ will be proportional to the sum of $C_s = C_\uparrow - C_\downarrow$ of the occupied bands. This is the quantum spin Hall effect (QSHE).^[37] Related ideas were discussed previously in the context of the planar state of ^3He .^[38] The number C_s is a \mathbb{Z}_2 topological invariant,^[39] usually called the spin Chern number, which characterizes the topological nature of time reversal invariant (TRI) bands of 2D systems with well-defined spin polarization (for instance, in the out-of-plane direction). Unless spin is well defined $C_{\uparrow,\downarrow}$ lose its meaning, although a \mathbb{Z}_2 topological invariant can always be defined for time-reversal symmetric 2D systems.^[39-47] In general the topological index for a given system is determined by its dimensionality and the discrete symmetries of the Bloch Hamiltonian.^[48] The notion of time-reversal symmetric topological insulators is not restricted to 2D system,^[45,49,50] but interestingly, also in 3D the SOC is the main microscopic ingredient needed to generate such state.

The \mathbb{Z}_2 nature of the topological index in the QSHE can be understood from the bulk-boundary correspondence.^[51-53] According to this correspondence, at the boundary between two insulators characterized by C_1 and C_2 Chern numbers there are $C_1 - C_2$ chiral (in the sense that they propagate along the edge) modes within the gap connecting bulk conduction and valence bands. These modes are topologically protected against disorder. In the TRI situation, the number of modes is twice, and they are doubly degenerate at the TRI points of the 1D BZ, the center and the edge. In the middle, the degeneracy is lifted in general by the SOC. There are two ways these states can be connected at the TRI points. If pairwise, then these modes can be pushed out by tuning the Fermi level. Otherwise, the Fermi level always intersect an odd number of times. As result, the number of time reversal pairs of edge modes (asuming that

one of the insulators is trivial, $C = 0$) is $(C_{\uparrow} - C_{\downarrow}) / 2 \bmod 2$. Each mode propagates in opposite directions and has opposite spin polarizations. The technological interest on the QSHE is obvious from the point of view of spintronics: in principle, it allows to create pure spin currents protected against disorder.

Structure of the thesis

The thesis is divided in four blocks, including the present introductory part. This includes also a more technical chapter reviewing the basic model Hamiltonians, showing how SOC is introduced both in tight-binding and low-energy effective models and its relation with the QSHE.

Part 1 is devoted to the study of the effect of flexural vibration modes on the electronic properties of graphene. This block is organized in two chapters. In the first chapter the electron-phonon coupling is discussed, with particular emphasis on the acoustic branch. The analysis is applied to the calculation of the resistivity limited by flexural phonons within the Boltzmann equation framework. We compare our results with the mobilities reported in suspended samples, which exhibit a clear quadratic dependence on temperature, as predicted by the theory. The second chapter deals with the effect of these phonon modes on the SOC. We compute their contribution to the Kane-Mele gap, dominated by the optical modes. This phonon-mediated Kane-Mele coupling is almost two orders of magnitude larger than the previously estimated one, so we conclude that the effect of flexural phonons is remarkable.

Part 2 is devoted to spin transport in graphene and MX_2 . We analyze spin relaxation mechanisms induced by the SOC in these materials. The contributions given by the Elliot-Yafet and D'yakonov-Perel' mechanisms are discussed in the first chapter. In the second we analyze how these conventional pictures change when the effect of curvature and flexural phonons is included.

We propose two different routes for engineering topological phases in Part 3. The first one relies on the ability to generate pseudo-magnetic fields by applying strain in MX_2 materials, described in the first chapter. The fact that these effective materials have opposite sign at each valley, together with the opposite spin splitting of the valence band, makes possible to realize the Bernevig-Zhang model in these materials. Also we point out that a superlattice arising from a Moiré pattern can lead to topologically non-trivial subbands in connection with Haldane-Kane-Mele model. The second chapter is devoted to the discussion of a possible QSHE state induced in graphene by the presence of lead. The existence of such state is suggested by STM-STs experiments in graphene on iridium with intercalated lead islands. Intercalated lead induces spin-orbit fields which can be interpreted as non-abelian gauge fields. Spatial variations

of these fields lead to electron confinement and opens topologically non-trivial gaps in the spectrum.

Finally, we conclude with a summary of the results of this thesis and prospects for future work, followed by the bibliography.

2

Model Hamiltonians for SOC and connection with QSHE state

2.1 Introduction

In this introductory chapter we review briefly the basic electronic properties of the 2D crystals discussed through the thesis. We derive effective Hamiltonians around high symmetry points of the BZ that will be employed as starting point in some of the problems tackled in this thesis. We show how to include the SOC both in tight-binding approaches and effective low energy models. Finally, we review the connection of the SOC in graphene with the Haldane's model and the QSHE state.

The physics discussed through the chapter is mostly at the single particle level, based on group theoretical arguments^[54] and tight-binding models.^[55] Many-body effects in graphene materials are nicely reviewed in Ref.56.

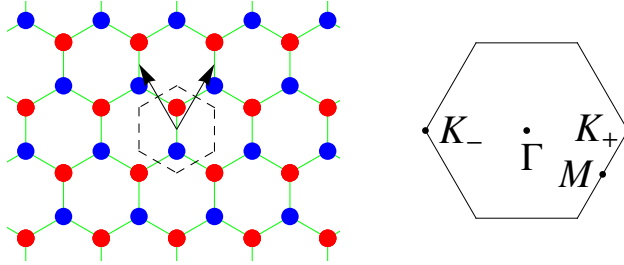


Figure 2.1: Honeycomb lattice (A sublattice in blue, B sublattice in red) and graphene BZ.

2.2 Basic electronic properties

2.2.1 Graphene

Graphene consists on a single layer of sp^2 hybridized carbon atoms. The in-plane $p_{x,y}$ orbitals and the s orbital participate in the strong σ bond which keeps carbon atoms covalently attached forming a trigonal planar structure with a distance between atoms of $a = 1.42$ Å. These σ electrons are the responsible for the structural properties of graphene, in particular its stiffness. The remaining electron occupying the p_z orbital perpendicular to the graphene plane is free to hop between neighboring sites, leading to the π bands responsible for the electronic properties.

The carbon atoms form a honeycomb lattice. The honeycomb lattice is a triangular Bravais lattice with two atoms per unit cell, or equivalently, two interpenetrating triangular sublattices (in this thesis both terminologies are equally employed). The lattice vectors according to Fig. 2.1 are $\mathbf{a}_1 = a/2 (\sqrt{3}, 3)$, $\mathbf{a}_2 = a/2 (-\sqrt{3}, 3)$. The BZ consists on an hexagon. As anticipated, in pristine graphene the Fermi level lies at the two inequivalent corners of the BZ, $\mathbf{K}_\pm = \pm \left(\frac{4\pi}{3\sqrt{3}a}, 0 \right)$, usually called valleys or Dirac points for reasons that will be clear later on.

The point group of the graphene crystal is C_{6v} (for notation, see Appendix A), which contains 12 elements: the identity, five rotations and six reflections in planes perpendicular to the crystal plane. Instead of dealing with degenerate states at two inequivalent points of the BZ one can enlarge the unit cell in order to contain six atoms. Therefore, the folded BZ is three times smaller and the \mathbf{K}_\pm points are mapped onto the Γ point. From the point of view of the lattice symmetries, this means that the two elementary translations $(t_{\mathbf{a}_1}, t_{\mathbf{a}_2})$ are factorized out of the translation group and

added to the point group, which becomes $C''_{6v} = C_{6v} + t_{\mathbf{a}_1} \times C_{6v} + t_{\mathbf{a}_2} \times C_{6v}$.^[57]

This apparent complication is compensated by the fact that this approach allows to treat electronic excitation at the corners of the BZ on the same footing, including also possible inter-valley couplings. The Bloch wave function is given by a 6-component vector which represents the amplitude of the p_z orbitals at the 6 atoms of the unit cell. This vector can be reduced as $A_1 + B_2 + G'$. The 1-dimensional irreducible representations (irreps) A_1 and B_2 correspond to the bonding and anti-bonding states at the original Γ point, whereas G' corresponds to the Bloch states at the original BZ corners. Then, in order to construct the electronic Hamiltonian for quasiparticles around \mathbf{K}_{\pm} points we must consider the 16 hermitian operators acting in a 4-dimensional space. These operators may be classified according to the transformation rules under the symmetry operations of C''_{6v} , taking into account the reduction

$$G' \times G' \sim A_1 + A_2 + B_1 + B_2 + E_1 + E_2 + E'_1 + E'_2 + G'.$$

In principle this can be done without specifying the particular basis over which these operators act, see Appendix A. Nevertheless, in order to make the discussion more clear we introduce the basis $(\psi_{A+}, \psi_{B+}, \psi_{A-}, \psi_{B-})$, where each entry represents the projection of the Bloch wave function around each valley \mathbf{K}_{\pm} on sublattice A/B . Then, we introduce two inter-commuting Pauli algebras σ_i and τ_i associated to sublattice and valley degrees of freedom respectively. The 16 possible electronic operators are generated by considering the direct products of the elements of these algebras (and the identity). Their symmetry properties are summarized in Tab. 2.1. We must take into account also the time reversal operation, which is implemented by the antiunitary operator $\mathcal{T} = \tau_x \mathcal{K}$, where \mathcal{K} represents the complex conjugation operation.

The effective low energy Hamiltonian is constructed as an expansion in powers of the crystalline momentum $\mathbf{q} = (q_x, q_y) \sim E_1$ around \mathbf{K}_{\pm} points. Up to second order in \mathbf{q} we have

$$\mathcal{H} = v (\tau_z \sigma_x q_x + \sigma_y q_y) + \frac{1}{2m_1^*} \left[(q_x^2 - q_y^2) \sigma_x - 2q_x q_y \tau_z \sigma_y \right] + \frac{1}{2m_2^*} (q_x^2 + q_y^2) \mathcal{G}. \quad (2.1)$$

Here v (sometimes we employ v_F), m_1^* and m_2^* must be interpreted as phenomenological constant whose values depend on the microscopic details of graphene. The first term is a Dirac Hamiltonian that describes the approximately conical dispersion of the π bands around \mathbf{K}_{\pm} . These points are usually called Dirac points due to this fact. The second one is the responsible for trigonal warping effects and starts to be important quite away from the Dirac points. The third term introduces electron-hole asymmetry in the spectrum.

A_1	$\mathcal{I} (+)$
A_2	$\tau_z \otimes \sigma_z (-)$
B_1	$\tau_z (-)$
B_2	$\sigma_z (+)$
E_1	$\begin{pmatrix} \tau_z \otimes \sigma_x \\ \sigma_y \end{pmatrix} (-)$
E_2	$\begin{pmatrix} \sigma_x \\ \tau_z \otimes \sigma_y \end{pmatrix} (+)$
E'_1	$\begin{pmatrix} \tau_x \otimes \sigma_x \\ \tau_y \otimes \sigma_x \end{pmatrix} (+)$
E'_2	$\begin{pmatrix} -\tau_y \otimes \sigma_y \\ \tau_x \otimes \sigma_y \end{pmatrix} (-)$
G'	$\begin{pmatrix} -\tau_y \\ \tau_x \otimes \sigma_z \\ -\tau_y \otimes \sigma_z \\ \tau_x \end{pmatrix} (+)$

Table 2.1: Classification of the electronic operators (without spin) according to how they transform under the symmetry operations of C''_{6v} . The signs \pm denote if the operator is even or odd under time reversal.

The Hamiltonian of Eq. (2.1) can be easily inferred from a microscopic theory. In the simplest tight-binding description π electrons are assumed to hop to both nearest neighbor and next nearest neighbor sites. The Hamiltonian in second quantization notation reads^[58-60]

$$\mathcal{H}_{TB} = -t \sum_{\langle i,j \rangle} a_i^\dagger b_j - t' \sum_{\langle\langle i,j \rangle\rangle} (a_i^\dagger a_j + b_i^\dagger b_j) + \text{H.C.} \quad (2.2)$$

Here c_i (c_i^\dagger) annihilates (creates) an electron on site i at sublattice $c = a, b$, and $\langle i, j \rangle$ ($\langle\langle i, j \rangle\rangle$) denotes (next) nearest neighbor sites i, j . By introducing the Fourier series of the electronic operators,

$$c_i = \frac{1}{\sqrt{N_c}} \sum_{\mathbf{k} \in \text{BZ}} e^{i\mathbf{k} \cdot \mathbf{R}_i} c_{\mathbf{k}},$$

where N_c is the number of unit cells, we can write the previous Hamiltonian as $\mathcal{H}_{TB} = \sum_{\mathbf{k}} \Psi_{\mathbf{k}}^\dagger \mathcal{H}_{\mathbf{k}} \Psi_{\mathbf{k}}$, with $\Psi_{\mathbf{k}} = (a_{\mathbf{k}}, b_{\mathbf{k}})$ and

$$\mathcal{H}_{\mathbf{k}} = \begin{pmatrix} -t' \sum_{\vec{\delta}_2} e^{i\mathbf{k} \cdot \vec{\delta}_2} & -t \sum_{\vec{\delta}_1} e^{i\mathbf{k} \cdot \vec{\delta}_1} \\ -t \sum_{\vec{\delta}_1} e^{-i\mathbf{k} \cdot \vec{\delta}_1} & -t' \sum_{\vec{\delta}_2} e^{i\mathbf{k} \cdot \vec{\delta}_2} \end{pmatrix}. \quad (2.3)$$

Here $\vec{\delta}_{1(2)}$ are the vectors connecting (next) nearest neighbors:

$$\vec{\delta}_1 = \left\{ a(0, 1), a \left(\frac{\sqrt{3}}{2}, -\frac{1}{2} \right), a \left(-\frac{\sqrt{3}}{2}, -\frac{1}{2} \right) \right\},$$

$$\vec{\delta}_2 = \{ \mathbf{a}_1, -\mathbf{a}_1, \mathbf{a}_2, -\mathbf{a}_2, \mathbf{a}_1 - \mathbf{a}_2, \mathbf{a}_2 - \mathbf{a}_1 \}.$$

This model describes a semimetal, where the density of states goes linearly to zero when approaching the intrinsic Fermi level,^[61] and certain electron-hole asymmetry introduced by t' . By expanding the exponentials around \mathbf{K}_\pm we obtain the Hamiltonian in Eq. (2.1). The phenomenological constants are related with t and t' as:

$$v = \frac{3ta}{2},$$

$$\frac{1}{m_1^*} = -\frac{3ta^2}{4},$$

$$\frac{1}{m_2^*} = -\frac{9t'a^2}{2}.$$

Typically $10^{-2}t \leq t' \leq 10^{-1}t$,^[62] so the electron-hole asymmetry and the third term in Eq. (2.1) can be neglected. Note also that the trigonal warping term has the same microscopic origin that the prefactor of the Dirac Hamiltonian, even so it comes from a higher order expansion in \mathbf{q} . Thus, it can be also neglected in first approximation. Since $t \approx 3 \text{ eV}$ ^[62] we get $v \approx 10^6 \text{ m/s}$ ($\hbar = 1$). Unless we mention expressly the opposite, v (the Fermi velocity from now on) is the only parameter that we take different from 0 in the effective low energy Hamiltonian of Eq. (2.1).

We have seen that graphene is a semimetal, where the intrinsic Fermi surface consists on two points lying on opposite corners of the BZ (thus, connected by time reversal symmetry), and approximately conical dispersion. The dynamics of long wavelength electronic modes around the Dirac points is well described by a Dirac Hamiltonian of the form

$$\mathcal{H} = -iv\vec{\Sigma} \cdot \nabla, \text{ with } \vec{\Sigma} = (\tau\sigma_x, \sigma_y). \quad (2.4)$$

Here $\tau = \pm 1$ labels the valleys. The difference with respect to Eq. (1.2) is that the matricial structure is not implied by the lorentzian invariance of the theory but due to the double basis and C_{6v} symmetry of graphene crystal. The wave function in momentum space of the electronic excitations around Dirac points reads

$$\psi_{\tau, \mathbf{q}} = \frac{1}{\sqrt{2}} \begin{pmatrix} e^{-\tau i\theta_{\mathbf{q}}/2} \\ \pm \tau e^{\tau i\theta_{\mathbf{q}}/2} \end{pmatrix}, \quad (2.5)$$

where $\theta_{\mathbf{q}} = \arctan \frac{q_y}{q_x}$ and the sign $+$ ($-$) holds for the upper (lower) π band. At this point, two important observations must be outlined:

1. The wave function in Eq. (2.5) has well defined helicity, defined as the projection of the sublattice operator $\vec{\Sigma}$ along the direction of motion $\vec{\Sigma} \cdot \mathbf{q}/|\mathbf{q}|$.
2. Under a complete rotation in momentum space, $\theta_{\mathbf{q}} \rightarrow \theta_{\mathbf{q}} + 2\pi$, the wave function changes sign, indicating that it acquires a phase $\pm\pi$. Actually, a straightforward calculation shows that the Berry curvature of upper/lower ($+/-$) band states is $\mp \frac{\tau}{2} \delta^{(2)}(\mathbf{q})$. Therefore, the wave function acquires a Berry phase of $\mp \tau \pi$ along paths which goes around the Dirac point.

Both observations confirm the spinorial nature of the wave function in Eq. (2.5). Note also that \mathcal{H} is not invariant under rotation about z axis generated by $-i\partial_\theta$ ($\hbar = 1$), as it can be easily checked by computing the commutator $[\mathcal{H}, -i\partial_\theta] = v\nabla \times \vec{\Sigma}|_z \neq 0$, hence, the angular momentum operator must be completed with a purely spinorial part, $L_z = -i\partial_\theta + \frac{\tau}{2}\sigma_z$.

The chiral nature of graphene π electrons is behind many transport and magneto-transport properties of graphene. The Klein paradox,^[63] or the perfect transparency of potential barriers under normal incidence,^[64-67] can be understood as a consequence of helicity conservation. That is why confinement by electrostatic means is a difficult task. Similarly, the $\pm\pi$ Berry phase of the electronic wave function would imply weak antilocalization behavior and then positive magnetoresistance.^[68] However, this expectation is strongly affected by the presence of inter-valley disorder, trigonal warping effects,^[69] and more importantly, some types of disorder, as curvature of the sample, whose coupling with graphene π electrons mimics the effect of magnetic fields, tending to suppress the interference corrections to the conductivity.^[70] As mentioned previously, these pseudo-magnetic fields may emerge as a result of the fictitious time reversal symmetry breaking which occurs at each valley.

The chiral nature of the quasiparticles is also clear in the sequence of Landau levels (LLs). We consider the problem of an uniform magnetic field $B > 0$ perpendicular to the graphene plane within the Dirac theory. In the Landau gauge $\mathbf{A} = (-By, 0)$, the previous Hamiltonian in the minimal coupling prescription admits solutions of the form $\psi = \phi(y) e^{iqx}$, where ϕ satisfies the eigenvalue equation ($\hbar = c = e = 1$)

$$\begin{aligned} \omega_c \begin{pmatrix} 0 & a \\ a^\dagger & 0 \end{pmatrix} \phi &= E\phi \text{ at } \mathbf{K}_+, \text{ and} \\ -\omega_c \begin{pmatrix} 0 & a^\dagger \\ a & 0 \end{pmatrix} \phi &= E\phi \text{ at } \mathbf{K}_-. \end{aligned}$$

The operators a, a^\dagger are usual ladder operators of the one-dimensional harmonic

oscillator defined as $a = (\partial_\zeta + \zeta) / \sqrt{2}$, where the dimensionless coordinate $\zeta \equiv y/\ell_B - \ell_B q$ is introduced. Here $\ell_B = B^{-1/2}$ is the magnetic length and $\omega_c = \sqrt{2}v/\ell_B$ is the cyclotron frequency. The solutions read

$$\begin{aligned}\phi &= \begin{pmatrix} \Psi_{N-1}(\zeta) \\ \pm \Psi_N(\zeta) \end{pmatrix} \text{ at } \mathbf{K}_+, \text{ and} \\ \phi &= \begin{pmatrix} \Psi_N(\zeta) \\ \mp \Psi_{N-1}(\zeta) \end{pmatrix} \text{ at } \mathbf{K}_-, \end{aligned}$$

where $\Psi_N(\zeta)$ are the solutions of the one-dimensional harmonic oscillator, and $N = 0, 1, 2, \dots$ is a positive integer which labels the eigenenergies, given by^[71]

$$E = \pm \omega_c \sqrt{N}. \quad (2.6)$$

This sequence of LLs was confirmed experimentally.^[72,73] There are two important differences with respect to the LL sequence of a conventional 2D electron gas. First, LLs are not equally distributed in energy due to the $N^{1/2}$ dependence. Secondly, and more importantly, the existence of a zero-energy LL, whose wave function reads as $\phi = (0, \Psi_0(\zeta))^T$ at \mathbf{K}_+ and $\phi = (\Psi_0(\zeta), 0)^T$ at \mathbf{K}_- . The zero-energy LL is responsible for the non conventional sequence of plateaus of the transverse conductivity in the QHE regime, in particular the absence of a plateau at $N = 0$. Note that in principle each LL is fourfold degenerate (spin and valley), so following Laughlin's gauge invariance argument^[74] each LL contribute to the Hall conductivity with 4 times the conductance quantum e^2/h , excepting the zero-energy LL, which is shared by electrons and holes. Therefore, the Hall conductivity reads $\sigma_{xy} = \pm 4(N + 1/2)e^2/h$, where N is the index of the last occupied LL and $+$ ($-$) sign holds for electrons (holes).

2.2.2 Bilayer graphene

The point group of bilayer graphene is D_{3d} . The symmetry approach carried out for graphene in order to deduce the form of the electronic Hamiltonian can be employed in this case given that both groups are isomorphic $D_{3d} \cong C_{6v}$. However, although the Hamiltonian in Eq. (2.1) is formally valid, the meaning of the sublattice operators σ_i must be clarified since now there are 4 atoms within the unit cell. We follow the convention of Fig. 2.2. The bonding and anti-bonding combinations of p_z orbitals in the dimer A_1 - B_2 belong, respectively, to the A_2 and A_1 irreps of the wave vector group at \mathbf{K}_\pm , D_3 , whereas the orbitals in the remaining atoms of the unit cell belong to the 2-dimensional E irrep. It can be easily seen that the A_1 and A_2 bands are away from the intrinsic Fermi level an energy of the order of the inter-layer coupling between the atoms of the dimer. The bands around \mathbf{K}_\pm correspond to the E doublet. Thus, the

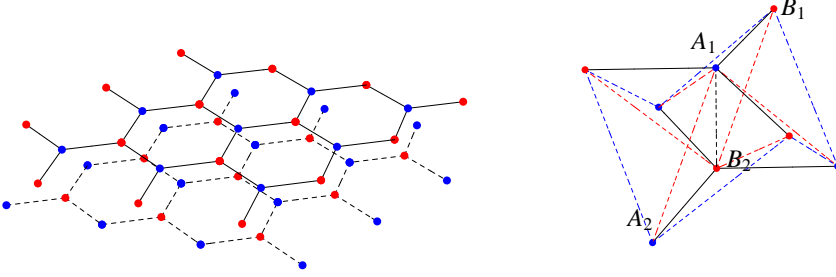


Figure 2.2: Left: Bilayer graphene lattice, continuum line represents top layer, dashed line bottom layer. Blue sites correspond to A sublattice, red sites to B sublattice. Right: 4 atoms unit cell of bilayer graphene and a few neighboring sites. The continuum black line represents the intra-layer hopping parameter γ_0 . The dashed lines represents inter-layer hopping parameters $\gamma_{i=1,3,4}$ (γ_1 in black, γ_3 in blue, γ_4 in red).

Hamiltonian of Eq. (2.1) describes the lowest energy bands, where now sublattice and valley operators act on the basis $(\psi_{B_1+}, \psi_{A_2+}, \psi_{B_1-}, \psi_{A_2-})$.

As before, the phenomenological Hamiltonian can be deduced from a microscopic tight-binding model. For each layer, we consider the Hamiltonian of Eq. (2.2) with $\gamma_0 = t$ and $t' = 0$ for simplicity, and additionally, the inter-layer hopping parameters $\gamma_1, \gamma_3, \gamma_4$ depicted in the right panel of Fig. 2.2. In reciprocal space, the Hamiltonian in first quantization notation reads as the matrix

$$\mathcal{H}_{\mathbf{k}} = \begin{pmatrix} 0 & -\gamma_0 \sum_{\vec{\delta}_1} e^{i\mathbf{k} \cdot \vec{\delta}_1} & \gamma_4 \sum_{\vec{\delta}_1} e^{-i\mathbf{k} \cdot \vec{\delta}_1} & \gamma_1 \\ -\gamma_0 \sum_{\vec{\delta}_1} e^{-i\mathbf{k} \cdot \vec{\delta}_1} & 0 & -\gamma_3 \sum_{\vec{\delta}_1} e^{i\mathbf{k} \cdot \vec{\delta}_1} & \gamma_4 \sum_{\vec{\delta}_1} e^{-i\mathbf{k} \cdot \vec{\delta}_1} \\ \gamma_4 \sum_{\vec{\delta}_1} e^{i\mathbf{k} \cdot \vec{\delta}_1} & -\gamma_3 \sum_{\vec{\delta}_1} e^{-i\mathbf{k} \cdot \vec{\delta}_1} & 0 & -\gamma_0 \sum_{\vec{\delta}_1} e^{i\mathbf{k} \cdot \vec{\delta}_1} \\ \gamma_1 & \gamma_4 \sum_{\vec{\delta}_1} e^{i\mathbf{k} \cdot \vec{\delta}_1} & -\gamma_0 \sum_{\vec{\delta}_1} e^{-i\mathbf{k} \cdot \vec{\delta}_1} & 0 \end{pmatrix}. \quad (2.7)$$

In order to derive the effective Hamiltonian for the low energy sector (non-dimer sites

B_1, A_2), note first that electronic Hamiltonian can be written in the block form

$$\begin{aligned}\mathcal{H}_{\mathbf{k}} &= \begin{pmatrix} \mathcal{H}_d & V \\ V^\dagger & \mathcal{H}_{nd} \end{pmatrix}, \text{ with} \\ \mathcal{H}_d &= \begin{pmatrix} 0 & \gamma_1 \\ \gamma_1 & 0 \end{pmatrix}, \\ \mathcal{H}_{nd} &= \begin{pmatrix} 0 & -\gamma_3 \sum_{\vec{\delta}_1} e^{i\mathbf{k}\cdot\vec{\delta}_1} \\ -\gamma_3 \sum_{\vec{\delta}_1} e^{-i\mathbf{k}\cdot\vec{\delta}_1} & 0 \end{pmatrix}, \\ V &= \begin{pmatrix} -\gamma_0 \sum_{\vec{\delta}_1} e^{i\mathbf{k}\cdot\vec{\delta}_1} & \gamma_4 \sum_{\vec{\delta}_1} e^{-i\mathbf{k}\cdot\vec{\delta}_1} \\ \gamma_4 \sum_{\vec{\delta}_1} e^{i\mathbf{k}\cdot\vec{\delta}_1} & -\gamma_0 \sum_{\vec{\delta}_1} e^{-i\mathbf{k}\cdot\vec{\delta}_1} \end{pmatrix}.\end{aligned}$$

Here \mathcal{H}_d acts over on the subspace span by orbitals at the dimer sites, \mathcal{H}_{nd} on the non-dimer sites, and V mixes them. Around the \mathbf{K}_\pm points, $\mathbf{k} = \mathbf{K}_\pm + \mathbf{q}$, we expand in powers of \mathbf{q} as before. We project out orbitals at dimer sites by a Schrieffer-Wolf transformation.^[75,76] We take the Green function $\mathcal{G} = (\epsilon - \mathcal{H})^{-1}$, evaluate the block \mathcal{G}_{nd} associated to the low-energy sector, and use it in order to identify the low-energy effective Hamiltonian. If we define $\mathcal{G}_{(nd)}^{(0)} = (\epsilon - \mathcal{H}_{(nd)})^{-1}$, then we can write

$$\begin{pmatrix} \mathcal{G}_d & \mathcal{G}_{d-nd} \\ \mathcal{G}_{nd-d} & \mathcal{G}_{nd} \end{pmatrix} = \begin{pmatrix} \left(\mathcal{G}_d^{(0)}\right)^{-1} & -V \\ -V^\dagger & \left(\mathcal{G}_{nd}^{(0)}\right)^{-1} \end{pmatrix}^{-1}$$

We obtain $\mathcal{G}_{nd} = \left[\left(\mathcal{G}_{nd}^{(0)}\right)^{-1} + V^\dagger \mathcal{G}_d^{(0)} V \right]^{-1}$, so $\epsilon - \mathcal{G}_{nd}^{-1} = \mathcal{H}_{nd} + V^\dagger \mathcal{G}_d^{(0)} V$. In the low energy sector ($\epsilon \approx 0$) the effective Hamiltonian reads:

$$\mathcal{H} \approx \mathcal{H}_d - V \mathcal{H}_{nd}^{-1} V^\dagger$$

Up to second order in \mathbf{q} the Hamiltonian in Eq. (2.1) is obtained, where now the phenomenological constants read:

$$\begin{aligned}v &= \frac{3\gamma_3 a}{2}, \\ \frac{1}{m_1^*} &= -\frac{9(t^2 + \gamma_4^2) a^2}{2\gamma_1} - \frac{3\gamma_3 a^2}{4}, \\ \frac{1}{m_2^*} &= \frac{9t\gamma_4 a^2}{\gamma_1}.\end{aligned}\tag{2.8}$$

The first thing that must be noted is that the low energy spectrum remains approximately electron-hole symmetric as in the case of graphene, given that it is governed

by the inter-layer hopping $\gamma_4 \sim 10^{-2}\gamma_0$.^[77] The main difference between single-layer and bilayer graphene is, however, the different microscopic origin of v and m_1^* parameters. In bilayer graphene, the linear term in \mathbf{q} comes from the inter-layer hopping $\gamma_3 \sim 10^{-1}\gamma_0$,^[77] whereas the quadratic term is governed by the intra-layer hopping γ_0 , and it is the result of a second order process involving virtual transitions to the higher bands localized at the dimer sites through the inter-layer hopping γ_1 . As result of this, the quadratic term dominates the low energy physics, and the linear term introduces trigonal warping. Neglecting those, the effective Hamiltonian reads^[76]

$$\mathcal{H} = \begin{pmatrix} 0 & \frac{(\tau q_x - i q_y)^2}{2m_1^*} \\ \frac{(\tau q_x + i q_y)^2}{2m_1^*} & 0 \end{pmatrix}. \quad (2.9)$$

The model describes a metal, since now the density of states at the intrinsic Fermi level remains finite. Furthermore, now it is easy to open a gap in the spectrum by breaking the inversion symmetry and turning the system into a semiconductor. This can be done by applying an electric field perpendicular to the sample.^[76,78,79] In the tight-binding model, that is simulated by different values of the on-site energies at sites B_1 and A_2 . The ability to open a gap makes this system even more interesting for technological applications.

The electronic quasiparticles are also chiral, but now the Berry phase picked up by the wave function along closed paths around Dirac points is $\pm 2\pi$. This means that, for instance, back-scattering is not suppressed as in the case of single-layer graphene.^[67] Therefore, negative magnetoresistance is expected as in conventional 2D electron gas since weak localization effects are restored.^[80] The chirality manifests itself in the QHE plateaus, which are also non conventional. The problem in the Landau gauge can be solved similarly to the case of single-layer. The sequence of LL read ($\hbar = 1$)^[76]

$$E = \pm \omega_c \sqrt{N(N-1)}, \quad (2.10)$$

where now the cyclotron frequency is $\omega_c = (\ell_B^2 m_1^*)^{-1}$. The LLs are almost equally distributed, and the energy separation depends linearly on the applied magnetic field, as in a conventional 2D electron gas. However, there exist a zero-energy LL, then there is no plateau at zero energy. Moreover, the degeneracy of the zero-energy LL is twice the degeneracy of the rest. Hence, applying the same arguments as before, we deduce $\sigma_{xy} = \pm 4(N+1)e^2/h$.

$C_{3h} = C_3 \times \sigma_h$	E	C_3	C_3^2	σ_h	S_3	S_3^2
A'	1	1	1	1	1	1
A''	1	1	1	-1	-1	-1
E'	1	w	w^2	1	w	w^2
	1	w^2	w	1	w^2	w
E''	1	w	w^2	-1	$-w$	$-w^2$
	1	w^2	w	-1	$-w^2$	$-w$

Table 2.2: Character table of C_{3h} , where $w = e^{i\frac{2\pi}{3}}$.

2.2.3 Graphene multilayers

We have seen that there are important differences between single-layer and bi-layer graphene regarding the electronic structure, although in both cases inversion (or sublattice) symmetry imposes that the lowest energy bands touch at the Dirac points, and the elementary excitations are described by chiral Hamiltonians, which is manifest, for instance, in the sequence of Hall conductivity plateaus in the QHE regime. We can consider also graphene stacks with an arbitrary number of layers, and importantly, different stackings. Both the number of layers and the stacking determines the low energy electronic structure. We examine the case of trilayer as a paradigm of what happens in multilayers with an arbitrary number of layers.

We consider first Bernal stacked trilayers. The unit cell is depicted in Fig. 2.3. Differently from the case of monolayer or bilayer, the system is not centrosymmetric. The point group is D_{3h} . Importantly, the wave vector group at the \mathbf{K}_{\pm} points, C_{3h} (check the character table in Tab. 2.2), only contains 1-dimensional irreps. Therefore, a gap at the Fermi level is not precluded by any symmetry. Both the Bloch wave functions of π orbitals at the central atom of the trimer (square in black) and the bonding combination at the top and bottom sites of the trimer (blue and red circles) sites belong to the A'' irrep of C_{3h} . These states can be hybridized in general and form the highest energy bands at energies of order of the inter-layer hopping γ_1 away from the intrinsic Fermi level. The anti-bonding combination of orbitals at the top and bottom layers in the trimer and non-trimer (blue and red squares) sites belong to the A' and E' irreps respectively. States belonging to A' and E' irreps may be hybridized away from the \mathbf{K}_{\pm} , but its degeneracy at these high symmetry points is purely accidental, in the sense that is not protected by the crystal symmetries.^[81] The same happens with the bonding combination at non-trimer sites and the remaining π orbital Bloch state at the non-trimer sites of the intermediate layer, which belong to the two different (related by complex conjugation) E'' irreps.

These symmetry considerations are confirmed by a simple tight-binding calculation

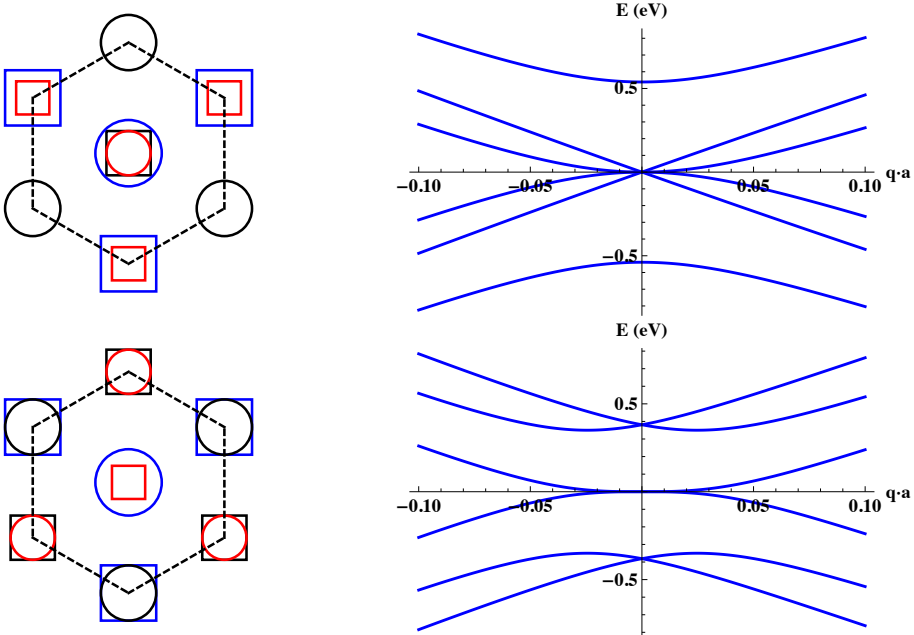


Figure 2.3: Top: Hexagonal unit cell and electronic bands around K_{\pm} points of trilayer graphene in the Bernal stacking. Bottom: The same for rhombohedral stacking. The notation is the same in both cases: in red and blue the atoms of the top and bottom layer, in black atoms of the intermediate layer. Squares correspond to A sites, and circles to B sites. The bands are computed within the tight-binding described through the text with $\gamma_0 = 3.16$ eV, $\gamma_1 = 0.381$ eV.

considering only non-zero γ_0 and γ_1 hopping terms, shown in Fig. 2.3. The states belonging to A'' irrep form the highest energy bands. The rest are degenerate at the Dirac point, but these degeneracies can be completely removed by including additional terms in the Hamiltonian consistent with the symmetries. In the absence of such terms, it is easy to understand that the anti-bonding combination of the orbitals at top and bottom layers form a Dirac cone, similarly to the case of single-layer graphene. However, the inclusion of different on-site energies for trimer and non-trimer sites of these layers opens a gap in the Dirac cone. Similarly, bands associated to the bonding combination and the remaining orbital at the non-trimer site of the intermediate layer look like the lowest energy bands of bilayer graphene. A layer-dependent on-site energy (with the only restriction that it must be the same for bottom and top layers) removes the degeneracy of these bands.

In the case of trilayer graphene with rhombohedral stacking, whose unit cell is shown in Fig. 2.3, the point group is D_{3d} . The bonding and anti-bonding combinations of π orbitals at the central atoms of the unit cell (blue circle and red square) belong to the A_2 and A_1 irreps of D_3 , the wave vector group at \mathbf{K}_\pm . The remaining orbitals at top and bottom layers form a E doublet, similarly to the orbitals at the intermediate layer. The E doublets, which are hybridized in general, form Dirac points away from the intrinsic Fermi level, and these degeneracies are protected by the symmetries of the crystal. The tight-binding calculation confirms this result. The A_1 and A_2 bands are degenerate at zero-energy. Projecting out the orbitals belonging to E irreps by a Schrieffer-Wolf transformation one finds that these bands disperse as $|\mathbf{q}|^3$. Even so, this degeneracy is not protected. For instance, an inter-layer hopping between atoms in the same sublattice of the top and bottom layer removes this degeneracy.

These results can be easily extrapolated to multilayers with an arbitrary number of layers.^[82,83] A Bernal stack with N layers, N even, possesses D_{3d} symmetry. It has $N/2$ electronlike and $N/2$ holelike parabolic bands touching at zero-energy. These degeneracies are protected by the D_{3d} symmetry. The low energy bands can be seen as $N/2$ copies of the low energy model of bilayer graphene. When N is odd, the point group of the crystal is D_{3h} . In the simplest description, an additional band with linear (Dirac) dispersion emerges. However, none of these degeneracies is protected by the crystal symmetries. Rhombohedral stacks (with D_{3d} symmetry in all the cases) have only two bands that touch at zero-energy. In the simplest tight-binding description, the effective low energy Hamiltonian for these bands read

$$\mathcal{H} \propto \frac{\gamma_0^N}{\gamma_1^{N-1}} \begin{pmatrix} 0 & (q_x + iq_y)^N \\ (q_x - iq_y)^N & 0 \end{pmatrix}$$

These bands become surface states localized at the top and bottom layers when $N \rightarrow \infty$. The remaining $2N - 2$ subbands of a rhombohedral stack become Dirac-like.

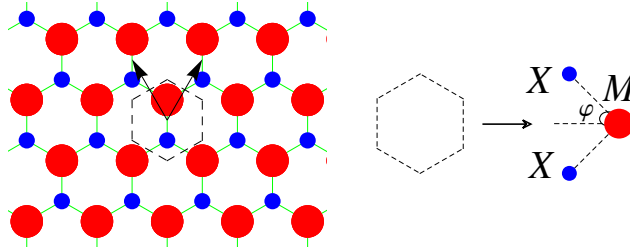


Figure 2.4: Top view of the lattice in real space of MX_2 monolayers.

2.2.4 MX_2

Bulk MX_2 crystals show different polytypes which vary in stacking and atom coordination.^[13,84] As mentioned at the beginning, their electronic properties range from metallic to semiconducting, depending, overall, on the transition metal. In this thesis we focus on semiconducting monolayers^[85,86] such as molybdenum disulfide (MoS_2), tungsten disulfide (WS_2), molybdenum diselenide (MoSe_2), or tungsten diselenide (WSe_2).

The main difference between the bulk and monolayer materials is that the bulk structure is centrosymmetric, whereas the monolayer is not. The point group of the monolayer crystal is D_{3h} , which is the direct product of D_3 , formed by the identity, the three-fold axis perpendicular to the atomic layers and 3 two-fold axes in the plane defined by the transition metal atoms along the directions which connect M and X atoms in a top view of the lattice (see Fig. 2.4), and σ_h , the inversion about the same plane. The lattice is a triangular Bravais lattice with three atoms (2 chalcogen and 1 metal) per unit cell. As in the case of graphene, the BZ consists on an hexagon and the Fermi level lies around the two inequivalent corners \mathbf{K}_\pm .

Nevertheless, the orbital character of the conduction and valence bands is completely different. These bands are dominated by d orbitals from the transition metal atoms, even so, there is a non-negligible weight in the p orbitals from the chalcogens. The symmetry properties of the Bloch wave functions at the BZ corners are summarized in Tab. 2.3 by indicating the suitable combination of atomic orbitals and the associated irreps of C_{3h} , the wave vector group at these points. In the case of X atoms, both bonding (b) and anti-bonding (ab) combinations of orbitals from the bottom and top layers are considered. The second and third column contain the phases picked up by the wave function when a $2\pi/3$ rotation or a mirror reflection is performed.

As in the case of graphene, instead of dealing with degenerate states at inequivalent points of the BZ one can triple the unit cell in such a way that the old \mathbf{K}_\pm points

Irreps	C_3	σ_h	M atom	X atoms
A'	1	1	$\frac{1}{\sqrt{2}} (d_{x^2-y^2} \pm id_{xy})$, $\frac{1}{\sqrt{2}} (p_x \mp ip_y)$	$\frac{1}{\sqrt{2}} (p_x \pm ip_y)$ (b)
A''	1	-1	$\frac{1}{\sqrt{2}} (d_{xz} \mp id_{yz})$	$\frac{1}{\sqrt{2}} (p_x \pm ip_y)$ (ab)
E'	$w^{\pm 1}$	1	$d_{3z^2-r^2}, s$	$\frac{1}{\sqrt{2}} (p_x \mp ip_y)$ (b)
E'	$w^{\mp 1}$	1	$\frac{1}{\sqrt{2}} (d_{x^2-y^2} \mp id_{xy})$, $\frac{1}{\sqrt{2}} (p_x \pm ip_y)$	p_z (ab), s (b)
E''	$w^{\pm 1}$	-1	p_z	$\frac{1}{\sqrt{2}} (p_x \mp ip_y)$ (ab)
E''	$w^{\mp 1}$	-1	$\frac{1}{\sqrt{2}} (d_{xz} \pm id_{yz})$	p_z (b), s (ab)

Table 2.3: Classification of the Bloch wave functions at the Brillouin zone corners according to the irreps of C_{3h} . The sign \pm corresponds to $\pm\mathbf{K}$ points. In the case of X atoms, both bonding (b) and anti-bonding (ab) combinations of orbitals from top and bottom layers are considered. The second and third column contain the phases picked up by the wave function when a $2\pi/3$ rotation or a mirror reflection is performed.

are now equivalent to the Γ point. Then, we consider the new point group $D''_{3h} = D_{3h} + \mathbf{t}_{a_1} \times D_{3h} + \mathbf{t}_{a_2} \times D_{3h}$, whose character table can be found in the Appendix.

Since C_{3h} does not contain 1-dimensional irreps, and given that the crystal fields due to the different atomic species occupying the two triangular sublattices prevent accidental degeneracies, the bands around \mathbf{K}_{\pm} remain gapped, with approximately quadratic dispersion. However, we construct an effective model which describes conduction and valence bands at \mathbf{K}_{\pm} points simultaneously. The conduction band is dominated by $d_{3z^2-r^2}$ orbitals from M, with a smaller contribution from the bonding combination of $p_x \mp ip_y$ orbitals from X atoms ($\sim E'_2$ irrep), whereas the valence band is mostly made of $d_{x^2-y^2} \pm d_{xy}$, with a smaller weight in the bonding combination $p_x \pm ip_y$ ($\sim E'_1$ irrep). We consider the space of 4-vectors $\sim (E'_2, E'_1)$ whose entries represent the projection of the Bloch wave function at conduction and valence states at these points, and construct an effective $\mathbf{k} \cdot \mathbf{p}$ Hamiltonian acting on it. We must consider the possible 16 hermitian matrices acting on this space, whose reduction in terms of irreps of D''_{3h} is inferred from:

$$(E'_2, E'_1) \times (E'_2, E'_1) \sim 2A'_1 + 2A'_2 + 2E' + E'_1 + E'_2 + 2E'_3.$$

As in the case of graphene, this space of electronic operators can be constructed from two commuting Pauli algebras σ_i, τ_i associated to conduction/valence and valleys degrees of freedom. The definitions are summarized in Tab. A.8. The basis is $(\psi_{c+}, \psi_{v+}, \psi_{c-}, \psi_{v-})$, where $\psi_{c,v\pm}$ represents the wave function of the conduction

Irrep	$t \rightarrow -t$ invariant	$t \rightarrow -t$ odd
A'_1	\mathcal{I}, σ_z	
A'_2		$\tau_z, \tau_z \otimes \sigma_z$
E'	$\begin{pmatrix} \sigma_x \\ \tau_z \otimes \sigma_y \end{pmatrix}$	$\begin{pmatrix} \tau_z \otimes \sigma_x \\ \sigma_y \end{pmatrix}$
E'_1	$\begin{pmatrix} \tau_x \otimes \sigma_z + \tau_x \\ \tau_y + \tau_y \otimes \sigma_z \end{pmatrix}$	
E'_2	$\begin{pmatrix} \tau_x - \tau_x \otimes \sigma_z \\ \tau_y - \tau_y \otimes \sigma_z \end{pmatrix}$	
E'_3	$\begin{pmatrix} \tau_x \otimes \sigma_x \\ \tau_y \otimes \sigma_x \end{pmatrix}$	$\begin{pmatrix} -\tau_y \otimes \sigma_y \\ \tau_x \otimes \sigma_y \end{pmatrix}$

Table 2.4: Definitions of the electronic operators in the two bands effective model at \mathbf{K}_\pm points.

or valence state at \mathbf{K}_\pm points, in such a way that the time reversal operation reads $i\tau_x \mathcal{K}$. The Hamiltonian up to second order in \mathbf{q} reads

$$\begin{aligned} \mathcal{H} = v \left(\tau_z \sigma_x q_x + \sigma_y q_y \right) + \frac{\Delta}{2} \sigma_z + \frac{1}{2m_1^*} \left(q_x^2 + q_y^2 \right) \mathcal{I} + \frac{1}{2m_2^*} \left(q_x^2 + q_y^2 \right) \sigma_z + \\ + \frac{1}{2m_3^*} \left[\left(q_x^2 - q_y^2 \right) \sigma_x - 2q_x q_y \tau_z \sigma_y \right]. \end{aligned} \quad (2.11)$$

This Hamiltonian looks like Eq. 2.1 with two additional terms proportional to σ_z . It describes a semiconductor with a gap Δ . Parameters m_1^* and m_2^* are associated to the different effective masses of electrons and holes. The third term introduces trigonal warping of conduction and valence bands.

We may derive the Hamiltonian in Eq. 2.11 from a microscopic theory. We consider a simplified tight-binding Hamiltonian acting on the subspace span by the symmetry-adapted Bloch wave functions $|\mathbf{M} d_{3z^2-r^2}\rangle$, $|\mathbf{M} d_{x^2-y^2} + \tau i d_{xy}\rangle$, $|\mathbf{X}(\mathbf{b}) p_y + i\tau p_x\rangle$, and $|\mathbf{X}(\mathbf{b}) p_y - i\tau p_x\rangle$. The model is strictly valid around \mathbf{K}_τ points, where $\tau = \pm 1$ labels the valleys. We consider the crystal field parameters:

$$\begin{aligned} \langle \mathbf{M} d_{3z^2-r^2} | \mathcal{H}_{TB} | \mathbf{M} d_{3z^2-r^2} \rangle &= \Delta_0, \\ \langle \mathbf{M} d_{x^2-y^2} + \tau i d_{xy} | \mathcal{H}_{TB} | \mathbf{M} d_{x^2-y^2} + \tau i d_{xy} \rangle &= \Delta_2, \\ \langle \mathbf{X}(\mathbf{b}) p_y \pm \tau i p_x | \mathcal{H}_{TB} | \mathbf{X}(\mathbf{b}) p_y \pm \tau i p_x \rangle &= \Delta_p, \end{aligned}$$

and also the hopping integrals sketched in Fig. 2.5, which can be expressed in terms

of the two-center Slater-Koster parameters $V_{dp\sigma}$, $V_{dp\pi}$ ^[55] as

$$\begin{aligned} t_x &= \frac{\sqrt{3}}{2} V_{pd\sigma} \cos \varphi, \\ t_y &= -V_{pd\pi} \cos \varphi, \\ t_z &= \cos \varphi \left(\sin^2 \varphi - \frac{1}{2} \cos^2 \varphi \right) V_{pd\sigma} - \sqrt{3} \cos \varphi \sin^2 \varphi V_{pd\pi}. \end{aligned}$$

The angle φ is introduced in Fig. 2.4. The matrix elements between Bloch states of orbitals of M and X atoms at \mathbf{k} read

$$\begin{aligned} \langle \text{M } d_{3z^2-r^2} | \mathcal{H}_{TB} | \text{X (b) } p_y \pm i\tau p_x \rangle &= \sum_{\hat{\delta}} e^{-i\mathbf{ak} \cdot \hat{\delta}} t_z (\hat{y} \pm i\tau \hat{x}) \cdot \hat{\delta}, \\ \langle \text{M } d_{x^2-y^2} + \tau i d_{xy} | \mathcal{H}_{TB} | \text{X (b) } p_y \pm i\tau p_x \rangle &= \\ = \sum_{\hat{\delta}} e^{-i\mathbf{ak} \cdot \hat{\delta}} t_x (\hat{y} \pm i\tau \hat{x}) \cdot \hat{\delta} \times \left[2 (\hat{x} \cdot \hat{\delta})^2 - 2i\tau (\hat{x}\hat{y} \cdot \hat{\delta})^2 + i\tau - 1 \right] + \\ + \sum_{\hat{\delta}} e^{-i\mathbf{ak} \cdot \hat{\delta}} t_y (\hat{y} \pm i\tau \hat{x}) \cdot \hat{\delta}_{\perp} \times \left[2 (\hat{\delta} \cdot \hat{x}) (\hat{\delta}_{\perp} \cdot \hat{x}) - 2i\tau (\hat{\delta} \cdot \hat{x}\hat{y}) (\hat{\delta}_{\perp} \cdot \hat{x}\hat{y}) \right], \end{aligned}$$

where we define the unit vectors:

$$\begin{aligned} \hat{x} &= (1, 0), \\ \hat{y} &= (0, 1), \\ \hat{x}\hat{y} &= \frac{1}{\sqrt{2}} (1, 1), \\ \text{and } \hat{\delta}_{\perp} &= (\delta_y, -\delta_x), \end{aligned}$$

with $\hat{\delta} = (\delta_x, \delta_y)$, the three unit vectors in the direction connecting nearest neighbors in the honeycomb lattice, previously introduced.

The bands deduced from this model in the case of MoS₂ are shown in Fig. 2.6. The values of the tight-binding parameters for MoS₂ are summarized in Tab. 2.5. Next, we derive the two-bands Hamiltonian in Eq. 2.11 from this tight-binding model.

At \mathbf{K}_{\pm} points the Hamiltonian in first quantization notation reads as the matrix

$$\mathcal{H}_{\mathbf{K}_{\pm}} = \begin{pmatrix} \Delta_0 & 0 & 3t_z & 0 \\ 0 & \Delta_2 & 0 & -3(t_x + t_y) \\ 3t_z & 0 & \Delta_p & 0 \\ 0 & -3(t_x + t_y) & 0 & \Delta_p \end{pmatrix}.$$

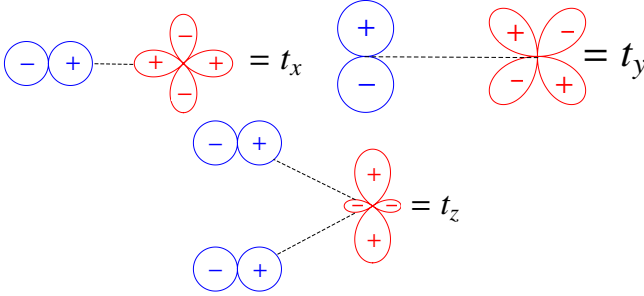
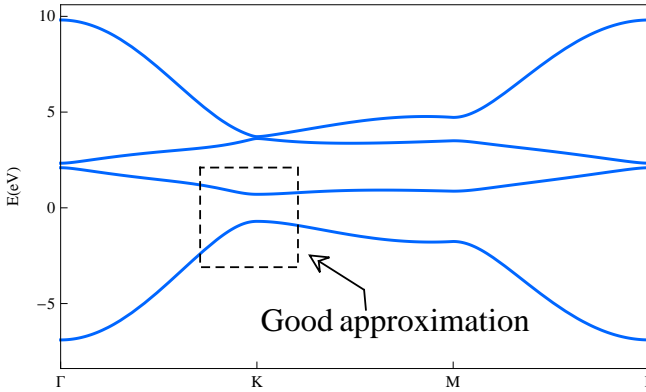


Figure 2.5: Hopping integrals considered in the tight-binding model.

Tight-binding parameter	Value (eV)	Phenomenological parameter	Value (eV)
Δ_0	-1.512	Δ	1.41
Δ_2	-3.025	$a^{-1}v$	1.19
Δ_p	-1.276	$(a^2 m_1^*)^{-1}$	0.28
$V_{pd\sigma}$	-2.619	$(a^2 m_2^*)^{-1}$	-0.03
$V_{pd\pi}$	-1.396	$(a^2 m_3^*)^{-1}$	0.04

 Table 2.5: Left: Tight-binding parameters considered in the calculation and their values for MoS₂ taken from Ref.87. Right: Phenomenological parameters of Eq. (2.11) deduced from the tight-binding model for MoS₂. Here a is the lattice parameter, and $\varphi = \arctan \sqrt{3}/2$.

 Figure 2.6: Bands calculated within the tight-binding model described in the text. The model is only valid around K_τ points (highlighted in the figure). We take the values summarized in Tab. 2.5 for MoS₂.

By diagonalizing this Hamiltonian we obtain the eigenvectors of the Bloch states maximally localized at $d_{3z^2-r^2}$ and $d_{x^2-y^2} + i\tau d_{xy}$ respectively, which define the conduction and band states respectively,

$$|\psi_c\rangle = \frac{1}{\sqrt{1+|\alpha|^2}} \begin{pmatrix} 1 \\ 0 \\ \alpha \\ 0 \end{pmatrix},$$

$$|\psi_v\rangle = \frac{1}{\sqrt{1+|\beta|^2}} \begin{pmatrix} 0 \\ 1 \\ 0 \\ \beta \end{pmatrix},$$

where

$$\alpha = -\frac{6t_z}{\sqrt{36t_z^2 + (\Delta_p - \Delta_0)^2} + \Delta_p - \Delta_0},$$

$$\beta = \frac{6(t_x + t_y)}{\sqrt{36(t_x + t_y)^2 + (\Delta_p - \Delta_2)^2} + \Delta_p - \Delta_2}.$$

The $\mathbf{k} \cdot \mathbf{p}$ Hamiltonian is just

$$\mathcal{H}_{\mathbf{k}\mathbf{p}} = \begin{pmatrix} \langle \psi_c | \mathcal{H}_{TB} | \psi_c \rangle & \langle \psi_c | \mathcal{H}_{TB} | \psi_v \rangle \\ \langle \psi_v | \mathcal{H}_{TB} | \psi_c \rangle & \langle \psi_v | \mathcal{H}_{TB} | \psi_v \rangle \end{pmatrix}. \quad (2.12)$$

If we write $\mathbf{k} = \mathbf{K}_\tau + \mathbf{q}$ and expand in powers of \mathbf{q} up to first order we get the

Hamiltonian of Eq. (2.11) with:

$$\begin{aligned}
 \Delta &= \frac{1}{2} \left(\Delta_0 - \Delta_2 - \sqrt{36tz^2 + (\Delta_0 - \Delta_p)^2} + \sqrt{36(t_x + t_y)^2 + (\Delta_2 - \Delta_p)^2} \right), \\
 v &= \frac{\sqrt{3}a [\alpha (t_x - t_y) + \beta t_z]}{2\sqrt{1 + |\alpha|^2}\sqrt{1 + |\beta|^2}}, \\
 \frac{1}{m_1^*} &= \frac{a^2\beta (t_x + t_y)}{2(1 + |\beta|^2)} - \frac{a^2\alpha t_z}{2(1 + |\alpha|^2)}, \\
 \frac{1}{m_2^*} &= \frac{a^2\beta (t_x + t_y)}{2(1 + |\beta|^2)} - \frac{a^2\alpha t_z}{2(1 + |\alpha|^2)}, \\
 \frac{1}{m_3^*} &= \frac{a^2(\beta t_z + \alpha t_y - \alpha t_x)}{4\sqrt{1 + |\alpha|^2}\sqrt{1 + |\beta|^2}}. \tag{2.13}
 \end{aligned}$$

Numerical values for these parameters in the case of MoS₂ are summarized in Tab. 2.5. The model reproduces well the main features of the conduction and valence bands around \mathbf{K}_\pm as compared with more sophisticated tight-binding^[87–89] and first principles calculations.^[90–95]

Conduction and valence band states are strongly hybridized away from \mathbf{K}_\pm , check the value of $a^{-1}v$ in comparison with $(a^2m_1^*)^{-1}$, $(a^2m_2^*)^{-1}$, $(a^2m_3^*)^{-1}$. Therefore, a massive Dirac Hamiltonian (neglecting quadratic terms in Eq. (2.11)) is a good approximation in order to describe both bands simultaneously. It is important to note that the 2-component wave function in this case is not a spinor. Indeed, it can be seen that the Berry curvature is not singular in this case:^[19]

$$\Omega_{\mathbf{q}}^{\tau,c/v} = \mp \tau \frac{2v^2\Delta}{(\Delta^2 + 4v^2|\mathbf{q}|^2)^{3/2}}. \tag{2.14}$$

The Berry phase accumulated by electronic states at the conduction (+) or valence (−) bands around \mathbf{K}_\pm is approximately $\pm\tau 2\pi \frac{\mu+\Delta}{2\mu+\Delta} \sim \pm\tau 2\pi$ (here μ is the chemical potential measured from the bottom/top of the conduction/valence band), so we expect negative magnetoresistance behavior^[96] and a regular sequence of plateaus in the QHE regime.

However, although non-singular, this non-zero Berry curvature produces an anomalous term in the velocity operator of the electron in the presence of in-plane electric fields which is the origin of the intrinsic contribution to the Hall conductivity.^[97–99]

Of course, this is zero due to time reversal symmetry, expressed in the fact that both valleys contribute with opposite sign. When considering the SOC, we will see that the Berry curvature of Eq. (2.14) is the origin of a non-zero (but not quantized) spin Hall conductivity.^[19, 94, 100] The SOC physics also affects the weak localization corrections to classical conductivity.^[101]

2.3 SOC in 2D hexagonal crystals

We discuss now how the electronic structure of these 2D materials changes when the spin-orbit interaction is included, in particular the low energy physics around \mathbf{K}_\pm points.

If we wanted to employ group theoretical arguments as in the previous section in order to describe spinful bands, in principle we should adapt our basis of Bloch states around high symmetry points of the BZ to the irreps of the double group associated to the original point group of the crystal. The double group consists on the original symmetry operations of the crystal plus the rotation by 2π , which is not longer equivalent to the identity for a spin 1/2 particle. Due to the inclusion of this rotation, the point group has now twice as many elements as before, however, the number of irreps is not in general twice as many as before. Among the new irreps, we have $D_{1/2}$, the 2-dimensional irrep associated to the spinorial part of the wave function. Microscopically, we have that, due to the inclusion of the SOC, the eigenstates of the electronic Hamiltonian are not longer eigenstates of the spin operators s_i , so the wave function becomes some linear combination of states with different spin polarizations (at different bands). The way to describe these states is in terms of the product $\Gamma \times D_{1/2}$, where Γ is the irrep of the double group associated to the orbital part of the wave function.

However, in the practice this approach can be simplified. The point is that typically the strength of the spin-orbit interaction is much weaker than the energy separation between states with different spin polarizations that are coupled by the SOC, therefore, the main orbital character of the bands does not change much. This is clearly true in the case of graphene materials, where the SOC is weak due to the lightness of carbon. But it is also true in the case of MX_2 , although the spin-orbit interaction is much stronger, given that the energy separation between different bands is governed by crystal fields of the order of several electron volts.

As consequence, we can construct the SOC terms by considering the previous analysis and adding a new set of Pauli matrices $\{s_i\}$ acting on the spin degrees of freedom. In order to construct invariants, we must determine the transformation rules of such operators. In order to do so, we must take into account that, on the one hand, spin

$\mathbf{s} = (s_x, s_y, s_z)$ is a 3D angular momentum operator, and on the other, all the systems that we are going to study possess a mirror symmetry plane. Therefore, if we choose $s_{x,y}$ as the spin components in the mirror symmetry plane (in-plane components from now on), it is clear that (s_x, s_y) will belong to a pseudo-vectorial irrep. Similarly, s_z will belong to a pseudo-scalar irrep.

Within the context of tight-binding models the SOC can be introduced by means of a pure intra-atomic spin-orbit interaction of the form

$$\mathcal{H}_{SO} = \Delta_{SO} \mathbf{L} \cdot \mathbf{s}, \quad (2.15)$$

where \mathbf{L} is the atomic angular momentum operator and Δ_{SO} represents the strength of the spin-orbit interaction for the subspace of orbitals considered in the calculation. In that sense, it may be interpreted as an additional tight-binding parameter.

2.3.1 Graphene materials

In the case of graphene it is not difficult to see that $(-s_y, s_x) \sim E_1$, $s_z \sim A_2$. Importantly, since we are now introducing a pseudovector in 3D space and graphene is truly a 2D system, we must distinguish between the SOC terms which contain s_z , that are even under a reflection in the graphene plane (mirror symmetry operation, $z \rightarrow -z$), and the terms which contain the in-plane components, which are odd. This mirror symmetry protects the out-of-plane spin polarization. Note also that the time reversal operator, including the spin degree of freedom, reads now $\mathcal{T} = i s_y \tau_x \mathcal{K}$. The possible SOC terms at \mathbf{K}_{\pm} points and their symmetry properties are summarized in Tab. 2.6.

The intrinsic SOC has the form of a mass term with opposite sign at different valleys and spin projections,^[37]

$$\mathcal{H}_{KM} = \Delta_{KM} \sigma_z \otimes \tau_z \otimes s_z. \quad (2.16)$$

Therefore, it opens a gap in the spectrum. As it will be discussed in detail later on, this gap possesses topologically non-trivial properties.

If the mirror symmetry of the system is broken, for instance, by the presence of the substrate or the application of an electric field perpendicular to the graphene sample, then a Bychkov-Rashba term is generated,^[37, 102]

$$\mathcal{H}_{BR} = \Delta_{BR} (\sigma_x \otimes \tau_z \otimes s_y - \sigma_y \otimes s_x). \quad (2.17)$$

This term splits the double degeneracy of the bands, a manifestation of the inversion symmetry breaking, and tends to close the Kane-Mele gap.

Irrep	$z \rightarrow -z$ symmetric	$z \rightarrow -z$ asymmetric
A_1	$\sigma_z \otimes \tau_z \otimes s_z$	$\sigma_x \otimes \tau_z \otimes s_y - \sigma_y \otimes s_x$
A_2		$\sigma_x \otimes \tau_z \otimes s_x + \sigma_y \otimes s_y$
B_2	$\tau_z \otimes s_z$	
E_1	$\begin{pmatrix} -\sigma_y \otimes s_z \\ \sigma_x \otimes \tau_z \otimes s_z \end{pmatrix}$	$\begin{pmatrix} -\sigma_z \otimes \tau_z \otimes s_y \\ \sigma_z \otimes \tau_z \otimes s_x \end{pmatrix}$
E_2		$\begin{pmatrix} \sigma_x \otimes \tau_z \otimes s_y + \sigma_y \otimes s_x \\ \sigma_x \otimes \tau_z \otimes s_x - \sigma_y \otimes s_y \end{pmatrix}, \begin{pmatrix} -\tau_z \otimes s_y \\ \tau_z \otimes s_x \end{pmatrix}$
E'_1	$\begin{pmatrix} -\sigma_y \otimes \tau_y \otimes s_z \\ \sigma_y \otimes \tau_x \otimes s_z \end{pmatrix}$	
G'		$\begin{pmatrix} -\sigma_y \otimes \tau_y \otimes s_x \\ -\sigma_y \otimes \tau_y \otimes s_y \\ \sigma_y \otimes \tau_x \otimes s_y \\ \sigma_y \otimes \tau_x \otimes s_x \end{pmatrix}$

Table 2.6: SOC terms within the low energy description of graphene.

Several *ab initio*^[103–105] and tight-binding^[106–108] studies in the recent years confirm this analysis. The spin-orbit interaction in confined geometries as graphene nanoribbons^[109–113] have been extensively studied also.

The minimal tight-binding model which captures spin-orbit effects should include at least both π and σ orbitals. The simplest model consists on an extension of the one presented in Eq. (2.2) with four orbitals $\{s, p_x, p_y, p_z\}$ per carbon atom and only nearest-neighbors hoppings,

$$\mathcal{H}_{TB} = \sum_{i,\lambda} t_\lambda c_{i,\lambda}^\dagger c_{i,\lambda} + \left[\sum_{\langle i,j \rangle} \sum_{\lambda,\lambda'} t_{\lambda,\lambda'}^{ij} c_{i,\lambda}^\dagger c_{j,\lambda'} + \text{H.C.} \right], \quad (2.18)$$

where the latin indices label the sites of the carbon atoms and $\lambda = s, p_x, p_y, p_z$ labels the orbitals considered in the calculation. For the on-site energies, we take $t_s = \epsilon_s$, $t_{p_i} = \epsilon_{p_i}$. The two-center matrix elements can be computed within the Slater-Koster approximation^[55] as indicated in Tab. 2.7. The electronic bands computed within this tight-binding approximation are shown in Fig. 2.7. We take the values summarized in Tab. 2.7.^[114, 115]

In order to estimate the strength of the effective SOC terms within the low energy sector of the electronic spectrum we include the spin-orbit interaction, Eq. (2.15),

2. MODEL HAMILTONIANS FOR SOC AND CONNECTION WITH QSHE STATE

$t_{s,s}^{AB}$	$V_{ss\sigma}$	TB parameter	Value (eV)
		ϵ_s	-7.3
t_{s,p_i}^{AB}	$(\hat{p}_i \cdot \vec{\delta}) V_{sp\sigma}$	ϵ_p	0
		$V_{ss\sigma}$	-3.63
t_{p_i,p_j}^{AB}	$(\hat{p}_i \cdot \vec{\delta})(\hat{p}_j \cdot \vec{\delta}) V_{pp\sigma} +$ $+ [(\hat{p}_i \cdot \hat{p}_j) - (\hat{p}_i \cdot \vec{\delta})(\hat{p}_j \cdot \vec{\delta})] V_{pp\pi}$	$V_{sp\sigma}$	4.2
		$V_{pp\sigma}$	5.38
		$V_{pp\pi}$	-2.24

Table 2.7: Two-center matrix elements in the Slater-Koster approximation as function of the tight-binding parameters (see the text). \hat{p}_i represents a unitary vector in the direction of maximum amplitude of the orbital p_i , and $\vec{\delta}$ is the vector which connects neighboring sites A and B.

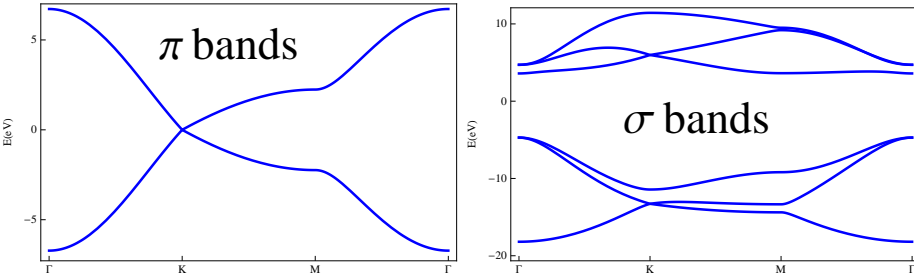


Figure 2.7: Electronic bands deduced from the tight-binding model of Eq. (2.18). The values of the Slater-Koster parameters are summarized in Tab. 2.7.

and we rewrite the complete Hamiltonian in the block form

$$\mathcal{H}_{TB} + \mathcal{H}_{SO} = \begin{pmatrix} \mathcal{H}_\pi & \mathcal{H}_{\pi\sigma} \\ \mathcal{H}_{\sigma\pi} & \mathcal{H}_\sigma \end{pmatrix}. \quad (2.19)$$

Then, we project out σ orbitals by a Schrieffer-Wolf transformation^[75] as we explained in the case of bilayer graphene when we reduced the 4-bands tight-binding model to a 2-bands effective model. Then, in the low energy sector we have

$$\mathcal{H}_\pi^{\text{eff}} \approx \mathcal{H}_\pi - \mathcal{H}_{\pi\sigma} \mathcal{H}_\sigma^{-1} \mathcal{H}_{\sigma\pi}. \quad (2.20)$$

In the absence of a mirror symmetry breaking term which hybridizes π (odd under a mirror reflection) and σ (even under a mirror reflection) orbitals, only the spin-orbit interaction enters in the $\pi - \sigma$ mixing blocks. The SOC term that appears to the lowest order in the spin-orbit interaction strength has the form of a Kane-Mele coupling, Eq. (2.16), with^[106-108]

$$\Delta_{KM} = \frac{\epsilon_s \Delta_{SO}^2}{18V_{sp\sigma}^2} \approx 9 \mu\text{eV}. \quad (2.21)$$

The coupling is quadratic on the spin-orbit interaction strength. The numerical estimation has been performed assuming $\Delta_{SO} = 20 \text{ meV}$.^[116]

If the mirror symmetry is broken, then a SOC term linear in the spin-orbit interaction strength is feasible. Obviously, this term should be proportional to the in-plane components of spin, and in general it will be of the form of the Bychkov-Rashba term of Eq. (2.17). The most handy example is the case of an electric field perpendicular to the graphene sample. Assuming a dipolar interaction of the form $\mathcal{H}_d = eE_z \cdot z$, it is easy to see that transitions between s and p_z orbitals are induced proportional to $\lambda \equiv \langle s|z|p_z \rangle$. If we include this perturbation in the previous scheme we obtain a Bychkov-Rashba coupling, Eq. (2.17), with^[106-108]

$$\Delta_{BR} = \frac{2eE_z \lambda}{3V_{sp\sigma}} \quad (2.22)$$

We have excluded higher energy orbitals, in particular d orbitals, from our analysis because: i) they are very separated in energy from p_z orbitals, so a possible hybridization between them should be very small, and ii) as Eq. (1.6) suggests, the spin-orbit interaction for these orbitals should be weaker. However, since the intrinsic contribution to the SOC is the result of a second order process and the coupling is then quadratic on Δ_{SO} as we have seen, where, indeed, Δ_{SO} represents the lowest energy scale of the problem, it is in principle necessary to reconsider our arguments.

As it was pointed out first by Slonczewski and Weiss^[60] in the context of graphite and showed by recent *ab initio* calculations,^[104] d orbitals contribute remarkably to the Kane-Mele coupling. This is because there is a non-negligible contribution of a certain combination of d_{xz} and d_{yz} orbitals to the π bands. Such combination,

$$\left(\begin{array}{c} \left| \frac{1}{\sqrt{2}} (d_{xz} - id_{yz}), A, \mathbf{K}_+ \right\rangle \\ \left| \frac{1}{\sqrt{2}} (d_{xz} + id_{yz}), B, \mathbf{K}_+ \right\rangle \\ \left| \frac{1}{\sqrt{2}} (d_{xz} + id_{yz}), A, \mathbf{K}_- \right\rangle \\ \left| \frac{1}{\sqrt{2}} (d_{xz} - id_{yz}), B, \mathbf{K}_- \right\rangle \end{array} \right) \sim G', \quad (2.23)$$

belongs to the 4-dimensional irrep of C''_{6v} . The weight of these orbitals on π bands is proportional to $3V_{pd\pi}/2\sqrt{2}\epsilon_d$.^[108] Therefore, the contribution from these orbitals to the Kane-Mele coupling would be^[108]

$$\Delta_{KM}^{(d)} \propto \frac{9V_{pd\pi}^2 \Delta_{SO}^{(d)}}{8\epsilon_d^2}, \quad (2.24)$$

where $\Delta_{SO}^{(d)}$ is the strength of the spin-orbit interaction in the subspace of d orbitals. According to *ab initio* calculations,^[104] $\Delta_{KM}^{(d)} \sim 12 \mu\text{eV}$.

As we have seen, the Kane-Mele gap induced by the spin-orbit interaction in graphene is very weak, of the order of few μeV . However, that is not the complete story. As Kane and Mele pointed out in their seminal paper,^[37] electron-electron interactions may help to stabilize this insulating phase by increasing the value of the gap. This can be seen within the same renormalization group (RG) analysis which leads to the renormalization of the Fermi velocity v .^[117–120] We consider the effective action associated to the Hamiltonian of Eq. (2.4) plus the SOC term of Eq. (2.16) and the presence of long-range Coulomb interactions (we set the chemical potential $\mu = 0$):

$$\begin{aligned} S &= S_{free} + S_{int}, \\ S_{free} &= S_0 + S_{mass}, \end{aligned}$$

where ($\hbar = 1$)

$$\begin{aligned}
 S_0 &= \int dt d^2\mathbf{x} \Psi^\dagger(\mathbf{x}) (i\partial_t + iv\vec{\Sigma} \cdot \nabla) \Psi(\mathbf{x}), \\
 S_{mass} &= \tau s \Delta_{KM} \int dt d^2\mathbf{x} \Psi^\dagger(\mathbf{x}) \sigma_z \Psi(\mathbf{x}), \\
 S_{int} &= \int dt d^2\mathbf{x} d^2\mathbf{x}' \frac{g}{|\mathbf{x} - \mathbf{x}'|} \Psi^\dagger(\mathbf{x}) \Psi(\mathbf{x}) \Psi^\dagger(\mathbf{x}') \Psi(\mathbf{x}').
 \end{aligned} \tag{2.25}$$

We have introduced the valley $\tau = \pm 1$ and spin $s = \pm 1$ indices. Of course, this model is only valid for wavelenths bigger than Λ^{-1} , where Λ is a certain ultraviolet cutoff in momentum space. We have introduced a long-range Coulomb interaction, where $g = e^2/\epsilon$ is the Coulomb coupling. It is useful to introduce the effective coupling

$$\alpha = \frac{g}{v}. \tag{2.26}$$

The coupling g is not renormalized by itself since it appears as the coefficient of a nonanalytic term in the action.^[121] Then, α is renormalized only through v . The free part of the action set the dimensions of all the parameters of the model in units of energy:

$$\begin{aligned}
 [\Psi] &= 1, \\
 [\alpha] &= 0, \\
 [\Delta] &= 1.
 \end{aligned} \tag{2.27}$$

We see that Δ_{KM} is going to be amplified by the effect of the interactions, whereas the effective coupling α is marginal at the classical level. We analyze the logarithmic divergence of the first order contribution in g to the electronic self-energy ($k = (\omega, \mathbf{k})$):

$$\hat{\Sigma}^{(1)}(\mathbf{p}) = \int \frac{d^3\mathbf{q}}{(2\pi)^3} \hat{G}_0(\mathbf{p} + \mathbf{q}) \frac{2\pi g}{|\mathbf{q}|}, \tag{2.28}$$

where $\hat{G}_0(\mathbf{k})$ is the propagator of the free theory,

$$\hat{G}_0(\mathbf{k}) = \frac{\omega + v(\tau\sigma_x k_x + \sigma_y k_y) + \tau s \Delta_{KM} \sigma_z}{\omega^2 + v^2 |\mathbf{k}| + \Delta_{KM}^2}. \tag{2.29}$$

It is easy to check that there is no divergence in the frequency domain, meaning that the wave function is not renormalized at one loop level. Eq. (2.28) can be written

as

$$\hat{\Sigma}^{(1)}(\mathbf{p}) = g \int \frac{d^2\mathbf{q}}{(2\pi)^2} \frac{1}{|\mathbf{q}|} \int_{-\infty}^{\infty} d\epsilon \frac{v(\mathbf{p}+\mathbf{q}) \cdot \vec{\Sigma} + \tau s \Delta_{KM} \sigma_z}{\epsilon^2 + v^2 |\mathbf{p}+\mathbf{q}|^2 + \Delta_{KM}^2}. \quad (2.30)$$

We compute the first order contributions to the β -functions of v and Δ as

$$\begin{aligned} \frac{\delta v}{v} &= \frac{\delta \hat{\Sigma}^{(1)}(\mathbf{p})}{\delta (v\mathbf{p} \cdot \vec{\Sigma})}, \\ \frac{\delta \Delta_{KM}}{\Delta_{KM}} &= \frac{\delta \hat{\Sigma}^{(1)}(\mathbf{p})}{\delta (\tau s \Delta_{KM} \sigma_z)}. \end{aligned}$$

For the former, we have

$$\frac{\delta v}{v} = g \int \frac{d^2\mathbf{q}}{(2\pi)^2} \frac{1}{|\mathbf{q}|} \int_{-\infty}^{\infty} d\epsilon \frac{\epsilon^2}{(\epsilon^2 + v^2 |\mathbf{q}|^2)^2} = g \int \frac{d^2\mathbf{q}}{(2\pi)^2} \frac{\pi}{2v |\mathbf{q}|^2}. \quad (2.31)$$

The last integral is logarithmically divergent. The integral is regularized by introducing a sharp cut-off Λ . Then, the integration in $|\mathbf{q}|$ is performed between Λ and the infrared cut-off $\Lambda_0 = \text{Max}(|\mathbf{p}|, \Delta)$. The result reads

$$\frac{\delta v}{v} = \frac{g}{4v} \ln \left(\frac{\Lambda}{\Lambda_0} \right). \quad (2.32)$$

For Δ_{KM} we have

$$\frac{\delta \Delta_{KM}}{\Delta_{KM}} = g \int \frac{d^2\mathbf{q}}{(2\pi)^2} \frac{1}{|\mathbf{q}|} \int_{-\infty}^{\infty} d\epsilon \frac{1}{(\epsilon^2 + v^2 |\mathbf{q}|^2)^2} = g \int \frac{d^2\mathbf{q}}{(2\pi)^2} \frac{\pi}{v |\mathbf{q}|^2} = \frac{g}{2v} \ln \left(\frac{\Lambda}{\Lambda_0} \right). \quad (2.33)$$

This gives us directly the RG equations at one loop. When the high-momentum degrees of freedom in the shell $\Lambda_\ell < |\mathbf{p}| < \Lambda$ are integrated out from the theory one obtains the corresponding changes in v and Δ_{KM} proportional to $\ln(\Lambda/\Lambda_\ell) \equiv \ell$ as the above equations indicate. Here ℓ must be taken as the dimensionless parameter that controls the RG flux. As deduced from the above calculation the RG procedure should stop at $\Lambda_\ell \sim \Lambda_0$. Therefore, the RG equations read

$$\begin{aligned} \frac{dv}{d\ell} &= \frac{g}{4}, \\ \frac{d\Delta_{KM}}{d\ell} &= \frac{g\Delta_{KM}}{2v}, \end{aligned} \quad (2.34)$$

although it is more convenient to write the above equations in terms of α as

$$\begin{aligned}\frac{d\alpha}{d\ell} &= -\frac{\alpha^2}{4}, \\ \frac{d\Delta_{KM}}{d\ell} &= \frac{\alpha\Delta_{KM}}{2}.\end{aligned}\quad (2.35)$$

The first equation implies automatically that long range electron-electron interactions in graphene are marginally irrelevant. The integration of the RG equations leads to

$$\begin{aligned}\alpha(\Lambda) &= \frac{\alpha_*}{1 + \frac{\alpha_*}{4} \ln\left(\frac{\Lambda}{\Lambda_*}\right)}, \\ \Delta_{KM}(\Lambda) &= \Delta_* \left[1 + \frac{\alpha_*}{4} \ln\left(\frac{\Lambda}{\Lambda_*}\right) \right],\end{aligned}\quad (2.36)$$

where $\alpha_* \equiv \alpha(\Lambda_*)$, $\Delta_* \equiv \Delta_{KM}(\Lambda_*)$. The renormalized gap is determined by the relation of consistency $\Delta_R = \Delta_{KM}(\Delta_R)$. If we take $\Lambda_* = 1$ eV, $\Delta_* = 10$ μ eV and $\alpha_* = 0.1$ (in agreement with the condition $\alpha \ll 1$) we get $\Delta_R \approx 16$ μ eV. We see that the enhancement provided by d orbitals in the single particle calculation is approximately the same as the renormalization induced by long-range Coulomb interaction.

In the case of bilayer graphene we have $(-s_y, s_x) \sim E_g$ and $s_z \sim A_{2g}$. The SOC terms within the 2-bands effective model can be constructed phenomenologically similarly to the case of single-layer graphene. The possible SOC terms are summarized in Tabs. 2.8 and 2.9. Since the bands are quadratic we consider SOC terms up to linear order in crystal momentum \mathbf{q} . The intrinsic SOC reads^[122-125]

$$\mathcal{H}_{bilayer}^{SO} = \Delta_{KM}\sigma_z \otimes \tau_z \otimes s_z + \Delta_{BR}\sigma_z \otimes (q_x s_y - q_y s_x) \quad (2.37)$$

The first term is a Kane-Mele coupling, with the same properties as in the case of single layer. The second term adopts the form of the usual Bychkov-Rashba coupling for the 2D electron gas ($\sim q_x s_y - q_y s_x$), but multiplied by a matrix σ_z . Note that in the 2-bands effective model the two sublattices are localized in different layers, therefore, this term is allowed by the symmetries of the crystal. In particular, note that it does not break parity. Of course, such term is forbidden in single-layer graphene. Another important difference is the different microscopic origin. By considering a model with only π and σ orbitals it can be seen that both Δ_{KM} and Δ_{BR} are linear in Δ_{SO} . The reason is that there is a non-zero hybridization between π and σ orbitals localized in different layers, leading to a first order contribution to the SOC. From *ab initio* calculations^[125] taking into account also d orbitals we have $\Delta_{KM} = 24$ μ eV, $\Delta_{BR} \approx 0.2$ eV \cdot \AA⁻¹.

Irrep	SOC terms ($\mathbf{q} = 0$)
A_{1g}	$\tau_z \otimes \sigma_z \otimes s_z$
E_g	$\begin{pmatrix} -\sigma_z \otimes \tau_z \otimes s_y \\ \sigma_z \otimes \tau_z \otimes s_x \end{pmatrix}$
A_{1u}	$\sigma_x \otimes \tau_z \otimes s_x + \sigma_y \otimes s_y$
A_{2u}	$\tau_z \otimes s_z, \sigma_x \otimes \tau_z \otimes s_y - \sigma_y \otimes s_x$
E_u	$\begin{pmatrix} -\sigma_y \otimes s_z \\ \sigma_x \otimes \tau_z \otimes s_z \end{pmatrix}, \begin{pmatrix} -\tau_z \otimes s_y \\ \tau_z \otimes s_x \end{pmatrix}$ $\begin{pmatrix} \sigma_x \otimes \tau_z \otimes s_x - \sigma_y \otimes s_y \\ \sigma_x \otimes \tau_z \otimes s_y + \sigma_y \otimes s_x \end{pmatrix}$
E'_u	$\begin{pmatrix} -\sigma_y \otimes \tau_y \otimes s_z \\ \sigma_y \otimes \tau_x \otimes s_z \end{pmatrix}$
G'	$\begin{pmatrix} -\sigma_y \otimes \tau_y \otimes s_x \\ -\sigma_y \otimes \tau_y \otimes s_y \\ \sigma_y \otimes \tau_x \otimes s_y \\ \sigma_y \otimes \tau_x \otimes s_x \end{pmatrix}$

 Table 2.8: SOC terms in the 2-bands effective model of bilayer graphene at \mathbf{K}_\pm .

The analysis can be extended to graphene multilayers. It is important to note the importance of inversion symmetry in the SOC physics. The bands of a centrosymmetric solid will be double degenerate (spin degeneracy), although spin components will not be well-defined in general due to the SOC, whereas in a non-centrosymmetric solid the spin degeneracy will be splitted due to the SOC. This principle can be deduced trivially as a corollary of Kramers theorem: each partner of a Kramers pair lies at points of the BZ related by parity.

Then, in the lowest bands of a centrosymmetric stack (D_{3d} symmetry) only a Kane-Mele coupling is permitted at $\mathbf{q} = 0$ (with the sublattice operators properly defined), whereas in the case of non-centrosymmetric stacks (D_{3h} symmetry) also a coupling of the form $\sim \tau_z \otimes s_z$ is allowed.^[124] This term splits both out-of-plane spin polarizations, which are still well-defined due to the mirror symmetry σ_h . Note also that this splitting has opposite sign at each valley.

2.3.2 MX_2

In the case of MX_2 monolayers we may repeat the same procedure in order to obtain the SOC terms within the 2-bands $\mathbf{k} \cdot \mathbf{p}$ theory. The SOC terms at the \mathbf{K}_\pm points are

Irrep	SOC terms ($\mathbf{q} \neq 0$)
A_{1g}	$\sigma_z \otimes (q_x s_y - q_y s_x)$
A_{2g}	$\sigma_z \otimes (q_x s_x + q_y s_y)$
E_g	$\begin{pmatrix} q_x \sigma_z \otimes s_z \\ q_y \sigma_z \otimes s_z \end{pmatrix}, \begin{pmatrix} \sigma_z \otimes (q_x s_x - q_y s_y) \\ \sigma_z \otimes (q_x s_y + q_y s_x) \end{pmatrix}$
A_{1u}	$q_x s_x + q_y s_y, -q_y \sigma_x \otimes s_z + q_x \sigma_y \otimes \tau_z \otimes s_z$ $(q_x s_x - q_y s_y) \otimes \sigma_x - (q_x s_y + q_y s_x) \otimes \sigma_y \otimes \tau_z$
A_{2u}	$q_x s_y - q_y s_x, q_x \sigma_x \otimes s_z + q_y \sigma_y \otimes \tau_z \otimes s_z$ $\sigma_x \otimes (q_x s_y + q_y s_x) + \sigma_x \otimes \tau_z \otimes (q_x s_x - q_y s_y)$
E_u	$\begin{pmatrix} -s_z q_y \\ s_z q_x \end{pmatrix}, \begin{pmatrix} q_y s_y - q_x s_x \\ q_x s_y + q_y s_x \end{pmatrix}, \begin{pmatrix} \sigma_x \otimes (q_x s_x + q_y s_y) \\ \sigma_y \otimes \tau_z (q_x s_x + q_y s_y) \end{pmatrix}$ $\begin{pmatrix} \sigma_y \otimes \tau_z \otimes (q_x s_y - q_y s_x) \\ \sigma_x \otimes (q_x s_y - q_y s_x) \end{pmatrix}, \begin{pmatrix} \sigma_x q_y + \sigma_y \otimes \tau_z q_x \otimes s_z \\ \sigma_y \otimes \tau_z q_y - \sigma_x q_x \otimes s_z \end{pmatrix}$ $\begin{pmatrix} \sigma_x \otimes (q_x s_x - q_y s_y) + \sigma_y \otimes \tau_z \otimes (q_x s_y + q_y s_x) \\ \sigma_y \otimes \tau_z \otimes (q_x s_x - q_y s_y) - \sigma_x \otimes (q_x s_y + q_y s_x) \end{pmatrix}$
E'_g	$\begin{pmatrix} -\tau_y \otimes \sigma_x (q_x s_y - q_y s_x) \\ \tau_x \otimes \sigma_x (q_x s_y - q_y s_x) \end{pmatrix}, \begin{pmatrix} s_z \otimes (\tau_x \otimes \sigma_z q_y - \tau_y q_x) \\ s_z \otimes (\tau_y \otimes \sigma_z q_y + \tau_x q_x) \end{pmatrix}$ $\begin{pmatrix} -\tau_x \otimes \sigma_z \otimes (q_x s_x - q_y s_y) + \tau_y \otimes (q_x s_y + q_y s_x) \\ \tau_y \otimes \sigma_z \otimes (q_x s_x - q_y s_y) + \tau_x \otimes (q_x s_y + q_y s_x) \end{pmatrix}$
E'_u	$\begin{pmatrix} -\tau_y \otimes \sigma_x \otimes (q_x s_x + q_y s_y) \\ \tau_x \otimes \sigma_x \otimes (q_x s_x + q_y s_y) \end{pmatrix}, \begin{pmatrix} -s_z \otimes (\tau_x \otimes \sigma_z q_x + \tau_y q_y) \\ s_z \otimes (-\tau_y \otimes \sigma_z q_x + \tau_x q_y) \end{pmatrix}$ $\begin{pmatrix} -\tau_x \otimes \sigma_z (q_x s_y + q_y s_x) - \tau_y (q_x s_x - q_y s_y) \\ -\tau_y \otimes \sigma_z (q_x s_y + q_y s_x) + \tau_x (q_x s_x - q_y s_y) \end{pmatrix}$
G'	$\begin{pmatrix} -\tau_x \otimes (q_x s_x + q_y s_y) \\ -\tau_y \otimes \sigma_z \otimes (q_x s_x + q_y s_y) \\ \tau_x \otimes \sigma_z \otimes (q_x s_x + q_y s_y) \\ -\tau_y \otimes (q_x s_x + q_y s_y) \end{pmatrix}, \begin{pmatrix} \tau_y \otimes \sigma_z \otimes (q_x s_y - q_y s_x) \\ -\tau_x \otimes (q_x s_y - q_y s_x) \\ \tau_y \otimes (q_x s_y - q_y s_x) \\ -\tau_x \otimes \sigma_z \otimes (q_x s_y - q_y s_x) \end{pmatrix}$ $\begin{pmatrix} s_z \otimes (-\tau_x \otimes \sigma_z q_x + \tau_y q_y) \\ s_z \otimes (-\tau_x \otimes \sigma_z q_y - \tau_y q_x) \\ s_z \otimes (\tau_y \otimes \sigma_z q_y - \tau_x q_x) \\ -s_z \otimes (\tau_y \otimes \sigma_z q_x + \tau_x q_y) \end{pmatrix}, \begin{pmatrix} \tau_x \otimes \sigma_x \otimes (q_x s_x - q_y s_y) \\ -\tau_x \otimes \sigma_x \otimes (q_x s_y + q_y s_x) \\ \tau_y \otimes \sigma_x \otimes (q_x s_y + q_y s_x) \\ \tau_y \otimes \sigma_x \otimes (q_x s_x - q_y s_y) \end{pmatrix}$ $\begin{pmatrix} \tau_x \otimes \sigma_x \otimes s_z q_y \\ -\tau_x \otimes \sigma_x \otimes s_z q_x \\ \tau_y \otimes \sigma_x \otimes s_z q_x \\ \tau_y \otimes \sigma_x \otimes s_z q_y \end{pmatrix}, \begin{pmatrix} -\tau_x \otimes \sigma_z \otimes (q_x s_y + q_y s_x) + \tau_y \otimes (q_x s_x - q_y s_y) \\ -\tau_x \otimes \sigma_z \otimes (q_x s_x - q_y s_y) - \tau_y \otimes (q_x s_y + q_y s_x) \\ \tau_y \otimes \sigma_z \otimes (q_x s_x - q_y s_y) - \tau_x \otimes (q_x s_y + q_y s_x) \\ -\tau_y \otimes \sigma_z \otimes (q_x s_y + q_y s_x) - \tau_x \otimes (q_x s_x - q_y s_y) \end{pmatrix}$

Table 2.9: (Continuation) SOC terms in the 2-bands effective model of bilayer graphene.

Irrep	SOC terms
A'_1	$\sigma_z \otimes \tau_z \otimes s_z, \tau_z \otimes s_z$
A''_1	$\sigma_x \otimes \tau_z \otimes s_y - \sigma_y \otimes s_x$
A''_2	$\sigma_x \otimes \tau_z \otimes s_x + \sigma_y \otimes s_y$
E'	$\begin{pmatrix} -\sigma_y \otimes s_z \\ \sigma_x \otimes \tau_z \otimes s_z \end{pmatrix}$
E''	$\begin{pmatrix} \sigma_x \otimes \tau_z \otimes s_y + \sigma_y \otimes s_x \\ \sigma_x \otimes \tau_z \otimes s_x - \sigma_y \otimes s_y \end{pmatrix}, \begin{pmatrix} -\tau_z \otimes s_y \\ \tau_z \otimes s_x \end{pmatrix}, \begin{pmatrix} -\sigma_z \otimes \tau_z \otimes s_y \\ \sigma_z \otimes \tau_z \otimes s_x \end{pmatrix}$
E''_1	$\begin{pmatrix} \sigma_y \otimes \tau_x \otimes s_x - \sigma_y \otimes \tau_y \otimes s_y \\ \sigma_y \otimes \tau_x \otimes s_y + \sigma_y \otimes \tau_y \otimes s_x \end{pmatrix}$
E''_2	$\begin{pmatrix} \sigma_y \otimes \tau_x \otimes s_x + \sigma_y \otimes \tau_y \otimes s_y \\ \sigma_y \otimes \tau_y \otimes s_x - \sigma_y \otimes \tau_x \otimes s_y \end{pmatrix}$
E'_3	$\begin{pmatrix} -\sigma_y \otimes \tau_y \otimes s_z \\ \sigma_y \otimes \tau_x \otimes s_z \end{pmatrix}$

 Table 2.10: SOC terms within the massive Dirac model for MX_2 .

classified according to the irreps of D_{3h} in Tab. 2.10. The intrinsic SOC reads

$$\mathcal{H}_{int} = \lambda_{KM} \sigma_z \otimes \tau_z \otimes s_z + \lambda_{SP} \tau_z \otimes s_z. \quad (2.38)$$

The first term adopts the form of a Kane-Mele gap. Note that MX_2 remains a trivial insulator since $\Delta \gg \lambda_{KM}$. The second term is present due to the lack of an inversion center in the solid. Then, opposite out-of-plane spin polarizations are energetically separated, with splittings in conduction (c) and valence (v) bands of $\lambda_{c,v} = \lambda_{KM} \pm \lambda_{SP}$.

However, although both bands are spin splitted, the splittings have different microscopic origins due to the different orbital character. The processes which lead to the splittings are shown in Fig. 2.8. Taking into account that the bands are dominated by d orbitals from M atoms, we see that the splitting of the valence band is first order on the intra-atomic spin-orbit interaction strength, whereas the splitting of the conduction band is second order. This picture agrees with *ab initio* calculations. Of course, there is also a contribution from the chalcogen atoms, which is important for the conduction band since the spin-orbit interaction in this case enters as a first order contribution to the splitting. This contribution is relevant in the case of Se compounds, whereas for Mo compounds can be neglected. For a complete tight-binding model and a detailed discussion on the microscopic mechanisms that have influence in the SOC of MX_2 materials check Ref. 126. Values extracted from DFT calculations^[93-95] are summarized in Tab. 2.11.

When the mirror symmetry σ_h is expressly broken by a substrate, electric fields,

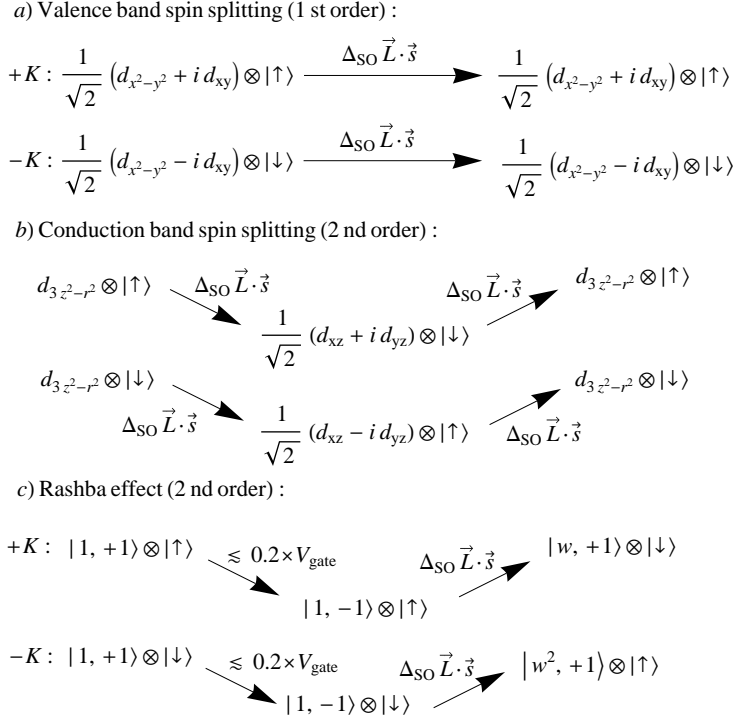


Figure 2.8: Sketch of the microscopic processes which lead to the effective SOC terms discussed in the text. (a) First-order processes which lead to the splitting of the valence band. (b) Second- order processes associated to the splitting of the conduction band. (c) Second-order processes which lead to a Bychkov-Rashba coupling when σ_h symmetry is broken.

Material	λ (meV)
e-MoS ₂	3
h-MoS ₂	140
h-WS ₂	430
h-MoSe ₂	180
h-WSe ₂	460

Table 2.11: Spin splitting in the conduction (e) and valence (h) bands in several MX₂ materials.^[93–95]

etcetera, then the SOC term belonging to the A_1' irrep can be generated. This term adopts the form of a Bychkov-Rashba coupling of the form

$$\mathcal{H}_{BR} = \Delta_{BR} (\sigma_x \otimes \tau_z \otimes s_y - \sigma_y \otimes s_x). \quad (2.39)$$

The possible processes which lead to such coupling are also sketched in Fig. 2.8. An electric field perpendicular to the sample would induce dipolar transitions between the Mo $d_{3z^2-r^2}$ orbitals of the conduction band and Mo p_z orbitals of bands at much higher energies. Then, the spin-orbit interaction would induce transitions between these states and the valence band flipping the spin. However, the orbital weight of the valence band in Mo p orbitals is very small, so this coupling is expected to be very weak. Nevertheless, this picture changes if orbitals from S atoms are also taken into account. For instance, if we consider the application of a gate voltage V_{gate} , which is necessary in order to induce charge carriers in this system, then we would have different on-site energies for the p orbitals of the top and bottom S atoms. This turns into a non-zero hybridization between valence-band states and d_{xz} , d_{yz} orbitals associated to higher bands proportional to V_{gate} . Then, the spin-orbit interaction induces transitions between d_{xz} , d_{yz} orbitals of these bands and $d_{3z^2-r^2}$ of the conduction band, flipping the spin. This kind of process is the one depicted in Fig. 2.8 (c). Since the orbital weight of S p orbitals in these bands is less than the 20%, we can estimate an upper limit for this coupling of the form

$$\Delta_{BR} \leq \frac{0.2V_{gate}\Delta_{SO}}{\epsilon_*}, \quad (2.40)$$

where ϵ_* represents the energy of the complex conjugated combination of $d_{x^2-y^2}$, d_{xy} (A'') orbitals involved in the calculation.

This coupling induces the relaxation of the out-of-plane spin component, which is a good quantum number if the mirror symmetry is not broken. Note that the intrinsic SOC tends to stabilize this spin component. Indeed, the splitting of the valence band protects the out-of-plane spin in such a way that any relaxation mechanism induced by a breaking of the mirror symmetry is much less efficient for hole dopings, as we will see.

Furthermore, the splitting of the bands has opposite sign at each valley, as imposed by time reversal symmetry. This observation plays a central role in spintronics and optoelectronics applications. Since the magnitude of the splitting is remarkable, particularly in the case of the valence band, for a broad range of dopings only one spin component is populated at each valley. Such identification of valley and spin degrees of freedom is usually called spin-valley coupling in the literature.^[19] As an example of its potential application, the spin-valley coupling allows to control the valley population by optically exciting the monolayer MX_2 samples with circularly polarized

light.^[20–22] Note that the absence of a center of inversion is crucial for this, and that is the reason why the monolayer is more interesting than the bilayer or the bulk material.

Another consequence is the non-zero (but not quantized) spin Hall conductivity,^[19] given by

$$\sigma_{SH} = e \sum_n \int d^2\mathbf{q} \left(f_{n,\uparrow} \Omega_{\mathbf{q},\uparrow}^{+,n} - f_{n,\downarrow} \Omega_{\mathbf{q},\downarrow}^{+,n} \right), \quad (2.41)$$

where n labels the band and the integration is performed around \mathbf{K}_{\pm} points (the valley degeneracy is already taken into account). From Eq. (2.14) we deduce, for moderate hole doping (the Fermi level lying between the splitted valence bands),

$$\sigma_{SH} = \frac{e\mu}{2\pi(\Delta - \lambda - 2\mu)} \approx \frac{e\mu}{2\pi\Delta} \neq 0, \quad (2.42)$$

where the chemical potential μ is measured from the top of the band. Note that this Hall conductivity is not *topologically* protected in the sense of the QSHE, and it is sensible to the occurrence of Rashba-like fields or other sources of disorder which relax the out-of-plane spin component.

Similarly, when inter-valley disorder dominates electron mobilities then a positive magnetoresistance behavior is expected. The weak antilocalization correction to the classical conductivity arises due to the spin-rotational symmetry breaking originated by the opposite spin polarizations of the valleys. Of course, this picture may change if the σ_h symmetry is also broken. The presence or absence of this symmetry in 2D hexagonal crystals could be detected in general in quantum transport experiments.^[101]

2.3.3 Heavy adatoms

As mentioned before, and for reasons that will become clear in next section, the gap opened due to the SOC in graphene has non trivial consequences in the topology of the π bands. That is why there is an interest in enhancing the SOC in graphene. A possible route is via heavy adatoms deposition.^[127,128] Of course, attached impurities break the $z \rightarrow -z$ mirror symmetry, so in principle both Kane-Mele and Bychkov-Rashba couplings would be generated. A predominance of the latter would close the gap and constitute an extrinsic source of spin relaxation.^[129,130] However, in some circumstances it can be proved that the Rashba coupling is smaller or even suppressed, so graphene could be tuned into a QSHE state. This situation corresponds to the most symmetric arrangement of the adatoms, when they occupy the center of the

graphene hexagons. Depending on the orbitals of the adatom leading to the SOC enhancement, it can be easily proved that the Bychkov-Rashba coupling at the \mathbf{K}_\pm points is suppressed.

In order to illustrate these ideas, let's consider the situation when the adatoms occupy the central position of the hexagon. In the limit of complete coverage, when there is an impurity at the center of all the hexagons, it is clear that the $z \rightarrow -z$ symmetry is broken but the C_{6v} symmetry is restored. The strength of the Kane-Mele and Bychkov-Rashba couplings, Eqs. (2.16) and (2.17) respectively, is dominated by the spin-orbit interaction in the orbitals of the heavy adatom, which will be hybridized with π states at the \mathbf{K}_\pm . Therefore, the effective SOC in the π bands subspace is understood as the result of virtual transitions into the impurity orbitals, where the electrons feel the strong spin-orbit interaction. The symmetry of the orbitals involved in such processes is crucial in order to determine which coupling is favored. If we denote by m the angular momentum quantum number (in the z direction) of the orbital at the impurity which forms the Bloch wave function at \mathbf{K}_\pm points, we see that

$$\begin{aligned} \text{if } |m| = 0 \pmod{6}, \text{ then } &\sim E'_1, \\ \text{if } |m| = 3 \pmod{6}, \text{ then } &\sim E'_2, \\ \text{otherwise } &\sim G'. \end{aligned}$$

Then, in the cases of $|m| = 0, 3 \pmod{6}$, orbitals at the impurity are not hybridized with the π Bloch states. The consequences of this observation on the SOC is crucial. For instance, in elements which exhibit partially filled p shells, so only these orbitals participate actively in the tunneling processes from graphene to the impurity and back, the Bychkov-Rashba coupling at the \mathbf{K}_\pm points is expected to be strongly suppressed. Since the hopping between the p_z orbital at the impurity and graphene π electrons is cancelled at \mathbf{K}_\pm points, only spin conserving tunneling processes through $p_{x,y}$ orbitals are allowed. Then, the Bychkov-Rashba coupling of Eq. (2.17) is 0, and the Kane-Mele coupling is enhanced. If we denote by t_{ad} the hopping between $p_{x,y}$ orbitals at the adatom and graphene π orbitals, ϵ_{ad} the difference of on-site energies, and Δ_{ad} the spin-orbit interaction strength of the adatom, then we obtain a contribution to the Kane-Mele coupling of the form

$$\Delta_{KM} = \frac{9\Delta_{ad}t_{ad}^2}{4\epsilon_{ad}^2}. \quad (2.43)$$

According to first principles calculation,^[127] among the elements in the 5th and 6th rows of the periodic table, which are expected to induce an enormous spin-orbit interaction, indium and thallium tends to occupy the centre of the hexagon and

exhibit non-magnetic behavior. Both species belong to the 13th column, with partially filled p shells, what ensures the absence of the Bychkov-Rashba coupling at the \mathbf{K}_\pm points. A partial covering around 6% seems to be enough to produce Kane-Mele gaps of the order of 10 meV.

2.4 Topological aspects

The Dirac points in graphene are *topologically* protected by the symmetries of the honeycomb lattice in combination with time-reversal symmetry.^[81] Depending on the broken symmetries, we end up with gapped band structures belonging to different topological sectors. In this sense, pristine graphene (in the absence of SOC) could be interpreted as a topological critical point.

In the absence of SOC and assuming that translational symmetry is respected, there are two ways of opening a gap in the spectrum: by breaking the sublattice equivalence, which generates a mass term of the form $\sigma_z \sim B_2$, or by breaking the inversion symmetry planes σ_v, σ'_v and time-reversal symmetry and then generating a term of the form $\tau_z \otimes \sigma_z \sim A_2$.

In the former case, we are reducing the original point group C_{6v} to C_{3v} . The situation remains exactly as in MX_2 . The system is a trivial insulator where the non-zero Berry curvature of the bands around each valley has opposite sign. The second case can be realized if a coupling with an out-of-plane magnetic field $B_z \sim A_2$ is considered. In that case, since the gap has opposite sign at each valley the Berry curvature has the same sign and it is not compensated. Therefore, the valence bands possess a non-zero Chern number. This is the famous Haldane model,^[131] a QHE system without LLs. The most interesting situation occurs when the SOC is considered. A Haldane mass with opposite sign for each spin component is naturally generated by the SOC. The total Chern number is zero, but the spin Chern number previously discussed is non-zero. Therefore, graphene is ideally a QSHE insulator.

2.4.1 Haldane model

We have already shown that including second nearest neighbors hoppings in the tight-binding description of graphene only breaks the non-protected electron-hole symmetry of the spectrum, which remains gapless. Nevertheless, this is true only for real hoppings, not for complex ones. Let's examine the problem. Fig. 2.9 shows hopping directions within the unit cell for which we introduce the amplitudes $t' e^{i\phi}$. For $\phi = n\pi$, n an integer, the C_{6v} symmetry is respected, otherwise the reflection planes

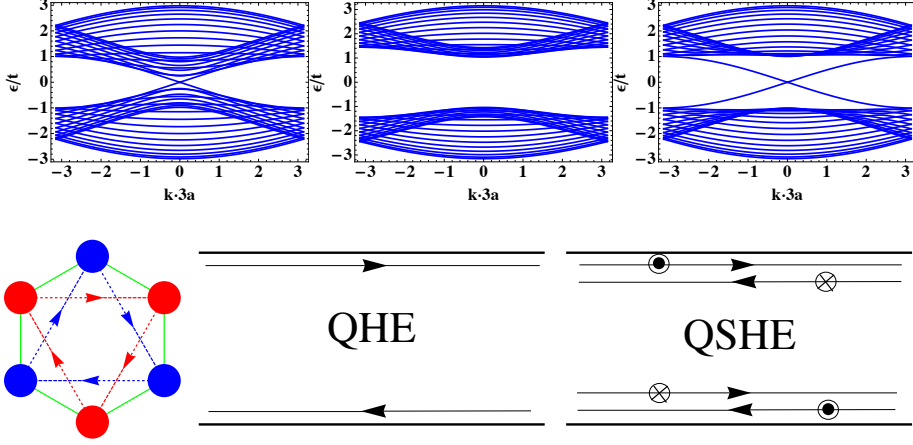


Figure 2.9: Top: Electronic bands of a graphene strip with a 20 unit cells width and armchair edges. Left: Only nearest neighbors hopping t . Middle: Staggered potential $M = 0.6\sqrt{3}t$. Right: Haldane second nearest neighbors hopping $t' = 0.2t$, $\phi = \pi/2$. Bottom: On the left, graphene unit cell where the arrows mark the directions of positive phase hopping. On the right, sketches of the edge states in the QHE and QSHE phases.

σ_v, σ'_v are absent and the point group is reduced to C_6 . Also time reversal symmetry is broken. The new point group only contains 1-dimensional irreps, therefore the spectrum is gapped in general. Moreover, the mass term adopts the form of $\tau_z \otimes \sigma_z$ (which belongs to A irrep of C_6 , whereas σ_z belongs to B irrep). The Hamiltonian around \mathbf{K}_\pm points read, up to linear terms in \mathbf{q} , as

$$\mathcal{H} = v \left(\tau_z \sigma_x q_x + \sigma_y q_y \right) + \Delta_H \tau_z \sigma_z, \quad \text{with } \Delta_H = 3\sqrt{3}t' \sin \phi. \quad (2.44)$$

Physically, the phase ϕ is associated to a magnetic field perpendicular to the graphene plane with the full symmetry of the lattice that is zero on average over the unit cell. Such magnetic field is incorporated by means of the Peierls substitution,^[132] $t_{ij} \rightarrow t_{ij} e^{i \frac{e}{\hbar} \int_{\mathbf{R}_i}^{\mathbf{R}_j} d\mathbf{r} \cdot \mathbf{A}}$. Since the total magnetic flux through the unit cell is zero the first neighbors hoppings t are unaffected, whereas the second nearest neighbors hoppings acquire a phase $\phi = 2\pi/3 \times \Phi/\Phi_0$, where $\Phi_0 = h/e$ is the flux quantum and Φ is the flux through the triangle inside the unit cell defined by the red or alternatively blue lines in Fig. 2.9.

If we also consider a sublattice imbalance or staggered potential then the point group is reduced to C_3 and then a mass term of the form $M\sigma_z$ is added to Eq. (2.44).

A straightforward calculation shows that the Chern number of the valence band inferred from the Hamiltonian in Eq. (2.44) in the presence of $M\sigma_z$ is just

$$C = \frac{1}{2\pi} \int d^2\mathbf{q} \left[\frac{v^2 (M + \Delta_H)}{2 \left((M + \Delta_H)^2 + v^2 |\mathbf{q}|^2 \right)^{3/2}} - \frac{v^2 (M - \Delta_H)}{2 \left((M - \Delta_H)^2 + v^2 |\mathbf{q}|^2 \right)^{3/2}} \right] =$$

$$= \begin{cases} +1 & \text{if } |M| < \Delta_H \text{ and } \phi \in (0, \pi), \\ -1 & \text{if } |M| < \Delta_H \text{ and } \phi \in (-\pi, 0), \\ 0 & \text{if } |M| > \Delta_H, \end{cases} \quad (2.45)$$

where the integration is performed around \mathbf{K}_\pm points. According to this result, in the situation when time reversal symmetry is broken, $\sin \phi \neq 0$, the ratio $|M|/\Delta_H$ controls a topological transition from a QHE state for $|M|/\Delta_H < 1$ characterized by a Hall conductivity $\sigma_{xy} = \pm e^2/h$ (when the Fermi level is within the gap) to a trivial insulator state for $|M|/\Delta_H > 1$ with $\sigma_{xy} = 0$. At the critical value $|M|/\Delta_H = 1$, the massless low energy theory of the model simulates a relativistic QFT exhibiting the so-called *parity anomaly*.^[133]

From the definition of the Chern number, Eq. (1.9), it is clear that the topological character of a band is a global property, defined in the entire BZ, so to infer topological properties of a system from an effective theory which is valid only around certain points of the BZ is always dangerous. Note, however, that the Berry curvature is peaked at the Dirac points, which justifies the result of Eq. (2.45). The analysis is confirmed by a tight-binding calculation, shown in Fig. 2.9. The bands of a graphene strip with armchair edges are computed. In the absence of second nearest neighbors hoppings the spectrum remains gapless. The Dirac point lies at the center of the folded BZ (note also that the lattice spacing of the 1D system is $3a$), and no edge states exist, as it can be deduced from topological arguments.^[134] When a staggered potential is introduced then a gap is opened. When instead of a staggered potential a imaginary t' hopping is introduced then a gap is opened in the bulk spectrum, but two sub-bands within the bulk gap appears connecting conduction and valence bands. These sub-bands correspond to chiral modes propagating along the edges of the ribbon, as shown in the sketch of Fig. 2.9, whose origin is purely topological as inferred from the bulk-boundary correspondence previously discussed.

2.4.2 QSHE in graphene

The physical implementation of the Haldane model is in principle a difficult task. In his seminal paper, Haldane proposed a possible route considering magnetic dipoles at the center of the hexagons ordered ferromagnetically perpendicular to the plane.

However, if the SOC in graphene is taken into account, then a Haldane mass $\sim \tau_z \otimes \sigma_z$ is naturally generated, where the out-of-plane spin component plays the role of the perpendicular magnetic field. The spin-orbit interaction mediates the second nearest neighbors complex hoppings of the Haldane model, through the σ orbitals in the case of pristine graphene, or heavy adatoms placed at the center of the hexagons as we have seen in the previous section. Hence, the Kane-Mele SOC term consists on two copies of the Haldane mass with opposite sign for each spin flavour. The total Chern number is zero, but the spin Chern number is $C_s = (C_\uparrow - C_\downarrow) / 2 = \pm 1$. The Kane-Mele model is a QSHE system, with spin-polarized edge modes as sketched in Fig. 2.9, responsible for the quantized spin Hall conductivity $\sigma_{SH} = e/2\pi$ (note that the spin current is defined as $\mathbf{J}_s = (\hbar/2e) (\mathbf{J}_\uparrow - \mathbf{J}_\downarrow)$).

This discussion seems to rely on the conservation of the out-of-plane spin. However, this is not the crucial symmetry. The edge states in the QSHE are robust, even when spin conservation is absent, due to their crossing at the center of the 1D BZ, protected by time reversal symmetry. Thus, the QSHE is a topological phase protected by time reversal symmetry and characterized by a \mathbb{Z}_2 invariant.

Although originally proposed in graphene,^[37,39] the weakness of the SOC and the subsequent narrowness of the non-trivial gap makes difficult to stabilize such topological phase. The QSHE has been theorized to exist in 2D semiconductor systems with uniform strain gradients,^[135] and also predicted to exist^[136] and observed in HgCdTe^[137] quantum wells.

PART 1:
FLEXURAL PHONONS AND SOC

3

Electron-phonon coupling and electron mobility in suspended graphene

3.1 Introduction

It has been found that the intrinsic mobility μ of charge carriers in graphene can exceed $20 \text{ m}^2/\text{Vs}$ at room temperature.^[138,139] So far, such high values have not been achieved experimentally, because extrinsic scatterers limit μ . The highest μ was reported in suspended devices^[140,141] and could reach $\sim 12 \text{ m}^2/\text{Vs}$ at 240 K.^[166] This however disagrees with the data of Ref. 140 where similar samples exhibited at room mobilities close to $1 \text{ m}^2/\text{Vs}$, the value that is routinely achievable for graphene on a substrate.

Vibrations of the atoms of the crystal around their equilibrium positions is a very important source of electron scattering. We show in this chapter that electron-phonon coupling constitutes an important scattering mechanism in suspended graphene and the likely origin of the above disagreement, and their contribution should be suppressed to allow ultra high μ . This can be done by applying strain.

Out of plane vibrations lead to a new class of low energy phonons, the flexural branch.^[142,143] In an ideal flat suspended membrane symmetry arguments show

that electrons can only be scattered by two flexural phonons simultaneously.^[138,150] Despite the weakness of this quadratic coupling, the low frequencies of these modes characterized by a quadratic dispersion relation makes them very easy to excite. As a result, the resistivity due to flexural phonons rises rapidly at high T where it can be described as elastic scattering by thermally excited intrinsic ripples.^[144] Explicitly, at experimentally relevant T , the non-strained samples show quadratic in T resistivity with logarithmic correction, $\varrho \sim T^2 \ln(T)$, and constant mobility. Electron scattering by two flexural phonons gives the main contribution to the resistivity in this case, and is responsible for the T^2 dependence. However, applying strain tends to linealize the dispersion relation of flexural phonons, then suppressing its density of states at low momenta. This manifests in the annihilation of scattering by flexural phonons. Therefore, temperature-dependent mobilities in strained samples are expected to be dominated by in-plane phonons.

In this chapter we give a detailed description of low energy phonon modes in graphene, with special emphasis in the flexural branch. We construct the electron-phonon coupling both for monolayer and bilayer graphene in the context of the low energy description of the electronic spectrum around Dirac points. Then, we employ this Hamiltonians in order to compute the resistivity due to scattering by phonons in the doped regime, when a semi-classical description of transport in terms of the Boltzmann equation is justified. We analyze the behavior of resistivity as a function of temperature, carrier concentration and strain, and we try to explain available data in suspended samples, where scattering by flexural phonons is expected to dominate transport.

3.2 Phonon modes in graphene

Phonon modes of graphene within the tripled unit cell can be classified according to the irreps of C_{6v}'' as shown in Tabs. 3.1 and 3.2. The modes belonging to the valley-diagonal irreps correspond to the acoustic and optical modes at the original Γ point, according to which atoms of different sublattices oscillate in phase or out-of-phase respectively. The modes belonging to the valley off-diagonal irreps correspond to the modes at the \mathbf{K}_{\pm} points, in particular, real linear combinations of displacements at both valleys.

In this chapter we are interested on the effect of phonons in DC transport. Therefore, we only consider for the moment the lowest energy modes, and those are the acoustic branches around Γ , both in-plane ($\sim E_1$) and out-of-plane or flexural ($\sim A_1$). The dynamics of such low energy modes are governed by the elastic constants of the solid, and a long-wavelength description in terms of a theory in the continuum

is valid since we focus on in-phase displacements only. The mechanics of solids, regarded as continuous media, constitute the theory of elasticity,^[142, 145] which can be constructed by purely geometrical means. The unit cells of the graphene crystal can be seen as points on a surface embedded in \mathbb{R}^3 , each of them labeled by a 3D vector \mathbf{r} . Graphene is then as example of a crystalline membrane.^[143] Two different forms allow to describe both intrinsic and extrinsic properties of the embedded surface. The first fundamental form is nothing but the pull-backed metric of the embedding space projected onto the surface,

$$g_{\alpha\beta} = \partial_\alpha \mathbf{r} \cdot \partial_\beta \mathbf{r}, \quad (3.1)$$

where ∂_α , $\alpha = 1, 2$, is the derivative with respect to the internal coordinates which parametrize the surface. Note that this is a complete intrinsic quantity and does not depend on the embedding. Such information, as changes from point to point of the normal vector to the surface, $\mathbf{n} = \partial_1 \mathbf{r} \times \partial_2 \mathbf{r} / |\partial_1 \mathbf{r} \times \partial_2 \mathbf{r}|$, is given by the second fundamental form,

$$\mathcal{F}_{\alpha\beta} = \mathbf{n} \cdot \partial_\alpha \partial_\beta \mathbf{r}. \quad (3.2)$$

As we are going to see, the elastic energy of the graphene membrane can be written in terms of scalars made of this two forms.

3.2.1 In-plane modes

Let's assume that carbon atoms in the equilibrium occupy positions labeled by $\mathbf{r}_0 = (x_0, y_0, 0)$. Then, we consider deviations from these equilibrium positions given by a vector of displacements $\mathbf{r} = \mathbf{r}_0 + \mathbf{u}$. The displacements are fields which depend on the position of the unit cell, $\mathbf{u}(x_0, y_0)$. This is the Monge representation, where x_0, y_0 correspond to the intrinsic coordinates that parametrizes the surface, so we substitute the greek indices by latin indices from now on. Then, the first fundamental form is given by

$$g_{ij} = \delta_{ij} + 2u_{ij}, \quad (3.3)$$

where u_{ij} is the strain tensor

$$u_{ij} = \frac{1}{2} (\partial_i u_j + \partial_j u_i + \partial_i u_k \partial_j u_k). \quad (3.4)$$

Here repeated indices imply summation.

For the moment, we consider only in-plane displacements $\mathbf{u} = (u_x, u_y, 0)$, and we estimate the energy cost due to stretching. In general, the elastic energy for a solid is

3. ELECTRON-PHONON COUPLING AND ELECTRON MOBILITY IN SUSPENDED GRAPHENE

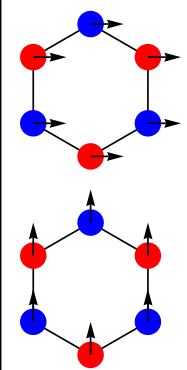
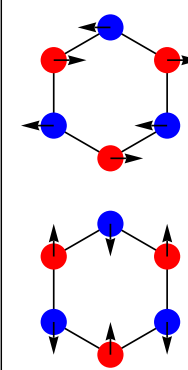
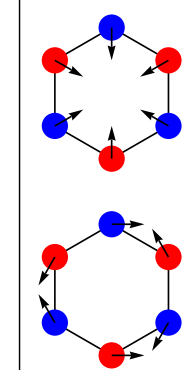
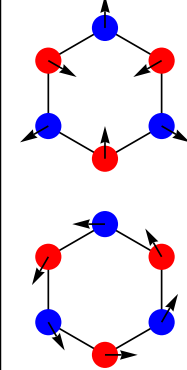
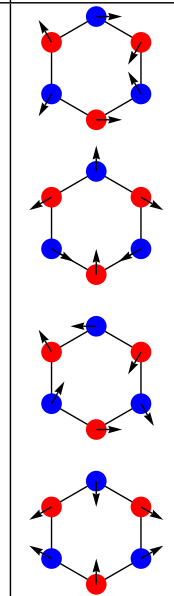
E_1	E_2	E'_1	E'_2	G'
				

Table 3.1: Classification of in-plane phonon modes according to the irreps of C''_{6v} .

quadratic in the strain tensor components,^[142, 145]

$$\mathcal{F}_{st} = \int d^2\mathbf{r} \mathcal{C}_{ijkl} u_{ij} u_{kl}, \quad (3.5)$$

where \mathcal{C}_{ijkl} is a tensor of the elastic constants. Since $u_{ij} = u_{ji}$ by definition, in principle there are only 6 independent elastic constants in a 2D solid. Additionally, the elastic energy density must be invariant under the point group symmetries of the crystal.

Note that for isotropic media only two elastic constants are independent. Since in that case the response of the solid must be independent of the direction, the only tensor available to construct higher order tensors is the Kronecker delta δ_{ij} . The only 4-rank tensors formed by δ_{ij} satisfying the symmetries of \mathcal{C}_{ijkl} are $\delta_{ij}\delta_{kl}$ and $\delta_{ik}\delta_{jl} + \delta_{il}\delta_{jk}$, therefore

$$\mathcal{C}_{ijkl} = \frac{\lambda}{2} \delta_{ij}\delta_{kl} + \frac{\mu}{2} (\delta_{ik}\delta_{jl} + \delta_{il}\delta_{jk}), \quad (3.6)$$

where λ, μ are the Lamé coefficients. In 2D, this is precisely the case of hexagonal crystals. In particular, for C_{6v} symmetry, the 3 independent components of u_{ij} transform according to

$$\begin{aligned} u_{xx} + u_{yy} &\sim A_1 \\ \begin{pmatrix} u_{xx} - u_{yy} \\ -2u_{xy} \end{pmatrix} &\sim E_2 \end{aligned} \quad (3.7)$$

Then, among the 6 independent combinations of the form $u_{ij}u_{kl}$, only 2 belongs to A_1 irrep. This is inferred from the reductions

$$\begin{aligned} A_1 \times A_1 &\sim A_1, \\ A_1 \times E_2 &\sim E_2, \\ E_2 \times E_2 &\sim A_1 + A_2 + E_2, \end{aligned} \quad (3.8)$$

and note that the combination belonging to A_2 irrep is exactly zero. Therefore, for crystals with C_{6v} there are only 2 independent elastic constants corresponding to the Lamé coefficients, λ, μ . As a final remark, note that the energy term in Eq. (3.5) is not a complete invariant under coordinate transformations since for that the integration measure should be completed with the factor $\det\sqrt{g} \approx u_{ii}$. The description in the continuum of a 2D crystal is essentially different from a fluid or any continuous media in the sense that the action must not be invariant under diffeomorphisms given that the atoms in the solid defines a special coordinate system.^[146]

The elastic energy due to the stretching of the graphene crystals reads

$$\mathcal{F}_{st} = \frac{1}{2} \int d^2\mathbf{r} \left(\lambda (u_{ii})^2 + 2\mu u_{ij}u_{ij} \right). \quad (3.9)$$

Then, the Lagrangian describing the dynamics of in-plane phonon modes is just

$$\mathcal{L} = \frac{1}{2} \int d^2\mathbf{r} \left(\rho \dot{u}_i \dot{u}_i - \lambda (u_{ii})^2 - 2\mu u_{ij}u_{ij} \right), \quad (3.10)$$

where ρ is the mass density of graphene. In the harmonic approximation we keep only linear terms in the displacements for the strain tensor, therefore the Euler-Lagrange equations are just

$$\rho \ddot{u}_i - \lambda \partial_i \partial_j u_j - \mu (\partial_j \partial_j u_i + \partial_i \partial_j u_j) = 0. \quad (3.11)$$

By introducing Fourier series of the form

$$u_i(\mathbf{r}) = \frac{1}{\sqrt{N}} \sum_{\mathbf{q}} u_{\mathbf{q}} e^{i\mathbf{q}\cdot\mathbf{r}}, \quad (3.12)$$

and decomposing in longitudinal u^L and transverse u^T components as usual, $\mathbf{u}_{\mathbf{q}} = u_{\mathbf{q}}^L \frac{\mathbf{q}}{|\mathbf{q}|} + u_{\mathbf{q}}^T \frac{\hat{\mathbf{e}}_z \times \mathbf{q}}{|\mathbf{q}|}$, we obtain usual linear dispersion relation for in-plane phonon modes, $\omega_{\mathbf{q}}^{L,T} = v_{L,T} |\mathbf{q}|$, with

$$\begin{aligned} v_L &= \sqrt{\frac{\lambda + 2\mu}{\rho}}, \\ v_T &= \sqrt{\frac{\mu}{\rho}}. \end{aligned} \quad (3.13)$$

3.2.2 Out-of-plane (flexural) modes

Let's allow now out-of-plane displacements of the unit cell, $\mathbf{u} = (u_x, u_y, h)$. The first consequence is that the normal to the surface is not globally defined since $\mathbf{n} \approx (-\partial_x h, -\partial_y h, 1)$ to the lowest order in h . Assuming smooth out-of-plane displacements, the leading contribution to the second fundamental form is just

$$\mathcal{F}_{ij} \approx \partial_i \partial_j h. \quad (3.14)$$

To stabilize the solid with respect to fluctuations in the out-of-plane direction an extrinsic term must be added to the elastic energy. Such term reflects the energy cost

A_1	B_2	G'
$1/\sqrt{6} \times$	$1/\sqrt{6} \times$	

 Table 3.2: Classification of flexural phonon modes according to the irreps of C_{6v}'' .

due to the bending of graphene, and depends explicitly on the embedding, so on the components of the second fundamental form. Two scalars may be constructed, the mean extrinsic curvature, \mathcal{F}_{ii} , and the intrinsic or gaussian curvature $\det \mathcal{F}$, but note that the latter is a purely geometrical term which does not affect the equations of motion. The former enters quadratically as a manifestation of the $z \rightarrow -z$ symmetry of the system, hence^[143]

$$F_b = \frac{\kappa}{2} \int d^2\mathbf{r} (\mathcal{F}_{ii})^2 \approx \frac{\kappa}{2} \int d^2\mathbf{r} (\nabla^2 h)^2. \quad (3.15)$$

Here κ is the bending rigidity. The dispersion relation is now quadratic,

$$\omega_{\mathbf{q}}^F = \sqrt{\frac{\kappa}{\rho}} |q|^2. \quad (3.16)$$

This fact has dramatic consequences on the mechanics of graphene. These modes are so easy to excite that the graphene membrane is mechanically unstable at this level. This can be seen from the normal-normal correlation function. Classically, we have

$$\langle (\mathbf{n}(\mathbf{x}_1) - \mathbf{n}(\mathbf{x}_2))^2 \rangle \approx \frac{K_B T}{\pi \kappa} \int dq \frac{1 - J_0(|\mathbf{x}_1 - \mathbf{x}_2|q)}{q} \sim \frac{K_B T}{\pi \kappa} \times \ln \left(\frac{|\mathbf{x}_1 - \mathbf{x}_2|}{a} \right), \quad (3.17)$$

when $\frac{|\mathbf{x}_1 - \mathbf{x}_2|}{a} \gg 1$. This large $|\mathbf{x}_1 - \mathbf{x}_2|$ behavior is the signature of a high temperature rough phase.

Nevertheless, the coupling with in-plane modes tends to stabilize the flat phase. Such coupling comes from including quadratic terms in the strain tensor. In particular, if we include only the lowest powers in u_i and h we have

$$u_{ij} = \frac{1}{2} (\partial_i u_j + \partial_j u_i + \partial_i h \partial_j h). \quad (3.18)$$

The mechanical stabilization due to the coupling with in-plane modes can be seen even in a quasi-harmonic approximation. Let's consider that the crystal is under tension. Then, a static deformation configuration is expected at the equilibrium. We assume that both in-plane and out-of-plane displacements have dynamic components that add to their static background, so we write $u_i = u_i^{st} + u_i^{dyn}$, $h = h^{st} + h^{dyn}$. For simplicity, we assume that the static background is spatially uniform. The dynamics of in-plane phonon modes are not affected by the presence of such static components, however, for the flexural modes the harmonic Lagrangian reads now

$$\mathcal{L} = \frac{1}{2} \int d^2\mathbf{r} \left(\rho (\dot{h}^{dyn})^2 - \kappa (\nabla^2 h^{dyn})^2 - \lambda u_{ii}^{st} \partial_j h^{dyn} \partial_j h^{dyn} - 2\mu u_{ij}^{st} \partial_i h^{dyn} \partial_j h^{dyn} \right), \quad (3.19)$$

so the Euler-Lagrange equation for h^{dyn} is just

$$\rho \ddot{h}^{dyn} + \kappa \nabla^4 h^{dyn} - \lambda u_{ii}^{st} \nabla^2 h^{dyn} - 2\mu u_{ij}^{st} \partial_i \partial_j h^{dyn} = 0. \quad (3.20)$$

From this equation we deduce the dispersion relation

$$\omega_{\mathbf{q}}^F = \sqrt{\frac{\kappa}{\rho} |\mathbf{q}|^4 + u_{ii}^{st} \frac{\lambda}{\rho} |\mathbf{q}|^2 + \frac{2\mu}{\rho} u_{ij}^{st} q_i q_j}. \quad (3.21)$$

Note that this is enough to stabilize the crystal since the linearization of the dispersion at low $|\mathbf{q}|$ suppresses the logarithmic divergence of $\langle (\mathbf{n}(\mathbf{x}_1) - \mathbf{n}(\mathbf{x}_2))^2 \rangle$, so now $\langle (\mathbf{n}(\mathbf{x}_1) - \mathbf{n}(\mathbf{x}_2))^2 \rangle \sim \text{constant}$ when $|\mathbf{x}_1 - \mathbf{x}_2|/a \gg 1$. Latter on, when discussing transport in the presence of strain, we will take an approximate isotropic dispersion relation of the form

$$\omega_{\mathbf{q}} = \sqrt{\frac{\kappa}{\rho} |\mathbf{q}|^4 + \bar{u} v_L^2 |\mathbf{q}|^2}. \quad (3.22)$$

3.3 Electron-phonon coupling

We study now the electron-phonon coupling in the long-wavelength approximation. From now on, we are going to describe simultaneously both single-layer and bilayer graphene. Note that as long as we do not deal with optical modes, we may regard the bilayer graphene as a thick membrane with mass density and elastic constants twice as high as those for single-layer.^[147] On the other hand, the electronic Hamiltonian in second quantization notation can be written as $H = \sum_{\mathbf{k}} \Psi_{\mathbf{k}}^{\dagger} \mathcal{H}_{\mathbf{k}} \Psi_{\mathbf{k}}$, where $\Psi_{\mathbf{k}} = (a_{\mathbf{k}}, b_{\mathbf{k}})^T$, $c_{\mathbf{k}} = a_{\mathbf{k}}, b_{\mathbf{k}}$ ($c_{\mathbf{k}}^{\dagger}$) annihilate (creates) electronic quasiparticles with momentum \mathbf{k} in sublattice a, b (at different layers in the case of bilayer graphene), and

$$\mathcal{H}_{\mathbf{k}} = \hbar v_F \begin{pmatrix} 0 & k_x - ik_y \\ k_x + ik_y & 0 \end{pmatrix} \quad (3.23)$$

in the case of single-layer, whereas for bilayer graphene

$$\mathcal{H}_{\mathbf{k}} = \frac{\hbar^2}{2m} \begin{pmatrix} 0 & (k_x - ik_y)^2 \\ (k_x + ik_y)^2 & 0 \end{pmatrix}. \quad (3.24)$$

This is only the effective description around a single valley. Since we neglect inter-valley scattering, we concentrate only in one valley and we double the degeneracy of fermionic species, $g_d = g_s \times g_v = 4$.

The electron-phonon coupling may be constructed phenomenologically. For single-layer graphene (the discussion is similar in bilayer since $C_{6v} \cong D_{3d}$) the strain tensor components transform as indicated in Eq. (3.7). Therefore, two different couplings must be considered

$$\begin{aligned} \mathcal{H}_{A_1} &= g_{A_1} u_{ii} \mathcal{G}, \text{ and} \\ \mathcal{H}_{E_2} &= g_{E_2} \left[(u_{xx} - u_{yy}) \sigma_x - 2u_{xy} \tau_z \sigma_y \right]. \end{aligned} \quad (3.25)$$

The first coupling is the so called *deformation potential*, induced by the local contraction/dilation of the lattice. The bare deformation potential constant is typically $g_{A_1} \equiv g_0 \approx 20 - 30$ eV.^[148] Since we are interested in doped systems, we must take into account screening by substituting g_0 in the Fourier transformed potential with $g_0/\epsilon(\mathbf{q})$, where we take a Thomas-Fermi-like dielectric function

$$\epsilon(\mathbf{q}) = 1 + \frac{e^2 \mathcal{D}(E_F)}{2\epsilon_0 q}, \quad (3.26)$$

with $\mathcal{D}(E_F)$ being the density of states at the Fermi level, which reads within the effective description as

$$\mathcal{D}(E_F) = \begin{cases} \frac{2E_F}{\pi\hbar^2 v_F^2} & \text{for single-layer graphene,} \\ \frac{2m}{\pi\hbar^2} & \text{for bilayer graphene.} \end{cases} \quad (3.27)$$

It is convenient to define $g \equiv g_0/\epsilon(k_F)$ for single layer graphene, which gives a density independent screened deformation potential

$$g \approx \frac{g_0}{e^2/(\pi\epsilon_0\hbar v_F)} \approx \frac{g_0}{8.75} \approx 2 - 3.5 \text{ eV.} \quad (3.28)$$

Note that the value just obtained is in complete agreement with recent *ab initio* calculations which give $g \approx 3 \text{ eV}$.^[158] It will become clear later on that g as defined in Eq. (3.28) is the relevant deformation potential electron-phonon parameter in single layer graphene. For bilayer graphene $g(q) = g_0/\epsilon(q)$ gives

$$g(k_F) \approx \frac{g_0}{e^2 m / (\pi\epsilon_0 \hbar^2 k_F)} \approx \frac{g_0}{11.25} \sqrt{n} \approx (2 - 3) \sqrt{n} \text{ eV,} \quad (3.29)$$

with n in 10^{12} cm^{-2} . We may then write a q dependent deformation potential electron-phonon parameter which has the form $g_M(q) = gq/k_F$ for monolayer graphene, and $g_B(q) = g\hbar q/(mv_F)$ for bilayer.

The second coupling in Eq. (3.25) may be interpreted as *gauge potential* with opposite sign at each valley. Microscopically, it comes from changes in the hopping t due to the displacements of the atoms. In general, the hopping between atoms at positions \mathbf{r}_α and \mathbf{r}_β is modified (up to first order in the displacements) as

$$t_{\alpha\beta} \rightarrow t_{\alpha\beta} + \frac{\partial t_{\alpha\beta}}{\partial r} \delta |\mathbf{r}_\alpha - \mathbf{r}_\beta|, \quad (3.30)$$

where $\delta |\mathbf{r}_\alpha - \mathbf{r}_\beta|$ expresses the change in the distance between α and β sites. Up to first order in in-plane displacements and second order in out-of-plane displacements we have

$$\delta |\mathbf{r}_\alpha - \mathbf{r}_\beta| \approx \vec{\delta}_{\alpha\beta} \cdot \frac{(\vec{u}_\alpha - \vec{u}_\beta)}{a} + \frac{(h_\alpha - h_\beta)^2}{2a^2}. \quad (3.31)$$

In the continuum approximation we take

$$\begin{aligned} \vec{u}_\alpha - \vec{u}_\beta &\approx (\vec{\delta}_{\alpha\beta} \cdot \vec{\partial}) \vec{u}, \\ h_\alpha - h_\beta &\approx \vec{\delta}_{\alpha\beta} \cdot \vec{\partial} h. \end{aligned} \quad (3.32)$$

Hence, the change in the hopping along the direction $\vec{\delta}$ can be written as

$$\delta t_{\vec{\delta}} \approx \frac{\beta}{a^2} t \delta_i \delta_j u_{ij}, \quad (3.33)$$

where $\beta \equiv -\partial \ln t / \partial \ln a$ is the Grüneisen parameter associated to the hopping t . Since at the Dirac points we have

$$-\sum_{\vec{\delta}} \delta t_{\vec{\delta}} \times e^{\pm i\mathbf{k}\cdot\vec{\delta}} \approx \frac{3t}{4} (u_{xx} - u_{yy} \pm 2iu_{xy}), \quad (3.34)$$

we obtain the effective gauge field (here e is the electric charge)

$$\mathbf{A} = \pm \frac{\beta}{2ea} \begin{pmatrix} u_{xx} - u_{yy} \\ -2u_{xy} \end{pmatrix}. \quad (3.35)$$

Note that in both cases the coupling with out-of-plane distortions is quadratic due to the $z \rightarrow -z$ symmetry of the system.

Quantizing Fourier transformed displacement fields^[149] and introducing usual annihilation and creation operators $d_{\mathbf{q}}^{v=L,T}$ and $(d_{\mathbf{q}}^{v=L,T})^\dagger$ for longitudinal (L) and transverse (T) in-plane phonons, we can write the \mathbf{q} component of the in-plane displacement as

$$u_{\mathbf{q}}^{L/T} = \sqrt{\frac{\hbar}{2M\omega_{\mathbf{q}}^v}} \left[d_{\mathbf{q}}^{L/T} + (d_{-\mathbf{q}}^{L/T})^\dagger \right]. \quad (3.36)$$

Similarly, for flexural phonons we introduce the bosonic fields $d_{\mathbf{q}}^F$ and $(d_{\mathbf{q}}^F)^\dagger$, and write the \mathbf{q} component of the out-of-plane displacement as

$$h_{\mathbf{q}} = \sqrt{\frac{\hbar}{2M\omega_{\mathbf{q}}^F}} \left[d_{\mathbf{q}}^F + (d_{-\mathbf{q}}^F)^\dagger \right]. \quad (3.37)$$

The electron-phonon interaction Hamiltonian may then be written either in mono-

layer or bilayer graphene as

$$\begin{aligned}
 H_{ep} = & \sum_{\mathbf{k}, \mathbf{k}'} (a_{\mathbf{k}}^\dagger a_{\mathbf{k}'} + b_{\mathbf{k}}^\dagger b_{\mathbf{k}'}) \left\{ \sum_{\nu, \mathbf{q}} V_{1, \mathbf{q}}^\nu [d_{\mathbf{q}}^\nu + (d_{-\mathbf{q}}^\nu)^\dagger] \delta_{\mathbf{k}', \mathbf{k} - \mathbf{q}} + \right. \\
 & \left. + \sum_{\mathbf{q}, \mathbf{q}'} V_{1, \mathbf{q}, \mathbf{q}'}^F [d_{\mathbf{q}}^F + (d_{-\mathbf{q}}^F)^\dagger] [d_{\mathbf{q}'}^F + (d_{-\mathbf{q}'}^F)^\dagger] \delta_{\mathbf{k}', \mathbf{k} - \mathbf{q} - \mathbf{q}'} \right\} + \\
 & + \sum_{\mathbf{k}, \mathbf{k}'} \left\{ \sum_{\nu, \mathbf{q}} V_{2, \mathbf{q}}^\nu a_{\mathbf{k}}^\dagger b_{\mathbf{k}'} [d_{\mathbf{q}}^\nu + (d_{-\mathbf{q}}^\nu)^\dagger] \delta_{\mathbf{k}', \mathbf{k} - \mathbf{q}} + \sum_{\mathbf{q}, \mathbf{q}'} + \right. \\
 & \left. + V_{2, \mathbf{q}, \mathbf{q}'}^F a_{\mathbf{k}}^\dagger b_{\mathbf{k}'} [a_{\mathbf{q}}^F + (a_{-\mathbf{q}}^F)^\dagger] [a_{\mathbf{q}'}^F + (a_{-\mathbf{q}'}^F)^\dagger] \delta_{\mathbf{k}', \mathbf{k} - \mathbf{q} - \mathbf{q}'} + \text{H.C.} \right\}. \quad (3.38)
 \end{aligned}$$

For monolayer graphene the matrix elements read

$$\begin{aligned}
 V_{1, \mathbf{q}}^L &= \frac{g_0}{\epsilon(q)} i q \sqrt{\frac{\hbar}{2M \omega_{\mathbf{q}}^L}}, \\
 V_{1, \mathbf{q}, \mathbf{q}'}^F &= -\frac{g_0}{\epsilon(|\mathbf{q} + \mathbf{q}'|)} q q' \cos(\phi_{\mathbf{q}} - \phi_{\mathbf{q}'}) \frac{\hbar}{4M \sqrt{\omega_{\mathbf{q}}^F \omega_{\mathbf{q}'}^F}}, \\
 V_{2, \mathbf{q}}^L &= \frac{\hbar v_F \beta}{2a} i q e^{i2\phi_{\mathbf{q}}} \sqrt{\frac{\hbar}{2M \omega_{\mathbf{q}}^L}}, \\
 V_{2, \mathbf{q}}^T &= -\frac{\hbar v_F \beta}{2a} q e^{i2\phi_{\mathbf{q}}} \sqrt{\frac{\hbar}{2M \omega_{\mathbf{q}}^T}}, \\
 V_{2, \mathbf{q}, \mathbf{q}'}^F &= -\frac{\hbar v_F \beta}{4a} q q' e^{i(\phi_{\mathbf{q}} - \phi_{\mathbf{q}'})} \frac{\hbar}{2M \sqrt{\omega_{\mathbf{q}}^F \omega_{\mathbf{q}'}^F}}. \quad (3.39)
 \end{aligned}$$

Note that $V_{1, \mathbf{q}}^T = 0$ (see also Refs. 150, 151). In the case of bilayer graphene the matrix elements are the same except for the gauge potential coupling, becoming dependent on fermionic momenta \mathbf{k} and \mathbf{k}' . This is due to the fact that the microscopic origin of this coupling resides in changes in the intra-layer hopping t as we have seen, whereas the operator associated to different sublattices are also associated to different layers. On the other hand, the changes in the inter-layer hopping for acoustic deformations are in principle negligible. We may obtain straightforwardly the couplings of Eq. (3.38) by the minimal coupling prescription in Eq. (3.24) and expanding up to linear order in the in-plane displacements and second order in the out of plane displacements. Thus, the matrix elements take exactly the same form as in Eq. (3.39) with the replacement $v_F \rightarrow \hbar(k e^{-i\theta_{\mathbf{k}}} + k' e^{-i\theta_{\mathbf{k}'}})/(2m)$.

3.4 Variational approach to semi-classical transport

Our aim here is to study the T dependent resistivity as a result of the electron-phonon interaction derived in the previous section. We assume the doped regime $E_F \gg \hbar/\tau$, where $1/\tau$ is the characteristic electronic scattering rate (due to phonons, disorder, etc). The doped regime immediately implies $k_F^{-1} \ll v_F \tau \equiv \ell$, where ℓ is the characteristic mean-free path, thus justifying the use of Boltzmann transport theory (even though graphene's quasiparticles are chiral the semiclassical approach still holds away from the Dirac point^[152,153]).

The Boltzmann equation is an integro-differential equation for the steady state probability distribution $f_{\mathbf{k}}$.^[154] It can be generally written as

$$\dot{\mathbf{r}} \cdot \nabla_{\mathbf{r}} f_{\mathbf{k}} + \dot{\mathbf{k}} \cdot \nabla_{\mathbf{k}} f_{\mathbf{k}} = \dot{f}_{\mathbf{k}} \Big|_{\text{scatt}}, \quad (3.40)$$

where the terms on the left hand side are due to, respectively, *diffusion* and *external fields*, while on the right hand side *scattering* provides the required balance at the steady state. The Boltzmann equation is quite intractable in practice, and its linearized version is used instead,

$$\dot{\mathbf{r}} \cdot \nabla_{\mathbf{r}} f_{\mathbf{k}}^{(0)} + \dot{\mathbf{k}} \cdot \nabla_{\mathbf{k}} f_{\mathbf{k}}^{(0)} = \delta \dot{f}_{\mathbf{k}} \Big|_{\text{scatt}}, \quad (3.41)$$

where $\delta \dot{f}_{\mathbf{k}} \Big|_{\text{scatt}}$ is the linearized collision integral. Expanding the distribution probability around its equilibrium value $f_{\mathbf{k}}^{(0)} = 1/\{\exp[(\varepsilon_{\mathbf{k}} - \mu)/k_B T] + 1\}$,

$$f_{\mathbf{k}} = f_{\mathbf{k}}^{(0)} - \frac{\partial f_{\mathbf{k}}^{(0)}}{\partial \varepsilon_{\mathbf{k}}} \Phi_{\mathbf{k}}, \quad (3.42)$$

and using the equilibrium property that $\dot{f}_{\mathbf{k}}^{(0)} \Big|_{\text{scatt}} = 0$, it can be seen that $\delta \dot{f}_{\mathbf{k}} \Big|_{\text{scatt}}$ is linear in $\Phi_{\mathbf{k}}$, see Appendix B, and that it can be written as a linear application in terms of the linear scattering operator $P_{\mathbf{k}}$,

$$\delta \dot{f}_{\mathbf{k}} \Big|_{\text{scatt}} = P_{\mathbf{k}} \Phi_{\mathbf{k}} \equiv - \sum_{\mathbf{k}_1, \dots, \mathbf{k}_n} \mathcal{P}_{\mathbf{k}, \mathbf{k}_1, \dots, \mathbf{k}_n} (\Phi_{\mathbf{k}} \pm \Phi_{\mathbf{k}_1} \cdots \pm \Phi_{\mathbf{k}_n}), \quad (3.43)$$

where $\mathcal{P}_{\mathbf{k}, \mathbf{k}_1, \dots, \mathbf{k}_n}$ is a generalized transition rate per unit energy.^[154] Writing the linearized Boltzmann equation, Eq. (3.41), in the form

$$X_{\mathbf{k}} = P_{\mathbf{k}} \Phi_{\mathbf{k}},$$

and defining the inner products,

$$\langle \Phi, X \rangle = \sum_{\mathbf{k}} \Phi_{\mathbf{k}} \left(\dot{\mathbf{r}} \cdot \nabla_{\mathbf{r}} f_{\mathbf{k}}^{(0)} + \dot{\mathbf{k}} \cdot \nabla_{\mathbf{k}} f_{\mathbf{k}}^{(0)} \right), \quad (3.44)$$

and

$$\begin{aligned} \langle \Phi, P\Phi \rangle &= \sum_{\mathbf{k}, \mathbf{k}_1, \dots, \mathbf{k}_n} \Phi_{\mathbf{k}} \mathcal{P}_{\mathbf{k}, \mathbf{k}_1, \dots, \mathbf{k}_n} \left(\Phi_{\mathbf{k}} \pm \Phi_{\mathbf{k}_1} \cdots \pm \Phi_{\mathbf{k}_n} \right) = \\ &= \frac{1}{(n+1)} \sum_{\mathbf{k}, \mathbf{k}_1, \dots, \mathbf{k}_n} \left(\Phi_{\mathbf{k}} \pm \Phi_{\mathbf{k}_1} \cdots \pm \Phi_{\mathbf{k}_n} \right)^2 \mathcal{P}_{\mathbf{k}, \mathbf{k}_1, \dots, \mathbf{k}_n}, \end{aligned} \quad (3.45)$$

the *variational principle* asserts that of all functions $\Phi_{\mathbf{k}}$ satisfying $\langle \Phi, X \rangle = \langle \Phi, P\Phi \rangle$, the solution of the linearized Boltzmann equation gives to the quantity $\langle \Phi, P\Phi \rangle / \{\langle \Phi, X \rangle\}^2$ its *minimum* value.^[154] In particular, the resistivity ϱ can be written as

$$\varrho = \frac{\mathcal{A}}{g_d} \times \frac{\langle \Phi, P\Phi \rangle}{\{\langle \Phi, X(E=1, \nabla_{\mathbf{r}} f^{(0)} = 0) \rangle\}^2}, \quad (3.46)$$

being thus expected to be a *minimum* for the right solution.^[154] Here \mathcal{A} is the area of the graphene sample. The quantity $X(E=1, \nabla_{\mathbf{r}} f^{(0)} = 0)$ refers to the left hand side of Eq. (3.41) in a unit electric field and no spatial gradients (for example, zero temperature gradient). It is easy to show that $\langle \Phi, X \rangle = \mathbf{E} \cdot \mathbf{J}$, where

$$\mathbf{J} = \sum_{\mathbf{k}} e \mathbf{v}_{\mathbf{k}} \Phi_{\mathbf{k}} \frac{\partial f_{\mathbf{k}}^{(0)}}{\partial \varepsilon_{\mathbf{k}}} \quad (3.47)$$

is the current per non-degenerate mode (per spin and valley in monolayer and bilayer graphene).

A well known solution to the Boltzmann equation exists when scattering is elastic, the Fermi surface isotropic, and the transition rate can be written as $\mathcal{P}_{\mathbf{k}, \mathbf{k}'} = \mathcal{P}(k, \theta_{\mathbf{k}, \mathbf{k}'})$, where $\theta_{\mathbf{k}, \mathbf{k}'} = \theta_{\mathbf{k}} - \theta_{\mathbf{k}'}$ is the angle between \mathbf{k} and \mathbf{k}' .^[154] Under these conditions the solution reads,

$$\Phi_{\mathbf{k}} = v_{\mathbf{k}} \cdot \left(e\mathbf{E} - \frac{\varepsilon_{\mathbf{k}}}{T} \nabla T \right) \tau(k),$$

where $\tau(k)$ is the isotropic scattering rate, and we have written $\nabla_{\mathbf{r}} f_{\mathbf{k}}^{(0)} = \partial f_{\mathbf{k}}^{(0)} / \partial \varepsilon_{\mathbf{k}} \nabla T$. Clearly, the later solution for $\Phi_{\mathbf{k}}$ can be cast in the form $\Phi_{\mathbf{k}} \propto \mathbf{k} \cdot \mathbf{u}$,^[154] where \mathbf{u} is a unit vector in the direction of the applied fields. So, in more complicated cases where there is a departure from the isotropic conditions and/or from elastic scattering, it is a good starting point to use Eq. (3.46) with $\Phi_{\mathbf{k}} \propto \mathbf{k} \cdot \mathbf{u}$ to get an approximate (from above) result for the resistivity. Note that the coefficient multiplying $\mathbf{k} \cdot \mathbf{u}$ is unimportant as it cancels out. This variational method is equivalent to a linear response Kubo-Nakano-Mori approach with the perturbation inducing scattering treated in the Born approximation.^[155]

3.5 Phonon limited resistivity

We use the variational method to get the T dependent resistivity in monolayer and bilayer graphene due to scattering by acoustic phonons. Using the quasi-elastic approximation, $\delta \dot{f}_{\mathbf{k}}|_{\text{scatt}}$ can indeed be cast in the form of Eq. (3.43) (see Appendix B for details),

$$\delta \dot{f}_{\mathbf{k}}|_{\text{scatt}} = - \sum_{\mathbf{k}'} \mathcal{P}_{\mathbf{k},\mathbf{k}'} (\Phi_{\mathbf{k}} - \Phi_{\mathbf{k}'}), \quad (3.48)$$

where for scattering by one in-plane phonon

$$\mathcal{P}_{\mathbf{k},\mathbf{k}'} = \frac{2\pi}{\hbar} \sum_{\mathbf{q},\nu} w_{\nu}(\mathbf{q}, \mathbf{k}, \mathbf{k}') \omega_{\mathbf{q}}^{\nu} \frac{\partial n_{\mathbf{q}}}{\partial \omega_{\mathbf{q}}^{\nu}} \frac{\partial f_{\mathbf{k}}^{(0)}}{\partial \varepsilon_{\mathbf{k}}} \delta_{\mathbf{k},\mathbf{k}'+\mathbf{q}} \delta(\varepsilon_{\mathbf{k}} - \varepsilon_{\mathbf{k}'}), \quad (3.49)$$

and for scattering by two flexural phonons

$$\begin{aligned} \mathcal{P}_{\mathbf{k},\mathbf{k}'} = & -\frac{2\pi}{\hbar^2} k_B T \frac{\partial f_{\mathbf{k}}^{(0)}}{\partial \varepsilon_{\mathbf{k}}} \sum_{\mathbf{q},\mathbf{q}'} w_F(\mathbf{q}, \mathbf{q}', \mathbf{k}, \mathbf{k}') \frac{\partial n_{\mathbf{q}}}{\partial \omega_{\mathbf{q}}^F} \frac{\partial n_{\mathbf{q}'}}{\partial \omega_{\mathbf{q}'}^F} \times \\ & \times \left(\frac{\omega_{\mathbf{q}}^F + \omega_{\mathbf{q}'}^F}{1 + n_{\mathbf{q}} + n_{\mathbf{q}'}} - \frac{\omega_{\mathbf{q}}^F - \omega_{\mathbf{q}'}^F}{n_{\mathbf{q}} - n_{\mathbf{q}'}} \right) \delta_{\mathbf{k},\mathbf{k}'+\mathbf{q}+\mathbf{q}'} \delta(\varepsilon_{\mathbf{k}} - \varepsilon_{\mathbf{k}'}), \end{aligned} \quad (3.50)$$

with $n_{\mathbf{q}} = 1/[\exp(\hbar\omega_{\mathbf{q}}/k_B T) - 1]$ the equilibrium phonon distribution. The kernel quantities $w_{\nu}(\mathbf{q}, \mathbf{k}, \mathbf{k}')$ and $w_F(\mathbf{q}, \mathbf{q}', \mathbf{k}, \mathbf{k}')$ are related to the matrix elements in Eq. (3.39). For monolayer graphene in the case of one phonon process we have

$$w_{\nu}(\mathbf{q}, \mathbf{k}, \mathbf{k}') \approx \left| V_{1,\mathbf{q}}^{\nu} \right|^2 (1 + \cos \theta_{\mathbf{k},\mathbf{k}'}) + \left| V_{2,\mathbf{q}}^{\nu} \right|^2, \quad (3.51)$$

with a similar expression for two phonon processes $w_F(\mathbf{q}, \mathbf{q}', \mathbf{k}, \mathbf{k}')$ with $V_{\mathbf{q}}^{\nu} \rightarrow V_{\mathbf{q},\mathbf{q}'}^F$. For bilayer graphene,

$$w_{\nu}(\mathbf{q}, \mathbf{k}, \mathbf{k}') \approx \left| V_{1,\mathbf{q}}^{\nu} \right|^2 (1 + \cos 2\theta_{\mathbf{k},\mathbf{k}'}) + \left| \tilde{V}_{2,\mathbf{q}}^{\nu} \right|^2 (k^2 + k'^2 + 2kk' \cos \theta_{\mathbf{k},\mathbf{k}'}) \quad (3.52)$$

for one phonon processes, where \tilde{V}_2 means the matrix elements given in Eq. (3.39) for the gauge potential without the term $(ke^{-i\theta_{\mathbf{k}}} + k'e^{-i\theta_{\mathbf{k}'}})$, and as before a similar expression for two phonon processes $w_F(\mathbf{q}, \mathbf{q}', \mathbf{k}, \mathbf{k}')$ with $V_{\mathbf{q}}^{\nu} \rightarrow V_{\mathbf{q},\mathbf{q}'}^F$.

By using the setting given above the resistivity is conveniently written as

$$\varrho = \frac{\mathcal{A}}{g_d} \frac{\frac{1}{2} \sum_{\mathbf{k},\mathbf{k}'} (\Phi_{\mathbf{k}} - \Phi_{\mathbf{k}'})^2 \mathcal{P}_{\mathbf{k},\mathbf{k}'}}{\left| e \sum_{\mathbf{k}} \Phi_{\mathbf{k}} \mathbf{v}_{\mathbf{k}} \frac{\partial f_{\mathbf{k}}^{(0)}}{\partial \varepsilon_{\mathbf{k}}} \right|^2} \approx \frac{\mathcal{A}}{8e^2} \frac{\int d\mathbf{k}d\mathbf{k}' (\mathbf{K} \cdot \mathbf{u})^2 \mathcal{P}_{\mathbf{k},\mathbf{k}'}}{\left| \int d\mathbf{k} \mathbf{k} \cdot \mathbf{u} \mathbf{v}_{\mathbf{k}} \frac{\partial f_{\mathbf{k}}^{(0)}}{\partial \varepsilon_{\mathbf{k}}} \right|^2}, \quad (3.53)$$

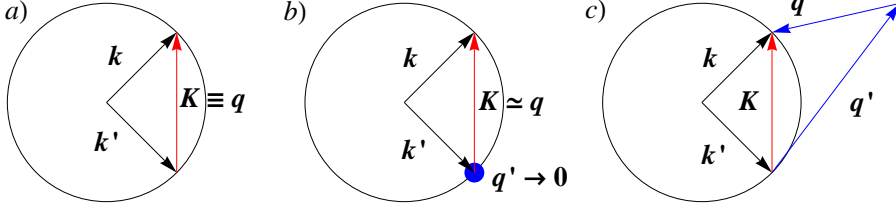


Figure 3.1: Kinematics of electron scattering by: (a) in-plane phonons, (b) non-strained flexural and (c) strained flexural phonons.

where we changed from summation over \mathbf{k} -space to integration, and defined $\mathbf{K} = \mathbf{k} - \mathbf{k}'$. The integral in the denominator can be done immediately assuming $\varepsilon_F \gg k_B T$. The result reads the same for monolayer and bilayer graphene,

$$\left| \int d\mathbf{k} \mathbf{k} \cdot \mathbf{u} \mathbf{v}_{\mathbf{k}} \frac{\partial f_{\mathbf{k}}^{(0)}}{\partial \varepsilon_{\mathbf{k}}} \right| \approx \frac{\pi k_F^2}{\hbar}, \quad (3.54)$$

and hence the resistivity reads

$$\varrho = \frac{\nu \hbar^2}{8\pi^2 e^2 k_F^4} \int d\mathbf{k} d\mathbf{k}' (\mathbf{K} \cdot \mathbf{u})^2 \mathcal{P}_{\mathbf{k}, \mathbf{k}'}. \quad (3.55)$$

In order to proceed analytically with the remaining integral we have to specify the T regime. For each scattering process (one or two phonon scattering) we may identify two different T regimes, *low* and *high* T , related to whether only small angle or every angle are available to scatter from $|\mathbf{k}\rangle$ to $|\mathbf{k}'\rangle$. Recall that since we are dealing with quasielastic scattering both \mathbf{k} and \mathbf{k}' sit on the Fermi circle, see Fig. 3.1, and $|\mathbf{k}\rangle$ and $|\mathbf{k}'\rangle$ are adiabatically connected through a rotation of $\theta_{\mathbf{k}, \mathbf{k}'}$ in momentum space. Large angle scattering is only possible if phonons with high enough momentum are available to scatter electrons. The characteristic Bloch-Grüneisen temperature T_{BG} separating the two regimes may thus be set by the minimum phonon energy necessary to have full back scattering,

$$k_B T_{BG} = \hbar \omega_{2k_F}. \quad (3.56)$$

For scattering by in-plane phonons T_{BG} takes the value

$$T_{BG}^{(L)} \approx 57\sqrt{n} \text{ K} \quad \text{and} \quad T_{BG}^{(T)} \approx 38\sqrt{n} \text{ K}, \quad (3.57)$$

for longitudinal and transverse phonons respectively, with density n in units of 10^{12} cm^{-2} . When scattering is by two non-strained flexural phonons, the crossover between low and high T regimes is given by

$$T_{BG} \approx 0.1n \text{ K}, \quad (3.58)$$

with n again measured in 10^{12} cm^{-2} , while in the presence of strain, using the approximated strained flexural phonon dispersion $\omega_{\mathbf{q}} \approx q\sqrt{\alpha^2 q^2 + \bar{u}v_L^2}$, with $\alpha = \sqrt{\kappa/\rho}$ and $v_L = \sqrt{(\lambda + 2\mu)/\rho}$, we get

$$T_{BG} \simeq 28\sqrt{n\bar{u}} \text{ K}. \quad (3.59)$$

It is obvious from Eqs. (3.58) and (3.59) that the high- T regime is the relevant one for flexural phonon scattering.

3.5.1 In-plane phonons

A sketch of the scattering process in momentum space involving one phonon is shown in Fig. 3.1(a). The monolayer case has been discussed extensively in the literature.^[150, 151, 156, 157] Here we discuss both monolayer and bilayer cases simultaneously. Inserting Eq. (3.49) for $\mathcal{A}_{\mathbf{k}, \mathbf{k}'}$ into Eq. (3.55) we get

$$\varrho_{in} = \frac{\mathcal{A}\hbar}{4\pi e^2 k_F^4} \int d\mathbf{k} d\mathbf{k}' (\mathbf{K} \cdot \mathbf{u})^2 \times \sum_{\nu} w_{\nu}(\mathbf{K}, \mathbf{k}, \mathbf{k}') \omega_{\mathbf{K}}^{\nu} \frac{\partial n_{\mathbf{K}}^{(0)}}{\partial \omega_{\mathbf{K}}^{\nu}} \frac{\partial f_{\mathbf{k}}^{(0)}}{\partial \epsilon_{\mathbf{k}}} \delta(\epsilon_{\mathbf{k}} - \epsilon_{\mathbf{k}'}), \quad (3.60)$$

where we have already performed the sum over \mathbf{q} . We can simplify the integral above by integrating over k and k' noting the presence of $\delta(\epsilon_{\mathbf{k}} - \epsilon_{\mathbf{k}'})$ and $\frac{\partial f_{\mathbf{k}}}{\partial \epsilon_{\mathbf{k}}} \approx -\delta(\epsilon_F - \epsilon_{\mathbf{k}})$. The result reads

$$\varrho_{in} \approx -\frac{\mathcal{A}\hbar}{4\pi e^2 k_F^4} \times \int d\theta_{\nu} d\theta_{\nu'} (\mathbf{K} \cdot \mathbf{u})^2 \sum_{\nu} \tilde{w}_{\nu}(\mathbf{K}, k_F \hat{\mathbf{e}}_{\mathbf{k}}, k_F \hat{\mathbf{e}}_{\mathbf{k}'}) \omega_{\mathbf{K}}^{\nu} \frac{\partial n_{\mathbf{K}}^{(0)}}{\partial \omega_{\mathbf{K}}^{\nu}}, \quad (3.61)$$

with $\mathbf{K} = k_F(\hat{\mathbf{e}}_{\mathbf{k}} - \hat{\mathbf{e}}_{\mathbf{k}'})$ and the modified kernel defined as

$$\tilde{w}_{\nu}(\mathbf{K}, k_F \hat{\mathbf{e}}_{\mathbf{k}}, k_F \hat{\mathbf{e}}_{\mathbf{k}'}) = w_{\nu}(\mathbf{K}, k_F \hat{\mathbf{e}}_{\mathbf{k}}, k_F \hat{\mathbf{e}}_{\mathbf{k}'}) \times \begin{cases} \frac{k_F^2}{\hbar^2 v_F^2} & \text{for monolayer,} \\ \frac{m^2}{\hbar^4} & \text{for bilayer.} \end{cases} \quad (3.62)$$

Making use of the matrix elements in Eq. (3.39) we get

$$\tilde{w}_{\nu}(\mathbf{K}, k_F \hat{\mathbf{e}}_{\mathbf{k}}, k_F \hat{\mathbf{e}}_{\mathbf{k}'}) \equiv \tilde{w}_{\nu}(K) = \frac{[D^{\nu}(K/k_F)]^2 k_F^2 K^2}{2\mathcal{A}\rho v_F^2 \hbar \omega_{\mathbf{K}}^{\nu}}, \quad (3.63)$$

where we have used the relation $K = 2k_F \sin(\theta_{\mathbf{k},\mathbf{k}'}/2)$, and we define

$$D^v(y) = \begin{cases} \left[2g^2 y^2 \left(1 - \frac{y^2}{4}\right) \delta_{vL} + \frac{\hbar^2 v_F^2 \beta^2}{4a^2} \right]^{1/2} & \text{for monolayer,} \\ \left[2g^2 y^2 \left(1 - \frac{y^2}{2}\right)^2 \delta_{vL} + \frac{\hbar^2 v_F^2 \beta^2}{4a^2} \left(1 - \frac{y^2}{4}\right) \right]^{1/2} & \text{for bilayer.} \end{cases} \quad (3.64)$$

The kernel depends only on $\theta_{\mathbf{k},\mathbf{k}'}$, or equivalently K (the norm of \mathbf{K}), as is the case of the rest of factors in the integrand of Eq. (3.61) but for $(\mathbf{K} \cdot \mathbf{u})^2$. The latter can be written as $(\mathbf{K} \cdot \mathbf{u})^2 = K^2 \cos^2 \gamma$, and the angular integration is then conveniently done by integrating over γ keeping $\theta_{\mathbf{k},\mathbf{k}'} = \theta_{\mathbf{k}} - \theta_{\mathbf{k}'} \equiv \theta$ constant, and integrate over θ afterward, or equivalently K . Using $d\theta = dK/\sqrt{k_F^2 - K^2/4}$, the resistivity becomes

$$\varrho_{in} \approx -\frac{\mathcal{A}\hbar}{2e^2 k_F^4} \sum_v \int_0^{2k_F} dK \frac{K^2 \tilde{w}_v(K) \omega_K^v}{\sqrt{k_F^2 - K^2/4}} \frac{\partial n_K^{(0)}}{\partial \omega_K^v}. \quad (3.65)$$

Inserting Eq. (3.63) for the kernel $\tilde{w}_v(K)$ into Eq. (3.65) we readily obtain

$$\varrho_{in} \approx \frac{8\hbar k_F^2}{e^2 \rho v_F^2 k_B T} \sum_v \int_0^1 dx [D^v(2x)]^2 \frac{x^4}{\sqrt{1-x^2}} \frac{e^{xz_v}}{(e^{xz_v} - 1)^2}, \quad (3.66)$$

where $z_v = \hbar\omega_{2k_F}^v/k_B T$. Typical T dependent resistivity due to scattering by in-plane phonons is shown in Fig. 5.1. In agreement with the analytical results that we are going to disclose next, there is no qualitative difference between monolayer and bilayer graphene.

In the low T regime, $T \ll T_{BG}$, we have $z_v \gg 1$, so that the integrand in Eq. (3.66) is only contributing significantly for $x \ll 1$. Since we have

$$D^v(y \ll 1) = \left[2g^2 y^2 \delta_{vL} + \frac{\hbar^2 v_F^2 \beta^2}{4a^2} \right]^{1/2}, \quad (3.67)$$

the resistivity reduces to

$$\varrho_{in} \approx \sum_v \left[g^2 \frac{3\Gamma(6)\zeta(6)}{\Gamma(4)\zeta(4)} \left(\frac{T}{T_{BG}} \right)^2 \delta_{vL} + \frac{\hbar^2 v_F^2 \beta^2}{4a^2} \right] \times \frac{\Gamma(4)\zeta(4)(k_B T)^4}{e^2 \rho \hbar^4 v_F^2 v_v^5 k_F^3}, \quad (3.68)$$

where $\Gamma(n) = (n-1)!$ is the *gamma function* and $\zeta(n)$ is the *Riemann zeta function*. The result is valid both for monolayer and bilayer cases. We have obtained the expected T^4 behavior at low T for coupling through gauge potential, which is the 2-dimensional analogue of the T^5 Bloch theory in 3-dimensional metals.^[154, 156] The

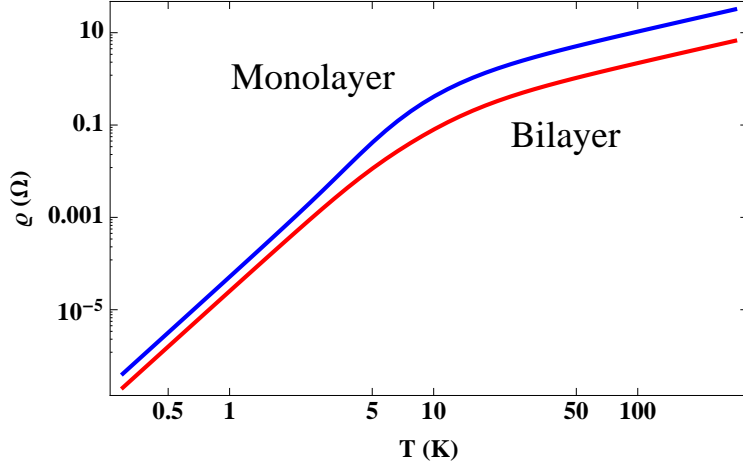


Figure 3.2: Resistivity due to scattering by in-plane phonons as a function of temperature (in blue, monolayer graphene, in red, bilayer). In both cases $n = 10^{12} \text{ cm}^{-2}$ and we take $g = 3 \text{ eV}$ and $\beta = 3$.

scalar potential contribution comes proportional to T^6 due to screening. It can be neglected in the low T regime; even though $3\Gamma(6)\zeta(6)/[\Gamma(4)\zeta(4)] \approx 50$, it is strongly suppressed by $T/T_{BG} \ll 1$.

In the high T regime, $T \gg T_{BG}$, the inequality $z_v \ll 1$ holds, so $e^{z_v x}/(e^{z_v x} - 1)^2 \approx 1/(z_v x)$ in Eq. (3.66). The usual linear in T resistivity for one phonon scattering is then recovered,

$$\rho_{in} \approx \frac{\pi k_B T}{4\hbar\rho e^2 v_L^2 v_F^2} \times \begin{cases} 2g^2 + \frac{\hbar^2 v_F^2 \beta^2 v_L^2}{8a^2 \bar{v}^2} & \text{for monolayer,} \\ 7g^2 + \frac{\hbar^2 v_F^2 \beta^2 v_L^2}{8a^2 \bar{v}^2} & \text{for bilayer,} \end{cases} \quad (3.69)$$

where $1/\bar{v}^2 = 1/v_L^2 + 1/v_T^2$. Note that, at odds with the low T regime, now the scalar potential contribution is higher than the gauge potential one for the typical coupling values discussed before.

A final remark regarding the temperature dependent resistivity due to in-plane phonons has to do with the value of the electron-phonon coupling parameters β and g . While β is expected to be restricted to the range $\beta \sim 2 - 3$, the value of the deformation potential parameter g is debated in the literature. Phenomenology gives $g \sim 10 - 30 \text{ eV}$; ^[148, 156] recent *ab initio* calculations provide a much smaller

value $g \sim 3 \text{ eV}$.^[158] On the other hand, experiments seem to confirm the higher values, giving $g \sim 15 - 25 \text{ eV}$.^[139, 159] Our claim here is that all these values make sense, if properly interpreted: phenomenology gives essentially unscreened deformation potential, which should take values of $\mathcal{O}(10) \text{ eV}$; screening effects suppress the deformation potential to $\mathcal{O}(1) \text{ eV}$, as we have seen within the Thomas Fermi approximation, in good agreement with *ab initio* results where screening is built in; the fact that transport experiments give a much higher deformation potential is a strong indication that phonon scattering through gauge potential, usually not included when fitting the data,^[139, 159] is at work. Indeed, using the monolayer version of Eq. (3.69), we readily find that the fitting quantity in Refs. 139 and 159 should be replaced by

$$\tilde{D} = \left[2g^2 + \frac{v_F^2 \hbar^2 \beta^2}{2a^2} \left(1 + \frac{v_L^2}{v_T^2} \right) \right]^{1/2}, \quad (3.70)$$

which keeping $g \sim 3 \text{ eV}$ takes values $\tilde{D} \sim 10 - 20 \text{ eV}$ for $\beta \sim 2 - 3$, in excellent agreement with experiments. Moreover, since the gauge potential is not screened it provides a natural explanation for the T^4 resistivity behavior recently reported at low T in Ref. 159, where the expected T^6 contribution due to scalar potential is absent.^[160]

3.5.2 Flexural phonons

We analyze now the case of flexural phonons. Inserting Eq. (3.50) for $\mathcal{D}_{\mathbf{k}, \mathbf{k}'}$ into Eq. (3.55) we get

$$\begin{aligned} \varrho_F = & -\frac{\mathcal{A} k_B T}{4\pi e^2 k_F^4} \int d\mathbf{k} d\mathbf{k}' (\mathbf{K} \cdot \mathbf{u})^2 \sum_{\mathbf{q}} w_F(\mathbf{q}, \mathbf{K} - \mathbf{q}, \mathbf{k}, \mathbf{k}') \times \\ & \times \frac{\partial n_{\mathbf{q}}}{\partial \omega_{\mathbf{q}}^F} \frac{\partial n_{\mathbf{q}'}}{\partial \omega_{\mathbf{q}'}^F} \frac{\partial f_{\mathbf{k}}^{(0)}}{\partial \varepsilon_{\mathbf{k}}} \delta(\varepsilon_{\mathbf{k}} - \varepsilon_{\mathbf{k}'}) \left(\frac{\omega_{\mathbf{q}}^F + \omega_{\mathbf{K}-\mathbf{q}}^F}{1 + n_{\mathbf{q}} + n_{\mathbf{K}-\mathbf{q}}} - \frac{\omega_{\mathbf{q}}^F - \omega_{\mathbf{K}-\mathbf{q}}^F}{n_{\mathbf{q}} - n_{\mathbf{K}-\mathbf{q}}} \right), \end{aligned} \quad (3.71)$$

where we have already performed the sum over \mathbf{q}' . We can simplify the integral above by integrating over k and k' noting the presence of $\delta(\varepsilon_{\mathbf{k}} - \varepsilon_{\mathbf{k}'})$ and $\frac{\partial f_{\mathbf{k}}}{\partial \varepsilon_{\mathbf{k}}} \approx -\delta(\varepsilon_F - \varepsilon_{\mathbf{k}})$. The result reads,

$$\begin{aligned} \varrho_F \approx & \frac{\mathcal{A} k_B T}{4\pi e^2 k_F^4} \int d\theta_{\mathbf{k}} d\theta_{\mathbf{k}'} (\mathbf{K} \cdot \mathbf{u})^2 \sum_{\mathbf{q}} \tilde{w}_F(\mathbf{q}, \mathbf{K} - \mathbf{q}, k_F \hat{\mathbf{e}}_{\mathbf{k}}, k_F \hat{\mathbf{e}}_{\mathbf{k}'}) \times \\ & \times \frac{\partial n_{\mathbf{q}}}{\partial \omega_{\mathbf{q}}^F} \frac{\partial n_{\mathbf{K}-\mathbf{q}}}{\partial \omega_{\mathbf{K}-\mathbf{q}}^F} \left(\frac{\omega_{\mathbf{q}}^F + \omega_{\mathbf{K}-\mathbf{q}}^F}{1 + n_{\mathbf{q}} + n_{\mathbf{K}-\mathbf{q}}} - \frac{\omega_{\mathbf{q}}^F - \omega_{\mathbf{K}-\mathbf{q}}^F}{n_{\mathbf{q}} - n_{\mathbf{K}-\mathbf{q}}} \right). \end{aligned} \quad (3.72)$$

The modified kernel is defined as before

$$\tilde{w}_F(\mathbf{K}, k_F \hat{\mathbf{e}}_{\mathbf{k}}, k_F \hat{\mathbf{e}}_{\mathbf{k}'}) = w_\nu(\mathbf{K}, k_F \hat{\mathbf{e}}_{\mathbf{k}}, k_F \hat{\mathbf{e}}_{\mathbf{k}'}) \times \begin{cases} \frac{k_F^2}{\hbar^2 v_F^2} & \text{for monolayer,} \\ \frac{m^2}{\hbar^4} & \text{for biayer,} \end{cases} \quad (3.73)$$

with $V_{\mathbf{q}}^\nu \rightarrow V_{\mathbf{q}, \mathbf{q}'}^F$. Inserting the matrix elements in Eq. (3.39) it takes the explicit form

$$\tilde{w}_F(\mathbf{q}, \mathbf{K} - \mathbf{q}, k_F \hat{\mathbf{e}}_{\mathbf{k}}, k_F \hat{\mathbf{e}}_{\mathbf{k}'}) \equiv \tilde{w}_F(q, K, |\mathbf{K} - \mathbf{q}|) = \frac{[D^F(K/k_F)]^2 q^2 k_F^2 |\mathbf{K} - \mathbf{q}|^2}{2^4 \mathcal{A}^2 \rho^2 v_F^2 \omega_q^F \omega_{|\mathbf{K} - \mathbf{q}|}^F}, \quad (3.74)$$

where we have used the relation $K = 2k_F \sin(\theta_{\mathbf{k}, \mathbf{k}'}/2)$, and $D^F(x)$ is given by

$$D^F(y) = \begin{cases} \left[g^2 y^2 \left(1 - \frac{y^2}{4} \right) + \frac{\hbar^2 v_F^2 \beta^2}{4a^2} \right]^{1/2} & \text{for monolayer,} \\ \left[g^2 y^2 \left(1 - \frac{y^2}{2} \right)^2 + \frac{\hbar^2 v_F^2 \beta^2}{4a^2} \left(1 - \frac{y^2}{4} \right) \right]^{1/2} & \text{for bilayer.} \end{cases} \quad (3.75)$$

In deriving Eq. (3.74) we have used $\cos^2(\phi - \phi') = [1 + \cos(2\phi - 2\phi')]/2$ and dropped the oscillatory part. The sum over \mathbf{q} can be replaced by an integral, $\sum_{\mathbf{q}} \rightarrow \frac{\mathcal{A}}{(2\pi)^2} \int q dq d\phi$, and owing to the relation $Q^2 \equiv |\mathbf{K} - \mathbf{q}|^2 = K^2 + q^2 - 2qK \cos \phi$ we can write the resistivity as

$$\varrho_F \approx \frac{\mathcal{A}^2 k_B T}{8\pi^3 e^2 k_F^4} \int d\theta_{\mathbf{k}} d\theta_{\mathbf{k}'} (\mathbf{K} \cdot \mathbf{u})^2 \int_0^\infty dq q \frac{\partial n_q}{\partial \omega_q^F} \times \\ \times \int_{|K-q|}^{|K+q|} dQ \frac{Q \tilde{w}_F(q, K, Q)}{\sqrt{q^2 K^2 - (K^2 + q^2 - Q^2)^2/4}} \frac{\partial n_Q}{\partial \omega_Q^F} \left(\frac{\omega_q^F + \omega_Q^F}{1 + n_q + n_Q} - \frac{\omega_q^F - \omega_Q^F}{n_q - n_Q} \right), \quad (3.76)$$

where we have used $d\phi = dQQ/\sqrt{q^2 K^2 - (K^2 + q^2 - Q^2)^2/4}$. As before, the angular integration over $\theta_{\mathbf{k}}$ and $\theta_{\mathbf{k}'}$ is conveniently done by integrating over γ , with $(\mathbf{K} \cdot \mathbf{u})^2 = K^2 \cos^2 \gamma$, keeping $\theta_{\mathbf{k}, \mathbf{k}'} = \theta_{\mathbf{k}} - \theta_{\mathbf{k}'} \equiv \theta$ and q and $|\mathbf{K} - \mathbf{q}| \equiv Q$ constant, and

integrate over θ afterward, q and Q . The resistivity may then be written as

$$\begin{aligned} \varrho_F \approx & \frac{k_B T}{2^6 \pi^2 e^2 \rho^2 v_F^2 k_F^2} \int_0^{2k_F} dK \frac{[D^F(K/k_F)]^2 K^2}{\sqrt{k_F^2 - K^2/4}} \times \\ & \times \int_0^\infty dq \frac{q^3}{\omega_q^F} \frac{\partial n_q}{\partial \omega_q^F} \int_{|K-q|}^{|K+q|} dQ \frac{Q^3}{\omega_Q^F \sqrt{q^2 K^2 - (K^2 + q^2 - Q^2)^2/4}} \times \\ & \times \frac{\partial n_Q}{\partial \omega_Q^F} \left(\frac{\omega_q^F + \omega_Q^F}{1 + n_q + n_Q} - \frac{\omega_q^F - \omega_Q^F}{n_q - n_Q} \right), \end{aligned} \quad (3.77)$$

where $d\theta = dK/\sqrt{k_F^2 - K^2/4}$ has been used, and we used Eq. (3.74) for the kernel.

In the absence of strain the dispersion of flexural phonons reads $\omega_q^F = \alpha q^2$. After rescaling momentum as $x \rightarrow \tilde{x} = x(\hbar\alpha/k_B T)^{1/2}$ we can rewrite the resistivity as

$$\begin{aligned} \varrho_F \approx & \frac{(k_B T)^2}{2^6 \pi^2 \hbar e^2 \rho^2 v_F^2 k_F^2 \alpha^4} \int_0^{2\tilde{k}_F} d\tilde{K} \frac{[D^F(\tilde{K}/\tilde{k}_F)]^2 \tilde{K}^2}{\sqrt{\tilde{k}_F^2 - \tilde{K}^2/4}} \times \\ & \times \int_0^\infty d\tilde{q} \tilde{q} n_{\tilde{q}}(n_{\tilde{q}} + 1) \int_{|\tilde{K}-\tilde{q}|}^{|\tilde{K}+\tilde{q}|} d\tilde{Q} \frac{\tilde{Q} n_{\tilde{Q}}(n_{\tilde{Q}} + 1)}{\sqrt{\tilde{q}^2 \tilde{K}^2 - (\tilde{K}^2 + \tilde{q}^2 - \tilde{Q}^2)^2/4}} \times \left(\frac{\tilde{q}^2 + \tilde{Q}^2}{1 + n_{\tilde{q}} + n_{\tilde{Q}}} - \frac{\tilde{q}^2 - \tilde{Q}^2}{n_{\tilde{q}} - n_{\tilde{Q}}} \right). \end{aligned} \quad (3.78)$$

The integral over \tilde{Q} is infrared divergent, dominated by the contribution $\tilde{K} \sim \tilde{q}$. Defining the small quantity $\delta x = |\tilde{K} - \tilde{q}|$, and noting that for $\tilde{Q} \ll 1$ we have $n_{\tilde{Q}} \sim 1/\tilde{Q}^2 \gg 1$, it is possible to identify the dominant contribution in the \tilde{Q} integral as

$$\begin{aligned} & \int_{|\tilde{K}-\tilde{q}|}^{|\tilde{K}+\tilde{q}|} d\tilde{Q} \frac{\tilde{Q} n_{\tilde{Q}}(n_{\tilde{Q}} + 1)}{\sqrt{\tilde{q}^2 \tilde{K}^2 - (\tilde{K}^2 + \tilde{q}^2 - \tilde{Q}^2)^2/4}} \times \left(\frac{\tilde{q}^2 + \tilde{Q}^2}{1 + n_{\tilde{q}} + n_{\tilde{Q}}} - \frac{\tilde{q}^2 - \tilde{Q}^2}{n_{\tilde{q}} - n_{\tilde{Q}}} \right) \\ & \sim 2\tilde{K}^2 \int_{\delta x}^{2\tilde{K}} d\tilde{Q} \frac{n_{\tilde{Q}} + 1}{\tilde{K}} \sim \frac{2\tilde{K}}{\delta x}. \end{aligned}$$

It is now obvious that the \tilde{q} integral has a logarithmic divergence for $\tilde{q} \sim \tilde{K}$. Note, however, that in the present theory phonons have an infrared cutoff, so that $\min|\tilde{K} - \tilde{q}| = \tilde{q}_c$, where $\tilde{q}_c \ll 1$ is either due to strain or anharmonic effects. The dominant

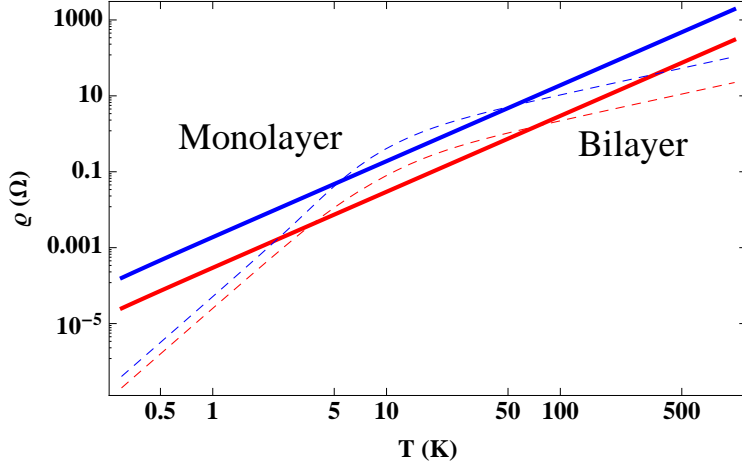


Figure 3.3: Resistivity due to scattering by out-of-plane phonons as a function of temperature (in blue, monolayer graphene, in red, bilayer). The logarithmic factor in Eq. (3.79) is dropped. Dashed lines show resistivity due to in-plane phonons, previously discussed. In both cases $n = 10^{12} \text{ cm}^{-2}$ and we take $g = 3 \text{ eV}$ and $\beta = 3$.

contribution to the \tilde{q} integral is then coming from the maximum of $1/|\tilde{K} - \tilde{q}|$, from which we obtain

$$2\tilde{K} \int_0^\infty d\tilde{q} \tilde{q} n_{\tilde{q}} (n_{\tilde{q}} + 1) \frac{1}{|\tilde{q} - \tilde{K}|} \sim -2\pi\tilde{K}^2 n_{\tilde{K}} (n_{\tilde{K}} + 1) \ln(\tilde{q}_c).$$

The resistivity may finally be written as a simple integral over \tilde{K} . Expressed in dimensionless variables, we just have

$$\varrho_F \approx \frac{\hbar k_F^2}{2\pi e^2 \rho^2 v_F^2 \alpha^2} \ln\left(\frac{k_B T}{\hbar \alpha q_c^2}\right) \int_0^1 dx \frac{[D^F(2x)]^2}{\sqrt{1-x^2}} \frac{x^4 e^{zx^2}}{(e^{zx^2} - 1)^2}, \quad (3.79)$$

where $z = \hbar \omega_{2k_F}^F / k_B T$. The numerical evaluation of this equation is shown in Fig. 3.3. As before, there are not substantial differences between monolayer and bilayer cases. The logarithmic correction, expected to be of order unity in the relevant T range, has been ignored. Scattering by flexural phonons dominates the contribution to resistivity in non-strained samples at both low and high T , except for the crossover region for in-plane phonons where $T \sim T_{BG}$.

In Fig. 3.1(b) a sketch of the two phonon scattering process in momentum space is provided. It shows that one of the two phonons involved in the scattering event

always has momentum $\mathbf{q}' \rightarrow 0$. This is a consequence of the quadratic dispersion of flexural phonons, which leads to a divergent number of modes with momentum $\mathbf{q}' \rightarrow 0$.^[2] This divergence is responsible for the logarithmic factor in Eq. (3.79), which stems from the existence of an infrared cutoff q_c for the dispersion. This cutoff is to be identified with the onset of anharmonic effects,^[161] or unavoidable built in strain.

In the low T regime, $T \ll T_{BG}$, one has $z \gg 1$, so that the integrand in Eq. (3.79) is only contributing for $x \ll 1$. The generalized electron-phonon coupling becomes

$$D^F(y \ll 1) \approx \left[g^2 y^2 + \frac{\hbar^2 v_F^2 \beta^2}{4a^2} \right]^{1/2}, \quad (3.80)$$

and the resistivity is then

$$\varrho_F \approx \left[g^2 \frac{6\Gamma(6)\zeta(6)}{\Gamma(4)\zeta(4)} \left(\frac{T}{T_{BG}} \right)^2 + \frac{\hbar^2 v_F^2 \beta^2}{4a^2} \right] \times \frac{\Gamma(4)\zeta(4)\hbar k_F^2}{2^4 \pi e^2 \rho^2 v_F^2 \alpha^2} \left(\frac{k_B T}{\hbar \alpha k_F^2} \right)^{5/2} \ln \left(\frac{k_B T}{\hbar \alpha q_c^2} \right). \quad (3.81)$$

A similar result has been derived in Ref. 150. Owing to the same arguments for one phonon scattering we can neglect the deformation potential contribution at low T .

At high T , i.e. $T \gg T_{BG}$, we have $z \ll 1$, so that $\exp(zx^2)/[\exp(zx^2) - 1]^2 \approx 1/(zx^2)$ in Eq. (3.79). The bilayer graphene resistivity becomes

$$\varrho_F \approx \frac{(k_B T)^2}{64 \hbar e^2 \rho^2 v_F^2 \alpha^4 k_F^2} \ln \left(\frac{k_B T}{\hbar \alpha q_c^2} \right) \times \begin{cases} \frac{g^2}{2} + \frac{\hbar^2 v_F^2 \beta^2}{4a^2} & \text{for monolayer,} \\ g^2 + \frac{\hbar^2 v_F^2 \beta^2}{8a^2} & \text{for bilayer.} \end{cases} \quad (3.82)$$

We have obtained that the resistivity due to flexural phonons is proportional to T^2/n , which implies mobility independent of the carrier density n . A similar result has been obtained in the context of microscopic ripples in graphene.^[144,162]

Strain changes completely this picture. Applying strain breaks the membrane rotational symmetry inducing linear dispersion at low momentum, as we have seen. A new energy scale appears in the problem,

$$\omega_{q^*}^F = \sqrt{2} \bar{u} v_L^2 / \alpha \approx 10^4 \bar{u} (\text{K}), \quad (3.83)$$

separating two regimes: linear dispersion below and quadratic dispersion above. The associated momentum scale, $q^* = \sqrt{\bar{u}} v_L / \alpha \approx 4.5 \sqrt{\bar{u}} \text{ \AA}^{-1}$, together with k_F and the thermal momentum q_T given by $\hbar \omega_{q_T}^F = k_B T$, define all regimes where analytic

treatment can be employed. In particular, in the low T regime where $q_T \ll k_F$ we may always take $q^* \gg q_T$ and use a linear dispersion for flexural phonons; otherwise the non strained case considered previously would be the appropriate starting point. In the high T regime we can distinguish between low strain for $q^* \ll q_T$ and high strain for $q^* \gg q_T$. Note that at high T relevant phonons scattering electrons have momentum q in the range $k_F \lesssim q \lesssim q_T$. Therefore, when strain is present in the high T regime we may always assume $q^* \gg k_F$; the opposite limit, $q^* \ll k_F$, would again be identified with the non-strained case considered previously.

The resistivity due to strained flexural phonons can be cast in the form of a triple integral over rescaled momenta,

$$\begin{aligned} \varrho_F \approx & \frac{(k_B T)^6}{2^6 \pi^2 \hbar^5 e^2 \rho^2 v_F^2 v_L^8 \bar{u}^4 k_F^2} \int_0^{2k_F} d\tilde{K} \frac{[D^F(\tilde{K}/\tilde{k}_F)]^2 \tilde{K}^2}{\sqrt{\tilde{k}_F^2 - \tilde{K}^2/4}} \int_0^\infty d\tilde{q} \frac{\tilde{q}^3}{\omega_{\tilde{q}}} n_{\tilde{q}}(n_{\tilde{q}} + 1) \times \\ & \times \int_{|\tilde{K}-\tilde{q}|}^{|\tilde{K}+\tilde{q}|} d\tilde{Q} \frac{\tilde{Q}^3 n_{\tilde{Q}}(n_{\tilde{Q}} + 1)}{\omega_{\tilde{Q}} \sqrt{\tilde{q}^2 \tilde{K}^2 - (\tilde{K}^2 + \tilde{q}^2 - \tilde{Q}^2)/4}} \left(\frac{\omega_{\tilde{q}} + \omega_{\tilde{Q}}}{1 + n_{\tilde{q}} + n_{\tilde{Q}}} - \frac{\omega_{\tilde{q}} - \omega_{\tilde{Q}}}{n_{\tilde{q}} - n_{\tilde{Q}}} \right), \end{aligned} \quad (3.84)$$

where the rescaled dispersion reads $\omega_{\tilde{x}} \approx \sqrt{\gamma^2 \tilde{x}^4 + \tilde{x}^2}$, with $\gamma = \sqrt{2} \omega_{q_T}^F / \omega_{q^*}^F$. The kinematics of the scattering process is schematically shown in Fig. 3.1(c).

In the low T case, $T \ll T_{BG}$, we have only small angle scattering with $K \ll k_F$. The argument of the generalized electron-phonon coupling becomes small, $K/k_F \ll 1$, and it can be written as before, Eq. (3.80). Since the inequality $q_T \ll k_F, q^*$ holds, relevant phonons have linear dispersion $\omega_q^F \approx \sqrt{\bar{u}} v_L q$ and the rescaled Fermi momentum obeys $\tilde{k}_F \approx k_F/q_T \gg 1$. We may take $\tilde{K} \rightarrow \infty$ as the upper limit in the \tilde{K} integral in Eq. (3.84), and the resistivity is then approximated by

$$\varrho_F \approx \left[g^2 \left(\frac{q_T}{k_F} \right)^2 \mathcal{K}_4 + \frac{\hbar^2 v_F^2 \beta^2}{4a^2} \mathcal{K}_2 \right] \frac{(k_B T)^7}{2^6 \pi^2 \hbar^6 e^2 \rho^2 v_F^2 v_L^9 \bar{u}^{9/2} k_F^3}, \quad (3.85)$$

where

$$\mathcal{K}_n = \int_0^\infty d\tilde{K} \tilde{K}^n \int_0^\infty d\tilde{q} q^2 n_{\tilde{q}}(n_{\tilde{q}} + 1) \times \int_{|\tilde{K}-\tilde{q}|}^{|\tilde{K}+\tilde{q}|} d\tilde{Q} \frac{\tilde{Q}^2 n_{\tilde{Q}}(n_{\tilde{Q}} + 1) \left(\frac{\tilde{q} + \tilde{Q}}{1 + n_{\tilde{q}} + n_{\tilde{Q}}} - \frac{\tilde{q} - \tilde{Q}}{n_{\tilde{q}} - n_{\tilde{Q}}} \right)}{\sqrt{\tilde{q}^2 \tilde{K}^2 - (\tilde{K}^2 + \tilde{q}^2 - \tilde{Q}^2)/4}}. \quad (3.86)$$

It can be shown numerically that $\mathcal{K}_2 \approx 4485$ and $\mathcal{K}_4 \approx 496850$. The large ratio $\mathcal{K}_4/\mathcal{K}_2 \gg 1$ is, however, compensated by $q_T/k_F \ll 1$ and the fact that $g < \hbar v_F \beta / (2a)$.

As in the case of scattering by in-plane phonons, also here the gauge potential contribution to resistivity dominates at low T .

Now we consider the high T regime, $T \gg T_{BG}$. At odds with the non-strained case, see Fig. 3.1(b), now phonons with momentum q in the range $k_F \lesssim q \lesssim q_T$ provide most of the scattering. We start by writing the \tilde{Q} integral in Eq. (3.84) as

$$\begin{aligned} \mathcal{I}(\gamma, \tilde{K}, \tilde{q}) \equiv & \int_{|\tilde{K}-\tilde{q}|}^{|\tilde{K}+\tilde{q}|} d\tilde{Q} \frac{\tilde{Q}^3 n_{\tilde{Q}}(n_{\tilde{Q}} + 1)}{\sqrt{\tilde{q}^2 \tilde{K}^2 - (\tilde{K}^2 + \tilde{q}^2 - \tilde{Q}^2)^2 / 4}} \times \\ & \times \frac{1}{\sqrt{\gamma^2 \tilde{Q}^4 + \tilde{Q}^2}} \left(\frac{\sqrt{\gamma^2 \tilde{q}^4 + \tilde{q}^2} + \sqrt{\gamma^2 \tilde{Q}^4 + \tilde{Q}^2}}{1 + n_{\tilde{q}} + n_{\tilde{Q}}} - \frac{\sqrt{\gamma^2 \tilde{q}^4 + \tilde{q}^2} - \sqrt{\gamma^2 \tilde{Q}^4 + \tilde{Q}^2}}{n_{\tilde{q}} - n_{\tilde{Q}}} \right), \end{aligned} \quad (3.87)$$

with $\gamma = \sqrt{2}\omega_{q_T}^F / \omega_{q^*}^F$. Having in mind that high T implies $\tilde{K} \ll 1$, we consider the integration in Eq. (3.87) in two limiting cases: when $\tilde{q} \lesssim \tilde{K} \ll 1$ and for $\tilde{q} \gg \tilde{K}$. In the former case, since $\tilde{q} \ll 1$ and $\tilde{Q} \ll 1$ hold, we can linearize the dispersion relation and approximate the Bose-Einstein distribution function by $n_{\tilde{q}} \approx 1/\tilde{q}$ and $n_{\tilde{Q}} \approx 1/\tilde{Q}$. The integral over \tilde{Q} in Eq. (3.87) may then be approximated by

$$\mathcal{I}(\gamma, \tilde{K}, \tilde{q}) \approx \int_{|\tilde{K}-\tilde{q}|}^{|\tilde{K}+\tilde{q}|} d\tilde{Q} \frac{2\tilde{q}\tilde{Q}}{\sqrt{\tilde{q}^2 \tilde{K}^2 - (\tilde{K}^2 + \tilde{q}^2 - \tilde{Q}^2)^2 / 4}}, \quad (3.88)$$

and the integral can be done as

$$\mathcal{I}(\gamma, \tilde{K}, \tilde{q}) \approx \int_{|\tilde{K}-\tilde{q}|}^{|\tilde{K}+\tilde{q}|} d\tilde{Q} \frac{4\tilde{q}\tilde{Q}}{\sqrt{Y(\tilde{q}, \tilde{Q}, \tilde{K})}} = 2\tilde{q} \arctan \left[\frac{\tilde{q}^2 + \tilde{K}^2 - \tilde{Q}^2}{\sqrt{Y(\tilde{q}, \tilde{Q}, \tilde{K})}} \right]_{|\tilde{K}-\tilde{q}|}^{|\tilde{K}+\tilde{q}|} = 2\pi\tilde{q} \equiv \mathcal{I}(\tilde{q}), \quad (3.89)$$

where we have defined

$$Y(\tilde{q}, \tilde{Q}, \tilde{K}) = -(\tilde{q} - \tilde{K} - \tilde{Q})(\tilde{q} - \tilde{K} + \tilde{Q})(\tilde{q} + \tilde{K} - \tilde{Q})(\tilde{q} + \tilde{K} + \tilde{Q}). \quad (3.90)$$

On the other hand, for $\tilde{q} \gg \tilde{K}$ the integration region is concentrated around \tilde{q} . We may then write the integral in Eq. (3.87) as a slowly varying function, which we can take

out of the integral, multiplied by an integral of the form of that in Eq. (3.88),

$$\mathcal{I}(\gamma, \tilde{K}, \tilde{q}) \approx \frac{\tilde{q}^2 n_{\tilde{q}} (n_{\tilde{q}} + 1)}{\sqrt{\gamma^2 \tilde{q}^4 + \tilde{q}^2}} \left(\frac{2\sqrt{\gamma^2 \tilde{q}^4 + \tilde{q}^2}}{1 + 2n_{\tilde{q}}} + \frac{1}{n_{\tilde{q}} (n_{\tilde{q}} + 1)} \right) \times \quad (3.91)$$

$$\times \int_{|\tilde{K}-\tilde{q}|}^{|\tilde{K}+\tilde{q}|} d\tilde{Q} \frac{\tilde{Q}}{\sqrt{\tilde{q}^2 \tilde{K}^2 - (\tilde{K}^2 + \tilde{q}^2 - \tilde{Q}^2)^2 / 4}} \approx \quad (3.92)$$

$$\approx \frac{\pi \tilde{q}^2 n_{\tilde{q}} (n_{\tilde{q}} + 1)}{\sqrt{\gamma^2 \tilde{q}^4 + \tilde{q}^2}} \left(\frac{2\sqrt{\gamma^2 \tilde{q}^4 + \tilde{q}^2}}{1 + 2n_{\tilde{q}}} + \frac{1}{n_{\tilde{q}} (n_{\tilde{q}} + 1)} \right) \equiv \mathcal{I}(\gamma, \tilde{q}). \quad (3.93)$$

Since for $\tilde{q} \lesssim \tilde{K}$ the later result reduces to $2\pi\tilde{q}$, as in Eq. (3.89), we can use $\mathcal{I}(\gamma, \tilde{q})$ in Eq. (3.93) to approximate the \tilde{Q} integral, Eq. (3.87), in the full region $\tilde{q} \lesssim \tilde{K} \ll 1$ to $\tilde{q} \gg \tilde{K}$. This has been tested numerically to be a good approximation as long as $\tilde{K} \ll 1$. The \tilde{q} integral in Eq. (3.84) may then be cast in the \tilde{K} independent form

$$\mathcal{G}(\gamma) = \int_0^\infty d\tilde{q} \frac{\tilde{q}^5 n_{\tilde{q}}^2 (n_{\tilde{q}} + 1)^2}{\gamma^2 \tilde{q}^4 + \tilde{q}^2} \left(\frac{2\sqrt{\gamma^2 \tilde{q}^4 + \tilde{q}^2}}{1 + 2n_{\tilde{q}}} + \frac{1}{n_{\tilde{q}} (n_{\tilde{q}} + 1)} \right), \quad (3.94)$$

being easily evaluated numerically. The resistivity can then be written as

$$\varrho_F \approx \left(7g^2 + \frac{\hbar^2 v_F^2 \beta^2}{4a^2} \right) \frac{(k_B T)^4}{27 \hbar^3 e^2 \rho^2 v_F^6 v_L^6 \bar{u}^3} \mathcal{G} \left(\frac{\alpha k_B T}{\hbar \bar{u} v_L^2} \right) \times \begin{cases} \left(2g^2 + \frac{\hbar^2 v_F^2 \beta^2}{a^2} \right) & \text{for monolayer,} \\ \left(7g^2 + \frac{\hbar^2 v_F^2 \beta^2}{4a^2} \right) & \text{for bilayer.} \end{cases} \quad (3.95)$$

When $\gamma \ll 1$, or equivalently $q_T \ll q^*$ (high strain), the function $\mathcal{G}(\gamma)$ behaves as $\mathcal{G}(\gamma \ll 1) \approx 18\zeta(3) - 93\zeta(5)/8$. For $\gamma \gg 1$, or equivalently $q_T \gg q^*$ (small strain), it gives $\mathcal{G}(\gamma \gg 1) \approx 1/\gamma^2$. In these asymptotic regimes one can obtain analytic expressions for the resistivity in Eq. (3.95). For monolayer graphene we have:

$$\varrho_F \approx \left(2g^2 + \frac{\hbar^2 v_F^2 \beta^2}{a^2} \right) \frac{1}{27 \hbar^3 e^2 v_F^2} \times \begin{cases} \left(18\zeta(3) - \frac{93}{8}\zeta(5) \right) \frac{(k_B T)^4}{\rho^2 v_L^6 \bar{u}^3} & \text{for } k_F \ll q_T \ll q^*, \\ \frac{\hbar^2 (k_B T)^2}{\rho \kappa v_L^2 \bar{u}} & \text{for } k_F \ll q^* \ll q_T. \end{cases} \quad (3.96)$$

Eq. (3.96) also holds for bilayer graphene with $\left(2g^2 + \frac{\hbar^2 v_F^2 \beta^2}{a^2} \right) \rightarrow \left(7g^2 + \frac{\hbar^2 v_F^2 \beta^2}{4a^2} \right)$.

3.5.3 Asymptotic behaviors

Scattering by in-plane and flexural phonons are always at work simultaneously. However, the two mechanisms provide completely different T dependent resistivity, and therefore we expect them to dominate at different temperature regimes.

When strain is absent, scattering by flexural phonons dominate. Using Eqs. (3.69) and (3.82) valid in the high T regime we get

$$\frac{\varrho_F}{\varrho_{in}} \approx \frac{K_B T (\lambda + 2\mu)}{\pi \kappa^2 k_F^2}, \quad (3.97)$$

We expect a crossover between in-plane to flexural phonon dominated scattering given by

$$T \approx 1 \times n[\text{cm}^{-2}] \text{ K}, \quad (3.98)$$

which is lower than T_{BG} for in-plane phonons, Eq. (3.57), so we deduce that flexural phonons always dominate at high temperatures. Using the low T approximation for ϱ_{in} , Eq. (3.68), we obtain the ratio

$$\frac{\varrho_F}{\varrho_{in}} \approx \frac{\hbar^3 \rho k_F}{64 \kappa^2 \Gamma(4) \zeta(4) (K_B T)^2 (v_L^{-5} + v_T^{-5})}, \quad (3.99)$$

from which we expect a crossover from flexural phonon to in-plane dominated scattering at

$$T_c \approx 6 \times (n[\text{cm}^{-2}])^{1/4} \text{ K}, \quad (3.100)$$

as T increases. We conclude that scattering by flexural phonon always dominates over scattering by in-plane ones, except for the intermediate regime $T_c \ll T \ll T_{BG}$. This is clearly seen in Fig. 3.3.

The presence of strain changes this picture. It can easily be shown that the crossover from in-plane to flexural phonon dominated scattering always occurs in the low strain regime, $q^* \ll q_T$. We have seen previously that the crossover temperature T separating high strain from low strain behavior is given by $\gamma = \sqrt{2} \omega_{q_T}^F / \omega_{q^*}^F \approx 1$. Using Eq. (3.83) we get a crossover temperature $T^* \approx 10^4 \bar{u}$ K. On the other hand, using the low strain approximation for the resistivity due to flexural phonons given in Eq. (3.96) and the resistivity due to in-plane ones in Eq. (3.69) we obtain

$$\frac{\varrho_F}{\varrho_{in}} \approx \frac{k_B T}{32 \pi \kappa \bar{u}}. \quad (3.101)$$

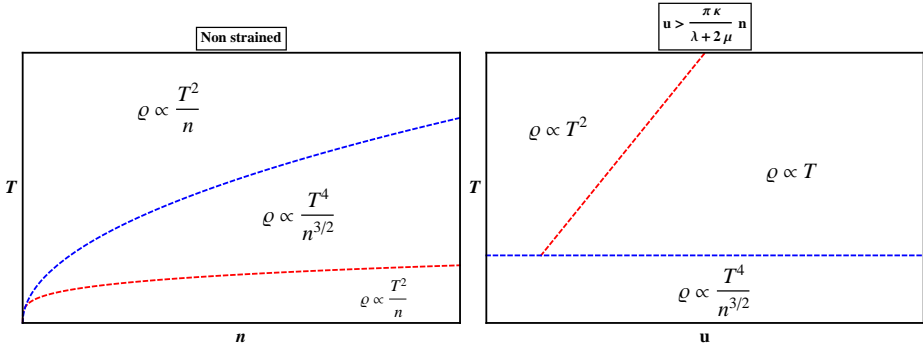


Figure 3.4: Different asymptotic behaviors of resistivity in the absence (left) and at the presence of non-negligible (right) strain. Dashed blue line represents T_{BG} for in-plane phonons, and dashed blue line corresponds to T_c in both cases.

The corresponding crossover T_c then reads

$$T_c \approx 10^6 \bar{u} \text{ K}. \quad (3.102)$$

Clearly $T_c \gg T^*$, justifying our low strain approximation. An important conclusion may be drawn. While in the non-strained case scattering by flexural phonons is the dominant contribution to the resistivity, it can be seen from Eq. (3.102) that applying small amounts of strain is enough to suppress this contribution at room T . The asymptotic behaviors of the resistivity at different regimes of temperature, carrier density and strain are summarized in Fig. 3.4.

3.6 Comparison with experiments

We compare our theoretical findings with available data from transport experiments in two-terminal suspended devices provided by A. Geim's group in Manchester. Typical changes in the resistance R as a function of the gate induced concentration n are shown in Fig. 3.5 (a). The devices exhibited $\mu \sim 1 \text{ m}^2/\text{Vs}$ but, after their *in situ* annealing by electric current, μ could reach above $100 \text{ m}^2/\text{Vs}$ at low T . To find the mobilities μ shown in Fig. 3.5 (b), the standard expression $R = R_0 + (l/w)(1/ne\mu)$ was used, where R_0 describes the contact resistance plus the effect of neutral scatterers, and both R_0 and μ are assumed n -independent.^[138, 139] The devices had the length $l \approx 1-2 \text{ }\mu\text{m}$ and the channel width w of $2-4 \text{ }\mu\text{m}$ (see the inset in Fig. 3(b)). At $T > 100 \text{ K}$, the above expression describes well the functional form of the experimental curves, yielding a constant μ over the whole range of accessible n , if R_0 is allowed

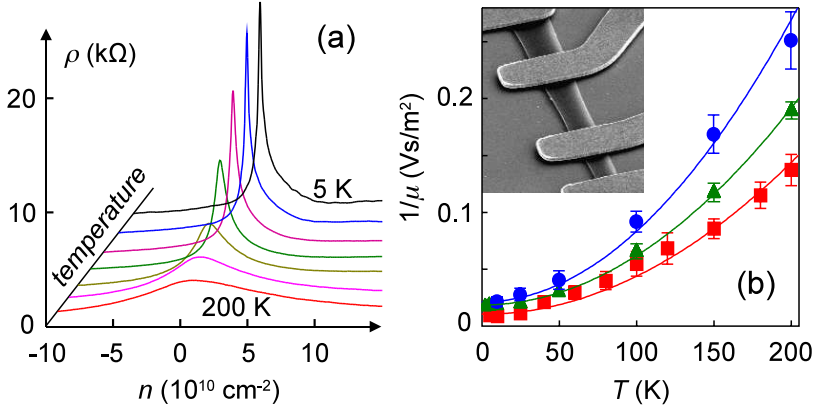


Figure 3.5: (a) Electron transport in suspended graphene. Graphene resistivity $\rho = R(w/l)$ as a function of gate-induced concentration n for $T = 5, 10, 25, 50, 100, 150$ and 200 K . (b) Examples of $\mu(T)$. The T range was limited by broadening of the peak beyond the accessible range of n . The inset shows a scanning electron micrograph of one of our suspended device. The darker nearly vertical stripe is graphene suspended below Au contacts. The scale is given by graphene width of about $1 \mu\text{m}$ for this particular device.

to be different for electrons and holes. This is expected because of an $n-p$ barrier that appears in the regime of electron doping due to the p -doping contacts.^[140,141] At $T < 100 \text{ K}$, the range of n over which the expression fits the data rapidly narrows. Below 20 K , we can use it only for $n < \pm 10^{10} \text{ cm}^{-2}$ because at higher n we enter into the ballistic regime. To make sure that μ extracted over the narrow range of n is also correct, they crosschecked the found μ against quantum mobilities inferred from the onset of Shubnikov-de Haas oscillations.^[140,141] For all the devices with μ ranging from $\sim 1 - 100 \text{ m}^2/\text{Vs}$, they found good agreement between transport and quantum mobilities at liquid-helium T . Fig. 3(b) shows the T dependence of μ . It is well described by the quadratic dependence $1/\mu = 1/\mu(T \rightarrow 0) + \gamma T^2$. Surprisingly, they found the coefficient γ to vary by a factor of ~ 2 for different devices, which is unexpected for an intrinsic phonon contribution. Such variations are however expected if strain modifies electron-phonon scattering as discussed below. Note that μ falls down to $4 - 7 \text{ m}^2/\text{Vs}$ at 200 K (see Fig. 3(b)) and the extrapolation to room T yields μ of only $2 - 3 \text{ m}^2/\text{Vs}$, which is significantly lower than the values reported in Ref. 141 but in agreement with Ref. 140.

The density independent μ indicates that experiments are in the non-strained regime,

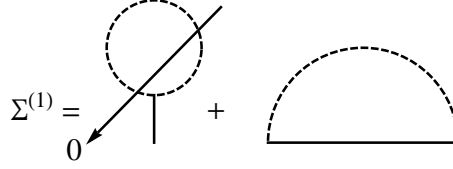


Figure 3.6: First order self-energy diagrams. The dashed line represents the phonon propagator, and the straight line the 4-point vertex. Note that the first diagram is 0 since the $\mathbf{q} = 0$ component of the vertex is integrated out.

where $\rho_F \propto T^2/n$. Here flexural phonons completely dominate and the coefficient γ defined above is given by

$$\gamma \approx \frac{D^2 k_B^2}{64\pi e \hbar \kappa^2 v_F^2} \ln \left(\frac{k_B T}{\hbar \omega_c} \right), \quad \text{with } D^2 = \frac{g^2}{2} + \frac{\hbar^2 v_F^2 \beta^2}{4a^2}, \quad (3.103)$$

where the infrared cutoff is the only free parameter. Experiment gives $\gamma \approx 6.19 \times 10^{-6} \text{ Vs}/(\text{mK})^2$ for the sample with lower mobility and $\gamma \approx 3.32 \times 10^{-6} \text{ Vs}/(\text{mK})^2$ for the higher mobility one. Neglecting the logarithmic correction of order unity, the analytic expression gives $\gamma \approx 3 \times 10^{-6} \text{ Vs}/(\text{mK})^2$ without adjustable parameters.

The difference between the two samples may be understood as due to a different cutoff under the logarithm due to strain. In non-strained samples there is a natural momentum cutoff $q_c \approx 0.1 \text{ \AA}^{-1}$ below which the harmonic approximation breaks down.^[161] Strain increases the validity of harmonic approximation, making q_c strain dependent, thus explaining different cutoff at different strain.^[163] Comparing $q_c \approx 0.1 \text{ \AA}^{-1}$ ^[161] and q^* gives $u \sim 10^{-4} - 10^{-3}$ as the strain involved in these experiments. Such small strain can be present even in slacked samples (where strain induced by gate and T is negligible) due to, for example, the initial strain induced by the substrate and remaining unrelaxed under and near metal contacts. A complete theory would require the treatment of anharmonic effects in transport theory, which is beyond the scope of this thesis. Here we only analyze perturbatively the effect of anharmonic effects on the dispersion relation of flexural phonons, and the effect of strain on such correction.

Since the free energy in Eq. (3.9) is quadratic in the in-plane displacements we can integrate them out to obtain the effective free-energy for the out-of-plane degree of freedom^[164]

$$F^{eff} = \frac{1}{2} \kappa \int dx dy (\nabla^2 h)^2 + \frac{1}{2} \int dx dy R_{ij,kl} \partial^i h \partial^j h \partial^k h \partial^l h, \quad (3.104)$$

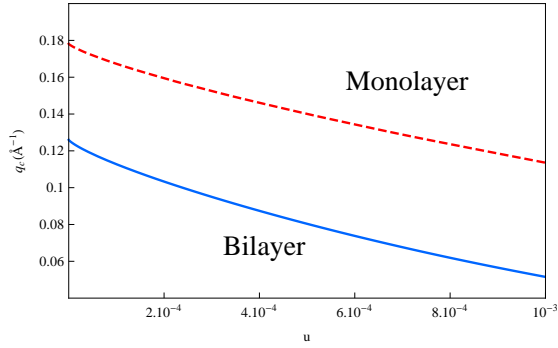


Figure 3.7: The infrared cutoff q_c as a function of the applied strain u for monolayer (in red dashed line) and bilayer graphene (in blue). In both cases $T = 300$ K.

where the four-point-coupling fourth-order tensor can be written as $R_{ij,kl} = \frac{K_0}{4} P_{ij}^T P_{kl}^T$, the operator P_{ij}^T is the transverse projector $P_{ij}^T = (\nabla^2)^{-1} \varepsilon_{ik} \varepsilon_{jl} \partial^k \partial^l$, and $K_0 = \frac{4\mu(\mu+\lambda)}{2\mu+\lambda}$. In order to include the effect of strain, we add to Eq. (3.104) the simplest term which breaks rotational symmetry,

$$\frac{1}{2} \gamma \int dx dy (\nabla h)^2,$$

where γ is a sample-dependent coefficient with units of tension which can be related with the strain of the sample. This approach follows the spirit of the effective isotropic dispersion relation of flexural phonons introduced before. If we add this term to the free energy and then we integrate out the in-plane degrees of freedom, we obtain a new two-point vertex whose contribution to the renormalization of the bending rigidity is weak and can be neglected.^[163] We are going to study the Fourier component of the height-height correlation function,

$$G(\mathbf{q}) = \langle |h(\mathbf{q})|^2 \rangle = \frac{1}{Z} \int \mathcal{D}h(\mathbf{q}) |h(\mathbf{q})|^2 e^{S^{eff}[h(\mathbf{q})]},$$

where obviously $Z = \int \mathcal{D}h(\mathbf{q}) e^{S^{eff}}$ is the partition function, the effective action is nothing but $S^{eff}[h(\mathbf{q})] = -\beta F^{eff}[h(\mathbf{q})]$, and the Fourier transformed effective free

energy reads

$$F^{eff} [h(\mathbf{q})] = \int \frac{d^2\mathbf{q}}{(2\pi)^2} \left(\frac{\kappa}{2} q^4 + \frac{\gamma}{2} q^2 \right) |h(\mathbf{q})|^2 + \frac{1}{2} \int \prod_{i=1}^4 \frac{d^2\mathbf{q}_i}{(2\pi)^8} q_1^i q_2^j q_3^k q_4^l R_{ij,kl}(\mathbf{q}_1 + \mathbf{q}_2) h_{\mathbf{q}_1} h_{\mathbf{q}_2} h_{\mathbf{q}_3} h_{\mathbf{q}_4} \delta^{(2)}(\mathbf{q}_1 + \mathbf{q}_2 + \mathbf{q}_3 + \mathbf{q}_4), \quad (3.105)$$

where $R_{ij,kl}(\mathbf{k}) = \frac{K_0}{4} P_{ij}^T(\mathbf{k}) P_{ij}^T(\mathbf{k})$, and the Fourier transformed transverse projector reads $P_{ij}^T(\mathbf{k}) = k^{-2} \varepsilon_{ik} \varepsilon_{jl} k^k k^l = \delta_{ij} - \frac{k_i k_j}{k^2}$. It is important to note that the $\mathbf{q} = 0$ Fourier component of the transverse projector is integrated out during the Gaussian integration of the in-plane modes.^[164] In the harmonic approximation and in the absence of strain ($\gamma = 0$), the (free) correlator is given by

$$G^{(0)}(\mathbf{q}) = \frac{K_B T}{\kappa q^4}. \quad (3.106)$$

When we assume a quadratic dispersion relation we are taking this correlator as the proper one. This approximation is obviously affected by the presence of strain and anharmonicities, which renormalizes the bending rigidity κ . Then, we can write $G^{-1}(\mathbf{q}) \propto \kappa(\mathbf{q}) q^4$ and study the renormalization of κ from the Dyson equation,

$$G^{-1}(\mathbf{q}) = \left(G^{(0)}(\mathbf{q}) \right)^{-1} + \Sigma(\mathbf{q}), \quad (3.107)$$

where now the correlator in the harmonic theory, including the effect of strain, is given by

$$G^{(0)}(\mathbf{q}) = \frac{K_B T}{\kappa q^4 + \gamma q^2}. \quad (3.108)$$

In order to estimate the anharmonic effects we compute the first order diagrams for self-energy, showed in Fig. 3.6. Only the rainbow-like diagram gives a non-zero contribution,

$$\Sigma^{(1)}(\mathbf{q}) = 4\beta \int \frac{d^2\mathbf{k}}{(2\pi)^2} q^i q^j q^k q^l R_{ij,kl}(\mathbf{k}) G^{(0)}(\mathbf{q} - \mathbf{k}). \quad (3.109)$$

Replacing this result in equation Eq. (3.107) we obtain

$$\kappa(\mathbf{q}) = \kappa + \frac{\gamma}{q^2} + K_B T K_0 \int \frac{d^2\mathbf{k}}{(2\pi)^2} \frac{\left(1 - \frac{(\mathbf{q}\cdot\mathbf{k})^2}{q^2 k^2} \right)^2}{\kappa |\mathbf{q} - \mathbf{k}|^4 + \gamma |\mathbf{q} - \mathbf{k}|^2}. \quad (3.110)$$

Follow the Ginzburg criterion,^[165] we estimate the cutoff of the theory nothing but comparing each correcting term of Eq. (3.110) with the bare value of κ . As we have already mentioned, there are two different cutoffs, the one given by strain in the harmonic approximation, and the other one associated to anharmonic effects. The first one is given by the second term of Eq. (3.110), and it is nothing but q^* ,

$$q^* = \sqrt{\frac{\gamma}{\kappa}}. \quad (3.111)$$

Identifying this result with the momentum scale defined by Eq. (3.83), we deduce the relation between γ and u ,

$$\gamma = (\lambda + 2\mu) u.$$

The cutoff of the harmonic theory is also affected by strain. Following the same criterion, its value comes from the solution to the equation

$$\kappa = \frac{K_B T K_0}{(2\pi)^2 \kappa} \int_0^{2\pi} d\theta \int_0^\infty dk \frac{k \sin^4(\theta)}{(k^2 + q^2 - 2kq \cos(\theta))^2 + (q^*)^2 (k^2 + q^2 - 2kq \cos(\theta))}. \quad (3.112)$$

In the absence of strain, we have $q_c = \sqrt{\frac{3K_B T K_0}{16\pi\kappa^2}}$, which gives at $T = 300$ K the value $q_c = 0.178 \text{ \AA}^{-1}$ in the case of monolayer, and $q_c = 0.126 \text{ \AA}^{-1}$ in the case of bilayer graphene. Its dependence on the applied strain is shown in Fig. 3.7. It is clear that q_c decreases as the strain increases, so the unavoidable little strain present in real samples increases the validity of the harmonic approximation.

3.7 Conclusions

We have studied the effect of acoustic phonon modes on the low energy electronic excitations of monolayer and bilayer graphene, in particular its effect on charge transport. According to our analysis, mobilities in suspended samples are strongly affected by flexural vibrations, which constitutes a very important source of electron scattering. This mechanism predicts mobilities $\mu \propto T^2$, independent of the carrier concentrations, as reported in the experiments. The changes from sample to sample can be attributed to strain. In general, strain tends to suppress the high density of flexural phonon modes at low momenta, reducing significantly its contribution to resistivity. As final remark, note that the data in Ref. 166 show higher mobilities than those in Fig. 3.5. This suggests that the samples of Ref. 166 are probably under strain.

4

Effect of flexural phonons on SOC

4.1 Introduction

In this chapter we analyze the SOC-assisted electron interaction with flexural phonons. The motivation is double. On the one hand, flexural phonon modes constitute an intrinsic source of spin relaxation.^[167] Like in the resistivity, studied in the previous chapter, it is natural to think that the interaction with flexural modes constitutes the main limitation to spin transport in suspended samples. It is important, however, to determine exactly the form and the strength of such couplings in order to deduce not only the magnitude but also the parametric dependence of the spin relaxation times on carrier concentration or temperature. On the other, flexural modes can contribute to enhance the intrinsic Kane-Mele coupling due to the mixing of π and σ orbitals caused by out-of-plane displacements of the atoms, leading to a first order contribution. In this sense, phonon modes contribute to stabilize a topological phase, contrary to the common belief that increasing temperature always destabilizes topological phases.^[168] According to our estimates, the ZO branch contributes remarkably to the Kane-Mele gap.

The chapter is organized in 4 sections. First we discuss the form of the spin-phonon couplings on symmetry grounds. Then we estimate the strength of such couplings

from a tight-binding model. We apply this analysis to study the effect of flexural phonons on the Kane-Mele gap. Finally, we summarize the results of this chapter and we explore possible routes to stabilize a topological phase by softening the flexural modes of graphene.

4.2 Spin-phonon coupling in graphene

We analyze the coupling with phonon modes around Γ and \mathbf{K}_{\pm} points of the BZ. The Hamiltonian reads in general

$$\mathcal{H}_{s-ph} = \mathcal{H}_{A_1} + \mathcal{H}_{B_2} + \mathcal{H}_{G'}.$$
 (4.1)

As mentioned in the previous chapter, in the lattice with 6 atoms per unit cell the amplitude of a flexural phonon mode at Γ ($\equiv \mathbf{K}_{\pm}$) is given by a 6-component vector whose entries are associated to the displacements of the atoms at each sublattice, $|h\rangle = (h_{A1}, h_{B1}, h_{A2}, h_{B2}, h_{A3}, h_{B3})$. This vector belongs to a 6-dimensional representation of C''_{6v} which can be reduced as $A_1 + B_2 + G'$. The polarization vectors associated to the 1-dimensional irreps correspond to the acoustic (ZA) and optical (ZO) modes at the original Γ points, whose polarization vectors in the 6 atoms basis read

$$\begin{aligned} |A_1\rangle &= \frac{1}{\sqrt{6}}(1, 1, 1, 1, 1, 1), \\ |B_2\rangle &= \frac{1}{\sqrt{6}}(1, -1, 1, -1, 1, -1). \end{aligned}$$
 (4.2)

The 4-dimensional irrep corresponds to the 4 degenerate modes at \mathbf{K}_{\pm} points,

$$\begin{aligned} |A, \mathbf{K}_+\rangle &= \frac{1}{\sqrt{3}}(1, 0, e^{i\frac{2\pi}{3}}, 0, e^{-i\frac{2\pi}{3}}, 0), \\ |B, \mathbf{K}_+\rangle &= \frac{1}{\sqrt{3}}(0, 1, 0, e^{i\frac{2\pi}{3}}, 0, e^{-i\frac{2\pi}{3}}), \\ |A, \mathbf{K}_-\rangle &= \frac{1}{\sqrt{3}}(1, 0, e^{-i\frac{2\pi}{3}}, 0, e^{i\frac{2\pi}{3}}, 0), \\ |B, \mathbf{K}_-\rangle &= \frac{1}{\sqrt{3}}(0, 1, 0, e^{-i\frac{2\pi}{3}}, 0, e^{i\frac{2\pi}{3}}). \end{aligned}$$
 (4.3)

Note that $|A/B, \mathbf{K}_-\rangle = (|A/B, \mathbf{K}_+\rangle)^*$, as implied by time reversal symmetry. In order to construct the couplings it is advisable to consider the real linear combinations of

the vectors of Eq. (4.3) which transforms according to G' . These are

$$\begin{aligned}
 |1\rangle &= \frac{i}{2} \left[-|AK_+\rangle + |AK_-\rangle - |BK_+\rangle + |BK_-\rangle \right], \\
 |2\rangle &= \frac{1}{2} \left[|AK_+\rangle + |AK_-\rangle - |BK_+\rangle - |BK_-\rangle \right], \\
 |3\rangle &= \frac{i}{2} \left[-|AK_+\rangle + |AK_-\rangle + |BK_+\rangle - |BK_-\rangle \right], \\
 |4\rangle &= \frac{1}{2} \left[|AK_+\rangle + |AK_-\rangle + |BK_+\rangle + |BK_-\rangle \right].
 \end{aligned} \tag{4.4}$$

The polarization vectors of Eqs. (4.2) and (4.4) form a symmetry adapted basis, in such a way that the displacement vector of a flexural mode can be written as $|h\rangle = u_{A_1} |A_1\rangle + u_{B_2} |B_2\rangle + u_1 |1\rangle + u_2 |2\rangle + u_3 |3\rangle + u_4 |4\rangle$, where u_i are the symmetry adapted (real) displacement fields. The results of this analysis was summarized in Tab. 3.2.

This analysis, together with the SOC terms introduced in Tab. 2.6, allows us to identify the spin-orbit assisted electron coupling with flexural phonons at the center and the corners of the BZ. The spin-phonon interaction Hamiltonian can be expanded in powers of the phonon displacement fields and their derivatives, in such a way that they are paired with the electronic operators corresponding to the same irrep taking into account that these combinations must be even under the operation $z \rightarrow -z$. Next we disclose the spin-phonon couplings corresponding to the leading terms in such expansion.

Since a uniform translation of the crystal cannot affect the electron motion, it is clear that the coupling with acoustic phonons only contains spatial derivatives of the corresponding displacement field. Moreover, being interested on the first order contribution in the spin-orbit interaction strenght due to the mixing of the bands, the coupling with ZA modes only depends on the extrinsic curvature of graphene viewed as a surface embedded in \mathbb{R}^3 . This implies that the leading term must depend on second derivatives $\partial_i \partial_j u_{A_1}$. Since $\partial_i \partial^i u_{A_1}$ transforms according to A_1 , and $(\partial_x^2 u_{A_1} - \partial_y^2 u_{A_1}, -2\partial_x \partial_y u_{A_1})$ forms a doublet which transforms according to E_2 , in principle three different couplings are allowed by the symmetries. We have

$$\begin{aligned}
 \mathcal{H}_{A_1} &= g_1 (\tau_z \otimes \sigma_x \otimes s_y - \sigma_y \otimes s_x) \partial_i \partial^i u_{A_1} + g_2 [\tau_z \otimes s_y (\partial_x^2 u_{A_1} - \partial_y^2 u_{A_1}) + \\
 &\quad + 2\tau_z \otimes s_x \partial_x \partial_y u_{A_1}] + g_3 [(\tau_z \otimes \sigma_x \otimes s_y + \sigma_y \otimes s_x) (\partial_x^2 u_{A_1} - \partial_y^2 u_{A_1}) + \\
 &\quad + 2(\tau_z \otimes \sigma_x \otimes s_x + \sigma_y \otimes s_y) \partial_x \partial_y u_{A_1}].
 \end{aligned} \tag{4.5}$$

In the case of optical phonons at the center of the BZ, note that there is no term which transforms according to the B_2 irrep in the column of $z \rightarrow -z$ asymmetric

operators, which means that the leading term must be quadratic on the phonon displacement fields. Since $B_2 \times B_2 \sim A_1$ we obtain a Kane-Mele-like coupling term of the form

$$\mathcal{H}_{B_2} = g_4 \tau_z \otimes \sigma_z \otimes s_z (u_{B_2})^2. \quad (4.6)$$

Finally, in the case of flexural phonons at the corners of the BZ, where both acoustic and optical branches are degenerate, the coupling reads as

$$\begin{aligned} \mathcal{H}_{G'} = g_5 [& (-\sigma_y \otimes \tau_y \otimes s_x)u_1 + (-\sigma_y \otimes \tau_y \otimes s_y)u_2 - \\ & -(\sigma_y \otimes \tau_x \otimes s_y)u_3 - (\sigma_y \otimes \tau_x \otimes s_x)u_4]. \end{aligned} \quad (4.7)$$

4.3 Tight-binding estimation

Values for the phenomenological constants $g_{1...5}$ introduced in Eqs. (4.5)-(4.7) can be deduced from the tight-binding model discussed before with 4 orbitals per carbon atom, Eq. (2.18). As before, once the low energy sector of π orbitals is identified, the effective Hamiltonian defined in such subspace is obtained by projecting out σ orbitals by means of a Schrieffer-Wolf transformation.^[75] Now both the spin-orbit interaction and the out-of-plane distortions enter in the $\pi - \sigma$ mixing blocks. In the case of B_2 phonons we must consider the effect of a vertical displacement of one sublattice respect to the other. If the calculation is performed with the 6 atoms unit cell one can identify the coupling with flexural phonons at \mathbf{K}_\pm (G'). In the case of A_1 phonons, since the coupling depends on the second derivatives of the phonon field, the calculation is not so straightforward.

4.3.1 Phonons at Γ

As we mentioned before, the coupling with ZA phonons can be inferred from the effect of extrinsic curvature of the graphene sample on the electronic degrees of freedom. The approach that we present here is quite similar to the calculation of the SOC in carbon nanotubes.^[106, 169] The crucial fact is how to choose the basis of π and σ orbitals. In carbon nanotubes the σ orbitals are chosen in such a way that they follow the shape of the nanotube, and the π orbital is chosen in the radial direction. Geometrically, this way of introducing the orbital basis has the following meaning. As we saw in the previous chapter, in the limit of long-wavelength distortions the graphene crystal can be described within a continuum theory. As before, we assume that the position of the carbon atoms lie on a smooth surface. Then, this way of

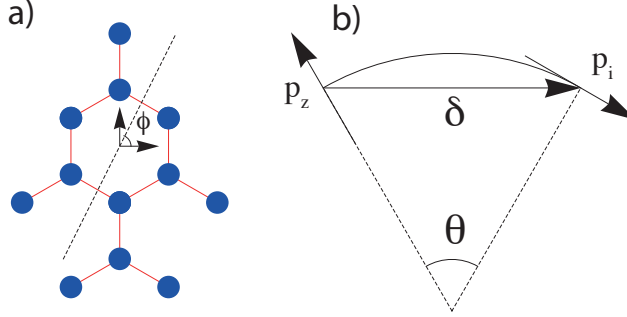


Figure 4.1: a) Definition of the angle ϕ . b) Sketch for the calculation of the new hoppings between p_z and p_i orbitals.

introducing the basis for p orbitals is uniquely determined if we assume that the bent graphene surface is isometric to a plane. This means that a diffeomorphism f from a flat graphene surface (S_{flat}) to a curved graphene surface (S_{curv}) exists in such a way that the metric on the bent surface is pull-backed to the flat one. Thus, the isomorphism f defines a unique way to introduce a local basis for the p_x and p_y atomic orbitals. Note that this is true in the case of nanotubes since a cylinder is isometric to a plane. Consider graphene in a flat configuration. We introduce unitary vectors \hat{p}_x, \hat{p}_y in the direction of maximum amplitude of the orbitals p_x, p_y respectively. From a geometrical point of view, these vectors are elements of the tangent bundle associated to S_{flat} .^[28] At the same time, the axis of maximum localization of the p_z orbital verifies $\hat{p}_z = \hat{p}_x \times \hat{p}_y$. Now consider a curved graphene which is related to the flat graphene by a isomorphism f . The push-forward of f maps the tangent bundle of S_{flat} to the tangent bundle of S_{curv} , which means that the vectors \hat{p}_x, \hat{p}_y at any position of the bent graphene are uniquely determined by the action of the push-forward of the isomorphism on the original \hat{p}_x, \hat{p}_y defined in the flat configuration. And of course, \hat{p}_z in the bent graphene surface is given by the vectorial product of the new \hat{p}_x, \hat{p}_y . This way of introducing the local basis in the bent graphene has two advantages: 1) we recover "smoothly" the original basis when we restore the curved graphene to the original flat configuration; 2) we keep the notion of parallelism by imposing f to be an isomorphism instead of just a diffeomorphism. Note that this apparent restriction does not affect the estimation of the spin-orbit assisted electron coupling with flexural phonons, since we are introducing extrinsic curvature and setting the Gaussian curvature to zero.

We know how to choose the orbital basis and then calculate the two-center matrix elements, at least locally, using the Koster-Slater parametrization. For simplicity, we consider a curved graphene surface with a constant curvature along a given direction (a cylinder), so essentially the same problem as a carbon nanotube. Thus, we have two parameters, the radius of curvature R and the angle ϕ between the direction of curvature and the x -axis (essentially the chiral angle in a nanotube), see Fig. 4.1 a). The new hoppings between π and σ orbitals can be calculated following the prescription of Tab. 2.7. These are function of the angle θ defined in Fig. 4.1 b). Assuming that $R \gg a$, we have to the leading term in a/R

$$\theta \approx \frac{|\delta_x \cos(\phi) + \delta_y \sin(\phi)|}{R}, \quad (4.8)$$

where $\delta_{x,y}$ are the components of the vector $\vec{\delta}$ which connects nearest neighbors. After a straightforward calculation, the block Hamiltonian that mixes π and σ states at \mathbf{K}_{\pm} can be written as the matrix

$$\mathcal{H}_{\sigma\pi} = \frac{3a}{8R} \begin{pmatrix} 0 & -V_{sp\sigma} e^{i\tau 2\phi} \\ -V_{sp\sigma} e^{-i\tau 2\phi} & 0 \\ 0 & i\tau (V_1 + e^{-i\tau 2\phi} V_2) \\ i\tau (V_1 + e^{i\tau 2\phi} V_2) & 0 \\ 0 & V_1 - e^{-i\tau 2\phi} V_2 \\ -V_1 + e^{i\tau 2\phi} V_2 & 0 \end{pmatrix}, \quad (4.9)$$

where $V_1 = V_{pp\sigma} + V_{pp\pi}$, $V_2 = (V_{pp\sigma} + 3V_{pp\pi})/2$, and $\tau = \pm 1$ labels the valley \mathbf{K}_{\pm} .

This expression is exact to the leading order in a/R assuming a constant R and ϕ along the graphene surface. Now we perform a local approximation, valid at long wavelengths: we assume that R and ϕ depends slightly on the position. Hence, they can be related with the second derivatives of the height profile, since the second fundamental form in the Monge's parametrization is just $\mathcal{F}_{ij} \approx \partial_i \partial_j h$ to the leading order in the out-of-plane displacements. At the same time, note that within the continuum description of graphene, the height profile h should be identified with the flexural acoustic phonon field at long wavelengths, u_{A_1} . Then, the local R and ϕ can be related with the second derivatives of u_{A_1} as

$$\begin{aligned} \partial_x \partial_x u_{A_1} &\approx -R^{-1} \cos^2 \phi, \\ \partial_y \partial_y u_{A_1} &\approx -R^{-1} \sin^2 \phi, \\ \partial_x \partial_y u_{A_1} &\approx -R^{-1} \sin \phi \cos \phi. \end{aligned} \quad (4.10)$$

By projecting out the σ electronic states we arrive at the electron-phonon coupling of Eq. 4.5 with

$$\begin{aligned} g_1 &= \frac{a\epsilon_s\Delta (V_{pp\sigma} + V_{pp\pi})}{12V_{sp\sigma}^2} \approx 3 \text{ meV} \cdot \text{Å}, \\ g_2 &= \frac{aV_{pp\pi}\Delta}{2(V_{pp\sigma} - V_{pp\pi})} \approx 4 \text{ meV} \cdot \text{Å}. \end{aligned} \quad (4.11)$$

Importantly, within the present Koster-Slater approximation we have to extend the tight-binding calculation to second-nearest neighbors in order to obtain a non-zero g_3 coupling. In that case we obtain

$$g_3 = \frac{a\Delta (3V_{pp\pi} + V_{pp\sigma}) (V_{pp\sigma}^{(2)} + V_{pp\pi}^{(2)})}{8(V_{pp\sigma} - V_{pp\pi})^2}, \quad (4.12)$$

where $V_{pp\sigma}^{(2)}$ and $V_{pp\pi}^{(2)}$ are new second-nearest neighbors hopping parameters.

In order to estimate the coupling with optical phonons we have to consider the effect of a vertical displacement of one sublattice with respect to the other, similarly to the case of silicene.^[170] Processes which involve only one phonon give a vanishing contribution as expected from symmetry considerations. We can repeat the same scheme as before by considering virtual processes mediated by two phonons ($\propto \mathcal{H}_{\pi\sigma}^{flex} \mathcal{H}_{\sigma}^{-1} \mathcal{H}_{\sigma\pi}^{flex}$, note that \mathcal{H}_{σ} also contains the SO interaction). We identify the Kane-Mele-like coupling with flexural optical phonons at Γ , whose strength reads

$$g_4 = \frac{2\epsilon_s^2\Delta (V_{pp\pi} - V_{pp\sigma})^2}{9a^2V_{sp\sigma}^4} \approx 20 \text{ meV} \cdot \text{Å}^{-2}. \quad (4.13)$$

4.3.2 Phonons at K_{\pm}

We estimate now the coupling with phonons at the corners of the BZ. We simplify the tight-binding model in order to treat the problem analytically. We consider the model described in Ref. 171 and adapted in Ref. 172 in order to describe the acoustic phonon modes in graphite. It contains only two parameters: V_{on} , which is the on-site energy of the σ orbitals, and V_{hop} , which is the hopping between σ orbitals at nearest neighbors when the orbitals are maximally localized in the direction which

links the two atoms, otherwise the hopping is taken to zero. These parameters can be estimated from the Slater-Koster parameters as

$$V_{on} = \frac{\epsilon_s - \epsilon_p}{3},$$

$$V_{hop} = \frac{V_{ss\sigma} - 2\sqrt{2}V_{sp\sigma} - 2V_{pp\sigma}}{3}. \quad (4.14)$$

This model was employed in Ref. 106 in order to estimate the SOC in graphene and carbon nanotubes. The Kane-Mele coupling reads $\Delta_I^{flat} = 3V_{on}\Delta^2/(4V_{hop}^2)$ within this model for flat graphene, in agreement with Ref. 106. Note also that this estimation is numerically very close to the one of Ref. 107.

We perform the calculation in the unit cell with 6 atoms. We can estimate the terms that mix π and σ states by considering the vertical displacement of one lattice respect to the other as indicated by Eqs. (4.3)-(4.4). By projecting out the σ orbitals we arrive to a 6x6 effective Hamiltonian for the π electronic states at the new Γ , which can be seen as a matrix expressed in the mono-electronic basis

$$(|\Gamma A_1 \pi\rangle, |\Gamma A_2 \pi\rangle, |\Gamma A_3 \pi\rangle, |\Gamma B_1 \pi\rangle, |\Gamma B_2 \pi\rangle, |\Gamma B_3 \pi\rangle).$$

In order to identify the effective Hamiltonian in the low energy sector we have to express this matrix in the mono-electronic basis associated to the lattice with 2 atoms per unit cell,

$$(|\Gamma A \pi\rangle, |\Gamma B \pi\rangle, |\mathbf{K}_+ A \pi\rangle, |\mathbf{K}_+ B \pi\rangle, |\mathbf{K}_- A \pi\rangle, |\mathbf{K}_- B \pi\rangle).$$

Both basis are related by the unitary transformation

$$U = \frac{1}{\sqrt{3}} \begin{pmatrix} 1 & 0 & 1 & 0 & 1 & 0 \\ 1 & 0 & e^{i\frac{2\pi}{3}} & 0 & e^{-i\frac{2\pi}{3}} & 0 \\ 1 & 0 & e^{-i\frac{2\pi}{3}} & 0 & e^{i\frac{2\pi}{3}} & 0 \\ 0 & 1 & 0 & 1 & 0 & 1 \\ 0 & 1 & 0 & e^{i\frac{2\pi}{3}} & 0 & e^{-i\frac{2\pi}{3}} \\ 0 & 1 & 0 & e^{-i\frac{2\pi}{3}} & 0 & e^{i\frac{2\pi}{3}} \end{pmatrix}. \quad (4.15)$$

By doing so, we identify the strength of the coupling with phonons at the corner of the BZ as

$$g_5 = \frac{\sqrt{3}V_{on}\Delta (\sqrt{2}V_{pp\sigma} - \sqrt{2}V_{pp\pi} + V_{sp\sigma})}{2\sqrt{2}aV_{hop}^2} \approx 4 \text{ meV} \cdot \text{\AA}^{-1}. \quad (4.16)$$

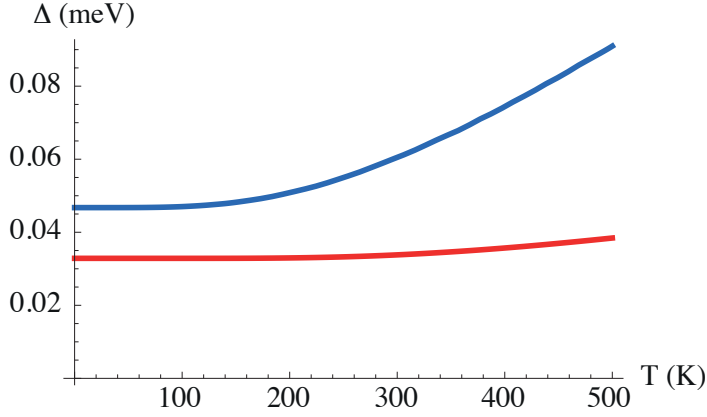


Figure 4.2: Effective Kane-Mele mass induced by the coupling with flexural phonons. In red (lower curve) the estimation neglecting the acoustic branch and the dispersion of the optical one. In blue (upper curve) the calculation within the model described in Appendix B.

4.4 Kane-Mele gap enhancement

One of the most interesting consequences of this analysis is the effect of the coupling in Eq. 4.6 on the electronic spectrum. The contribution of flexural phonons to the Kane-Mele coupling can be written as

$$\Delta_{ph} = g_4 \langle (u_{B_2})^2 \rangle, \quad (4.17)$$

where the brackets express the thermal average over the entire BZ. A rough estimate consists on neglecting the contribution from the acoustic branch and the dispersion of the optical mode. Since $\hbar\omega_{\Gamma}^{ZO} \approx 110 \text{ meV}$ ^[173] temperature plays no role, see the red curve in Fig. 4.2. However, the zero-point motion contribution $\Delta_0 = \frac{\hbar g_4}{2M\omega_{\Gamma}^{ZO}} \approx 0.03 \text{ meV}$ is non-negligible as compared to the intrinsic value (here M is the mass of the carbon atom).

This is a very crude approximation, since the identification of u_{B_2} with the ZO mode is strictly true at the Γ point. The entire BZ contributes to the average, so away from Γ both flexural acoustic (ZA) and optical branches enter. We can use the symmetry-adapted basis $|A_1\rangle$ and $|B_2\rangle$ phonons as a basis in order to describe the polarizations

of the $\nu = ZA, ZO$ phonons,

$$|\nu\rangle = \eta_{A_1}^\nu(\mathbf{q})|A_1\rangle + \eta_{B_2}^\nu(\mathbf{q})|B_2\rangle. \quad (4.18)$$

Note that $\eta(\mathbf{q}) = [\eta(-\mathbf{q})]^*$ due to time reversal symmetry. Thus, we have

$$\langle (u_{B_2})^2 \rangle \approx \frac{1}{N} \sum_{\mathbf{q} \in BZ} \sum_{\nu} \left| \eta_{B_2}^\nu(\mathbf{q}) \right|^2 \left\langle \left| u_{\mathbf{q}}^\nu \right|^2 \right\rangle_T, \quad (4.19)$$

where

$$u_{\mathbf{q}}^\nu = \frac{1}{\sqrt{N}} \sum_{i=1}^N u^\nu(\mathbf{R}_i) e^{-i\mathbf{q}\cdot\mathbf{R}_i} \quad (4.20)$$

is the Fourier transform of the phonon displacement field in branch ν , and the brackets denote thermal average.

We need a model in order to describe the deviations of the polarizations vectors and the frequencies of both branches in the entire BZ. We consider the simpler nearest-neighbor forces model where the elastic energy of the lattice can be written as

$$E = \frac{\alpha}{a^2} \sum_i \left[\left(h_{A_i} - \frac{1}{3} \sum_{\langle ij \rangle} h_{B_j} \right)^2 + \left(h_{B_i} - \frac{1}{3} \sum_{\langle ij \rangle} h_{A_j} \right)^2 \right]. \quad (4.21)$$

Here a is the carbon-carbon distance and α is a constant with units of energy which can be related with the bending rigidity κ of graphene in the continuum description shown in the previous chapter. This model leads to the dynamical matrix

$$\mathcal{D}(\mathbf{q}) = \frac{2\alpha}{3a^2} \begin{pmatrix} 3 + \frac{|f(\mathbf{q})|^2}{3} & -2f(\mathbf{q}) \\ -2f(\mathbf{q})^* & 3 + \frac{|f(\mathbf{q})|^2}{3} \end{pmatrix}, \quad (4.22)$$

where $f(\mathbf{q}) = \sum_{\alpha} e^{i\mathbf{q}\cdot\vec{\delta}_{\alpha}}$, and the sum is extended to nearest-neighbors. The frequencies read

$$\omega_{\pm} = \sqrt{\frac{2\alpha}{3Ma^2} \left(3 + \frac{|f(\mathbf{q})|^2}{3} \pm 2|f(\mathbf{q})| \right)}, \quad (4.23)$$

with polarization vectors $|\pm\rangle = \frac{1}{\sqrt{2}} \left(\frac{f(\mathbf{q})}{|f(\mathbf{q})|}, \mp 1 \right)^T$. The two branches in Eq. (4.23) are plotted in Fig. 4.3. The upper branch ω_+ must be identified with the optical one, whereas ω_- corresponds to the acoustic one.

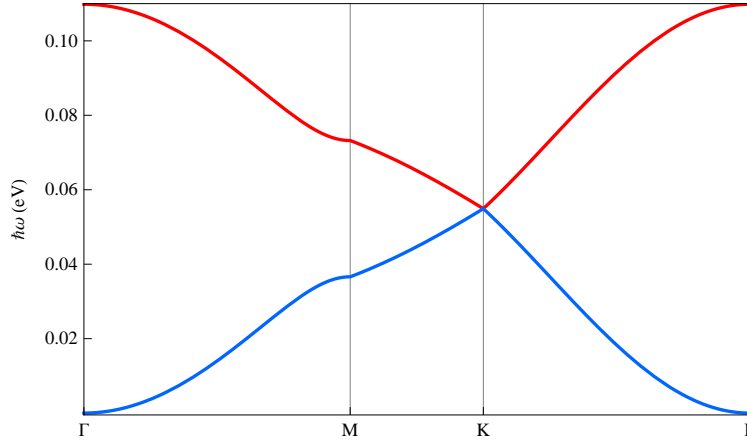


Figure 4.3: Dispersion of flexural phonons computed within the nearest-neighbor force model described in the text with $\alpha = 8.5$ eV. In red (upper curve) the dispersion for the optical branch, in blue (lower curve) the acoustic branch.

The model reproduces very well the dispersion of flexural phonons. At $\mathbf{q} \sim \Gamma$ we have

$$\begin{aligned}\omega_+ &\equiv \omega_{\mathbf{q}}^{ZO} \approx \sqrt{\frac{8\alpha}{Ma^2}} - \sqrt{\frac{\alpha a^2}{8M}} q^2, \\ \omega_- &\equiv \omega_{\mathbf{q}}^{ZA} \approx \sqrt{\frac{\alpha}{8Ma^{-2}}} q^2.\end{aligned}\quad (4.24)$$

Note that the dispersion relation of ZA phonons is quadratic, as expected from symmetry considerations. On the other hand, both branches are degenerate at \mathbf{K}_{\pm} ($\omega_{\mathbf{K}_{\pm}}^{ZA} = \omega_{\mathbf{K}_{\pm}}^{ZO} = \omega_{\Gamma}^{ZO}/2$), as expected from symmetry arguments. When we compare this model with the theory of elasticity we deduce the relation

$$\alpha = 6\sqrt{3}\kappa. \quad (4.25)$$

We set the value of α from the frequency of the flexural optical phonon at Γ . We obtain $\alpha = 8.5$ eV. By using the relation of Eq. (4.25) we obtain $\kappa \approx 0.8$ eV, which is a very reasonable value for the bending rigidity of graphene. This agreement confirms

the reliability of the model. Additionally, we have

$$\begin{aligned} \left| \eta_{B_2}^{ZO}(\mathbf{q}) \right|^2 &= \frac{1}{2} \left(1 + \frac{\Re f(\mathbf{q})}{|f(\mathbf{q})|} \right), \\ \left| \eta_{B_2}^{ZA}(\mathbf{q}) \right|^2 &= \frac{1}{2} \left(1 - \frac{\Re f(\mathbf{q})}{|f(\mathbf{q})|} \right), \end{aligned} \quad (4.26)$$

where $\Re f$ denotes the real part of f .

We compute the induced Kane-Mele mass from Eqs. (4.17) and (4.19) within this model. The results are shown in Fig. 4.2 (blue curve). Remarkably, the Kane-Mele gap induced by phonons $2\Delta_{ph}$ is of the order of 0.1 meV even at low temperatures due to the zero-point motion contribution.

4.5 Conclusions

We have constructed the spin-phonon coupling in graphene from symmetry considerations and computed their strengths within a tight-binding model. In comparison with previous works,^[106,174] our analysis sheds light on the microscopic origin of all the possible couplings induced by curvature that are allowed by the symmetries of the graphene crystal. This analysis is particularly useful in order to study spin transport limited by flexural phonons, where in principle both intra- and inter-valley processes could be considered.

We have applied this analysis to the study of the effect of flexural phonon modes on the Kane-Mele gap. We have found a remarkable contribution $2\Delta_{KM} \sim 1$ K, an order of magnitude larger than the intrinsic gap including also the effect of d orbitals.^[104,108] Of course, this value is still negligible for practical purposes. Nevertheless, this mechanism of enhancing the Kane-Mele gap may be exploited with strain engineering. The flexural modes are softened by applying compression.^[175-177] This softening is consistent with the negative Grüneisen coefficients reported in the literature.^[178-181] Although other failure mechanisms for graphene under tension cannot be discarded,^[182] it is natural to think that graphene under compressive stress may develop a sp^3 -like buckled phase, similarly to silicene. Such distortions under stress have been observed in STM experiments.^[183] We conclude that this mechanism residing on the π - σ orbitals mixing would be stabilized in compressed graphene samples, leading to higher values of the Kane-Mele gap.

PART 2:
SPIN RELAXATION

5

SOC-mediated spin relaxation

5.1 Introduction

When a spin polarized current is injected in a device its spin polarization decays during the diffusive propagation of electrons. The time scale which characterizes this decay is what we call spin lifetime τ_s . In general, defining rigorously τ_s is a difficult task. Indeed, two different quantities are usually introduced:^[18] T_1 and T_2 . The former is the spin relaxation time, whereas the latter is the dephasing time. These quantities are formally defined through the Bloch-Torrey equations for magnetization dynamics,^[184–186] which describe the diffusion of the magnetization, \mathbf{M} , treated as a classical magnitude. In the presence of a magnetic field $\mathbf{B}(t) = \mathbf{B}_0 + \mathbf{B}_1(t)$ these equations read

$$\begin{aligned}\frac{\partial M_{i=x,y}}{\partial t} &= \gamma (\mathbf{M} \times \mathbf{B})_{i=x,y} - \frac{M_{i=x,y}}{T_2} + D \nabla^2 M_{i=x,y}, \\ \frac{\partial M_z}{\partial t} &= \gamma (\mathbf{M} \times \mathbf{B})_z - \frac{M_z - M_z^0}{T_1} + D \nabla^2 M_z,\end{aligned}\tag{5.1}$$

where the static component \mathbf{B}_0 is taken in the \hat{z} direction for convenience. The precession frequency reads $\gamma = \mu_B g / \hbar$, where μ_B and g are the Bohr magneton and

electron gyromagnetic factor respectively. Here D is the diffusion constant. These equations describe, in a phenomenological way, the dynamics of itinerant electron spins. In order to determine T_1 , T_2 microscopically, we need a model for the dynamics of the spin system, from which the dynamics for the magnetization can be derived and compared with the Bloch-Torrey equations in order to determine T_1 , T_2 .

The kinetic spin Bloch equation (KSBE) provides a semi-classical description of the dynamics of the spin system. The KSBE can be understood as a spin-dependent version of the Boltzmann equation. The KSBE has been applied to the problem of spin relaxation in single-layer^[187–190] and bilayer^[191] graphene, and more recently in MX_2 materials.^[192, 193] In the former studies a random Rashba field was considered as the main source of spin relaxation. Such assumption is justified since in the experiments the samples are placed on a substrate, which is by itself one of the possible sources of this random Rashba field,^[194] as well as resonant impurities or vacancies.^[129] The studies on MX_2 were focused on the role of the intrinsic SOC in combination with different types of disorder. An alternative approach, full quantum mechanical, is based on the Mori-Kawasaki formula,^[195, 196] first applied to the study of the spin relaxation in graphene in Ref. 197.

In graphene-based spin valves, spin lifetimes are obtained from Hanle precession experiments in the so called non-local geometry,^[198] although alternative geometries have been proposed.^[199] This has been a very active field of research in the last few years.^[200–216] These are the main features of spin transport in graphene:

1. The reported spin lifetimes go from 100 ps to 1 ns, much shorter than the theoretically expected ones.
2. Spin relaxation time and momentum scattering time show approximately the same behavior as a function of the carrier concentration, both growing as $\sim \sqrt{n}$. Therefore, spin relaxation and momentum scattering seem to be correlated.
3. Despite 2., it has been recently reported^[217–220] that spin relaxation times increase when disorder is introduced in the sample. This observation is even more surprising in the case of heavy adatoms deposition,^[217] or hydrogenation,^[220] when the SOC is expected to be enhanced.
4. Recently, the behavior of spin lifetimes as a function of applied magnetic field has been studied, revealing the role of magnetic moments as an important source of spin relaxation.^[221] Importantly, this is only observed after hydrogenation, being the magnetic moments associated to such defects, in apparent contradiction with 3.

Four mechanisms are usually discussed for spin relaxation in semiconductors:^[18] the Elliot-Yafet,^[222, 223] D'yakonov-Perel',^[224, 225] Bir-Aronov-Pikus,^[226] and hyperfine-interaction mechanisms.^[227] The latter, which accounts for the interaction between

the magnetic moments of electrons and nuclei, is negligible in the diffusive regime due to the itinerant nature of the electrons. The hyperfine interaction with the nuclei spins is dynamically narrowed since the electrons move fast through nuclei with random spins, averaging to zero their action. The Bir-Aronov-Pikus mechanism accounts for electron spin-flip processes mediated by the electron-hole exchange interaction, and it is typically relevant in heavily p -doped semiconductors.^[226,228] For itinerant carriers, the main contributions to the spin relaxation are due to the entanglement of the spin and orbital degrees of freedom through the SOC.

The Elliot-Yafet (EY) mechanism takes into account the change in the spin polarization of a Bloch electron due to momentum scattering. This mechanism is the dominant one in the case of centrosymmetric systems. It is characterized by a linear relation between the spin relaxation time and momentum scattering time, $\tau_s^{-1} = \alpha \tau_p^{-1}$, where α can be interpreted as the spin-flip probability during a momentum relaxation event. Elliot deduced this relation by using a perturbative approach. Due to the SOC, Bloch states with well-defined spin polarization are not longer eigenstates of the complete Hamiltonian. However, in the case of systems with a center of inversion, at each point of the BZ two degenerate states can still be defined,^[222]

$$[a_{\mathbf{k}}(\mathbf{r})|\uparrow\rangle + b_{\mathbf{k}}(\mathbf{r})|\downarrow\rangle] e^{i\mathbf{k}\cdot\mathbf{r}}, \quad (5.2)$$

$$[(a_{-\mathbf{k}}(\mathbf{r}))^*|\downarrow\rangle - (b_{-\mathbf{k}}(\mathbf{r}))^*|\uparrow\rangle] e^{i\mathbf{k}\cdot\mathbf{r}}. \quad (5.3)$$

These states are connected by spatial inversion and time reversal symmetries and may be identified with spin-up and spin-down states because typically $|b| \ll 1$. Since the spin-orbit interaction couples electronic states with opposite spin projections in different bands, perturbation theory gives $|b| \approx \Delta_{SO}/\Delta E$, where ΔE is the energy difference between the two bands involved. The spin flip amplitude during the scattering by an obstacle with no spin degrees of freedom itself can be computed using the Born approximation, leading to $\alpha \approx \langle |b|^2 \rangle$ where the symbol $\langle \rangle$ expresses an average over the Fermi surface. These arguments are quite general and do not depend on the nature of the scatterers. Realistic calculations can be done in some cases, for instance in the case of III-V semiconductors.^[228,229] The Elliot relation holds experimentally for most conventional metals.^[230]

The D'yakonov-Perel' (DP) mechanism accounts for the spin dephasing in between momentum scattering events, and it is relevant in non-centrosymmetric materials, where the form of the Bloch states are not longer as Eqs. (5.2)-(5.3) dictate. When inversion symmetry is broken the doubly degeneracy of the bands is lifted. In this situation, a new contribution to spin relaxation must be taken into account due to the precession of electron spin in between scattering events. The SOC can be understood as an effective magnetic field which makes the electron spin to precess. Note that this effective magnetic field is momentum-dependent, so momentum scattering

randomizes the process. Therefore, the spin lifetime scales inversely as the momentum scattering time. In between scattering events the electron spin precesses an angle δ , which can be estimated from the natural frequency defined through the Rashba coupling Δ_R . Then, $\delta \sim \Delta_R/\hbar \times \tau_p$. As a result of the motional narrowing,^[231,232] after N collisions the precession angle is about $\delta \sim \Delta_R/\hbar \times \tau_p \times \sqrt{N}$. The spin lifetime may be defined as the time scale τ_s after which the precession angle is $\delta \sim 1$. After $N = \tau_s/\tau_p$ collisions we have $\delta \sim \Delta_R/\hbar \times \tau_p \times \sqrt{\tau_s/\tau_p} \sim 1$, so we deduce $\tau_s^{-1} \sim \Delta_R^2/\hbar^2 \times \tau_p$.

The fact that the spin relaxation times and the momentum scattering times behave similarly as a function of the carrier concentration in the experiments suggests that the EY mechanism limits spin transport in graphene. Such short spin lifetimes are also an indication of an extrinsic source of spin relaxation. However, some other experimental evidences as the increasing of the spin lifetimes under hydrogenation put several restrictions to the origin of such SOC enhancement.

In this chapter we study in detail conventional EY and DP mechanisms in graphene and MX_2 materials. From our estimates we conclude that EY mechanism cannot explain spin transport in graphene. Then, we analyze the problem of the spin-flip induced by an impurity which enhances locally the SOC. We consider the case of a resonant impurity, such as hydrogen, which induces a sp^3 -like distortion of the lattice coordination, leading to an enhancement of the SOC. Our results indicate a strong anisotropy in spin relaxation, since this relaxation mechanism seems to be much more efficient for in-plane spins.

5.2 EY and DP mechanisms in graphene and MX_2

In this section we compute the spin relaxation rates due to EY and DP mechanisms with the Mori-Kawasaki formula. Our starting point is the phenomenological Hamiltonian valid around the Dirac points,

$$\mathcal{H} = v \left(\tau_z \sigma_x k_x + \sigma_y k_y \right) + \frac{\Delta}{2} \sigma_z. \quad (5.4)$$

We describe simultaneously graphene and MX_2 . For the former, we must take $\Delta = 0$. For the intrinsic SOC terms, in the case of graphene we take a Kane-Mele coupling, whereas for MX_2 we take

$$\mathcal{H}_{\text{SO}} = \frac{\lambda}{2} \tau_z s_z (\mathcal{I} - \sigma_z). \quad (5.5)$$

We neglect the splitting of the conduction band since it is the result of second order processes as we saw before.

For SOC mediated spin relaxation mechanisms a relevant parameter of the theory is the amount of disorder $\Gamma = \hbar/\tau_p$, where τ_p is the lifetime of the quasiparticles with momentum \mathbf{p} . Disorder is introduced in the calculation in a phenomenological manner, by adding the imaginary self-energy $i\Gamma/2$ to the Matsubara Green's operator associated to the free Hamiltonian (5.4),

$$\hat{G}(\mathbf{k}, i\omega) = \frac{1}{2} \sum_{\alpha=\pm 1} G_{\alpha}(\mathbf{k}, i\omega) \left[\mathcal{I} + \alpha \left(at\mathbf{k} \cdot \vec{\sigma} + \frac{\Delta}{2} \sigma_z \right) / \epsilon_{\mathbf{k}} \right], \quad (5.6)$$

where we define

$$G_{\alpha}(\mathbf{k}, i\omega) = \frac{1}{i\omega - \alpha\epsilon_{\mathbf{k}} + \mu + i\Gamma/2}. \quad (5.7)$$

Here $\epsilon_{\mathbf{k}} = \sqrt{v^2|\mathbf{k}|^2 + \Delta^2/4}$ is the dispersion relation of conduction ($\alpha = +1$) and valence ($\alpha = -1$) bands of our effective model and μ is the chemical potential. Note that the valley is omitted since we do not consider short-range scatterers which could connect both valleys. We also neglect the momentum dependence of Γ , so it enters just as a parameter which in principle can be determined from transport experiments.

5.2.1 Mori-Kawasaki formula

We compute the spin relaxation rates by using the Mori-Kawasaki formula.^[195,196] Originally, the Mori-Kawasaki formula was deduced in order to compute the broadening of the signal peak in an electron spin resonance experiment due to the breaking of the $SU(2)$ spin symmetry of the system. As it has been shown recently,^[233] it can be related with the inverse of the spin lifetime $\Gamma_s = \hbar/\tau_s$. The Mori-Kawasaki formula treats the SOC terms as perturbations to the electronic Hamiltonian, something that in principle is valid since in our model the strength of the SOC terms are at least one order of magnitude smaller than the other energy parameters of the model, namely the gap Δ and the bandwidth $2v/a$. The spin lifetime is computed as

$$\Gamma_s = -\frac{1}{\chi} \lim_{\omega \rightarrow 0} \text{Im} \frac{\chi_{\mathcal{A}\mathcal{A}^\dagger}(\omega)}{\omega}, \quad (5.8)$$

where χ is the spin susceptibility and $\chi_{\mathcal{A}\mathcal{A}^\dagger}(\omega)$ is the Fourier transform of the response function

$$\chi_{\mathcal{A}\mathcal{A}^\dagger}(t) = -i\theta(t) \left\langle \left[\mathcal{A}(t), \mathcal{A}^\dagger(0) \right] \right\rangle, \quad (5.9)$$

with $\mathcal{A} = [\mathcal{H}^{SO}, s_+]$ and $s_{\pm} = (s_x \pm is_y)/2$. The spin susceptibility is defined as

$$\chi = \frac{1}{g\mu_B} \left(\frac{\partial \langle s_z \rangle}{\partial H} \right)_{H=0}, \quad (5.10)$$

where H is the field strength associated to a Zeeman term in the Hamiltonian $\mathcal{H}_Z = -g\mu_B H s_z$.^[234] The expectation values in Eqs. (5.9) and (5.10) are referred to the Hamiltonian without the SOC terms. The expectation value of the z -component of spin is

$$\langle s_z \rangle = \frac{1}{N} \sum_{\mathbf{k}} (n_{\mathbf{k}\uparrow} - n_{\mathbf{k}\downarrow}), \quad (5.11)$$

where N is the number of unit cells and $n_{\mathbf{k}s}$ is the occupation number of quasiparticles with momentum \mathbf{k} and spin s in the presence of the Zeeman term \mathcal{H}_Z . This can be calculated in terms of the spectral functions $A_{\alpha}(\mathbf{k}, \omega)$, defined from the retarded version of the Green's functions of Eq. (5.7) as

$$A_{\alpha}(\mathbf{k}, \omega) \equiv -2 \operatorname{Im} G_{\alpha}^R(\omega, \mathbf{k}) = \frac{\Gamma}{(\omega - \alpha \epsilon_{\mathbf{k}} + \mu)^2 + \frac{\Gamma^2}{4}}. \quad (5.12)$$

Then, we can write

$$n_{\mathbf{k}s} = 2 \sum_{\alpha=\pm 1} \int_{-\infty}^{\infty} \frac{d\omega}{2\pi} n_F(\omega) A_{\alpha}(\mathbf{k}, \omega + s g \mu_B H), \quad (5.13)$$

where $n_F(\omega)$ is the Fermi-Dirac distribution function and the factor 2 accounts for the valley degeneracy. From the definition of Eq. (5.10) we get

$$\chi = 4 \sum_{\alpha=\pm 1} \frac{1}{N} \sum_{\mathbf{k}} \int_{-\infty}^{\infty} \frac{d\omega}{2\pi} A_{\alpha}(\mathbf{k}, \omega) \left(-\frac{\partial n_F(\omega)}{\partial \omega} \right). \quad (5.14)$$

In the zero temperature limit ($T \ll T_F$, where T_F is the Fermi temperature) we can approximate $-\frac{\partial n_F(\omega)}{\partial \omega} \approx \delta(\omega)$. The sum in \mathbf{k} can be written as an integral through the standard procedure $\frac{1}{N} \sum_{\mathbf{k}} \rightarrow \frac{A_c}{(2\pi)^2} \int d^2\mathbf{k}$, where A_c is the area of the unit cell. The isotropy of the dispersion relation allows to integrate in angles straightforwardly and to write down the remaining integral in $|\mathbf{k}|$ as an integral in energies. At this point, it is necessary to introduce an energy cutoff D for the effective model, which can be related with the area of the unit cell as $D = v \sqrt{\pi/A_c}$. After some algebra the spin susceptibility can be written as

$$\chi = \frac{\Gamma}{\pi D} \sum_{\alpha=\pm 1} \int_{\frac{\Delta}{2D}}^1 dx \frac{x}{\left(x - \alpha \frac{\mu}{D}\right)^2 + \frac{\Gamma^2}{4D^2}}. \quad (5.15)$$

If we drop logarithmically small terms that appear in Eq. (5.15) after integration in x , we obtain a simple analytical formula for χ which is valid for $\mu \ll D$,

$$\chi \approx \frac{2\mu}{\pi D} \sum_{\alpha=\pm 1} \arctan \left(\frac{2\mu - \alpha\Delta}{\Gamma} \right). \quad (5.16)$$

We compute now the numerator of Eq. (5.8). The calculation is easily performed in the Matsubara frequency domain. We can write

$$\chi_{\mathcal{A}\mathcal{A}\mathcal{A}^\dagger}(i\omega) = \frac{1}{\beta N} \sum_{\mathbf{k}} \sum_{iv} \sum_{\alpha,\alpha'} f_{\alpha\alpha'}(\mathbf{k}) G_{\alpha}(\mathbf{k}, i\omega + iv) G_{\alpha'}(\mathbf{k}, iv), \quad (5.17)$$

where β is the usual thermal factor and $f_{\alpha\alpha'}(\mathbf{k})$ is defined as

$$f_{\alpha\alpha'}(\mathbf{k}) = \frac{1}{2} \text{Tr} \left[\mathcal{A} \cdot \left(\mathcal{S} + \alpha \frac{at\mathbf{k} \cdot \vec{\sigma} + \frac{\Delta}{2}\sigma_z}{\epsilon_{\mathbf{k}}} \right) \cdot \mathcal{A}^\dagger \cdot \left(\mathcal{S} + \alpha' \frac{at\mathbf{k} \cdot \vec{\sigma} + \frac{\Delta}{2}\sigma_z}{\epsilon_{\mathbf{k}}} \right) \right]. \quad (5.18)$$

The trace is performed in the space of 2-components Bloch functions, and the valley degeneracy has already been taken into account in this definition. The sum in frequencies can be performed easily by using the Lehmann representation in terms of the spectral functions introduced before. After the summation and the analytical continuation we have for the imaginary part of $\chi_{\mathcal{A}\mathcal{A}\mathcal{A}^\dagger}(\omega)$,

$$-\text{Im} \chi_{\mathcal{A}\mathcal{A}\mathcal{A}^\dagger}(\omega) = \frac{1}{N} \sum_{\mathbf{k}} \sum_{\alpha,\alpha'} f_{\alpha\alpha'}(\mathbf{k}) \times \int_{-\infty}^{\infty} \frac{d\epsilon}{4\pi} A_{\alpha}(\mathbf{k}, \epsilon + \omega) A_{\alpha'}(\mathbf{k}, \epsilon) [n_F(\epsilon) - n_F(\epsilon + \omega)]. \quad (5.19)$$

Hence, in the $\omega \rightarrow 0$ limit we obtain

$$\lim_{\omega \rightarrow 0} -\text{Im} \frac{\chi_{\mathcal{A}\mathcal{A}\mathcal{A}^\dagger}(\omega)}{\omega} = \frac{1}{N} \sum_{\mathbf{k}} \sum_{\alpha,\alpha'} f_{\alpha\alpha'}(\mathbf{k}) \times \int_{-\infty}^{\infty} \frac{d\epsilon}{4\pi} A_{\alpha}(\mathbf{k}, \epsilon) A_{\alpha'}(\mathbf{k}, \epsilon) \left(-\frac{\partial n_F(\epsilon)}{\partial \epsilon} \right). \quad (5.20)$$

After the same approximations as before we can write, in the zero temperature limit,

$$\Gamma_s = \frac{1}{4\pi\chi} \frac{A_c}{(2\pi)^2} \sum_{\alpha,\alpha'} \int d^2\mathbf{k} f_{\alpha\alpha'}(\mathbf{k}) A_{\alpha}(\mathbf{k}, 0) A_{\alpha'}(\mathbf{k}, 0). \quad (5.21)$$

The remaining part of the section is devoted to the estimation, using Eq. (5.21), of the spin relaxation for graphene and MoS₂.

5.2.2 Graphene

We consider first in-plane spin relaxation induced by the intrinsic Kane-Mele SOC in graphene. We have $\mathcal{A} = 2\Delta_{KM}\sigma_z s_+$, leading to $f_{\alpha\alpha'}(\mathbf{k}) = 4\Delta_{KM}^2 \delta_{\alpha',-\alpha}$. Only inter-band processes contribute. This is a manifestation of the inversion symmetry of the system. For the same reason, we expect that only the EY mechanism is present. Therefore, we conclude that inter-band processes within the Mori-Kawasaki formalism leads to the EY mechanism, in agreement with Elliot's argument. According to it and taking $\Delta E \approx 2\mu$, the energy separation between electronic states coupled by the Kane-Mele coupling, our expectation for the spin relaxation rate reads $\Gamma_s \approx \Delta_{KM}^2 / (2\mu)^2 \times \Gamma$. More formally, we have

$$\Gamma_s = \frac{\Delta_{KM}^2 \Gamma^2}{\pi \chi D^4} I_{inter}, \quad (5.22)$$

where we define

$$I_{inter} = \int_0^1 dx \frac{x}{\left[\left(x - \frac{\mu}{D}\right)^2 + \frac{\Gamma^2}{4D^2} \right] \left[\left(x + \frac{\mu}{D}\right)^2 + \frac{\Gamma^2}{4D^2} \right]}. \quad (5.23)$$

In the limit $D \gg \mu, \Gamma$, the integral can be approximated by

$$I_{inter} \approx \frac{D^2}{\mu\Gamma} \arctan\left(\frac{2\mu}{\Gamma}\right). \quad (5.24)$$

As expected, the spin relaxation rate is just

$$\Gamma_s \approx \frac{\Delta_{KM}^2}{4\mu^2} \Gamma. \quad (5.25)$$

The picture changes if we consider a Bychkov-Rashba SOC term. In that case, we have $\mathcal{A} = -2i\Delta_{BR}\sigma_+ s_z$, leading to $f_{\alpha\alpha'}(\mathbf{q}) = 4\Delta_{BR}^2$. We see that, due to the inversion symmetry breaking, both inter-band and intra-band processes enter. The latter are expected to be dominant. We have now

$$\Gamma_s = \frac{\Delta_{BR}^2 \Gamma^2}{\pi \chi D^4} [I_{inter} + I_{intra}], \quad (5.26)$$

where we define

$$I_{intra} = \frac{1}{2} \sum_{\alpha=\pm 1} \int_0^1 dx \frac{x}{\left[\left(x - \alpha \frac{\mu}{D}\right)^2 + \frac{\Gamma^2}{4D^2} \right] \left[\left(x - \alpha \frac{\mu}{D}\right)^2 + \frac{\Gamma^2}{4D^2} \right]}. \quad (5.27)$$

In the limit $D \gg \mu, \Gamma$, the integral can be approximated by

$$I_{intra} \approx \frac{4\mu D^2}{\Gamma^3} \arctan\left(\frac{2\mu}{\Gamma}\right). \quad (5.28)$$

Then, we obtain for the spin relaxation rate in this case

$$\Gamma_s \approx \frac{\Delta_{BR}^2}{4\mu^2} \Gamma + \frac{\Delta_{BR}^2}{\Gamma}. \quad (5.29)$$

We have seen with this calculation that intra-band processes lead to the DP contribution to the spin relaxation rate. Note that the DP mechanism is expected to be dominant since for typical carrier concentrations $|\mu| \gg \Gamma$.

This result is against the experimental observation: neither the DP mechanism nor the EY mechanism can explain the experiments. The former predicts a inversely proportional relation between τ_s and τ_p . On the other hand, if the EY mechanism were operating and given that $\tau_p \propto \sqrt{n}$, then we would have $\tau_s \propto n^{3/2}$. However, the dependence of τ_s on n is clearly sublinear in the experiments. Note that this unusual dependence on the carrier concentration ultimately arises from the absence of a energy gap between the conduction and valence π bands and can be expected also in narrow gap semiconductors in the doped regime, where the Fermi energy is larger than the gap.

5.2.3 MX_2

We start by computing the in-plane spin relaxation rate due to the intrinsic SOC. For this, we use Eq. (5.21) with $\mathcal{A} = \lambda_{int} (\mathcal{S} - \sigma_z) s_+$, leading to

$$f_{\alpha\alpha'}(\mathbf{k}) = 2\lambda^2 \left(1 - (\alpha + \alpha') \frac{\Delta}{2\epsilon_{\mathbf{k}}} + \alpha\alpha' \frac{\Delta^2}{4\epsilon_{\mathbf{k}}^2} \right). \quad (5.30)$$

As before, in-plane relaxation rate can be written as the sum of two contributions, one coming from intra-band transitions and the other from inter-band transitions,

$$\Gamma_s = \frac{\lambda^2 \Gamma^2}{2\pi\chi D^4} [I_{intra} + I_{inter}], \quad (5.31)$$

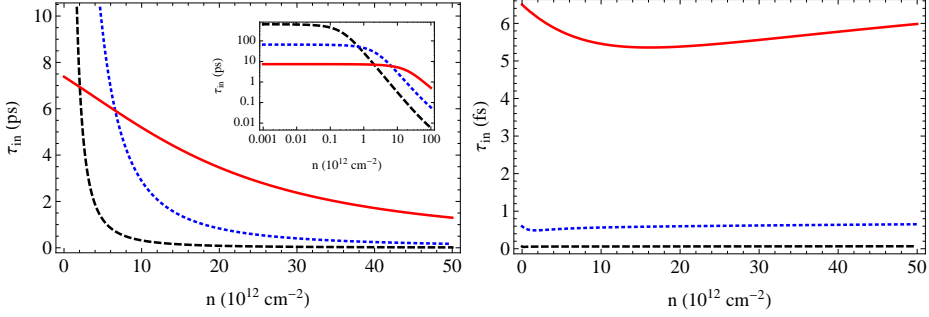


Figure 5.1: In-plane spin lifetimes as a function of the carrier concentration. Left: Electron doping. Right: Hole doping. Dashed black line corresponds to $\Gamma = 0.001$ eV, dotted blue to $\Gamma = 0.01$ eV, and solid red $\Gamma = 0.1$ eV. Inset: In-plane spin lifetimes for electron concentrations in double logarithmic scale. Notice the different time scale in the top and bottom panels.

where

$$\begin{aligned}
 I_{intra} &= \frac{1}{2} \sum_{\alpha=\pm 1} \int_{\frac{\Delta}{2D}}^1 dx \frac{x - \alpha \frac{\Delta}{D} + \frac{\Delta^2}{4xD^2}}{\left[\left(x - \alpha \frac{\mu}{D} \right)^2 + \frac{\Gamma^2}{4D^2} \right] \left[\left(x - \alpha \frac{\mu}{D} \right)^2 + \frac{\Gamma^2}{4D^2} \right]}, \\
 I_{inter} &= \int_{\frac{\Delta}{2D}}^1 dx \frac{x - \frac{\Delta^2}{4xD^2}}{\left[\left(x - \frac{\mu}{D} \right)^2 + \frac{\Gamma^2}{4D^2} \right] \left[\left(x + \frac{\mu}{D} \right)^2 + \frac{\Gamma^2}{4D^2} \right]}. \quad (5.32)
 \end{aligned}$$

As we have seen before, the intra-band transitions account the DP processes, whereas the inter-band term leads to the EY contribution. In the present case this is more clear in the doped regime $|\mu| > \Delta/2$. If we drop logarithmic corrections in the above integrals, as we did in order to get Eq. (5.16), we arrive at

$$\begin{aligned}
 \Gamma_s^{intra} &\approx \frac{\lambda^2}{2\Gamma} \left[1 - \frac{\Delta}{\mu} + \frac{\Delta^2 \left(\mu^2 + \frac{3\Gamma^2}{4} \right)}{4 \left(\mu^2 + \frac{\Gamma^2}{4} \right)^2} \right], \\
 \Gamma_s^{inter} &\approx \frac{\lambda^2 \Gamma}{8\mu^2} \left[1 - \frac{\Delta^2 \left(\mu^2 - \frac{\Gamma^2}{4} \right)}{4 \left(\mu^2 + \frac{\Gamma^2}{4} \right)^2} \right]. \quad (5.33)
 \end{aligned}$$

The inter-band transitions lead to an EY contribution characterized by the linear scaling between the spin lifetime and momentum scattering time $\Gamma_s^{inter} \propto \Gamma$. The intra-band transitions, however, leads to the DP mechanism, characterized by $\Gamma_s^{intra} \propto \Gamma^{-1}$.

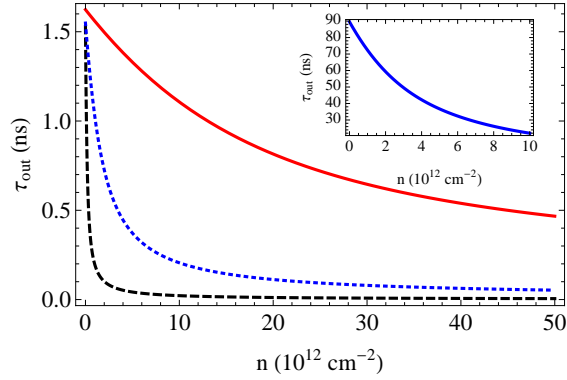


Figure 5.2: Out-of-plane spin lifetimes as a function of the carrier concentration. In black (dashed) $\Gamma = 0.001 \text{ eV}$, in blue (dotted) $\Gamma = 0.01 \text{ eV}$, in red $\Gamma = 0.1 \text{ eV}$. In all the cases $\Delta_{BR} = 10^{-2}\lambda$. Inset: Spin lifetime for hole concentrations where the correction given by Eq. (5.37).

This mechanism is clearly the dominant one as expected. Assuming that $\Gamma \ll \mu, \Delta$ we have

$$\frac{\Gamma_s^{\text{intra}}}{\Gamma_s^{\text{inter}}} \approx \frac{1 - \frac{\Delta}{2\mu}}{1 + \frac{\Delta}{2\mu}} \cdot \left(\frac{\mu}{\Gamma/2} \right)^2, \quad (5.34)$$

and therefore $\Gamma_s^{\text{intra}}/\Gamma_s^{\text{inter}} \gg 1$ unless the chemical potential lies at the bottom of the conduction band. It is important to note that the DP mechanism is clearly electron-hole asymmetric due to the different spin splittings of the conduction and valence bands.

These features are clearly shown in Fig. 5.1, where the in-plane spin lifetime is computed numerically. We see that the DP mechanism is clearly dominant for hole dopings. From mobilities reported in transport experiments^[235–237] we deduce $\Gamma \approx 0.02 \text{ eV}$, and therefore $\tau_{in} \sim 2\hbar\Gamma/\lambda^2 \approx 5 \text{ fs}$. For electron concentrations, it is interesting to note the crossover from DP to EY dominated regimes when the concentration is decreased, as it can be seen in the inset of the top panel of Fig. 5.1. Such crossover is possible when the strength of disorder is comparable with the chemical potential measured with respect to the bottom of the band. In this case the spin lifetimes are 3 orders of magnitude larger than in the case of hole doping. Note that in the electron doped regime a more realistic calculation should take into account also the spin splitting of the conduction band.

We compute now the out-of-plane spin relaxation rate due to a Bychkov-Rashba

coupling. In this case we have $\mathcal{A} = -2i\Delta_{BR}\sigma_{+s_z}$, leading to

$$f_{\alpha\alpha'}(\mathbf{k}) = 4\Delta_{BR}^2 \left(1 - (\alpha - \alpha') \frac{\Delta}{2\epsilon_{\mathbf{k}}} - \alpha\alpha' \frac{\Delta^2}{4\epsilon_{\mathbf{k}}^2} \right). \quad (5.35)$$

The calculation is formally identical to the previous one. In the doped regime we have the approximate results

$$\begin{aligned} \Gamma_s^{intra} &\approx \frac{\Delta_{BR}^2}{\Gamma} \left[1 - \frac{\Delta^2 \left(\mu^2 + \frac{3\Gamma^2}{4} \right)}{4 \left(\mu^2 + \frac{\Gamma^2}{4} \right)^2} \right], \\ \Gamma_s^{inter} &\approx \frac{\Delta_{BR}^2 \Gamma}{4\mu^2} \left[1 + \frac{\Delta^2 \left(\mu^2 - \frac{\Gamma^2}{4} \right)}{4 \left(\mu^2 + \frac{\Gamma^2}{4} \right)^2} \right]. \end{aligned} \quad (5.36)$$

In Fig. 5.2 the numerical computation of the spin lifetime as a function of the carrier concentration is shown. We take $\Delta_{BR} = 10^{-2}\lambda$, which is the correct order of magnitude given that this coupling is the result of second order processes as we explained previously. The spin lifetimes are in this case electron-hole symmetric and clearly dominated by the DP mechanism. The $1/n$ behavior is expected from the first expression in Eq. (5.36). For $\mu \geq \Delta/2$ we have $\tau_{out} \sim \hbar\Gamma\Delta^2/(4\pi\lambda_{BR}^2 a^2 t^2 n)$, so for $\Gamma = 0.02$ eV and $n = 10^{12}$ cm $^{-2}$ we obtain $\tau_{out} \approx 1 - 2$ ns.

Note that the spin splitting of the valence band is not taken into account in this calculation, but its effect is relevant since it tends to stabilize the out-of-plane spin polarization, in a similar way as an applied magnetic field in the out-of-plane direction does. We can take into account this effect by correcting the spin relaxation rate for hole concentrations as^[197,225]

$$\Gamma_s^{(holes)} \approx \Gamma_{out} \times \frac{1}{1 + \left(\frac{2\lambda}{\Gamma} \right)^2}, \quad (5.37)$$

where $2\lambda_{int}$ can be interpreted as the Zeeman splitting created by an effective magnetic field whose origin is the intrinsic SOC. Therefore, for $\Gamma = 0.02$ eV and $n = 10^{12}$ cm $^{-2}$ we expect:

$$\tau_{out}^{(holes)} \approx 60 \times \tau_{out} \approx 50 - 100 \text{ ns} \quad (5.38)$$

This correction is taken into account in the calculation shown in the inset of Fig. 5.2. It is interesting to notice that our results quantitatively agree with the experimental measurements of Mak *et al.*, who have reported spin lifetimes exceeding 1 ns in single layers of MoS $_2$.^[21]

5.3 Beyond EY mechanism in graphene: SOC scatterers

We have seen in the previous section that conventional EY mechanism is not able to explain spin relaxation in graphene. However, the similar behaviors of τ_s and τ_p suggests that momentum scattering and spin-flip processes are correlated somehow or other. There are several candidates which could explain these experiments. The most relevant ones are (i) spin flip induced by impurities covalently attached to graphene carbon atoms,^[129] (ii) the effect of a fluctuating Rashba field created by ripples,^[238] and (iii) scattering by local spins.^[221,239] In the first two cases, the spin-flip process is induced in regions where the SOC is locally enhanced. Next chapter is devoted to study the effect of ripples and curvature on spin relaxation. For the moment, we focus on resonant impurities.

In this section we study the problem of a single impurity which enhances locally the SOC, therefore, opening new channels for spin-flip processes. We focus on the case of impurity which induces a distortion of the lattice from a sp^2 to a sp^3 coordination, such as hydrogen.^[129] We consider the low-energy effective theory for graphene π electrons, consisting in two copies of the massless Dirac Hamiltonian at each inequivalent corner of the Brillouin zone. We neglect inter-valley scattering, which is justified for defects of order equal to or larger than the lattice spacing. We model the impurity as showed in Fig. 5.3. Far away from the impurity no SOC is induced, and then the spin polarization is asymptotically well-defined. Then, we are going to consider as in-coming wave function a Bloch-state with momentum \mathbf{k} and spin-polarization s ,

$$\hat{\psi}_{in} = e^{ikx} \hat{u}_{\mathbf{k}} \otimes |s\rangle, \quad (5.39)$$

where $\hat{u}_{\mathbf{k}} = \frac{1}{\sqrt{2}} (1, e^{i\theta_{\mathbf{k}}})^T$ and

$$|s\rangle = \begin{pmatrix} \cos \frac{\phi_s}{2} \\ \sin \frac{\phi_s}{2} e^{i\theta_s} \end{pmatrix}. \quad (5.40)$$

The incoming current can be defined as

$$\mathbf{J}_{in} \propto \hat{\psi}_{in}^\dagger \vec{\sigma} \hat{\psi}_{in} = \hat{u}_{\mathbf{k}}^\dagger \vec{\sigma} \hat{u}_{\mathbf{k}} = \frac{1}{|\mathbf{k}|} (k_x, k_y). \quad (5.41)$$

In order to write down the suitable form of the out-going waves, consider first the Lippman-Schwinger equation,

$$\psi(\mathbf{r}) = \psi_{in}(\mathbf{r}) + \int d^2\mathbf{r}' \hat{G}(\epsilon, \mathbf{r} - \mathbf{r}') [\mathcal{H}_0 + \epsilon \hat{\mathcal{S}}] U(\mathbf{r}') \psi(\mathbf{r}'), \quad (5.42)$$

where

$$\hat{G}(\epsilon, \mathbf{r}) = [(\epsilon + i0)^2 - \hat{\mathcal{H}}_0^2]^{-1}. \quad (5.43)$$

The Green function (5.43) has a trivial structure in spin and sublattice indices, $\hat{G}(\epsilon, \mathbf{r}) = G(\epsilon, \mathbf{r}) \mathcal{I}$, where

$$G(\epsilon, \mathbf{r}) = \frac{1}{(2\pi)^2} \int d^2 \mathbf{q} \frac{e^{i\mathbf{q}\cdot\mathbf{r}}}{(\epsilon + i0)^2 - (\hbar v_F q)^2} = -\frac{i}{4(\hbar v_F)^2} H_0^{(1)}(kr) \quad (5.44)$$

determines the asymptotic form of the scattered wave function. Note that $G(\epsilon, \mathbf{r})$ is nothing but the 2D Klein-Gordon propagator ($H_n^{(1)}$ are the Hankel functions of first kind). The asymptotic form of the Green function is just

$$G(\epsilon, \mathbf{r}) \approx -\frac{(\hbar v_F)^{-2}}{\sqrt{-i8\pi kr}} \cdot e^{ikr}. \quad (5.45)$$

As result, we can write the out-going wave function in the asymptotic limit as the superposition of two radial waves with opposite spin polarizations s and \bar{s} of the form

$$\hat{\psi}_{out} = \frac{f_s(\theta) e^{ikr}}{\sqrt{-ir}} \hat{u}_\theta \otimes |s\rangle + \frac{f_{\bar{s}}(\theta) e^{ikr}}{\sqrt{-ir}} \hat{u}_\theta \otimes |\bar{s}\rangle, \quad (5.46)$$

where $\hat{u}_\theta = \frac{1}{\sqrt{2}} (1, e^{i\theta})^T$ and

$$|\bar{s}\rangle = \begin{pmatrix} \sin \frac{\phi_s}{2} \\ -\cos \frac{\phi_s}{2} e^{i\theta_s} \end{pmatrix}. \quad (5.47)$$

Proceeding as before, we can define the scattered current as

$$\mathbf{J}_{scatt} \propto \hat{\psi}_{out}^\dagger \vec{\sigma} \hat{\psi}_{out} = \frac{|f_s(\theta)|^2 + |f_{\bar{s}}(\theta)|^2}{r} \hat{u}_\theta^\dagger \vec{\sigma} \hat{u}_\theta = \frac{|f_s(\theta)|^2 + |f_{\bar{s}}(\theta)|^2}{r} (\cos \theta, \sin \theta), \quad (5.48)$$

which can be interpreted as the sum of the scattered currents at s and \bar{s} channels. Then, we can define the differential scattering cross section as

$$\frac{d\vartheta_{sc}}{d\theta} = \frac{r|\mathbf{J}_{scatt}|}{|\mathbf{J}_{in}|} = |f_s(\theta)|^2 + |f_{\bar{s}}(\theta)|^2, \quad (5.49)$$

and in the same way, the differential cross section at the \bar{s} channel, what we are going to call the spin-flip cross section,

$$\frac{d\vartheta_{sf}}{d\theta} = |f_{\bar{s}}(\theta)|^2. \quad (5.50)$$

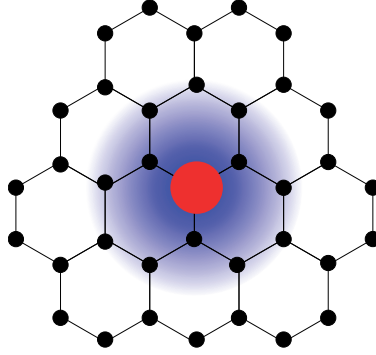


Figure 5.3: Geometry of the scattering problem.

In order to compute the scattering amplitudes f_s and $f_{\bar{s}}$, we model the defect as follows. Consider the geometry of Fig. 5.3. We describe the defect as a circular void of radius R_1 (in red in Fig. 5.3), which is of the order of the lattice constant, surrounded by a region of radius R_2 , where the SOC is induced. We assume that the wave function vanishes at $r \leq R_1$.^[240] We can use the cylindrical geometry of the problem in order to decompose the solutions at each region in partial waves, taking into account that the free Dirac Hamiltonian and the SOC entangle the orbital motion and the spin dynamics with the pseudospin, in such a way that the global symmetry of the problem is the generalized angular momentum operator $J_z = \ell_z + \frac{\hbar}{2}\sigma_z + \frac{\hbar}{2}s_z$, where σ and s represents the pseudospin and spin degree of freedoms and ℓ_z is the third component of the orbital angular momentum operator $\ell_z = -i\hbar(x\partial_y - y\partial_x)$.

In region I, if we suppose that both intrinsic Kane-Mele Δ_{KM} and Bychkov-Rashba Δ_{BR} couplings are induced, the Hamiltonian reads

$$\mathcal{H} = -i\hbar v_F \vec{\sigma} \cdot \nabla + \Delta_I \sigma_z \otimes s_z + \Delta_{BR} (\vec{\sigma} \times \vec{s})_z. \quad (5.51)$$

The most general wave function solution with well-defined $J = l + 1$ and energy ϵ

reads

$$\begin{aligned}
 \hat{\psi}_{\epsilon,J}^I = & A_+^l \left[\begin{pmatrix} J_l(k_+r) e^{il\theta} \\ ic_+ J_{l+1}(k_+r) e^{i(l+1)\theta} \end{pmatrix} \otimes |\uparrow\rangle - \begin{pmatrix} c_+ J_{l+1}(k_+r) e^{i(l+1)\theta} \\ iJ_{l+2}(k_+r) e^{i(l+2)\theta} \end{pmatrix} \otimes |\downarrow\rangle \right] + \\
 & + A_-^l \left[\begin{pmatrix} J_l(k_-r) e^{il\theta} \\ ic_- J_{l+1}(k_-r) e^{i(l+1)\theta} \end{pmatrix} \otimes |\uparrow\rangle + \begin{pmatrix} c_- J_{l+1}(k_-r) e^{i(l+1)\theta} \\ iJ_{l+2}(k_-r) e^{i(l+2)\theta} \end{pmatrix} \otimes |\downarrow\rangle \right] + \\
 & + B_+^l \left[\begin{pmatrix} Y_l(k_+r) e^{il\theta} \\ ic_+ Y_{l+1}(k_+r) e^{i(l+1)\theta} \end{pmatrix} \otimes |\uparrow\rangle - \begin{pmatrix} c_+ Y_{l+1}(k_+r) e^{i(l+1)\theta} \\ iY_{l+2}(k_+r) e^{i(l+2)\theta} \end{pmatrix} \otimes |\downarrow\rangle \right] + \\
 & + B_-^l \left[\begin{pmatrix} Y_l(k_-r) e^{il\theta} \\ ic_- Y_{l+1}(k_-r) e^{i(l+1)\theta} \end{pmatrix} \otimes |\uparrow\rangle + \begin{pmatrix} c_- Y_{l+1}(k_-r) e^{i(l+1)\theta} \\ iY_{l+2}(k_-r) e^{i(l+2)\theta} \end{pmatrix} \otimes |\downarrow\rangle \right],
 \end{aligned}$$

where $J_l(x)$ and $Y_l(x)$ are Bessel functions of first and second kind, $c_{\pm} = \frac{\epsilon - \Delta_I}{\hbar v_F k_{\pm}}$, and

$$\hbar v_F k_{\pm} = \sqrt{\epsilon^2 - \Delta_I^2 \mp 2\Delta_R \epsilon \pm 2\Delta_I \Delta_R}. \quad (5.52)$$

In region II we have just "free" graphene. We can write the solutions with well-defined $\epsilon = \hbar v_F |\mathbf{k}|$ and $J = l + 1$ as

$$\begin{aligned}
 \hat{\psi}_{\epsilon,J}^{II} = & \frac{\cos \frac{\phi_s}{2} e^{-il\theta_k} (i)^l}{\sqrt{2}} \begin{pmatrix} J_l(kr) e^{il\sigma} \\ iJ_{l+1}(kr) e^{i(l+1)\sigma} \end{pmatrix} \otimes |\uparrow\rangle + \\
 & + \frac{\sin \frac{\phi_s}{2} e^{i\theta_s} e^{-i(l+1)\theta_k} (i)^{l+1}}{\sqrt{2}} \begin{pmatrix} J_{l+1}(kr) e^{i(l+1)\sigma} \\ iJ_{l+2}(kr) e^{i(l+2)\sigma} \end{pmatrix} \otimes |\downarrow\rangle + \\
 & + C_+^l \begin{pmatrix} H_l(kr) e^{il\sigma} \\ iH_{l+1}(kr) e^{i(l+1)\sigma} \end{pmatrix} \otimes |\uparrow\rangle + C_-^l \begin{pmatrix} H_{l+1}(kr) e^{i(l+1)\sigma} \\ iH_{l+2}(kr) e^{i(l+2)\sigma} \end{pmatrix} \otimes |\downarrow\rangle \quad (5.53)
 \end{aligned}$$

where $H_l(x) = J_l(x) + iY_l(x)$ are Hankel functions. Note that with this choice, if we consider the superposition of all the partial waves, from the first two terms we recover the in-coming Bloch state with spin polarization $|s\rangle$, and then the out-coming wave must be given by

$$\hat{\psi}_{out} = \sum_{l=-\infty}^{\infty} \left[C_+^l \begin{pmatrix} H_l(kr) e^{il\sigma} \\ iH_{l+1}(kr) e^{i(l+1)\sigma} \end{pmatrix} \otimes |\uparrow\rangle + C_-^l \begin{pmatrix} H_{l+1}(kr) e^{i(l+1)\sigma} \\ iH_{l+2}(kr) e^{i(l+2)\sigma} \end{pmatrix} \otimes |\downarrow\rangle \right]. \quad (5.54)$$

Taking into account the asymptotic behavior of the Hankel functions, $H_l(x) \approx \sqrt{\frac{-2i}{\pi x}} (-i)^l e^{ix}$, the scattering amplitudes f_s and $f_{\bar{s}}$ can be easily written in terms of the coefficients

C_{\pm}^l as

$$f_s(\theta) = \frac{2}{\sqrt{\pi k}} \sum_{l=-\infty}^{\infty} \left[\cos \frac{\phi_s}{2} (-i)^{l-1} e^{il\theta} C_+^l + \sin \frac{\phi_s}{2} e^{-i\theta_s} (-i)^l e^{i(l+1)\theta} C_-^l \right], \quad (5.55)$$

$$f_{\bar{s}}(\theta) = \frac{2}{\sqrt{\pi k}} \sum_{l=-\infty}^{\infty} \left[\sin \frac{\phi_s}{2} (-i)^{l-1} e^{il\theta} C_+^l - \cos \frac{\phi_s}{2} e^{-i\theta_s} (-i)^l e^{i(l+1)\theta} C_-^l \right]. \quad (5.56)$$

The total scattering cross section and spin-flip cross section after integrating over the angle θ read

$$\vartheta_{sc} = \frac{8}{k} \sum_{l=-\infty}^{\infty} \left(|C_+^l|^2 + |C_-^l|^2 \right), \quad (5.57)$$

$$\vartheta_{sf} = \frac{8}{k} \sum_{l=-\infty}^{\infty} \left| \sin \frac{\phi_s}{2} C_-^{l-1} - \cos \frac{\phi_s}{2} e^{-i\theta_s} C_+^l \right|^2. \quad (5.58)$$

By imposing matching conditions for each partial wave at $r = R_2$ zig-zag boundary conditions at $r = R_1$,^[241] we obtain a system of 6 equations for each l which completely determines the unknowns, in particular C_+^l , C_-^l . These equations read

$$\begin{aligned} & A_+^l J_l(k_+ R_1) + A_-^l J_l(k_- R_1) + B_+^l Y_l(k_+ R_1) + B_-^l Y_l(k_- R_1) = 0, \\ & A_+^l c_+ J_{l+1}(k_+ R_1) - A_-^l c_- J_{l+1}(k_- R_1) + B_+^l c_+ Y_{l+1}(k_+ R_1) - B_-^l c_- Y_{l+1}(k_- R_1) = 0, \\ & A_+^l J_l(k_+ R_2) + A_-^l J_l(k_- R_2) + B_+^l Y_l(k_+ R_2) + B_-^l Y_l(k_- R_2) = \\ & \quad = \frac{\cos \frac{\phi_s}{2} e^{-il\theta_k} (i)^l}{\sqrt{2}} J_l(kR_2) + C_+^l H_l(kR_2), \\ & A_+^l c_+ J_{l+1}(k_+ R_2) + A_-^l c_- J_{l+1}(k_- R_2) + B_+^l c_+ Y_{l+1}(k_+ R_2) + B_-^l c_- Y_{l+1}(k_- R_2) = \\ & \quad = \frac{\cos \frac{\phi_s}{2} e^{-il\theta_k} (i)^l}{\sqrt{2}} J_{l+1}(kR_2) + C_+^l H_{l+1}(kR_2), \\ & A_+^l c_+ J_{l+1}(k_+ R_2) - A_-^l c_- J_{l+1}(k_- R_2) + B_+^l c_+ Y_{l+1}(k_+ R_2) - B_-^l c_- Y_{l+1}(k_- R_2) = \\ & \quad = -\frac{\sin \frac{\phi_s}{2} e^{i\theta_s - i(l+1)\theta_k} (i)^{l+1}}{\sqrt{2}} J_{l+1}(kR_2) - C_-^l H_{l+1}(kR_2), \\ & A_+^l J_{l+2}(k_+ R_2) - A_-^l J_{l+2}(k_- R_2) + B_+^l Y_{l+2}(k_+ R_2) - B_-^l Y_{l+2}(k_- R_2) = \\ & \quad = -\frac{\sin \frac{\phi_s}{2} e^{i\theta_s - i(l+1)\theta_k} (i)^{l+1}}{\sqrt{2}} J_{l+2}(kR_2) - C_-^l H_{l+2}(kR_2). \end{aligned} \quad (5.59)$$

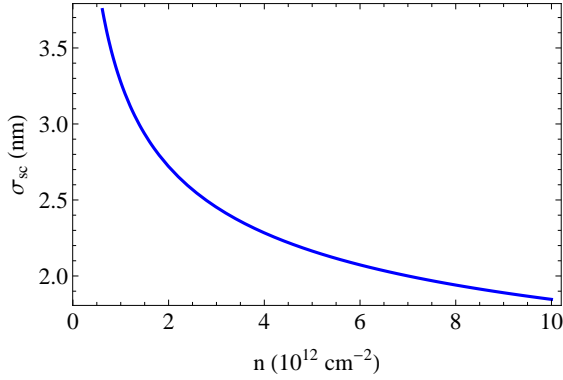


Figure 5.4: Scattering cross section as a function of the carrier concentration.

When no enhancement of the spin-orbit is induced, it is clear from these equations that no spin-flip is produced. In that case, it is easy to see that the scattering cross section is given by

$$\vartheta_{sc} = \frac{4}{k} \sum_l \left| \frac{J_l(kR_1)}{H_l(kR_1)} \right|^2, \quad (5.60)$$

as expected for resonant scatterers.

According to recent *ab initio* calculations,^[130] we take $\Delta_{KM} = 0.21$ meV, $\Delta_{BR} = 0.33$ meV. The sp^3 distortion is essentially local, as well as the SOC due to the dispersion of the involved σ bands. In the calculations we take $R_1 = a$, $R_2 = 2a$. The results are shown in Figs. 5.4-5.6.

The total scattering cross section is unaffected by the SOC. Its dependence as a function of the carrier concentration is shown in Fig. 5.4, and it follows Eq. (5.60). From this we deduce the relation $\tau_p \propto k_F \propto \sqrt{n}$, as expected for resonant impurities.

The spin-flip cross sections are shown in Figs. 5.5 and 5.6 for out-of-plane and in-plane polarizations respectively. They show completely different monotonies, and the in-plane spin-flip cross section is (note the units in both plots) 3 orders of magnitude larger. These differences are due to the presence of the Kane-Mele coupling.

In the light of these results, we conclude that spin transport experiments in graphene may not be explained by this model. The order of magnitude of the spin-flip cross sections lead to spin relaxation times of the order of 100 ns in the most favourable scenario (in-plane polarization), at least 2 orders of magnitude larger than the observed ones. On the other hand, the out-of-plane spin-flip cross sections goes like

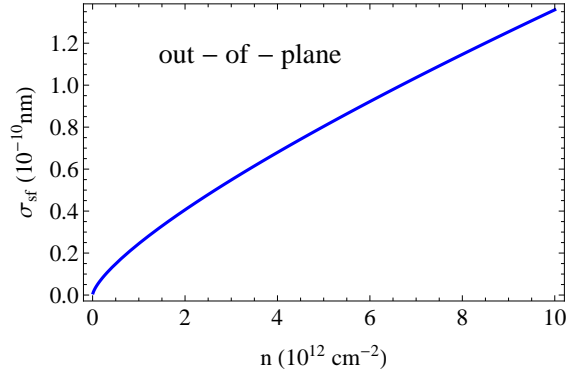


Figure 5.5: Spin-flip cross section for out-of-plane spin polarization as a function of carrier concentration.

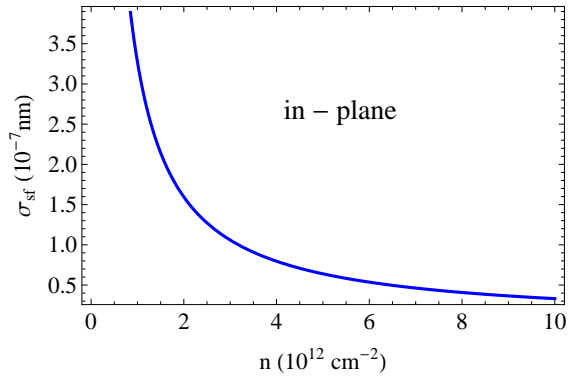


Figure 5.6: Spin-flip cross section for in-plane spin polarization as a function of carrier concentration.

$\propto k_F$, in contradiction with the experiments. This observation is general and does not depend on the magnitude of the induced SOC or the extension of the defect, therefore, the same behavior is expected for heavy adatoms or other sources for the SOC enhancement. Nevertheless, note that the model does not include the effect of local magnetic moments created by the defects, which is expected for resonant impurities or vacancies.^[242,243]

5.4 Conclusions

We have studied the SOC-mediated spin relaxation mechanisms in graphene and MX_2 materials. Whereas for the latter DP mechanism leads to spin lifetimes in agreement with recent optical experiments,^[21] in the case of graphene, neither DP nor EY mechanisms explain spin transport experiments. The values of the experimental spin lifetimes suggest extrinsic sources of spin relaxation. However, it is difficult to find an explanation based on a single mechanism given the amount of experimental features that seem to be contradictory each other in some cases. We have seen that the hypothesis according to which spin transport would be limited by adatoms increasing locally the SOC seems to be insufficient by itself in order to explain the experiments. On the other hand, the formation of local magnetic moments associated to these defects seem to play a role according to recent experiments.^[221] Other sources of spin relaxation are the ferromagnetic contacts due to the *conductivity mismatch problem*.^[244] Spin injection efficiency in graphene-based spin valves has been also a very active field of research,^[245-248] although its effect on spin transport measurements is still under debate.

6

Spin-lattice relaxation

6.1 Introduction

As mentioned in the previous chapter, conventional EY and DP mechanisms seem to be insufficient in order to explain spin transport experiments in graphene. Additionally, we have shown that extrinsic curvature and flexural phonons couple to electron spin and constitute an intrinsic source of spin relaxation mediated by the SOC. In this chapter we analyze the role of flexural phonons and curvature in disorder-assisted spin relaxation in 2D hexagonal crystals. In particular, we apply our findings to discuss spin relaxation in MX_2 materials.

In principle, we must distinguish two different contributions to the spin-lattice coupling Hamiltonian. On the one hand, an electron-phonon contribution arises as result of the modification of the orbital composition of the Bloch states by out-of-plane displacements of the atoms in the lattice. This coupling depends on the local curvature since the tilting of the crystal does not change the orbital composition of electronic states as we justified in Chapter 4. On the other hand, the absence of a global quantization axis induces relaxation with respect to an external probe defining a global frame for spin dynamics. The origin of this relaxation is purely geometrical, therefore, it does not depend on the microscopic details of the bands. This is usually

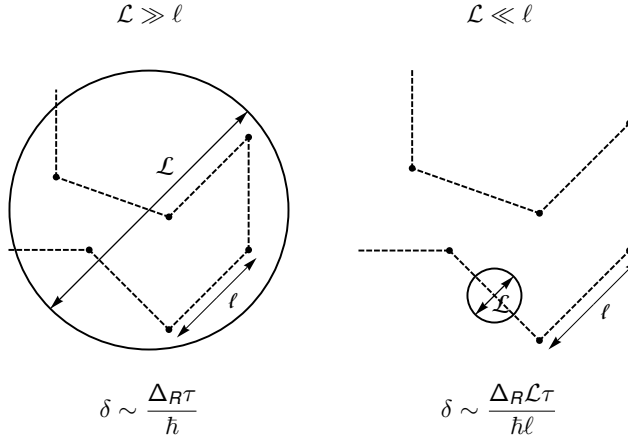


Figure 6.1: Two different situations for spin relaxation in the presence of a non-uniform SOC. When $\ell \ll \mathcal{L}$, the situation resembles the conventional DP mechanism, whereas for $\ell \gg \mathcal{L}$ the same scaling as for the EY mechanism is obtained.

called *deflection coupling*, introduced in carbon nanotubes,^[249] and studied also in graphene quantum dots.^[250]

The effective SOC terms generated by the presence of curvature, phonons, etc, contributes to spin relaxation, but in a slightly different way as compared to the conventional SOC-mediated mechanisms due to the spatial variations of the SOC. We must take into account two different length scales in our estimates, as sketched in Fig. 8.6. The motional narrowing is governed by the mean free path $\ell \sim v_F \tau$ (here v_F is the Fermi velocity of the spin carriers), but now we must take into account additionally the typical length scale \mathcal{L} over which the SOC varies.

In a region of radius \mathcal{L} we can take the SOC strength approximately uniform. If $\mathcal{L} \gg \ell$ we are in the same situation as in the case of uniform SOC. If we denote by Δ_R the approximate constant value of the SOC strength in this region we obtain the same scaling relation as in the conventional DP mechanism, $\tau_s^{-1} \sim \Delta_R^2 / \hbar^2 \times \tau$. However, for $\mathcal{L} \ll \ell$ the situation is not longer as in the uniform case. The spatial variations of the SOC adds another source of randomization which tends to compete with the motional narrowing. This can be seen by repeating the previous estimate, taking into account that now the dephasing between scattering events is governed by the averaged value of the SOC strength, which can be approximated as

$$\sqrt{\langle (\Delta_R(\mathbf{r}))^2 \rangle} \sim \Delta_R \times \frac{\mathcal{L}}{\ell}.$$

We end up with $\delta \sim \Delta_R \times \mathcal{L} / (\hbar\ell) \times \tau = \Delta_R \times \mathcal{L} / (\hbar v_F)$, which does not depend on τ . Hence, we obtain a Elliot-like relation of the form $\tau_s^{-1} \sim \Delta_R^2 \mathcal{L}^2 / (\hbar^2 v_F^2) \times \tau^{-1}$. We see that, in some sense, the ratio \mathcal{L}/ℓ interpolates between DP and EY-dominated regimes.

In this chapter we formalize this crossover within the framework of diagrammatic perturbation theory for disordered systems.^[251] Since spin relaxation times limited by flexural phonons in graphene are of the order of microseconds,^[167] whereas the experiments give values in the range of hundreds of picoseconds up to few nanoseconds, we focus our analysis on MX_2 materials, where this mechanism is expected to be more relevant. The structure of the chapter is the following. First we review the spin-phonon coupling from a geometrical point of view, and we determine the model Hamiltonian that we are going to employ through the calculation. Then, we analyze in detail the spin relaxation induced by curvature, distinguishing two cases: static wrinkles and flexural phonon modes. We pay special attention to the parametric dependence of the spin lifetimes on adjustable parameters as temperature. Finally, we conclude with some numerical estimates in experimentally relevant scenarios.

6.2 Spin-lattice coupling: geometrical perspective

In this section we construct the spin-lattice coupling in the long wavelength limit for general 2D crystals with hexagonal symmetry. Due to the mirror symmetry of these 2D materials we can write in general

$$\mathcal{H}(\mathbf{K}_\pm + \mathbf{p}) = \mathcal{H}_{\text{band}}(\mathbf{K}_\pm + \mathbf{p}) + \epsilon_z \hat{\mathcal{L}}_z \hat{S}_z. \quad (6.1)$$

The first term describes the electron/hole orbital motion in the band, and the second term takes into account the SOC. The microscopic form of the angular momentum operator $\hat{\mathcal{L}}_z$ depends on the particular symmetry of the system. As we have seen, for centrosymmetric point groups as C_{6v} (graphene), D_{3d} (bilayer graphene or silicene), $\hat{\mathcal{L}}_z = \tau_z \sigma_z$, whereas for non-centrosymmetric groups as D_{3h} (MX_2) we have $\hat{\mathcal{L}}_z = \tau_z$. The size of the coupling constant ϵ_z depends on the material and band-specific orbital composition of the electron Bloch states. In all the cases the out-of-plane direction defines as global quantization axis for electron spin. The lack of a global definition of the normal to the crystal makes the electron spin to relax.

In general, spin-lattice coupling between electrons and wrinkles can be incorporated in Eq. (6.1) by treating the crystal as a flexible membrane, as we did in the case of graphene. We introduce the local vertical displacements $h(x, y)$. The local normal vector is just $\mathbf{n} \approx (-\partial_x h, -\partial_y h, 1)$ to the leading order in h . Then, we use the global

coordinate system for the 3D electron spin \mathbf{s} to write down its coupling to the local angular momentum oriented along $\mathbf{n}(x, y)$,

$$\begin{aligned} H_{SO} &= \epsilon_z \mathcal{L}_z \hat{\mathbf{s}} \cdot \mathbf{n} \approx \epsilon_z \mathcal{L}_z \hat{s}_z + \delta H_g; \\ \delta H_g &\approx -\epsilon_z \mathcal{L}_z \left(\partial_x h \hat{s}_x + \partial_y h \hat{s}_y \right). \end{aligned} \quad (6.2)$$

Here, the inhomogenous term δH_g is responsible for spin-lattice relaxation, whereas the first term $\epsilon_z \mathcal{L}_z \hat{s}_z$ sets a global quantization axis for the electron spin. Additionally, we take into account contributions towards spin-phonon coupling arising from the modification of the orbital composition of the Bloch states of electrons, due to the mixing of bands (and corresponding atomic orbitals) by mutual displacements of atoms in the lattice. Such couplings depend on the components of the second fundamental form $\mathcal{F}_{ij} \approx \partial_i \partial_j h$ rather than \mathbf{n} , as we justified in Chapter 4. Phenomenologically, such additional couplings,

$$\begin{aligned} \delta H_o &= \lambda_{\parallel} \left[2\partial_x \partial_y h \hat{s}_x + \left(\partial_y \partial_y h - \partial_x \partial_x h \right) \hat{s}_y \right] \mathcal{L}_z + \hbar \beta (\mathbf{v} \times \mathbf{s})_z \nabla^2 h + \\ &+ \hbar \tilde{\beta} \left[\left(\hat{v}_x \hat{s}_y + \hat{v}_y \hat{s}_x \right) \left(\partial_x \partial_x h - \partial_y \partial_y h \right) + 2 \left(\hat{v}_y \hat{s}_y - \hat{v}_x \hat{s}_x \right) \partial_x \partial_y h_{xy} \right], \end{aligned} \quad (6.3)$$

appear as invariants of the point group of the crystal, C_{6v} for graphene and $D_{3h} = D_3 \times \sigma_h$ for MX_2 , built from the components of the electron spin operator $s_{x,y}$, velocity operator, and components of the second fundamental form to the leading order in h . Note that the terms in the first row of Eq. (6.3) can be written as $\lambda_{\parallel} \mathcal{L} \cdot \hat{\mathbf{s}}$, where $\mathcal{L} = \pm \left(2\partial_x \partial_y h, \partial_y^2 h - \partial_x^2 h \right)$ for \mathbf{K}_{\pm} has the properties of an in-plane component of atomic angular momentum operator, and the other two terms are similar to Bychkov-Rashba^[102] and Dresselhaus^[252] SOC terms. In those bands where electrons originate from atomic $p_{x,y}$ and d_{xy, x^2-y^2} orbitals (e.g., valence band in MX_2), the influence of δH_o should be less than that of δH_g . In the bands where electrons originate from s , p_z or d_{z^2} orbitals, SOC arises from their weak mixing with high energy orbitals, and hence δH_g and δH_o should be treated on equal footing.

As they stand in Eqs. (6.2)-(6.3), the spin-lattice coupling terms $\delta H_{g,o}$ can be used to evaluate the rate of spin relaxation of electrons due to the short-wavelength ripples with a Fourier spectrum h_q in the range of wave numbers $q \gg \epsilon_z/v$. To describe spin of electrons flying across such short-wavelength ripples, we use a spin-coordinate frame related to the median orientation of the crystal, averaged over many ripple periods. In contrast, it is more practical to analyze the influence of long-wavelength wrinkles, with $q < \epsilon_z/v$, in the local, adiabatically varying spin frame, adjusted to the local flake orientation. The electron spinor states in the global and local frames are related by the non-Abelian gauge transformation $\tilde{U} = e^{\frac{i}{2} \nu \cdot \hat{\mathbf{s}}}$, $\nu = \left(\partial_y h, -\partial_x h \right)$, which diagonalizes Eq. (6.2) into $H_{SO} = \epsilon_z \mathcal{L}_z \hat{s}_z$, but also produces an additional smaller

perturbation,

$$\hat{U} \mathcal{H}_{band}(\mathbf{K}_{\pm} + \mathbf{p}) \hat{U}^{\dagger} \approx \mathcal{H}_{band}(\mathbf{K}_{\pm} + \mathbf{p}) + \delta \tilde{H}_g, \text{ where}$$

$$\delta \tilde{H}_g = \frac{1}{2} \left\{ \frac{\partial \mathcal{H}_{band}}{\partial \mathbf{p}}, \hat{U} (-i\hbar \partial) \hat{U}^{\dagger} \right\} = \frac{\hbar}{2} \left[\hat{v}_y \hat{s}_x \partial_y^2 h - \hat{v}_x \hat{s}_y \partial_x^2 h + (\hat{v}_x \hat{s}_x - \hat{v}_y \hat{s}_y) \partial_x \partial_y h \right].$$

Note that, upon gauge transformation \hat{U} , spin-lattice coupling δH_o remains almost unchanged (only terms in the higher order in qh_q can appear), hence $\delta \tilde{H}_g$ is the leading term in the Taylor expansion of $\hat{U} \mathcal{H}_{band} \hat{U}^{\dagger} - \mathcal{H}_{band}$ in small qh_q .

This gauge transformation allows us to express all the couplings in the local spin frame, in such a way that only the components of the second fundamental form may appear. The geometrical origin of $\delta \tilde{H}_g$ becomes evident within this formulation. Note that:

1. $\delta \tilde{H}_g$ has the same structure as a combination of Bychkov-Rashba and Dresselhaus terms in the phenomenological Hamiltonian of Eq. (6.3), with the universal (non material dependent) coupling constants $\beta = \tilde{\beta} = -1/4$. Therefore, in the following analysis of spin relaxation induced by smooth ripples, we combine $\delta \tilde{H}_g$ and δH_o by redefining the coupling constants β and $\tilde{\beta}$.
2. Such combination of Bychkov-Rashba and Dresselhaus terms corresponds to the situation where spin relaxation is maximum along the direction of bending, and it is absent in the orthogonal direction.

This last statement can be checked straightforwardly. By setting the gaussian curvature to 0, we can define locally the direction of bending forming an angle ϕ with the x axis. Then, the curvature is locally determined by the radius of curvature along such direction, R . If we write the velocity operator \mathbf{v} as $\mathbf{v} = v_F (\cos \theta, \sin \theta)$, then we have

$$\delta \tilde{H}_g \approx \frac{\hbar v_F}{2R} (\cos \phi \hat{s}_y - \sin \phi \hat{s}_x) \cos(\phi - \theta). \quad (6.4)$$

Hence, spin relaxation is maximum when $\theta = \phi \pmod{\pi}$, and it is absent for $\theta = \phi + \pi/2 \pmod{\pi}$.

6.3 Spin-lattice relaxation

Spin-lattice relaxation of electrons is determined by the cumulative contribution of both short- and long-wavelength lattice deformations, which produces the sum $\tau_s^{-1} = \tau_d^{-1} + \tau_b^{-1}$ of *diffusive* spin relaxation assisted by disorder and *ballistic* contribution

$$\prod_{nm}^{(2)} = \text{Diagram 1} + \text{Diagram 2} + \text{Diagram 3}$$

$$G^{R,A}(\omega, \vec{p}) = \xrightarrow{R,A} = \frac{(\omega - \epsilon_p \pm i\hbar/2\tau) + \epsilon_z/2s_z}{(\omega - \epsilon_p \pm i\hbar/2\tau)^2 - \epsilon_z^2/4}$$

$$\bullet \text{---} \bullet = \begin{cases} \beta_{\text{so}}^2 \hbar^2 v^2 \langle |h_q|^2 \rangle & \text{if } q < \epsilon_z/\hbar v \\ \epsilon_z^2 \langle |h_q|^2 \rangle & \text{if } q > \epsilon_z/\hbar v \end{cases}$$

Figure 6.2: The three diagrams which contribute to Π operator to the lowest order in the spin-lattice coupling.

determined by a simultaneous momentum $|\mathbf{p} - \mathbf{p}'| \sim q$ and spin transfer to the ripples.

The diffusive contribution to the spin relaxation rate can be estimated using the framework of diagrammatic perturbation theory applied to the analysis of a disorder averaged spin-density matrix of electrons, $\frac{1}{2}\vec{\rho} \cdot \vec{\sigma}$. Diagrammatically, Fig. 6.2, spin-lattice coupling is incorporated in the polarization operator Π , which governs spin diffusion, $[\partial_t - \Pi]\vec{\rho}(t) = \vec{\rho}(0)\delta(t)$. Without spin-lattice coupling, $\Pi \approx D\nabla^2$, where $D = \frac{1}{2}v_F^2\tau = \frac{1}{2}\ell v_F$, τ and ℓ stands for the electron diffusion coefficient, scattering time and mean free path, respectively. Valley-dependent spin splitting, $\pm\epsilon_z s_z$, generates independent precession of $\vec{\rho}_{\pm}$ in \mathbf{K}_{\pm} valleys. Spin-lattice relaxation of electrons, assisted by disorder, is incorporated into Π via three diagrams, Fig. 6.2, where solid lines indicate the disorder averaged electron Green functions, the dashed lines are correlators $\langle h(\mathbf{r})h(\mathbf{r}') \rangle$ and dots are spin-lattice coupling vertices corresponding to Eqs. (6.2)-(6.3). The kinetics of spin polarization of carriers is then described by

$$[\partial_t - D\nabla^2] \vec{\rho}_{\pm} \pm \lambda_{z_2} \mathbf{n}_z \times \vec{\rho}_{\pm} + \tau_d^{-1} \vec{\rho} = \vec{\rho}_{\pm}(0)\delta(t), \quad (6.5)$$

where \pm identifies \mathbf{K}_{\pm} valley, and we have neglected the difference between the in-plane and out-of-plane spin relaxation rates, regarding the fact that, in all possible regimes, it should be superceded by a faster spin precession due to ϵ_z term in

Eq. (6.1). The three diagrams in Fig. 6.2 lead to

$$\tau_d^{-1} = \sum_{\mathbf{q}} \mathcal{M}(q) \frac{\tau q^2}{N} \langle |h_{\mathbf{q}}|^2 \rangle \times \begin{cases} q^2 \beta_{SO}^2 v^2 & q < \frac{\epsilon_z}{\hbar v} \\ \epsilon_z^2 / \hbar^2 & q > \frac{\epsilon_z}{\hbar v} \end{cases}$$

$$\text{with } \mathcal{M}(q) = \frac{1 + \ell^2 q^2 + \frac{\tau^2 \epsilon_z^2}{\hbar^2}}{1 + 2 \left(\ell^2 q^2 + \frac{\tau^2 \epsilon_z^2}{\hbar^2} \right) + \left(\ell^2 q^2 - \frac{\tau^2 \epsilon_z^2}{\hbar^2} \right)^2},$$

$$\text{and } \beta_{SO}^2 \equiv \beta^2 + \tilde{\beta}^2 + \frac{\lambda_{\parallel}^2}{\hbar^2 v^2}. \quad (6.6)$$

The above expressions link together DP and EY regimes. Indeed, for $q\ell \ll 1$ spin relaxation takes place over several momentum scattering events while electron diffuses in an interval of space with almost homogeneous SOC which causes its spin to precess randomly. Therefore, the spin relaxation rate is expected to obey the DP relation $\tau_d^{-1} \propto \tau$. On the contrary, for $q\ell > 1$ spin flips take place over single scattering events involving external disorder, and spin relaxation is expected to obey the Elliot relation $\tau_d^{-1} \propto \tau^{-1}$.

The ballistic contribution is determined by a simultaneous momentum, $|\mathbf{p} - \mathbf{p}'| \sim q$, and spin transfer to the lattice upon electron scattering off the ripples. From the Fermi's golden rule we estimate

$$\tau_b^{-1} = \frac{2\pi}{N\hbar} \sum_{\mathbf{q}} e^{-\frac{1}{q\ell}} |\langle \mathbf{p} + \mathbf{q} \uparrow | \delta H_g | \mathbf{p} \downarrow \rangle|^2 \delta \left(\epsilon_{\mathbf{p}+\mathbf{q}}^{\uparrow} - \epsilon_{\mathbf{p}}^{\downarrow} \right).$$

Here, a factor $e^{-\frac{1}{q\ell}}$ takes into account the fact that this contribution does not involve any externally promoted momentum transfer. This contribution is generated by the short-wavelength flexural deformations h_q with $q > \epsilon_z / \hbar v$, which permit electron's scattering between isoenergy lines separated by $\epsilon_z / \hbar v$ on the momentum plane near the \mathbf{K}_{\pm} points, where the local spin quantization axis is defined as a normal to the median plane averaging wrinkles over $\hbar v / \epsilon_z$ scale.

Next, we apply this analysis to the cases of static wrinkles and flexural phonon modes.

6.3.1 Static wrinkles

We analyze spin relaxation of electrons produced by static wrinkles characterized by lateral size q^{-1} and height $\sqrt{\langle h^2 \rangle}$. We distinguish two asymptotic regimes characterized by the ratio $q\ell$, see Fig. 6.3. For $q\ell \ll 1$, the ballistic contribution is exponentially suppressed, and τ_s can be understood as result of the DP mechanism in the

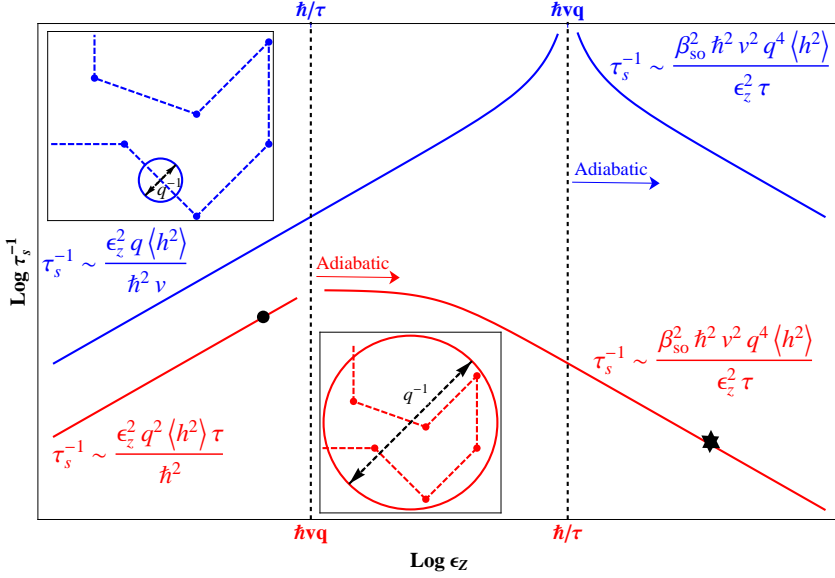


Figure 6.3: Schematic behavior of spin relaxation induced by wrinkles of typical size q^{-1} and height $\sqrt{\langle h^2 \rangle}$. The top and bottom lines correspond to $q\ell > 1$ and $q\ell < 1$, respectively. The experimental situation^[235–237, 253] for electrons and holes in MoS₂ is denoted by a dot and a star, respectively.

presence of an effective Zeeman term ϵ_z . Asymptotic formulas for τ_s are summarized in Fig. 6.3.

In the case of $q\ell > 1$ we expect a EY behavior for the diffusive contribution, in particular, if we distinguish between long-wavelength and short-wavelength modes,

$$\tau_d^{-1} \approx \begin{cases} \frac{\hbar^2 \beta_{\text{so}}^2 \nu^2 q^4 \langle |h_q|^2 \rangle}{\epsilon_z^2 \tau} & \text{if } \epsilon_z \gg \hbar\nu q, \\ \frac{\epsilon_z^2 \langle |h_q|^2 \rangle}{\hbar^2 \nu^2 \tau} & \text{if } \epsilon_z \ll \hbar\nu q. \end{cases} \quad (6.7)$$

When $\epsilon_z \gg \hbar\nu q$ the ballistic contribution is absent, whereas in the short-wavelength regime,

$$\tau_b^{-1} \approx \frac{2\pi}{\hbar} \epsilon_z^2 q^2 \langle |h_q|^2 \rangle \times \int \frac{d\theta_q}{2\pi} \delta(\epsilon_{\mathbf{p}+\mathbf{q}}^\uparrow - \epsilon_{\mathbf{p}}^\downarrow) = \frac{\epsilon_z q \langle |h_q|^2 \rangle}{\hbar^2 \nu}. \quad (6.8)$$

Note that in that case spin relaxation is dominated by the ballistic contribution

since

$$\frac{\tau_b^{-1}}{\tau_d^{-1}} \sim q\ell \gg 1.$$

As before, asymptotic formulas are summarized in Fig. 6.3. Note that a non-monotonic dependence of τ_s^{-1} on ϵ_z is expected due to a double role it plays: on the one hand ϵ_z determines the strength of the spin-lattice coupling according to Eq. (6.2), and on the other it represents the intrinsic SOC splitting leading to a pseudo-Zeeman field which protects spin polarization.

6.3.2 Flexural phonons

Spin relaxation due to flexural phonons is evaluated taking into account their quadratic dispersion, $\omega_q = \sqrt{\frac{\kappa}{\rho}} |q|^2$ (where κ is the bending rigidity of the system and $\rho = M/A_c$ the mass density) and the resulting low frequencies allow us to treat them as quasi-static deformations parametrized by spectral density $\langle |h_q|^2 \rangle$,

$$\langle |h_q|^2 \rangle = \frac{\hbar}{2M\omega_q} \left[2n_B \left(\frac{\omega_q}{T} \right) + 1 \right],$$

where n_B is the Bose-Einstein distribution function.

For the sake of convenience, we introduce two characteristic temperature scales associated to ℓ and ϵ_z through the dispersion relation,

$$\begin{aligned} T_\ell &\equiv \sqrt{\kappa/\rho} \times \frac{\hbar}{\ell^2 K_B}, \\ T_Z &\equiv \sqrt{\kappa/\rho} \times \frac{\epsilon_z^2}{\hbar v^2 K_B}. \end{aligned} \quad (6.9)$$

For $T \ll T_Z$, spin relaxation is dominated by long wavelength ($q < \epsilon_z/\hbar v$) phonons, whereas at $T \gg T_Z$, short wavelength modes dominate. On the other hand, at $T < T_\ell$ only modes with $q < \ell^{-1}$ contribute to spin relaxation. At low temperatures DP behavior is expected if $T_\ell > T_Z$, whereas for $T_\ell < T_Z$ the Elliot relation $\tau_s \propto \tau$ is anticipated. At high temperatures, however, the analysis is not so straightforward since also the ballistic contribution must be taken into account. Two regimes of disorder are defined by the ratio T_Z/T_ℓ , which controls the relative importance of both contributions.

The dependence on temperature of τ_d can be easily inferred from Eq. (6.6). The integration over flexural phonon modes, after the substitution $\frac{1}{N} \sum_{\mathbf{q}} \rightarrow \frac{\mathcal{A}_c}{4\pi^2} \int_{BZ} d^2\mathbf{q}$, where \mathcal{A}_c is the area of the unit cell, can be expressed as

$$\tau_d^{-1} = \frac{\beta_{SO}^2 T^2}{8\pi\tau\kappa T_\ell} \int_0^{\frac{T_Z}{T}} dx x \mathcal{M}(x) [2n_B(x) + 1] + \frac{\tau \epsilon_z^2 T}{8\pi\hbar^2 \kappa} \int_{\frac{T_Z}{T}}^{\frac{T}{T_\ell}} dx \mathcal{M}(x) [2n_B(x) + 1], \quad (6.10)$$

where we distinguish the contributions from long- and short-wavelength modes, respectively, and

$$\mathcal{M}(x) = \frac{1 + \frac{T}{T_\ell} x + \frac{T_Z}{T_\ell}}{1 + 2 \left(\frac{T}{T_\ell} x + \frac{T_Z}{T_\ell} \right) + \left(\frac{T}{T_\ell} x - \frac{T_Z}{T_\ell} \right)^2}. \quad (6.11)$$

After the integration over thermally excited flexural phonon modes, we find

$$\tau_d^{-1} \approx \begin{cases} \frac{\pi\beta_{SO}^2 T^2}{24\tau\kappa T_\ell} & T \ll T_Z \ll T_\ell; \\ \frac{T_Z T}{4\pi\tau\kappa T_\ell} \times \ln\left(\frac{T}{T_Z}\right) & T_Z \ll T \ll T_\ell; \\ \frac{T_Z T}{4\pi\tau\kappa T_\ell} \times \ln\left(\frac{T_\ell}{T_Z}\right) & T_Z \ll T_\ell \ll T; \\ \frac{\pi\beta_{SO}^2 T^2}{24\tau\kappa T_Z} & T_\ell, T \ll T_Z; \\ \frac{T}{4\pi\kappa\tau} & T_\ell \ll T_Z \ll T. \end{cases} \quad (6.12)$$

Among all these regimes, only the asymptotic of $T \gg T_Z \gg T_\ell$ is dominated by ballistics, whose contribution can be written as

$$\tau_b^{-1} = \frac{2\varepsilon T_Z}{\hbar\kappa} \cdot f\left(\frac{T_M}{T}, \frac{T_m}{T}, \frac{T_\ell}{T}\right). \quad (6.13)$$

Here $T_{M,m}$ are temperature scales associated to energy-momentum conservation constrains, given by

$$T_{M,m} = \frac{4\varepsilon T_Z}{\epsilon_z} \left(\sqrt{\varepsilon/\epsilon_z} \pm \sqrt{\varepsilon/\epsilon_z - 1} \right)^2, \quad (6.14)$$

and the function $f(X, x, z)$ is defined as

$$f(X, x, z) \equiv \int_x^X \frac{dy}{2\pi} \frac{\frac{e^y + 1}{e^y - 1} \times e^{-\sqrt{z/y}}}{\sqrt{(y-x)(X-y)}}. \quad (6.15)$$

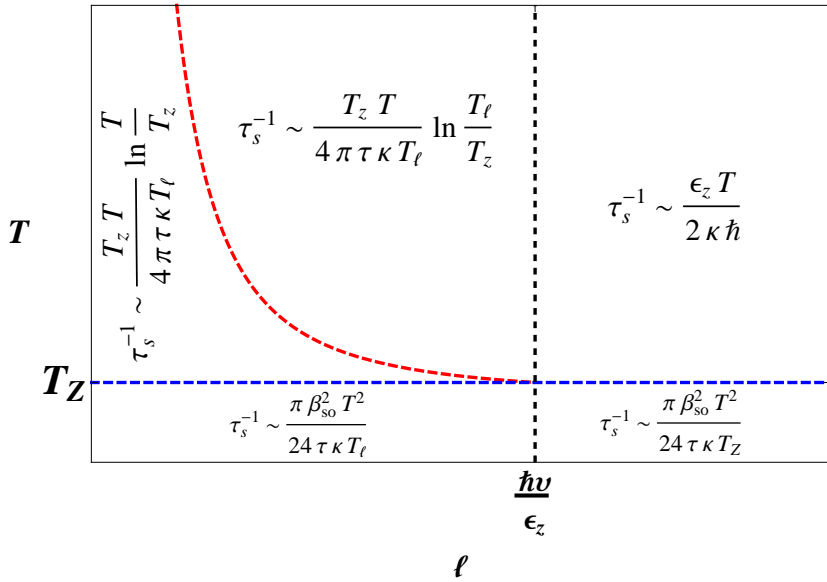


Figure 6.4: Spin relaxation induced by flexural phonons for different regimes of temperature and disorder. Red dashed line represents T_ℓ .

If $z \gg X, x$ then f is exponentially suppressed. When $z \ll X, x$ we have

$$f \approx \begin{cases} \sqrt{\frac{1}{Xx}} & X, x \ll 1; \\ \sqrt{\frac{1}{\pi X}} e^{-x} \text{Erf}(\sqrt{X-x}) & X, x \gg 1. \end{cases} \quad (6.16)$$

For $T > T_M > T_\ell$, we find that $\frac{\tau_b^{-1}}{\tau_d^{-1}} \sim 2\pi \frac{\tau \epsilon_z}{\hbar} \gg 1$, otherwise the ballistic contribution is exponentially small and the diffusive one dominates. Thus, having compared both contributions and combined them in $\tau_s^{-1} = \tau_d^{-1} + \tau_b^{-1}$, we summarize the resulting behaviors in Fig. 6.4.

6.4 Conclusions

We have derived the general form of the spin-lattice coupling in 2D hexagonal crystals. We distinguish two different contributions: the deflection coupling, whose origin is purely geometrical, and the spin-phonon coupling due to changes in the orbital composition of electronic Bloch states as result of out-of-plane displacements of the atoms in the crystal. We have applied this theory to the study of spin relaxation induced by static wrinkles and flexural phonon modes in MX_2 materials. We have analyzed both diffusive and ballistic contributions to spin relaxation, and studied its parametric dependence on external disorder (expressed in τ or alternatively ℓ), spin splitting of the occupied bands ϵ_z , and temperature in the case of phonons. Next, we try to perform numerical estimates in experimentally relevant situations.

In currently available MoS_2 -based devices, the mobilities extracted from transport experiments^[235-237] indicate that it is the diffusive contribution that limits spin lifetimes of electrons and holes in this material. The experimental situation in both cases is indicated on Fig. 6.3. For wrinkles with a typical height of 1 nm and lateral length scale of 10 nm, as reported in Ref. 253, and SOC splitting of $\epsilon_z = 3$ (140) meV for conduction (valence) bands respectively, we find

$$\tau_s^{-1} \approx \begin{cases} \frac{\epsilon_z^2 q^2 \langle \hbar^2 \rangle \tau}{\hbar^2} \sim 1 \text{ ns} & \text{for electrons,} \\ \frac{\beta_{SO}^2 \hbar^2 v^2 q^4 \langle \hbar^2 \rangle}{\epsilon_z^2 \tau} \sim 10 \text{ ns} & \text{for holes.} \end{cases} \quad (6.17)$$

In the case of holes we have taken $\beta_{SO}^2 = \frac{1}{16}$ (note that in addition the spin-phonon coupling Eq. (6.3)) should be included in β_{SO}^2).

For perfectly flat MoS₂, flexural vibrations thermally activated at room temperature would also produce spin relaxation. We describe a MoS₂ monolayer as a plate of thickness $\delta \approx 6.75$ Å, where δ is the inter-layer distance in bulk MoS₂.^[254] Then, we estimate the bending rigidity of a single layer as^[142]

$$\kappa = \frac{Y \delta^3}{24(1 - \sigma^2)} \approx 27 \text{ eV}, \quad (6.18)$$

where $Y = 0.33$ TPa is the Young modulus^[255] and $\sigma = 0.125$ is the Poisson ratio.^[256] Thus, for electrons we estimate $T_\ell \sim 10$ K and $T_Z \sim 10^{-3} T_\ell$, so for the spin relaxation time we have

$$\tau_s^{-1} \approx \frac{T_Z T}{4\pi\tau\kappa T_\ell} \ln\left(\frac{T_\ell}{T_Z}\right) \sim 5 \text{ ns}. \quad (6.19)$$

For holes, since $T_Z \sim 3000$ K, we estimate

$$\tau_s^{-1} \approx \frac{\pi\beta_{SO}^2 T^2}{24\tau\kappa T_Z} \sim 20 \text{ ns}. \quad (6.20)$$

The latter estimates are produced without taking into account that an atomically flat substrate will quench bending modes,^[257] so that we expect MoS₂-hBN structures to exhibit longer spin memory of charge carriers and therefore offer a perfect platform for spintronics devices. Regardless, the above estimates constitute the upper limit to spin lifetimes in MoS₂, and it can be extrapolated to other MX₂ systems by choosing the suitable values for the material dependent parameters.

PART 3:
NEW PLATFORMS FOR
TOPOLOGICAL PHASES

7

QSHE in MX_2 monolayers

7.1 Introduction

As we have seen in Chapters 1 and 2, the SOC may lead to a novel state of matter which resemble a TRI version of the QHE rather than a symmetry broken phase within the Landau's paradigm. We showed how graphene promised the perfect laboratory to explore this phenomena, however, the weakness of the SOC prevents the stabilization of such topological phase. Even so, MX_2 monolayers share a similar crystal structure and some common electronic properties, but with the big advantage of its much larger SOC, the microscopic basis for the emergence of TRI topological phases.

In this chapter, we present a proposal for engineering the QSHE in strained 2D crystals and heterostructures made using MX_2 materials. Strain is known to induce pseudo-magnetic fields in 2D crystals.^[258–261] These fields have been predicted^[259] and experimentally found^[260,261] to produce LLs in the electronic spectrum of graphene. As explained below, it is also possible to exploit these pseudo-magnetic fields to engineer TRI topological phases in other 2D crystals such as MX_2 monolayers.

This approach has several attractive features. Using MoS_2 as an example, we find that gaps between LLs scale as $\hbar\omega_c/k_B \simeq 2.7 B_0[T] \text{ K}$, where $B_0[T]$ is the strength of the pseudo-magnetic field in Tesla. In the case of graphene, fields $B_0[T] \sim 10 - 10^2$

It has been experimentally demonstrated,^[259–261] which in the case of MX_2 could lead to LL gaps of up to ≈ 100 K. A more accurate estimation should take into account the maximum tensile strength of these materials. We argue that LL gaps of 20 K can be realistically achieved in strained MoS_2 samples. By comparison, the gaps achievable by straining GaAs are in the range of tens of milli-Kelvin.^[135] However, in multi-valley systems like graphene, strain only leads to (spin) unpolarized LLs. What sets monolayers of MX_2 apart is the SOC that produces a large spin splitting of the valence (and to a smaller extent, the conduction) band due to the lack of a center of inversion in the crystal structure, as we have seen. For small doping, this leads to spin-polarized LLs in different valleys, which opens the possibility of realizing TRI topological phases. Furthermore, given that the valence and conduction band of MX_2 have strong d character, along with the poor screening of the Coulomb interaction in 2D, electron interactions can have interesting effects on properties of the topological phases realized in MX_2 monolayers.

Alternatively, we show how a superlattice can be used to create, within each valley, a band with non trivial topological properties. If we neglect trigonal warping, each valley has a fictitious time-reversal-like symmetry. This symmetry is broken by "gauge" terms proportional to σ_x and σ_y which can arise from strain or from virtual hopping processes to the substrate. A suitable combination of periodic scalar and a gauge potentials can^[262] separate the lowest leading subbands from the rest by opening a gap at the edges of the superlattice BZ, and give a total Chern number of ± 1 to the subbands arising at the \mathbf{K}_\pm valleys, respectively.

The chapter is organized as follows. In the first part we discuss the possibility of engineering a QSHE phase in strained MX_2 monolayer crystals. We infer how strain modifies the band structure of such materials from group theory and the simplified tight-binding model presented in Chapter 2. Then, we discuss the experimental consequences for a particular realization considering a pure shear strain configuration. In the second part, we speculate about the possibility of creating topologically non-trivial subbands with superlattice potentials.

7.2 QSHE created by strain

In this section we analyze the emergence of a QSHE state in strained MX_2 monolayers. We discuss first how strain affects the dynamics of electrons at \mathbf{K}_\pm valleys. Then, we show explicitly, for a pure shear strain configuration, how the system resembles a realization of the Bernevig-Zhang model for the QSHE,^[135] and we conclude with some general remarks on the experimental consequence and theoretical implications of the present proposal.

Irrep	TR Even	TR Odd
A'_1	$1, \sigma_z, \sum_{\alpha} u_{\alpha\alpha}$	-
A'_2	-	τ_z, s_z
E'	$(\sigma_x, \tau_z \sigma_y), (u_{xx} - u_{yy}, -2u_{xy})$	$(\tau_z \sigma_x, \sigma_y), \mathbf{p} = (p_x, p_y)$
E''	-	(s_x, s_y)

Table 7.1: Symmetry classification of the electronic operators within the 2 bands effective model and strain tensor components according to the irreps of D_{3h} and time reversal operation.

7.2.1 Strain in MX_2 monolayers

In order to turn a MX_2 monolayer into a TRI topological insulator, we consider the effect of strain on the band structure. As we have seen previously when discussing the electron-phonon coupling in graphene, in the theory of elasticity strain is described by a rank-2 tensor, $u_{ij} \approx \frac{1}{2}(\partial_i u_j + \partial_j u_i + \partial_i h \partial_j h)$, where $\mathbf{u} = (u_x, u_y, h)$ is the displacement of the unit cell in the long-wave length limit. In the present case, the three components of u_{ij} can be split according to irreps of D_{3h} as shown in Table 7.1. Thus, within the 2-bands effective model the coupling with strain reads

$$H_{\text{strain}} = \beta_0 t u_{ii} + \beta_1 t u_{ii} \sigma_z + \beta_2 t \left[(u_{xx} - u_{yy}) \sigma_x - 2u_{xy} \tau_z \sigma_y \right]. \quad (7.1)$$

The trace of the strain tensor generates scalar potentials of different strength in the valence and conduction bands. In addition, strain can be introduced in the 2-bands Hamiltonian as a minimal coupling $\mathbf{p} \rightarrow \mathbf{p} - e\mathbf{A}$ to a vector potential

$$e\mathbf{A} = \frac{\hbar\beta_2}{a} \tau \begin{pmatrix} u_{yy} - u_{xx} \\ 2u_{xy} \end{pmatrix}. \quad (7.2)$$

Here $\tau = \pm 1$ labels the valleys \mathbf{K}_{\pm} . The pseudo-magnetic field has opposite sign on different valleys, which is necessary as strain does not violate time reversal symmetry.

Microscopically, the origin of these couplings can be understood as the change in the hybridization between d orbitals from M atoms and p orbitals from X atoms due to the distortion of the lattice. Note that, additionally, in the case of the couplings with the trace of the strain tensor, $\beta_{0,1}$, the coupling is also affected by the deformation potential due to local changes of the area of the unit cell, which could be incorporated in a tight-binding description as changes in the associated crystal field parameters. However, being interested in the gauge field term, which is not affected by the deformation potential, we neglect these changes. Therefore, in our microscopic tight-binding model the phenomenological constants $\beta_{0,1,2}$ are related

with the Grüneisen parameters^[258] associated to the hopping amplitudes previously considered, $t_{x,y,z}$ (see Fig. 2.5). In order to see this, we repeat the calculation outlined in Chapter 2 by considering the change in the hopping integrals $t_{x,y,z}$ due to the displacement of the atoms. For the hopping integral between atoms at sites α, β we have

$$t_{\alpha\beta} \rightarrow t_{\alpha\beta} + \frac{\partial t_{\alpha\beta}}{\partial \mathbf{r}} (\mathbf{u}_\alpha - \mathbf{u}_\beta), \quad (7.3)$$

where $\mathbf{u}_{\alpha(\beta)}$ is the displacement of the atom at site α (β). For small displacements we can approximate

$$\mathbf{u}_\alpha - \mathbf{u}_\beta \approx \frac{a}{\sqrt{3}} (\hat{\delta}_{\alpha\beta} \cdot \vec{\partial}) \mathbf{u}. \quad (7.4)$$

In the spirit of the two-center Slater-Koster approximation, we assume that the hopping only depends on the distance between neighboring sites, $t_{\alpha\beta}(|\mathbf{r}|)$, as we did in the case of graphene. Then we have

$$\frac{\partial t_{\alpha\beta}}{\partial \mathbf{r}} \approx \frac{\partial t_{\alpha\beta}}{\partial a} \frac{\mathbf{r}}{|\mathbf{r}|} = \frac{\sqrt{3}}{a} t_{\alpha\beta} \beta_{\alpha\beta} \hat{\delta}_{\alpha\beta}, \quad (7.5)$$

where $\beta_{\alpha\beta} \equiv -\partial \ln |t_{\alpha\beta}| / \partial \ln a$ is the Grüneisen parameter associated to $t_{\alpha\beta}$. Therefore, in the the matrix elements we have to consider now

$$t_{x,y,z} \rightarrow t_{x,y,z} (1 + \beta_{x,y,z} \delta_i \delta_j u_{ij}), \quad (7.6)$$

where u_{ij} are the components of the strain tensor. By repeating the previous calculation at \mathbf{K}_τ we obtain the Hamiltonian in Eq. (7.1) with:

$$\begin{aligned} t\beta_0 &= \frac{3}{2} \left(\frac{c\beta_z t_z}{1 + |c|^2} - \frac{v(\beta_x t_x + \beta_y t_y)}{1 + |v|^2} \right), \\ t\beta_1 &= \frac{3}{2} \left(\frac{c\beta_z t_z}{1 + |c|^2} + \frac{v(\beta_x t_x + \beta_y t_y)}{1 + |v|^2} \right), \\ t\beta_2 &= \frac{3(c\beta_x t_x - c\beta_y t_y - v\beta_z t_z)}{4\sqrt{1 + |c|^2}\sqrt{1 + |v|^2}}. \end{aligned} \quad (7.7)$$

From now on, we focus on the effect of the gauge field term on holes.

7.2.2 Realization of the Bernevig-Zhang model

We assume that the system is doped with holes and therefore the Fermi level crosses the valence band. Integrating out the conduction band to leading order in Δ^{-1} yields

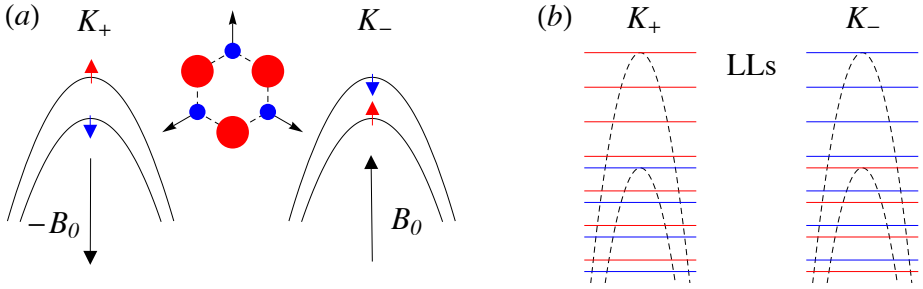


Figure 7.1: (a) Low-energy spectrum of a semiconducting transition metal dichalcogenide around the \mathbf{K}_{\pm} points of the BZ described by the continuum-limit Hamiltonian in Eq. (7.8). The inset shows the orientation of the stress tensor field discussed through the text with respect to the lattice. (b) Schematic representation of the Landau Levels (LLs) induced in the valence band when strain is applied.

at each valley

$$H_v^{(\tau)} = -\frac{\Pi_+^{(\tau)}\Pi_-^{(\tau)}}{2m^*} + U(\mathbf{r}) + \tau\lambda_{\text{SO}}s_z, \quad (7.8)$$

where $m^* = \Delta/2v^2 \simeq 0.5m_0$, $U(\mathbf{r}) = g(u_{xx} + u_{yy})$ with $g = t(\beta_0 - \beta_1)$, and

$$\Pi_{\pm}^{(\tau)} = (\tau p_x \pm ip_y) - e(\tau A_x \pm iA_y),$$

which obey the commutation relation $[\Pi_+^{(\tau)}, \Pi_-^{(\tau)}] = 2e\hbar\tau B(\mathbf{r})$, where $B(\mathbf{r}) = \partial_x A_y - \partial_y A_x$. Corrections of $\mathcal{O}(\Delta^{-2})$ are also obtained and can lead to mixing of the LLs, but they can be neglected as for typical parameters $\hbar\omega_c \lesssim 10^{-2}\Delta$.

In the absence of strain ($\mathbf{A} = U = 0$), Eq. (7.8) describes the Bloch states at the top of the valence band near \mathbf{K}_{\pm} points. Owing to the SOC, for small hole doping, $|\epsilon_F| \ll \lambda_{\text{SO}}$, the spin and valley quantum number of the holes are locked to each other, then only holes with either (\mathbf{K}_+, \uparrow) or $(\mathbf{K}_-, \downarrow)$ can exist, see Fig. 7.1. This feature is crucial for the realization of a TRI topological phase, as we argue below.

Applying a pure shear strain, then $u_{xx} + u_{yy} = 0$ ($U = 0$), and $u_{xx} = -u_{yy} = -Cy$, $u_{xy} = -Cx$, we have $B(\mathbf{r}) = \partial_x A_y - \partial_y A_x = -\tau B_0$, with

$$B_0 = \frac{4C\hbar\beta_2}{ea}.$$

We assume $C > 0$. The Hamiltonian in (7.8) can be diagonalized after introducing the operators

$$a_\tau = \frac{\Pi_-^{(\tau)}}{\sqrt{2e\hbar B_0}},$$

leading to

$$H^{(\tau)} = -\hbar\omega_c a_\tau^\dagger a_\tau + \tau\lambda_{\text{SO}}s^z, \quad (7.9)$$

where $\omega_c = eB_0/m^*$. As stated above, even for the largest achievable pseudo-magnetic fields ($B_0 \sim 10^2$ T) $\hbar\omega_c \ll \lambda_{\text{SO}}$, and therefore, provided $|\epsilon_F| \ll \lambda_{\text{SO}}$, LLs at different valleys are occupied by holes with opposite spin. The resulting model has been shown by Bernevig and Zhang^[135] to display the QSHE, meaning that the Hall conductivity σ_H^{xy} is zero but the spin-Hall conductivity σ_{SH}^{xy} is quantized in units of $e/2\pi$.

The strain configuration described above can be created by the methods described in Ref. 259. For a MX_2 flake under trigonal strain (see the inset in Fig. 7.1 (a)), one concern is the sample size. The latter is limited by the maximum tensile strength of the MX_2 crystals, T_{max} . The stress tensor σ_{ij} is related with the strain tensor by the thermodynamic relation $\sigma_{ij} = \left(\frac{\partial F}{\partial u_{ij}}\right)_T$. For pure shear strain, these relations read just $\sigma_{ij} = 2\mu u_{ij}$. Considering a circular geometry for simplicity, the previous strain configuration can be achieved by applying a tension on the border of the form $\mathbf{T} = -\mu CL(\sin 2\theta, \cos 2\theta)$, where L is the diameter. From the above thermodynamic relations we estimate the maximum diameter L where this strain configuration can be performed before breaking the crystal, $L = \frac{T_{\text{max}}}{\mu C}$. The values of $T_{\text{max}} \simeq 16.5$ N/m and $\mu \simeq 50.4$ N/m can be obtained from DFT calculations.^[263] The latter is estimated from the Young's modulus $E = 130$ N/m and Poisson's ratio $\nu = 0.29$ as $\mu = \frac{E}{2(1+\nu)}$. This yields a relation between the maximum pseudo-magnetic field (in Tesla) and the sample size L in μm : $B_0[T] \approx 8/L[\mu\text{m}]$. Using $\hbar\omega_c/k_B = 2.7B_0[T]$ and taking $L \approx 1 \mu\text{m}$, we estimate $\hbar\omega_c/k_B \simeq 20$ K for MoS_2 .

For small strained MX_2 flakes, it is necessary to take into account the effect of an inhomogeneous pseudo-magnetic field resulting from a non-uniform strain distribution. In this regard, we note that the lowest LL eigenfunctions are null eigenvectors of $\Pi_-^{(\tau)}$,

$$\Pi_-^{(\tau)}\psi(\mathbf{r}) = 0. \quad (7.10)$$

Therefore, following Ref. 264, we write $\mathbf{A}(\mathbf{r}) = \tau(\hat{z} \times \nabla\chi(\mathbf{r}) + \nabla\phi(\mathbf{r}))$, which allows to solve Eq. (7.10) as

$$\psi(\mathbf{r}) = f(x, y)e^{\frac{2\pi}{\Phi_0}(\chi(\mathbf{r}) + i\tau\phi(\mathbf{r}))}. \quad (7.11)$$

From Eq. (7.10) we see that $f(x, y)$ satisfies the equation $(\partial_x - i\tau\partial_y)f(x, y) = 0$, therefore $f(x, y) \equiv f(x - i\tau y)$ is an entire function (anti-holomorphic at valley \mathbf{K}_+ , holomorphic at valley \mathbf{K}_-). Since $(\partial_x^2 + \partial_y^2)\chi = \tau B(\mathbf{r}) = -B_0(\mathbf{r})$, and the fundamental solution (propagator) of the Laplacian in 2D is $\ln|\mathbf{r}|/2\pi$, we have

$$\chi(\mathbf{r}) = - \int \frac{d\mathbf{r}'}{2\pi} \ln(|\mathbf{r} - \mathbf{r}'|) B_0(\mathbf{r}'). \quad (7.12)$$

Asymptotically, $\chi(\mathbf{r}) \sim -\frac{\Phi}{2\pi} \ln(|\mathbf{r}|)$ as $|\mathbf{r}| \rightarrow \infty$, and therefore $\psi(\mathbf{r}) \sim f(x - i\tau y) |\mathbf{r}|^{-\frac{\Phi}{\Phi_0}}$, where $\Phi = \int d\mathbf{r} B_0(\mathbf{r}) > 0$ is the total flux, assumed to be positive in consistency with the previous choice of $C > 0$, and $\Phi_0 = h/e$ is the flux quantum. Thus, we conclude that $f(z)$ is a polynomial of maximum degree $N = [\Phi/\Phi_0]$. Hence, the wave-function describing $N_\uparrow = N_\downarrow = N$ (non-interacting) electrons in the lowest LL read^[264,265]

$$\Phi_0(\{\mathbf{r}_{i\tau}\}) = e^S \prod_{i < j} (z_{i+}^* - z_{j+}^*)(z_{i-} - z_{j-}), \quad (7.13)$$

where $S(\{\mathbf{r}_{i\tau}\}) = \frac{2\pi}{\Phi_0} \sum_{i=1, \tau=\pm 1}^N [\chi(\mathbf{r}_{i\tau}) + i\tau\phi(\mathbf{r}_{i\tau})]$.

Larger sample sizes can be achieved by other methods such in 2D crystal bubbles.^[259–261] A periodic array of such bubbles will lead to periodic modulation of strain and pseudo-magnetic field, which allows to create topologically non-trivial band structures.^[259,266]

7.2.3 Experimental consequences

Next, we discuss some experimental consequences of our predictions. For the previous strain configuration, the wave-function for spin $+1/2$ holes (at valley \mathbf{K}_+), apart from the confining factor, is anti-holomorphic as discussed previously, therefore, their Hall conductivity is expected to be quantized in units of $-e^2/h$. For spin $-1/2$ holes at the opposite valley, the wave-function is holomorphic, so the Hall conductivity is quantized in units of $+e^2/h$. Both contributions are cancelled out, but the spin Hall conductivity is expected to be quantized in units of $-e/2\pi$. However, if the total s_z is not a good quantum number this picture is not longer valid and the spin Hall conductivity is not exactly quantized. Instead, charge transport through the (helical) edge channels provides a clearer signature of existence of a topological phase.^[137,267]

Nevertheless, we must be careful in qualifying the strained 2D crystal as a topological insulator for arbitrary LL filling. This is because adatoms, the substrate, a

perpendicular electric field, out of plane deformations, etc. break the mirror symmetry about the 2D crystal plane, which induces a Bychkov-Rashba SOC as we have seen, leading to spin-flip processes and therefore the possibility of backscattering between counter-propagating edge channels. For an odd number of occupied LLs, an odd number of Kramers' pairs of edge modes cross the Fermi energy and, for weak to moderate electron-electron interactions, the integrity of at least one Kramers' pair of edge modes against TRI perturbations is always ensured.^[268,269] Thus, for $2n + 1$ (with n integer) occupied LLs, the system is a protected topological phase and a two-terminal measurement of the conductance will yield at least $-2e^2/h$ and at most $-2(2n + 1)e^2/h$, depending of degree of edge disorder and other s_z non-conserving perturbations.

On the other hand, if the number of occupied LLs is even ($= 2n$), there will an even number of pairs of edge modes crossing the Fermi level and this situation is no longer protected against Bychkov-Rashba-type disorder potential^[268,269] (although edge modes survive for strong enough electron-electron interactions^[268,269]). However, in sufficiently clean samples and provided that interactions are weak, quantized conductance of $4ne^2/h$ may be observable. Furthermore, the existence of bulk LLs can be detected by means of scanning tunneling microscopy as in the case of graphene.^[260,261]

Finally, let us discuss the possible effect of interactions. The strong d character of the valence and conduction bands means that electron correlations can have a important effect on the topological phases, especially on the edge states.^[268,269,271] Indeed, for MoS_2 the short-range part of the interaction (the Hubbard U) has been estimated in Ref. 270 to be $U \sim 2 - 10$ eV. Thus, MoS_2 may present a scenario comparable to the Iridates.^[271] However, the QSH effect in the MX_2 monolayers may allow for a more complete understanding of the interplay between electron correlation and QSH physics, since correlation effects decrease as the metal atom M is varied from the $4d$ series (as in MoS_2) to $5d$ series (as in WS_2).

7.3 Alternative route: superlattice potentials

In this section we show how a superlattice can be used to induce subbands with topological properties in a doped MX_2 monolayer. We approximate the bands of the homogeneous system by the 2 bands effective Hamiltonian, whose eigenvalues and

eigenfunctions read (around valley \mathbf{K}_{\pm})

$$\begin{aligned}\epsilon_{\mathbf{k}} &= \pm \sqrt{\frac{\Delta^2}{4} + (v|\mathbf{k}|)^2}, \\ |\mathbf{k}+\rangle &= \begin{pmatrix} \cos\left(\frac{\theta_{\mathbf{k}}}{2}\right) \\ \sin\left(\frac{\theta_{\mathbf{k}}}{2}\right) e^{i\phi_{\mathbf{k}}} \end{pmatrix}, \\ |\mathbf{k}-\rangle &= \begin{pmatrix} \sin\left(\frac{\theta_{\mathbf{k}}}{2}\right) \\ -\cos\left(\frac{\theta_{\mathbf{k}}}{2}\right) e^{i\phi_{\mathbf{k}}} \end{pmatrix},\end{aligned}\quad (7.14)$$

where $\theta_{\mathbf{k}} = \arctan[2v_F|\mathbf{k}|/\Delta]$ and $\phi_{\mathbf{k}} = \arctan(k_y/k_x)$. The \pm signs correspond to conduction and valence bands respectively.

A superlattice potential hybridizes states $|\mathbf{k}\rangle$ and $|\mathbf{k}+\mathbf{G}\rangle$ where the vectors \mathbf{G} define the superlattice. We consider the six lowest vectors \mathbf{G} , see Fig. 7.2, with $|\mathbf{G}| = (4\pi)/(\sqrt{3}L)$, where $L = Na$ is the lattice constant of the $N \times N$ superlattice. We assume that $v|\mathbf{G}| \ll \Delta$ and that the superlattice potential, $V_{\mathbf{G}}$, is such that $V_{\mathbf{G}} \ll (v|\mathbf{G}|)^2/(2\Delta)$, so that perturbation theory in $V_{\mathbf{G}}$ applies. We also assume that the lattice potential is sufficiently smooth, $|\mathbf{G}| \ll |\mathbf{K}_+ - \mathbf{K}_-|$, where \mathbf{K}_{\pm} are the corners of the original BZ of the MX_2 lattice, and neglect intervalley scattering. Therefore, we focus the discussion on a single valley.

Using first order perturbation theory, each set of three points at one valley connected by superlattice reciprocal vectors, $\kappa = \{\kappa_1, \kappa_2, \kappa_3\}$ and $\kappa' = \{\kappa'_1, \kappa'_2, \kappa'_3\}$ points, leads to a 3×3 matrix of the form

$$\mathcal{H}_{\kappa, \kappa'} \equiv \begin{pmatrix} \epsilon_{\kappa, \kappa'} \pm \bar{v}k_x & V_{\kappa, \kappa'} & V_{\kappa, \kappa'}^* \\ V_{\kappa, \kappa'}^* & \epsilon_{\kappa, \kappa'} \pm \bar{v} \left(-\frac{k_x}{2} + \frac{\sqrt{3}k_y}{2} \right) & V_{\kappa, \kappa'} \\ V_{\kappa, \kappa'} & V_{\kappa, \kappa'}^* & \epsilon_{\kappa, \kappa'} \pm \bar{v} \left(-\frac{k_x}{2} - \frac{\sqrt{3}k_y}{2} \right) \end{pmatrix}, \quad (7.15)$$

where $\epsilon_{\kappa, \kappa'} = \epsilon_0 = (v|\kappa|)^2/\Delta$, $\bar{v} \approx (2v^2|\kappa|)/\Delta$, and the two signs correspond to the κ and κ' points respectively. For $V_{\kappa, \kappa'} = |V_{\kappa, \kappa'}| e^{i\phi_{\kappa, \kappa'}}$, the energies and eigenfunctions

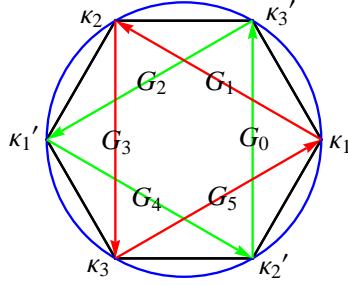


Figure 7.2: Sketch of the effect of the BZ in a superlattice, and states mixed by the superlattice potential.

at the κ and κ' points in the basis used to write Eq. (7.15) are:

$$\begin{aligned}
 \epsilon_a &= \epsilon_0 + 2 |V_{\kappa, \kappa'}| \cos(\phi_{\kappa, \kappa'}) & |a\rangle &= \frac{1}{\sqrt{3}} (|1\rangle + |2\rangle + |3\rangle) \\
 \epsilon_b &= \epsilon_0 + 2 |V_{\kappa, \kappa'}| \cos\left(\frac{2\pi}{3} + \phi_{\kappa, \kappa'}\right) & |b\rangle &= \frac{1}{\sqrt{3}} (|1\rangle + e^{2\pi i/3} |2\rangle + e^{-2\pi i/3} |3\rangle) \\
 \epsilon_c &= \epsilon_0 + 2 |V_{\kappa, \kappa'}| \cos\left(\frac{4\pi}{3} + \phi_{\kappa, \kappa'}\right) & |c\rangle &= \frac{1}{\sqrt{3}} (|1\rangle + e^{-2\pi i/3} |2\rangle + e^{2\pi i/3} |3\rangle)
 \end{aligned} \tag{7.16}$$

In the case of $\phi_{\kappa, \kappa'} = 0, \pi$, then $V_{\kappa, \kappa'}$ real, an expansion in powers of $|\mathbf{k}|$ shows that states $|b\rangle$ and $|c\rangle$ define an effective 2×2 Dirac Hamiltonian with velocity $\bar{v}/2$. The degeneracy of these Dirac points is lifted for complex values of $V_{\kappa, \kappa'}$. The problem is equivalent to a gapped Dirac equation with gap $\Delta_{\kappa, \kappa'} = 2\sqrt{3}|V_{\kappa, \kappa'}| \sin(\phi_{\kappa, \kappa'})$, with $\phi_{\kappa, \kappa'}$ defined mod $2\pi/3$. If ϕ_{κ} and $\phi_{\kappa'}$ have different signs, the two gaps also have opposite signs, leading to a lowest subband with a Chern number equal to 1. This is a realization of Haldane's model.^[131]

The superlattice potential is a 2×2 matrix in the space span by conduction and valence band states, and can be divided into scalar, mass and vector components, which, in turn, can be even or odd under spatial inversion. Following Ref. 272 we define the functions:

$$\begin{aligned}
 f_1(\mathbf{r}) &= \sum_{m=0\dots5} e^{i\mathbf{G}_m \cdot \mathbf{r}}, \\
 f_2(\mathbf{r}) &= i \sum_{m=0\dots5} (-1)^m e^{i\mathbf{G}_m \cdot \mathbf{r}}.
 \end{aligned} \tag{7.17}$$

Then, we can construct the inversion-symmetric superlattice potentials as

$$\begin{aligned} V_s &= v |\mathbf{G}| \Delta_s f_1(\mathbf{r}), \\ V_m &= v |\mathbf{G}| \Delta_m f_1(\mathbf{r}) \sigma_z, \\ V_g &= v \Delta_g (\sigma_x, \tau_z \sigma_y) \cdot (\hat{\mathbf{z}} \times \nabla) f_2(\mathbf{r}). \end{aligned} \quad (7.18)$$

The coefficients $\Delta_{s,m,g}$ in these expressions are dimensionless phenomenological constants with the energy scale set by $v |\mathbf{G}| = \frac{4\pi t}{\sqrt{3}N}$.

We focus on valence band states. The scalar potential has matrix elements

$$\begin{aligned} \langle \mathbf{k} + \mathbf{G}_m | V_s | \mathbf{k} \rangle &= v |\mathbf{G}| \Delta_s \left[\sin \left(\frac{\theta_{\mathbf{k} + \mathbf{G}_m}}{2} \right) \sin \left(\frac{\theta_{\mathbf{k}}}{2} \right) + \right. \\ &\quad \left. + \cos \left(\frac{\theta_{\mathbf{k} + \mathbf{G}_m}}{2} \right) \cos \left(\frac{\theta_{\mathbf{k}}}{2} \right) e^{i(\phi_{\mathbf{k}} - \phi_{\mathbf{k} + \mathbf{G}_m})} \right], \end{aligned} \quad (7.19)$$

and equivalently for the mass potential,

$$\begin{aligned} \langle \mathbf{k} + \mathbf{G}_m | V_m | \mathbf{k} \rangle &= v |\mathbf{G}| \Delta_m \left[\sin \left(\frac{\theta_{\mathbf{k} + \mathbf{G}_m}}{2} \right) \sin \left(\frac{\theta_{\mathbf{k}}}{2} \right) - \right. \\ &\quad \left. - \cos \left(\frac{\theta_{\mathbf{k} + \mathbf{G}_m}}{2} \right) \cos \left(\frac{\theta_{\mathbf{k}}}{2} \right) e^{i(\phi_{\mathbf{k}} - \phi_{\mathbf{k} + \mathbf{G}_m})} \right]. \end{aligned} \quad (7.20)$$

The edges of the first subband are determined by the shifts in the energies of the corners of the superlattice BZ. We assume that $|\mathbf{k}| = |\mathbf{k} + \mathbf{G}_m| = \kappa = (4\pi)/(3Na)$, hence,

$$\langle \mathbf{k} + \mathbf{G}_m | V_{s,m} | \mathbf{k} \rangle \approx \pm v |\mathbf{G}| \Delta_{s,m} e^{i(\phi_{\mathbf{k}} - \phi_{\mathbf{k} + \mathbf{G}_m})} \left[1 - \frac{v^2 \kappa^2}{\Delta^2} \left(1 \mp e^{i(\phi_{\mathbf{k} + \mathbf{G}_m} - \phi_{\mathbf{k}})} \right) \right]. \quad (7.21)$$

For the gauge potential we have

$$\begin{aligned} \langle \mathbf{k} + \mathbf{G}_m | V_g | \mathbf{k} \rangle &= i (-1)^m v |\mathbf{G}| \Delta_g \left[\cos \left(\frac{\theta_{\mathbf{k} + \mathbf{G}_m}}{2} \right) \sin \left(\frac{\theta_{\mathbf{k}}}{2} \right) e^{i(\phi_{\mathbf{G}_m} - \phi_{\mathbf{k} + \mathbf{G}_m})} - \right. \\ &\quad \left. - \sin \left(\frac{\theta_{\mathbf{k} + \mathbf{G}_m}}{2} \right) \cos \left(\frac{\theta_{\mathbf{k}}}{2} \right) e^{i(\phi_{\mathbf{k}} - \phi_{\mathbf{G}_m})} \right] \approx \\ &\quad (-1)^{m+1} \frac{2v\kappa}{\Delta} v |\mathbf{G}| \Delta_g e^{i \frac{\phi_{\mathbf{k}} - \phi_{\mathbf{k} + \mathbf{G}_m}}{2}} \cos \left(\frac{m\pi}{3} - \frac{\phi_{\mathbf{k}} + \phi_{\mathbf{k} + \mathbf{G}_m}}{2} \right). \end{aligned} \quad (7.22)$$

The same can be done with the inversion-asymmetric superlattice potentials, defined as

$$\begin{aligned}\tilde{V}_s &= v |\mathbf{G}| \tilde{\Delta}_s f_2(\mathbf{r}), \\ \tilde{V}_m &= v |\mathbf{G}| \tilde{\Delta}_m f_2(\mathbf{r}) \sigma_z, \\ \tilde{V}_g &= v \tilde{\Delta}_g (\sigma_x \tau_x \sigma_y) \cdot (\hat{\mathbf{z}} \times \nabla) f_1(\mathbf{r}).\end{aligned}\quad (7.23)$$

By repeating the same calculation we obtain

$$\begin{aligned}\langle \mathbf{k} + \mathbf{G}_m | \tilde{V}_{s,m} | \mathbf{k} \rangle &\approx \pm i (-1)^m v |\mathbf{G}| \tilde{\Delta}_{s,m} e^{i(\phi_{\mathbf{k}} - \phi_{\mathbf{k} + \mathbf{G}_m})} \left[1 - \frac{v^2 \kappa^2}{\Delta^2} \left(1 \mp e^{i(\phi_{\mathbf{k} + \mathbf{G}_m} - \phi_{\mathbf{k}})} \right) \right], \\ \langle \mathbf{k} + \mathbf{G}_m | \tilde{V}_g | \mathbf{k} \rangle &\approx i \frac{2v\kappa}{\Delta} v |\mathbf{G}| \tilde{\Delta}_g e^{i \frac{\phi_{\mathbf{k}} - \phi_{\mathbf{k} + \mathbf{G}_m}}{2}} \cos \left(\frac{m\pi}{3} - \frac{\phi_{\mathbf{k}} + \phi_{\mathbf{k} + \mathbf{G}_m}}{2} \right).\end{aligned}\quad (7.24)$$

From this analysis it is clear that inversion-asymmetric potentials are needed in order to induce a topological subband structure. To the leading order in $v\kappa/\Delta$, considering scalar potentials only, we have

$$\begin{aligned}V_{\kappa} &= \langle \kappa_1 = \kappa_2 + \mathbf{G}_4 | V_s + \tilde{V}_s | \kappa_2 \rangle = v |\mathbf{G}| e^{\frac{i2\pi}{3}} (\Delta_s + i\tilde{\Delta}_s), \\ V_{\kappa'} &= \langle \kappa'_1 = \kappa'_2 + \mathbf{G}_1 | V_s + \tilde{V}_s | \kappa'_2 \rangle = v |\mathbf{G}| e^{\frac{i2\pi}{3}} (\Delta_s - i\tilde{\Delta}_s).\end{aligned}\quad (7.25)$$

So $V_{\kappa, \kappa'} = v |\mathbf{G}| \sqrt{\Delta_s^2 + \tilde{\Delta}_s^2} \times e^{\frac{i2\pi}{3} \pm i \arctan(\frac{\tilde{\Delta}_s}{\Delta_s})}$. Hence, the gap is $\Delta_{\kappa, \kappa'} = \pm 2\sqrt{3}v |\mathbf{G}| \tilde{\Delta}_s$. The highest valence subbands derived from the bands at the spin polarized valley \mathbf{K}_+ in the band structure of the MX_2 monolayer have a Chern number $C_{\uparrow} = 1$. This Chern number is compensated by the opposite value from the other valley \mathbf{K}_- due to time-reversal symmetry, $C_{\downarrow} = -1$. Therefore, $C_s = (C_{\uparrow} - C_{\downarrow})/2 = 1$, so the system is effectively a realization of the Kane-Mele model.^[37]

7.4 Conclusions

We propose to engineer TRI topological insulators in monolayers of MX_2 taking advantage of the huge SOC provided by transition metal atoms and the lack of an inversion center in the crystal structure. At low doping, monolayers of MX_2 under shear strain will develop spin-polarized Landau levels residing in different valleys with opposite spin polarization. As a result, the edge transport becomes quantized, which can be probed in multi-terminal devices using strained 2D crystals of these materials. The strong d character of valence and conduction bands may also allow for the investigation of the effects of electron correlations on the topological phases.

Alternatively, we propose to employ superlattice potentials in order to create subbands with topological properties. This approach, which relies on an effective periodic magnetic field with zero average, leads to a Quantum Hall insulator^[273] in the absence of a global magnetic flux.^[131] The periodicity of the potential should be such that the width of the subbands is smaller than the spin splitting in each valley. Large enough periodicities where subbands can be resolved have been achieved for graphene on Boron Nitride.^[274–277] Finally, note that a different scheme leading to the QSH effect based on a Moiré pattern in a single valley semiconductor like GaAs has been recently suggested in Ref. 278.

8

Electronic confinement in graphene due to spatially varying SOC

8.1 Introduction

The electronic band structure of a material may acquire interesting topological properties in the presence of a magnetic field, or due to the SOC as we have already seen. At the same time, hybrid structures made up of different two dimensional layers can have properties different from each of their components. In this chapter we study graphene on iridium (Ir), with islands of an ordered lead (Pb) monolayer intercalated between graphene and the Ir surface. Experiments performed by the group of Rodolfo Miranda show that, while the graphene layer is structurally unaffected by the presence of the Pb layer, its electronic properties change dramatically, appearing regularly spaced resonances in the local density of states (LDOS).

The linear dispersion of the graphene bands allows for the existence of a variety of mechanisms which can induce gauge fields^[258, 279–281] other than strains. Hopping between two graphene layers, for instance, can be formulated as a non abelian field,^[281] and this approach can be generalized in a straightforward way to the Bychkov-Rashba SOC in graphene. We show in this chapter that the existence of a strong and non

uniform SOC is consistent with the existence of sharp resonances observed experimentally. Electrons from graphene tunneling through the Pb atoms can feel the large SOC characteristic of these heavy atoms.^[282] A non-uniform spatial change of the strength of the SOC generated by going from the Pb intercalated graphene to the one directly grown on Ir leads to a spatial modulation of the non-abelian gauge field, which, in turn, leads to a pseudo magnetic field confining Dirac electrons. We argue that the peaks present at the STS spectra are, thus, due to electronic confinement induced by spatially varying SOC fields. In spite of the local character of SOC, the effect is detected at long distances from the physical edge of the Pb-intercalated islands. Note that the gauge fields associated to the SOC are more complex than the abelian field induced by strains, leading to novel structures not observable in real magnetic fields or in the presence of strains.

The structure of the chapter is the following: first of all, we summarize the experimental results that we try to explain with our theory. Then, we present the model and the tight-binding calculations which qualitatively agree with the experiments, and finally we comment on additional implications of the theory.

8.2 STM/STS experiments on graphene on Ir(111) with intercalated Pb

Graphene can be grown on Ir(111) by CVD techniques, in this case by direct decomposition of 8×10^{-8} Torr of ethylene at 1000 °C on the Ir surface as explained in Refs. 283, 284. The bonding between graphene and Ir(111) is weak. The graphene overlayer presents a well known incommensurate 9.3×9.3 moiré superstructure, see Fig. 8.1, with a small corrugation of 20 pm,^[285] arising from the lattice mismatch with respect to the iridium substrate. In addition, the graphene overlayer is weakly p-doped by charge transfer to the substrate with the Dirac energy at +100 meV (above the Fermi level), and it displays the conical band dispersion characteristic of free standing graphene.

Intercalation of Pb under the graphene monolayer is achieved by evaporating Pb onto the graphene/Ir(111) sample kept at 800 K. The graphene/Ir regions present a hexagonal network that corresponds to the already mentioned moiré pattern, whereas the intercalated regions present a negligible corrugation. Some Pb intercalated islands appear in the terraces (frequently close to graphene wrinkles), but most of them are located at the step edges. The Pb coverage has been selected so that the lateral size of the islands ranges from 5 to 15 nm and their average separation from 20 to 40 nm. The thickness of Pb intercalated below graphene is strictly one monolayer, according to the measured apparent height of the islands.

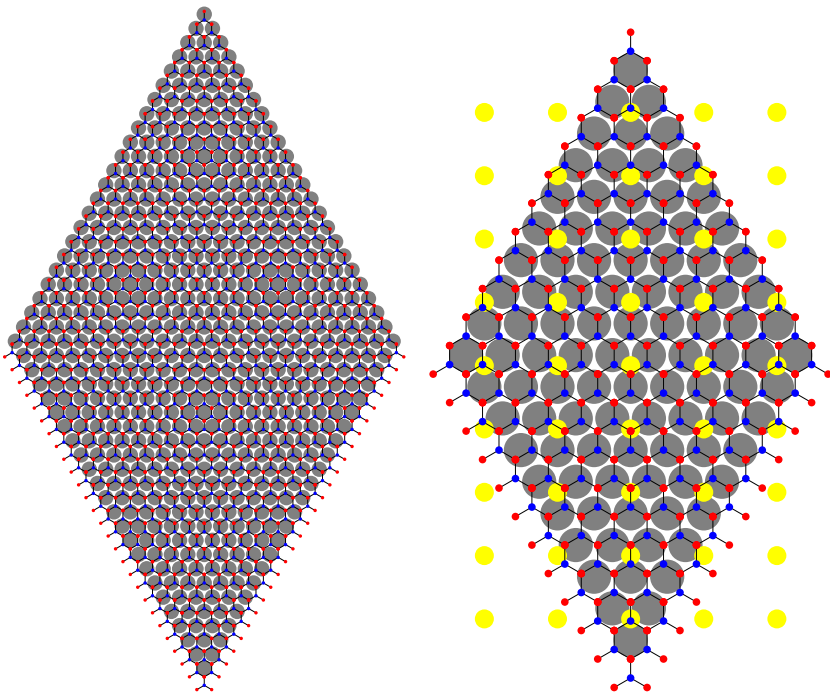


Figure 8.1: Left: 9.3×9.3 moiré structure formed by graphene grown directly on Ir(111). Right: Original moiré unit cell in the intercalated region where the atoms in yellow correspond to the Pb atoms.

According to Low Energy Electron Diffraction (LEED) patterns and Fourier Transforms of large scale atomically resolved STM images, neither graphene nor iridium lattice parameters change upon lead intercalation, so that the 9.3×9.3 moiré pattern is maintained. In the interlayer Pb atoms form a rectangular lattice commensurate with Ir and, therefore, incommensurate with graphene, see Fig. 8.1. The Dirac point for the Pb intercalated graphene can be estimated to be at $\pm 110 \pm 20$ meV according to the diameter of the inter-valley scattering half-moon rings observed in the STM Fourier Transforms. The density of Pb atoms in the intercalated layer is relatively high, i.e. $1/7$ of the density of carbon atoms in graphene.

The LDOS at the graphene regions intercalated with Pb was measured locally by STS at 4.6 K. The differential conductance spectrum measured on a 10 nm-wide Pb intercalated island that appears in Fig. 8.2 (red cross on panel A and red curve on panel C) shows up to 10 clearly defined, intense and sharp peaks in a ~ 3 eV wide region. The (rather featureless) spectra recorded on the pristine graphene/Ir(111) surface do not show this series of sharp states. Plotting the estimated Dirac point at -110 meV below the Fermi energy (orange line in Fig. 8.2, the Pb-intercalated graphene is slightly n-doped), the peaks appear to be symmetrically distributed above and below it. The separation between peaks is nearly constant, $\Delta \sim 340$ meV. The effect is observed in all graphene/Pb islands, and it is robust, independent of the detailed shape of the Pb islands and of the defects present at the edges (or interior) of the islands. The peaks can be clearly detected even at 80 K.

The recorded STS spectra when going from the Pb intercalated graphene region (red cross on panel A and red curve on panel C) into the graphene/Ir area (blue cross on panel A and blue curve on panel C) show that all the peaks shift, essentially in a rigid fashion. The quantized levels (labelled from 1 to 6 starting at the Dirac point) appear in both regions with the same energy separation, $\Delta \sim 340$ meV, but shifted in energy by near 200 meV, which is close to the difference in Dirac energy between both regions (-110 meV for gr/Pb and +100 meV for gr/Ir). The smooth shift of the quantized levels can be clearly seen in the central part of panel C, where we show (in inverted grey scale) the spatial map of the dI/dV intensity along the green arrow of panel A. The shift follows strictly the variation of the Dirac point when moving between the two regions (in fact there is an exception, namely the unlabelled peak between peaks 5 and 6 that shifts by near 300 meV). All the peaks are clearly visible even at 10 nm away from the physical edge of the Pb island into the gr/Ir region (i.e. at the position signalled by the blue cross). Fig. 8.2 D shows the energy position of the quantized levels as a function of their quantum number, n . A lineal dependence that intersects at the respective Dirac points is evident for both graphene/Pb/Ir(111) and graphene/Ir(111) data sets.

8.2 STM/STS experiments on graphene on Ir(111) with intercalated Pb

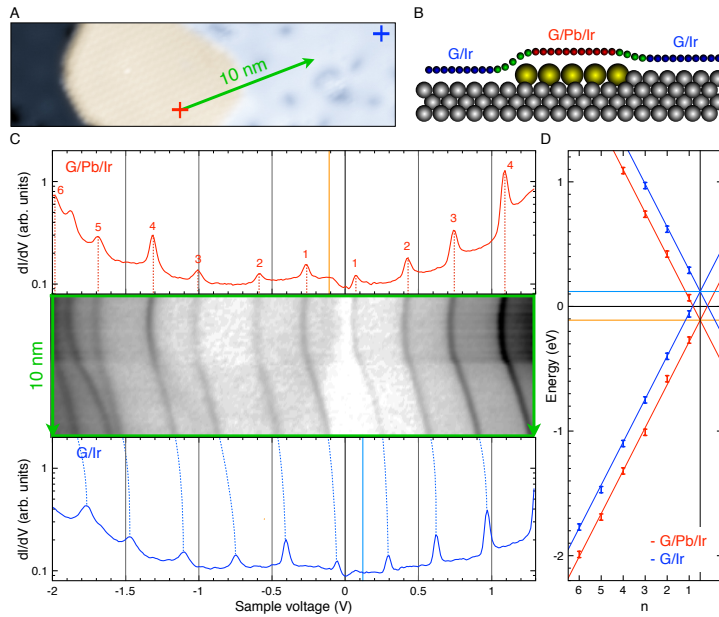


Figure 8.2: Courtesy of Fabián Calleja. A) STM topograph over a graphene/Pb/Ir area located next to a monoatomic step of the Ir(111) substrate. B) Schematic model of the atomic arrangement on the Pb intercalated island. C) Differential conductivity of graphene/Pb/Ir(111) (in red) and graphene/Ir(111) (in blue) at the points indicated by the crosses in panel A. The dI/dV intensity map recorded along the highlighted line in panel A is shown between the spectra at the extremes. D) Energy positions of the peaks as a function of the assigned quantum number n .

8.3 Phenomenological model

The sharp resonances described in the previous section imply the existence of quasi-localized states. The scale of the confinement can be inferred from the gaps Δ between resonances, $\ell \approx v_F/\Delta \approx 2\text{-}3$ nm. The confinement of electrons in graphene by potential energy barriers (e.g. at the island edges) over lengths much greater than the interatomic distance is prevented by the Klein tunneling associated to the chirality of the wavefunctions, and localized states are typically only found in the presence of defects at the Dirac energy. Furthermore, although the n-p barriers (≈ 200 meV) at the interfaces between graphene/Pb/Ir(111) and graphene/Ir(111) can confine electrons it is hard to imagine that the confinement can extend to states that have energies of several electron volts as observed here. On the other hand, the confinement could be associated to the out-of-plane direction, however, steps instead of sharp resonance peaks are expected in that case.

As we have seen, the most common sources of confinement at arbitrary energies are gauge fields. The effective magnetic field required to generate the observed gaps is $B(\text{T}) \approx (25/\ell(\text{nm}))^2 \approx 80 - 100$ T. The graphene layer studied here does not show appreciable strains, however. If we assume that the observed confinement is induced by a varying strain which changes by \bar{u} over a distance of the order of the size of the Pb island, $R \approx 10$ nm, we obtain $\bar{u} \approx aR/(\beta\ell^2) \approx 0.05 - 0.2$, $t \approx 3$ eV is the hopping between nearest neighbors atoms and β the Gruneisen parameter previously introduced. The graphene layer studied here is flat and uniform, and there is no hint of strains like the ones estimated earlier.

On the other hand, the spin-flipping SOC terms can be interpreted as non-abelian gauge fields. Electrons tunneling from graphene to Pb monolayer and back feel the enormous SOC characteristic of this material. The SOC is a very local interaction, however, for irregular shapes of the Pb islands we expect that the strength of the SOC decays smoothly from the center with a characteristic length determined by the size of the islands.

As we mentioned in the previous chapter in the case of the 2 bands effective model for MX_2 monolayers, superlattice perturbations enter in the $\mathbf{k} \cdot \mathbf{p}$ Hamiltonian around \mathbf{K}_\pm points as scalar ($\sim \mathcal{S}$), mass ($\sim \sigma_z$) and gauge potentials ($\sim (\sigma_x, \pm\sigma_y)$). Since we assume that the Pb layer induces a strong SOC in graphene, manifesting as spin-dependent superlattice potentials, now we must take into account, additionally, $s_{x,y,z}$ operators acting on the spinorial part of the wave function. We deduce the form of such potentials from group theory arguments.

The point group of graphene on an incommensurate substrate is the intersection of the original hexagonal group C_{6v} with the point group of the substrate. In this case,

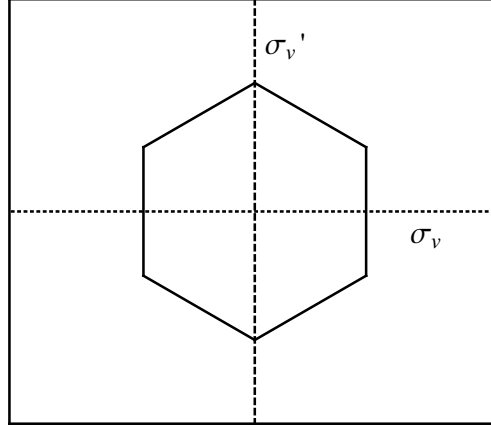


Figure 8.3: Unit cells of the hexagonal (C_{6v}) graphene crystal and rectangular (orthorhombic, C_{2v}) substrate of Pb atoms.

Irrep	TR Even	TR Odd
A_1	σ_x	-
A_2	-	s_z
B_1	-	τ_z, s_y
B_2	σ_z	σ_y, s_x

Table 8.1: Classification of electronic operators according to the irreducible representations of C_{2v} and time reversal (TR) operation.

being interested only on the effect of Pb, and given that Pb atoms form a rectangular lattice, we conclude that the symmetry group of the substrate is orthorhombic, C_{2v} , which is a subgroup of C_{6v} . Therefore, only the symmetry operations of the original group contained in C_{2v} survive. Those are the C_2 rotation about the axis orthogonal to the graphene plane and inversion operations about the vertical planes defined by the dashed and dotted lines in Fig. 8.3. Now the electronic operators must be classified according to the irreducible representations of C_{2v} , as shown in Tab. 8.1. Only complete scalars ($\sim A_1$) which are even under time reversal symmetry may appear in the Hamiltonian. Such combinations containing $s_{x,y,z}$ operators are $\tau_z \sigma_z s_z$, $\tau_z s_y$, $\tau_z \sigma_x s_y$, and $\sigma_y s_x$.

This can be checked straightforwardly by considering the unitary operators that implement the symmetry operations of C_{2v} and time inversion in the Hilbert space of the Bloch wave functions at the \mathbf{K}_{\pm} points. As explained in Appendix A, the orbital part of

8. ELECTRONIC CONFINEMENT IN GRAPHENE DUE TO SPATIALLY VARYING SOC

Irreps of C_{2v} double group	E	\bar{E}	$2C_2$	$2\sigma_v$	$2\sigma'_v$
A_1	1	1	1	1	1
A_2	1	1	1	-1	-1
B_1	1	1	-1	1	-1
B_2	1	1	-1	-1	1
$D_{1/2}$	2	-2	0	0	0

Table 8.2: Character table for C_{2v} double group.

the wave function can be written as a vector of the form $\Psi = (\psi_{A,+}, \psi_{B,+}, \psi_{A,-}, \psi_{B,-})^T$, belonging to the 4-dimensional irrep G of C_{6v} , where each entry $\psi_{A/B,\pm}$ represents the amplitude of the wave function on sublattice A/B at valley \mathbf{K}_\pm . The matrices of C_{2v} and time reversal operations in this basis are:

$$\begin{aligned}
 C_2 &: \tau_x \sigma_x \\
 \sigma_v &: \sigma_x \\
 \sigma'_v &: \tau_x \\
 \mathcal{T} &: \tau_x \mathcal{K}
 \end{aligned} \tag{8.1}$$

Note that the operators of C_2 , σ_v and σ'_v operations commute each other since C_{2v} is abelian. With this and the character table of the group we classify valley diagonal operators $\sigma_{x,y,z}$ and τ_z according to the irreducible representations of C_{2v} as indicated in Tab. 8.1.

The spinorial part of the wave function transforms according to the 2-dimensional irreducible representation $D_{1/2}$ of the C_{2v} double group, check the character table in Tab. 8.2. In such representation the symmetry operations read:

$$\begin{aligned}
 C_2 &: is_z \\
 \sigma_v &: s_y \\
 \sigma'_v &: s_x \\
 \mathcal{T} &: is_y \mathcal{K}
 \end{aligned} \tag{8.2}$$

The transformation properties of s_i matrices are trivially inferred from the reduction

$$D_{1/2} \times D_{1/2} \sim A_1 + A_2 + B_1 + B_2,$$

or equivalently from the transformation of s_i matrices under the operations of C_{2v} double group in the $D_{1/2}$ representation. Note that now these operators do not commute each other because the double group is not longer abelian.

Then, one may form invariants using Tabs. 8.1 and 8.2, obtaining the mentioned SOC terms. It is very easy to check that such terms transform trivially under the matrices of the $G \times D_{1/2}$ representation:

$$\begin{aligned}
 C_2 &: i\tau_x \sigma_x s_z \\
 \sigma_y &: \sigma_x s_y \\
 \sigma'_y &: \tau_x s_x \\
 \mathcal{T} &: i\tau_x s_y \mathcal{H}
 \end{aligned} \tag{8.3}$$

Thus, the phenomenological Hamiltonian valid around the BZ corners read

$$\mathcal{H} = v_F \vec{\Sigma} \cdot (-i\nabla + \mathbf{A}) \pm A_0 s_y \pm \Delta_{KM} \sigma_z s_z, \tag{8.4}$$

where $\vec{\Sigma} = (\pm\sigma_x, \sigma_y)$, $\mathbf{A} = (A_x s_y, A_y s_x)$, and \pm holds for valleys \mathbf{K}_\pm . It can be easily checked that the Hamiltonian in Eq. (8.4) is invariant under the symmetry operations of Eq. (8.3), and it represents the most general effective Hamiltonian at valleys \mathbf{K}_\pm containing all the possible SOC terms with the only constraint of the reduced C_{2v} symmetry of the system.

We have the Kane-Mele coupling, also present (although negligible) in the absence of the Pb layer, which can be interpreted as a mass potential, and new SOC terms which can be interpreted as a gauge field \mathbf{A} and a scalar field A_0 which sets the y -component as the quantization axis for spin. At this level, the fields $A_{0,x,y}$ are phenomenological couplings associated to the three independent SOC terms that emerge due to the presence of the Pb layer. For the particular case when the Pb monolayer is completely commensurate with graphene it is possible to perform some analytical estimates based on tight-binding, see Appendix C.

The gauge field \mathbf{A} is non-abelian since in general $[A_i, A_j] \neq 0$. This situation is formally identical to the one in the context of twisted bilayer graphene,^[281] where the inter-layer couplings can be also interpreted as components of non-abelian gauge fields, but in that case the additional internal degrees of freedom is the layer instead of the spin. As in that case, a non-uniform spatial dependence of these fields could lead to electronic confinement.

8.4 Tight-binding simulation

8.4.1 Two-bands tight-binding model

In order to simulate the Hamiltonian of Eq. 8.4 at \mathbf{K}_\pm points, we consider the usual tight-binding description of graphene in terms of first-neighbors hopping t between

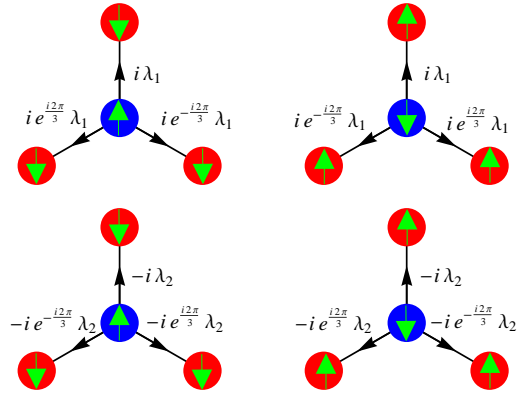


Figure 8.4: Hopping terms which lead to \mathbf{A} at the $\pm\mathbf{K}$ points.

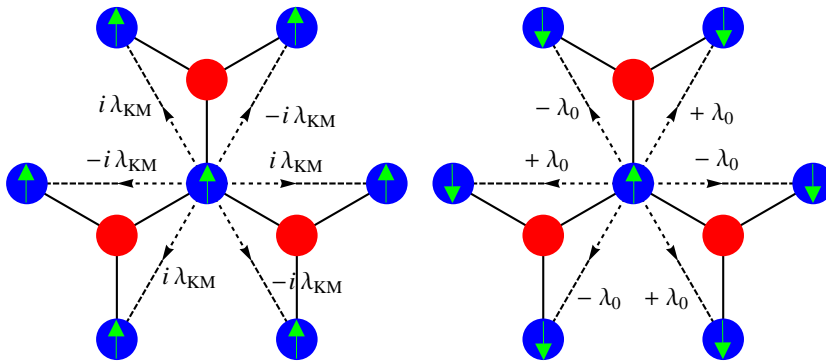


Figure 8.5: Hopping terms which lead to Δ_{KM} (left) and A_0 (right) at the $\pm\mathbf{K}$ points.

π orbitals. The SOC terms are then introduced by considering the suitable spin-dependent hoppings. The first neighbors complex hoppings shown in Fig. 8.4 generate the gauge field $\mathbf{A} = (A_x s_y, A_y s_x)$. In second quantization notation these read

$$H_{\mathbf{A}} = i\lambda_1 \sum_{\langle ij \rangle} c_i^\dagger (\vec{s} \times \hat{\delta}_{ij})_z c_j - i\lambda_2 \sum_{\langle ij \rangle} c_i^\dagger (\vec{s}_* \times \hat{\delta}_{ij})_z c_j, \quad (8.5)$$

with $\vec{s} = (s_x, s_y)$, $\vec{s}_* = (s_x, -s_y)$, and $c_i^\dagger = (c_{i\uparrow}^\dagger, c_{i\downarrow}^\dagger)$, where c_{is}^\dagger (c_{is}) creates (annihilates) an electron at site i with spin $s = \uparrow, \downarrow$. The hopping λ_1 respects the original C_{6v} symmetry and leads to the Bychkov-Rashba coupling, $\frac{3\lambda_1}{2} (\tau_z \sigma_x s_y - \sigma_y s_x)$, which is nothing but the antisymmetric combination of x and y components of \mathbf{A} . The easiest way to reduce the symmetry down to C_{2v} is to consider the complex conjugate hoppings, leading to the symmetric combination $\frac{3\lambda_2}{2} (\tau_z \sigma_x s_y + \sigma_y s_x)$. Therefore, the components of $\mathbf{A} = (A_x s_y, A_y s_x)$ read

$$\begin{aligned} A_x &= \frac{\lambda_1 + \lambda_2}{ta}, \\ A_y &= \frac{\lambda_2 - \lambda_1}{ta}. \end{aligned} \quad (8.6)$$

Similarly, we must consider hoppings between second nearest neighbors in order to generate the scalar and mass (Kane-Mele) terms. The Kane-Mele coupling is associated to the hoppings resembling the Haldane's model represented in the left panel of Fig. 8.5. Such hoppings (note that the hoppings in the left panel of Fig. 8.5 reverse their sign for the \downarrow component of spin and for hoppings within atoms of the other sublattice) respect the original C_{6v} symmetry of graphene. In second quantization notation the Hamiltonian reads

$$H_{KM} = i\lambda_{KM} \sum_{\langle\langle ij \rangle\rangle} v_{ij} c_i^\dagger s_z c_j, \quad (8.7)$$

where $v_{ij} = \frac{2}{\sqrt{3}} (\hat{\delta}_1 \times \hat{\delta}_2)_z = \pm 1$, and $\hat{\delta}_1, \hat{\delta}_2$ are the nearest neighbors vectors along the two bonds that the electron traverses going from j to i site. This Hamiltonian leads to the Kane-Mele coupling with $\Delta_{KM} = 3\sqrt{3}\lambda_{KM}$. The hoppings between second nearest neighbors shown in the right panel of Fig. 8.5 are not compatible with C_{6v} , and actually reduce the symmetry down to C_{2v} . In second quantization notation we have

$$H_{KM} = i\lambda_0 \sum_{\langle\langle ij \rangle\rangle} v_{ij} (a_i^\dagger s_y a_j - b_i^\dagger s_y b_j), \quad (8.8)$$

leading to $A_0 = 3\sqrt{3}\lambda_0$.

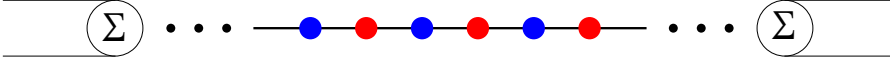


Figure 8.6: Translation invariance in the zig-zag direction is assumed. The problem for each k_x can be mapped to a 1 dimensional tight-binding chain with 2 atoms per unit cell. A finite chain (the region where the SOC changes) is connected to two semi-infinite leads (where the SOC is taken as a constant). The effect of the semi-infinite leads is incorporated to the Green operator of the chain by means of a self-energy, which is computed from the solution of the Dyson equation for the leads.

8.4.2 Scheme of calculation

The transition from graphene/Ir(111) to graphene/Pb/Ir(111) is modeled as a region where the SOC change from 0 to a certain finite value. For simplicity, we assume that the SOC changes in the armchair direction (y). Translation invariance in the direction along the border between the two regions is assumed, so the crystalline momentum (k_x) along the zig-zag direction is conserved. For each k_x , the problem can be mapped to a generalized tight-binding chain with two atoms per unit cell with k_x -dependent inter-cell hoppings, see Fig. 8.6. We compute the retarded Green function at the sites of the chain where the SOC changes, modeled as a finite chain connected to semi-infinite leads where the SOC is taken as a constant. The spatial variation of the SOC is introduced in the modulation of the spin-dependent hoppings previously introduced. The effect of the leads are incorporated as a self-energy, which is computed from the Dyson equation for the leads. Then, the Green operator for the chain is calculated, and from this we have the LDOS for each k_x . Finally we integrate in k_x .

8.4.3 Results

In all the cases the modulation of the spin-dependent hoppings follows the profile shown in Fig. 8.7 (a), consisting in an error function spread in 60 unit cells of graphene along the armchair direction,

$$\lambda(y) = \frac{\lambda_{max}}{2} \left(\operatorname{erf}\left(\frac{y}{L}\right) + 1 \right), \quad (8.9)$$

where y is referred to the center of the chain. Here λ_{max} is the maximum strength of the spin-dependent hopping and L is the length scale that characterizes the decay, a certain fraction of the typical size of the islands. In all the results shown in this section we take $L = 15a$. The LDOS is computed at the center, $y = 0$. The main result of this

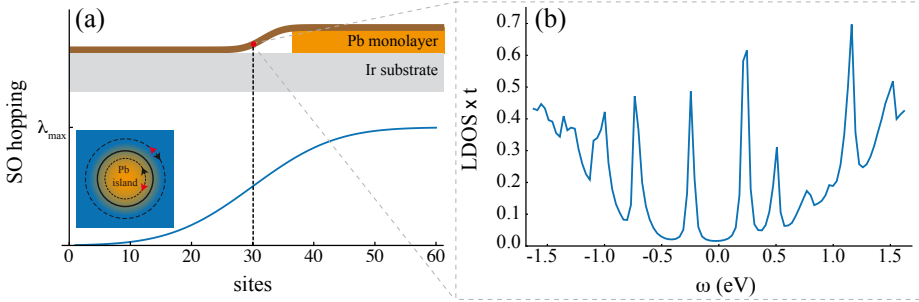


Figure 8.7: (a) Spatial evolution of the SOC across the border of the Pb intercalated regions. The non-uniform SOC profile follows an error function spread in 60 unit cells of graphene along the armchair direction, and the results shown in (b) correspond to the LDOS in the middle. The inset shows a Pb island with its physical edge in black, and the in-plane spin-polarized counter-propagating modes expected at the edges of the region where the SOC changes. The color of the arrows indicates opposite in-plane spin polarizations. (b) LDOS calculated for gr/Pb/Ir(111). A non-uniform SOC with a maximum strength of $\lambda_1 = \lambda_2 = 0.5t$ is assumed. The parameters correspond to $A_x(y) = 2\lambda(y)/at$, $A_y = 0$, and we assume $A_0 = 0.06\sqrt{3}t$ (≈ 0.3 eV). Here t is the first neighbor hopping parameter of graphene (3 eV) and a is the distance between carbon atoms.

investigation is shown in Fig. 8.7 (b), where the computed LDOS qualitatively agrees with the STS spectra. Next, we disclose the steps that lead us to this result.

We consider first the effect of the spatially varying gauge field \mathbf{A} . The results when only λ_1, λ_2 hoppings are included are shown in Fig. 8.8. The LDOS develops peaks for considerable strong SOC, $\lambda_1, \lambda_2 \geq 0.1t$. The more advantageous situation corresponds to the case of $\lambda_1 \sim \lambda_2$, when more peaks appear. In that case, the spectrum resembles the one of graphene LLs.

In order to obtain a sequence of peaks qualitatively more similar to the ones obtained in the experiments we must include the scalar potential A_0 , i.e. λ_0 hoppings. The calculation shown in Fig. 8.7 (b) corresponds to an uniform value of $\lambda_0 = 0.02t$. If the same profile as for $\lambda_{1,2}$ is taken for λ_0 then we obtain a similar result, see Fig. 8.9 (left). However, the inclusion of a Kane-Mele coupling destroys completely the sequence of peaks. For a certain value of the maximum λ_{KM} all the resonances disappear and a gap around $\omega = 0$ is opened.

8. ELECTRONIC CONFINEMENT IN GRAPHENE DUE TO SPATIALLY VARYING SOC

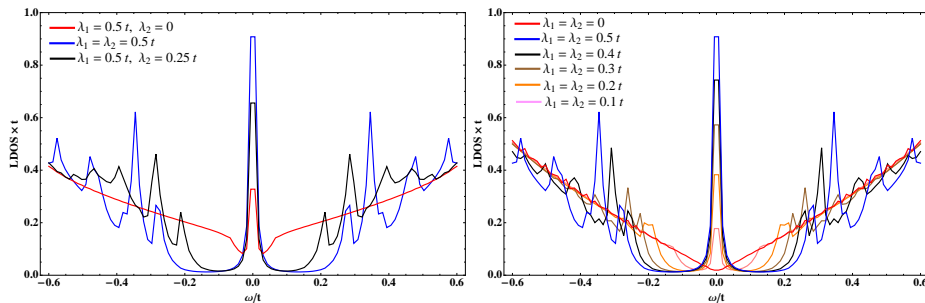


Figure 8.8: LDOS when only the gauge potential $\hat{\mathbf{A}}$ is considered (λ_1 and λ_2 hoppings). The values in the legend refer to the maximum value at the center of the Pb islands.

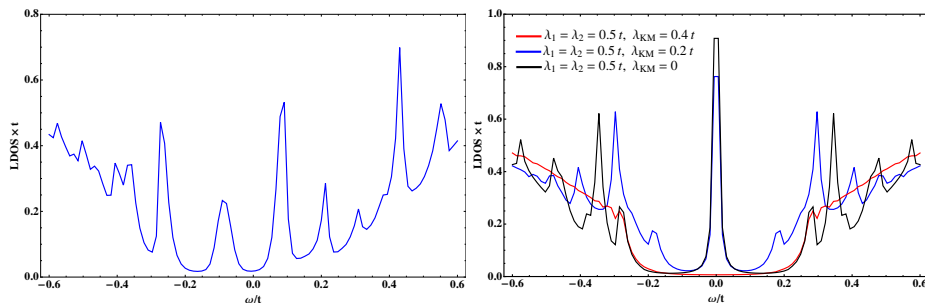


Figure 8.9: Left: LDOS when both the gauge $\hat{\mathbf{A}}$ and scalar \hat{A}_0 potentials are considered. The profile is the same in both cases. The maximum values of the couplings are $\lambda_1 = \lambda_2 = 0.5t$, $\lambda_0 = 0.02t$. Right: LDOS for different values of a non-uniform Kane-Mele coupling.

8.5 Interpretation

As shown in the previous section, spatially varying SOC fields may lead to electronic confinement. According to the tight-binding calculation, the resonances are more clear when λ_1 and λ_2 are of the same order, and they seem to follow the same sequence as the LLs of the Dirac Hamiltonian. In that case, the gauge field reduces to

$$\mathbf{A}(y) = \begin{pmatrix} \frac{2\lambda(y)}{ta} s_y \\ 0 \end{pmatrix}. \quad (8.10)$$

Note that this field, under a U(2) (global) transformation of the form

$$U = \exp \left[i \frac{\pi}{4} \mathcal{J} - i \frac{\pi}{3\sqrt{3}} \sum_{x,y,z} s_i \right], \quad (8.11)$$

it is equivalent to an abelian gauge field with opposite sign for each spin component,

$$\hat{\mathbf{A}}(y) \xrightarrow{U(2)} U \hat{\mathbf{A}}(y) U^\dagger = \begin{pmatrix} \frac{2\lambda(y)}{ta} s_z \\ 0 \end{pmatrix}. \quad (8.12)$$

Therefore, under this U(2) transformation the Hamiltonian is mapped to two copies of the Dirac equation in the presence of an out-of-plane magnetic field with opposite sign for each spin projection. This situation resembles the quantum valley hall state proposed in graphene, where strain generates pseudo-magnetic fields with opposite sign at each valley,^[259] but in this case the valley degree of freedom is replaced by spin. Moreover, the present model consists on two copies of the QSHE state proposed by Bernevig and Zhang,^[135] one for each valley. Thus, surrounding Pb regions we expect a situation qualitatively similar to the one discussed in the previous chapter for strained MX₂. As depicted in the inset of Fig. 8.7 (a), we assume that the Pb islands induce a strong SOC in graphene, which decays as we get away from the islands. Surrounding the region where the SOC changes, symbolized by the colour gradient, we expect spin-polarized counter-propagating edge states. Note that the spin polarization is in-plane (in the simulation, along the armchair direction), which makes these spin currents more difficult to be detected in a spin-polarized STM/STS experiment.

Interestingly, the scalar field A_0 separates in energy the sequence of Landau peaks associated to each Kramers pair (different valley numbers) for which the system is a \mathbb{Z}_2 topological insulator. This energy separation allows to populate an odd number

of LLs. In that situation, an odd number of Kramers pairs of edge modes cross the Fermi level, and therefore, at least one pair of the counter propagating edge channels is topologically protected by time-reversal symmetry. The characteristic decay length of these modes into the region where the SOC changes goes like $\ell \sim \frac{3ta}{\sqrt{2}\Delta}$, where Δ is the energy separation between pseudo-LLs. From the experiments we have roughly $\Delta \sim 0.1t$, so we expect $\ell \sim 20a$, which is less than the characteristic length ($\sim 60a$) over which the spin-orbit changes in the numerical calculation.

Finally, the robustness of this picture is discussed. First of all, in the previous disertation we assumed $\lambda_1 = \lambda_2$. If $\lambda_1 \neq \lambda_2$, then we have $\hat{A}_y(y) = \frac{\lambda_1(y) - \lambda_2(y)}{ta} s_x$. This component of the field can be gauged away by the local U(2) transformation $U(y) = e^{i \int^y d\zeta \hat{A}_y(\zeta)}$, then

$$\hat{\mathbf{A}}(y) \rightarrow U(y) [-i\nabla + \hat{\mathbf{A}}(y)] U^\dagger(y) = \begin{pmatrix} \frac{\lambda_1(y) + \lambda_2(y)}{ta} \\ 0 \end{pmatrix} \otimes \left[\cos \left(\frac{2}{ta} \int^y d\zeta \lambda_1(\zeta) - \lambda_2(\zeta) \right) s_y + \sin \left(\frac{2}{ta} \int^y d\zeta \lambda_1(\zeta) - \lambda_2(\zeta) \right) s_z \right]. \quad (8.13)$$

The x component of the gauge field oscillates in spin space during the characteristic length $\mathcal{L} = \frac{\pi ta}{\langle \lambda_1 - \lambda_2 \rangle}$, where the brackets denote the mean value. The problem is not longer equivalent to two copies of the Dirac equation in the presence of a magnetic field with opposite sign for each spin projection. The precession in spin space is the manifestation of the non-abelian nature of the gauge field. Nevertheless, for slow precession, $\ell/\mathcal{L} \ll 1$, the LLs are expected to survive, as shown in the numerical calculation. Given that the Landau gaps remain open the survival of the topological properties of the system are guaranteed. Similarly, the Kane-Mele coupling mixes the two in-plane spin polarizations, tending to suppress the LL peaks. On the other hand, such coupling opens a bulk gap with non-trivial properties. Therefore, the Kane-Mele coupling drives a topological transition from a Landau-Bernevig-Zhang to a Haldane-Kane-Mele QSHE phase.

8.6 Conclusions

The sharp resonances observed in graphene grown on Ir(111) with intercalated Pb islands may be interpreted as pseudo-LLs originated due to spatially varying SOC fields. Microscopically, the SOC is provided by the intercalated Pb monolayer. For irregular shapes of the Pb islands, we expect the induced SOC in the graphene layer to decay from the center of the islands to the graphene grown directly on Ir with a characteristic length scale determined by the size of the islands.

Such spatial modulations of the SOC generate pseudo-magnetic fields which confine graphene electrons. Note that in the tight-binding simulation the maximum strength of the induced SOC giving the best qualitative agreement with the experiments is $\lambda_{max} = 0.5t \approx 1.4$ eV, which is compatible with the SOC in Pb.^[282] Such large SOC is expected to be induced at the center of the Pb-intercalated regions, and to be independent of the size of such regions due to the local nature of the SOC. On the other hand, the length scale over which the SOC profile varies visibly, L , is expected to be proportional to the size of the irregular Pb islands. This is also compatible with the experiments, which show that the confinement (measured by the gaps between resonances Δ) is larger for smaller sizes of the Pb islands.

According to this model, the regions surrounding the borders of the islands resemble a topological state of matter similar to the one proposed by Bernevig and Zhang.^[135] At the edges of the regions where the SOC varies we expect in-plane spin-polarized counter-propagating modes. However, in this case the polarization is in-plane, what makes these states difficult to be detected by spin-polarized STM/STS experiments.

Conclusions

Both stretching and bending deformations of 2D crystals have dramatic consequences on the electronic structure of these materials when combined with spin-orbit effects. We have discussed the manifestation of such phenomena in transport properties or STM/STS probes, so either our theoretical findings try to explain experimental observations or we propose possible routes to test our predictions.

We have shown in Chapter 3 that scattering by flexural phonons constitute the main limitation to electronic transport in suspended graphene samples, characterized by mobilities which show a quadratic dependence on temperature, independently of the carrier concentration. The changes from sample to sample are attributed to residual strain, which eventually suppresses this scattering mechanism.

We have seen in Chapter 4 that these phonon modes contribute remarkably to the Kane-Mele SOC term, however, the strength of the atomic SOC is very weak due to the lightness of carbon, making this effect difficult to be detected. Nevertheless, applying compression is a suitable strategy in order to generate buckled regions of graphene where such effects may be observed.

In Chapter 5 we discussed conventional SOC-mediated spin relaxation mechanisms assisted by external disorder. The main conclusion of this work is that neither Elliot-Yafet nor D'yakonov-Perel' mechanisms are able to explain the observed spin relaxation times in graphene-based spin valves. We have examined different possibilities going beyond these standard theories. As we have seen, impurities may enhance the SOC locally, but this seems to be insufficient in order to reproduce spin transport experiments. An important prospect for future work is to include in these models the effect of the formation of local magnetic moments associated to such defects, which seem to play a role in spin transport as inferred from recent experiments.

In Chapter 6 we introduced the effect of a spatially varying SOC associated to the presence of curvature in the sample due to static wrinkles or flexural phonons. We applied this theory to the case of MX_2 monolayers, where there are not experiments on spin transport yet, but our estimations are at least in agreement with recent optical experiments.

We have proposed in Chapter 7 a route to create a QSHE state in MX_2 monolayers by applying tension. Shear strain couples to electronic quasiparticles as an effective magnetic field with opposite sign for different valley excitations. At the same time, the lack of a center of inversion in the crystal structure and the large SOC provided by the transition metal atoms split the electronic bands with opposite sign at each valley. These fictitious time reversal symmetry breaking allows to create a state analogous to

the QHE, previously proposed by Bernevig and Zhang in a different semiconducting compound. The strong d character of the MX_2 bands stimulates the search for correlation effects on this topological phase, for instance on the edge states, which is an interesting line of research for the future.

We have developed a model in order to explain the sequence of sharp resonances in the STS spectra recorded in graphene grown on Ir(111) with intercalated Pb islands. The model relies on spatially modulated SOC fields induced by the Pb monolayer, which agrees qualitatively with the experiments. The irrefutable evidence in favor of the model would be the vanishing of the peaks at the center of large Pb islands. Unfortunately, it is not possible to control the size of these islands in practice. This work opens the door to the study of different hybrid structures combining the mechanical stability and good electronic properties of graphene with materials with large SOC. In particular, Pb is a good candidate given that it can be tuned into a superconducting state at low temperatures.

Finally, it is unavoidable to emphasize the importance of controlling the electron's spin degree of freedom for potential applications which go from solid state platforms for quantum computation to novel electronics based on this property. The ability to control these features by mechanical means instead of applying large magnetic fields is a great goal for present and future technologies in Condensed Matter systems.

Conclusiones

Tanto las deformaciones de estiramiento como las de pandeo tienen consecuencias dramáticas en la estructura electrónica de los materiales 2D cuando se combinan con los efectos de la interacción espín-órbita. Hemos discutido la manifestación de dichos fenómenos en las propiedades de transporte o en pruebas STM/STS, por lo que bien nuestros hallazgos teóricos tratan de explicar observaciones experimentales o bien proponemos posibles rutas para comprobar nuestras predicciones.

Hemos visto en el Capítulo 3 que la dispersión por fonones flexurales constituye la mayor limitación para el transporte electrónico en muestras de grafeno suspendido, caracterizado por movilidades que muestran una dependencia cuadrática en la temperatura independientemente de la concentración de portadores. Los cambios de muestra a muestra son atribuidos a tensiones residuales que eventualmente suprimen este mecanismo de dispersión.

Hemos visto en el Capítulo 4 que estos modos de fonones contribuyen remarcablemente al término espín-órbita de Kane y Mele, sin embargo, la magnitud del acoplo espín-órbita atómico es tan débil debido al bajo número atómico del carbono que este efecto es difícil de detectar. No obstante, una posible estrategia es aplicar compresión para generar regiones corrugadas de tal forma que estos efectos puedan ser observados.

En el Capítulo 5 discutimos los mecanismos convencionales de relajación de espín mediados por el acoplo espín-órbita y asistidos por el desorden. La conclusión principal de este trabajo es que ni el mecanismo de Elliot-Yafet ni el de D'yakonov-Perel' son capaces de explicar los tiempos de relajación de espín en válvulas de espín basadas en grafeno. Hemos examinado diferentes posibilidades más allá de estas teorías convencionales. Como hemos visto, las impurezas pueden aumentar la interacción espín-órbita localmente, pero esto parece insuficiente para reproducir los experimentos de transporte de espín. Una posibilidad de trabajo para el futuro consiste en incorporar en estos modelos el efecto de la formación de momentos magnéticos asociados a dichos defectos, lo que parece jugar un papel en el transporte de espín a la luz de experimentos recientes.

En el Capítulo 6 introdujimos el efecto de acoplos espín-órbita variables en el espacio asociados a la presencia de curvatura en la muestra debida a arrugas o fonones flexurales. Aplicamos esta teoría al caso de monocapas de dicalcogenuros de metales de transición, donde no hay experimentos de transporte de espín aún, pero nuestras estimaciones son al menos compatibles con experimentos ópticos recientes.

Hemos propuesto en el Capítulo 7 una ruta para crear un efecto Hall cuántico de

espín en monocapas de dicalcogenuros de metales de transición aplicando tensiones. Las tensiones de cizalladura se acoplan de manera efectiva a las cuasi-partículas electrónicas como un campo magnético con signo opuesto para excitaciones en torno a diferentes valles. Al mismo tiempo, la ausencia de un centro de inversión en la estructura cristalina y el acoplo espín-órbita tan grande provisto por los átomos del metal de transición separan las bandas de energía con signo opuesto en cada valle. Esta ruptura ficticia de la simetría de inversión temporal permite crear un estado análogo al del efecto Hall cuántico, propuesto anteriormente por Bernevig y Zhang en un compuesto semiconductor diferente. El carácter orbital de las bandas de los dicalcogenuros de metales de transición estimula el estudio de los efectos de las correlaciones electrónicas en esta fase topológica, por ejemplo en los estados de borde, lo que constituye una muy interesante línea de investigación para el futuro.

Hemos desarrollado un modelo para tratar de explicar la secuencia de resonancias en los espectros STS registrados en muestras de grafeno crecidas sobre la cara (111) de iridio con islas de plomo intercaladas. El modelo se basa en la modulación espacial de campos espín-órbita inducidos por la presencia de las monocapas de plomo, lo que concuerda cualitativamente con los experimentos. La evidencia irrefutable en favor del modelo sería la desaparición de los picos en el centro de islas de plomo muy grandes. Desafortunadamente, no es posible controlar el tamaño de estas islas en la práctica. Este trabajo abre la puerta al estudio de diferentes estructuras híbridas que combinen la estabilidad mecánica y las buenas propiedades electrónicas del grafeno con materiales que aporten un acoplo espín-órbita grande. En particular, el plomo es un buen candidato dado que puede inducirse un estado superconductor a temperaturas muy bajas.

Por último, es necesario destacar la importancia que tiene poder controlar el grado de libertad de espín del electrón en aplicaciones que van desde las plataformas de estado sólido para computación cuántica hasta la electrónica basada en esta propiedad, la espintrónica. El control del espín por medios mecánicos en lugar de aplicando campos magnéticos supone una gran ventaja para tecnologías presentes y futuras en sistemas de Materia Condensada.

APPENDIX



Point groups

Symmetry is probably the most important concept in Physics. Generally speaking, physical processes are governed by selection rules that are the consequence of symmetry constraints. In modern Physics, the manifestation of underlying symmetries is even more profound. For example, our understanding of the fundamental forces in nature is based on the existence of some local (gauge) symmetries of the action describing the dynamics of matter fields.

Symmetry transformations form an algebraic structure defined as a *group*. The definition of a group with respect to a certain internal operation is of course axiomatic. A set of elements with an internal operation form a group when i) such internal operation fulfills the associative law, ii) when there exists a unit element (usually denoted by E) such that the product of E with any group element leaves that element unchanged, and iii) when for every element there exists an inverse element, such that the product of an element and its inverse is equal to E . In this appendix we review some basic properties of finite groups which are used through the thesis.

The concept of *representation* is probably the most useful tool in group theory. A representation of a certain group is basically a group of square matrices which is isomorphic to the original one. The dimensionality of the representation is equal to the dimensionality of each of its matrices. Of course, the representations are not unique. By an unitary transformation we generate a new set of matrices which

provides an equally good representation. If all the matrices in the representation of a group can be made to acquire the same block form by an unitary transformation, then the representation is said to be reducible, otherwise it is irreducible. Thus, an irreducible representation (irrep) is the simpler one in the sense that it cannot be expressed in terms of representations of lower dimensionality.

Another important concept is the conjugacy class. An element B conjugate to A is by definition $B \equiv XAX^{-1}$, where X is an arbitrary element of the group. A conjugacy class is the totality of elements which can be obtained from a given element by conjugation. An important result is that the number of irreps of a group is equal to the number of conjugacy classes, which can be deduced from a central theorem in group theory (based on the Schur's lemma), the wonderful orthogonality theorem.

Given the arbitrariness in the definition of representations, the trace (invariant under an unitary transformation) is introduced. The *character* of the representation of a given element of the group is the trace of the associated matrix. The character for each element in a class is the same. For many applications it is sufficient to know just the *character table* without the actual matrix representation in a particular basis. The character table is a square table whose rows correspond to the irreps and whose columns correspond to the conjugacy classes; the entries consist of the characters of the representations. Importantly, in most cases the character tables of a certain group can be inferred from simple rules implied by the Schur's lemma and the wonderful orthogonality theorem.

Transformations which appear in the symmetry group of a body of finite dimensions must be such that at least one point of the body remains fixed when the symmetry transformations are applied. This means that all axes and planes of symmetry must have at least one common point of intersection. Symmetry groups having this property are called *point groups*. In the case of a crystal lattice we concern about its *space group*, which consists of both discrete translational symmetry operations and point group symmetry operations. Both kind of operations leave the electronic Hamiltonian invariant. Consequently, by virtue of Wigner's theorem, the eigenstates of the Hamiltonian are arranged in multiplets of the space group. In reciprocal space, this means that Bloch states are arranged according to the irreps of the point group of the crystal. Sometimes one must deal with the wave vector group at points of the BZ different than Γ . Nevertheless, in many cases one can use tricks, as enlarging the unit cell of the crystal, in such a way that high symmetry points of the BZ are mapped onto the Γ point due to the BZ folding. From the point of view of the lattice symmetries, this means that the two elementary translations of the crystal are factorized out from the translational group and added to the point group.

The point groups of the 2D crystals that this thesis deals with can be easily determined in a systematic way. There is always an axis of symmetry of order n perpendicular to

the crystal plane. If we add to this axis a plane of symmetry passing through it, this automatically generates another $n - 1$ planes intersecting along the axis at angles of π/n . This is the way to obtain the C_{nv} group, which contains $2n$ elements: n rotations about the axis of order n , and n reflections σ_v in vertical planes. The point group of graphene is precisely C_{6v} .

However, if we add to an axis of symmetry of order n an axis of second order perpendicular to it, this involves the appearance of $n - 1$ additional axes of this type intersecting at angles π/n . The resulting group is D_n , which contains $2n$ elements: n rotations about an axis of n order and n rotations through an angle π about horizontal axes. If we add to this group a horizontal plane of symmetry passing through the n axes of second order, n vertical planes automatically appear, each of them passing through the vertical axis and one of the horizontal axis. The resulting group is D_{nh} , which can be written as the direct product of D_n and the group associated to the horizontal plane of symmetry σ_h : $D_{nh} = D_n \times \sigma_h$. Hence, the new group contains $4n$ elements: the $2n$ elements of D_n , n reflections σ_v and n rotary-reflection transformations. This is the point group of monolayers of MX_2 .

There is another way of adding planes of symmetry to D_n : by considering vertical planes through the axis of order n , midway between each adjacent pair of horizontal axes of the second order. The adding of one such plane again involves the appearance of another $n - 1$ planes. The resulting group is D_{nd} , which contains $4n$ elements: to the $2n$ elements of D_n we add n reflections in the vertical planes σ_d and n transformations made of one of these reflections followed by a rotation through an angle π about horizontal axes. This is the point group of bilayer graphene D_{3d} .

A.1 C_{6v}

The point group of the graphene crystal is C_{6v} . The character table of this group is shown in Tab. A.1. The wave vector group at \mathbf{K}_{\pm} is C_{3v} , since the rotations $C_{\pi/3, \pi, 5\pi/3}$ and reflections σ'_v that swap the two valleys are absent. However, instead of dealing with degenerate states at two inequivalent points of the BZ one can enlarge the unit cell in order to contain six atoms, in such a way that the folded BZ is three times smaller and the \mathbf{K}_{\pm} points are mapped onto the Γ point. The new point group $C''_{6v} = C_{6v} + t_{\mathbf{a}_1} \times C_{6v} + t_{\mathbf{a}_2} \times C_{6v}$ contains 36 elements in total. The character table is shown in Tab. A.2. Three new irreducible representations (2-dimensional E'_1 and E'_2 and 4-dimensional G') must be considered now. The Bloch wave function is now represented by a 6-component vector which represents the p_z orbitals at the 6 sites within the enlarged unit cell. This vector belongs to a 6 dimensional representation which can be reduced as $A_1 + B_2 + G'$. The 1-dimensional irreducible representations

C_{6v}	E	C_2	$2C_3$	$2C_6$	$3\sigma_v$	$3\sigma'_v$
A_1	1	1	1	1	1	1
A_2	1	1	1	1	-1	-1
B_1	1	-1	1	-1	1	-1
B_2	1	-1	1	-1	-1	1
E_1	2	-2	-1	1	0	0
E_2	2	2	-1	-1	0	0

 Table A.1: Character table of C_{6v} group.

C''_{6v}	E	T	$2C_3$	$T2C_3$	$3\sigma_v$	$T3\sigma_v$	C_2, TC_2	$2C_6, T2C_6$	$3\sigma'_v, T3\sigma'_v$
A_1	1	1	1	1	1	1	1	1	1
A_2	1	1	1	1	-1	-1	1	1	-1
B_1	1	1	1	1	1	1	-1	-1	-1
B_2	1	1	1	1	-1	-1	-1	-1	1
E_1	2	2	-1	-1	0	0	-2	1	0
E_2	2	2	-1	-1	0	0	2	-1	0
E'_1	2	-1	2	-1	-2	1	0	0	0
E'_2	2	-1	2	-1	2	-1	0	0	0
G'	4	-2	-2	1	0	0	0	0	0

 Table A.2: Character table of C''_{6v} group.

A'_1 and B_2 correspond to the bonding and anti-bonding states at the original Γ point, whereas G' corresponds to the Bloch states at the original BZ corners. Then, in order to construct the electronic Hamiltonian for quasiparticles around K_{\pm} points we must consider the 16 hermitian operators acting in a 4-dimensional space. These operators may be classified according to how they transform under the symmetry operations of C''_{6v} , taking into account the reduction:

$$G' \times G' \sim A_1 + A_2 + B_1 + B_2 + E_1 + E_2 + E'_1 + E'_2 + G'.$$

This can be done without specifying the particular basis over which these operators act. The simplest way to introduce these operators is to express the 16 matrices in terms of two inter-commuting Pauli algebras. We introduce 4×4 matrices $\{\Sigma_x, \Sigma_y, \Sigma_z\}$ and $\{\Lambda_x, \Lambda_y, \Lambda_z\}$. The matrices from the same set satisfy the Pauli-matrix algebra, while matrices from different sets commute. The 16 possible electronic operators are generated by considering the products of the elements of these algebras (and the identity). We identify $\Sigma_{x,y}$ matrices with the valley diagonal irreps and $\Lambda_{x,y}$ matrices with the valley off-diagonal irreps. By definition $(\Sigma_x, \Sigma_y) \sim E_1$,

A_1	A_2	B_1	B_2	E_1	E_2	E'_1	E'_2	G'
\mathcal{I}	Σ_z	Λ_z	$\Sigma_z \Lambda_z$	$\begin{pmatrix} \Sigma_x \\ \Sigma_y \end{pmatrix}$	$\begin{pmatrix} \Lambda_z \Sigma_x \\ \Lambda_z \Sigma_y \end{pmatrix}$	$\begin{pmatrix} \Sigma_z \Lambda_x \\ \Sigma_z \Lambda_y \end{pmatrix}$	$\begin{pmatrix} \Lambda_x \\ \Lambda_y \end{pmatrix}$	$\begin{pmatrix} \Lambda_x \Sigma_y \\ -\Lambda_x \Sigma_x \\ \Lambda_y \Sigma_x \\ \Lambda_y \Sigma_y \end{pmatrix}$

Table A.3: Classification of the electronic operators (without spin) according to how they transform under the symmetry operations of C''_{6v} .

and then $[\Sigma_x, \Sigma_y] \sim A_2$ since $E_1 \times E_1 \sim A_1 + A_2 + E_2$, so then $\Sigma_z \sim A_2$. At the same time, since $E_2 \times E_2 \sim A_1 + A_2 + E_2$ it is clear that the matrices of E_2 doublet and Σ_z form a Pauli algebra so then $(\Lambda_z \Sigma_x, \Lambda_z \Sigma_y) \sim E_2$. Since $B_1 \times E_1 \sim E_2$ is clear that $\Lambda_z \sim B_1$, and therefore $\Lambda_z \Sigma_z \sim B_2$. This is consistent, since $C_{2v} = \{E, C_2, \sigma_v, \sigma'_v\}$ is an abelian subgroup of C_{6v} , and hence the matrices belonging to the 1-dimensional irreps must commute. On the other hand, since $E'_2 \times E'_2 \sim A_1 + B_1 + E'_2$, it is clear that $(\Lambda_x, \Lambda_y) \sim E'_2$. The same can be repeat with Λ_x, Λ_y . All definitions are summarized in Tab. A.3.

In the main text the basis $\Psi = (\psi_{A, \mathbf{K}_+}, \psi_{B, \mathbf{K}_+}, \psi_{A, \mathbf{K}_-}, \psi_{B, \mathbf{K}_-})^T$ is employed, where $\psi_{A/B, \mathbf{K}_\pm}$ represents the amplitude of the Bloch wave function at \mathbf{K}_\pm points on sublattice A/B . Then, the matrices Σ_i, Λ_i are given by:

$$\begin{aligned}
 \Sigma_{x,y} &= \tau_z \otimes \sigma_{x,y}, \\
 \Sigma_z &= \mathcal{I} \otimes \sigma_z, \\
 \Lambda_{x,y} &= \tau_{x,y} \otimes \sigma_z, \\
 \Lambda_z &= \tau_z \otimes \mathcal{I}.
 \end{aligned} \tag{A.1}$$

In some references a different basis is employed, where the order of the projection of the Bloch functions at each sublattice in different valleys is inverted, and also a minus sign is introduced: $\Psi = (\psi_{A, \mathbf{K}_+}, \psi_{B, \mathbf{K}_+}, \psi_{B, \mathbf{K}_-}, -\psi_{A, \mathbf{K}_-})^T$. This basis is very convenient because the notation is simplified. In this basis the operators Σ_i, Λ_i are related with the matrices acting in sublattice and valley indices as

$$\begin{aligned}
 \Sigma_i &= \mathcal{I} \otimes \sigma_i, \\
 \Lambda_i &= \tau_i \otimes \mathcal{I}.
 \end{aligned} \tag{A.2}$$

The notation is simplified essentially because in this basis the time reversal operation is implemented by $\mathcal{T} = \Sigma_y \Lambda_y \mathcal{K}$, in such a way that all the matrices are odd under

	E	T	$2C_3$	$T2C_3$	$3C'_2$	$T3C'_2$	i, Ti	$2iC_3, T2iC_3$	$3iC'_2, T3iC'_2$
A_{1g}	1	1	1	1	1	1	1	1	1
A_{2g}	1	1	1	1	-1	-1	1	1	-1
E_g	2	2	-1	-1	0	0	2	-1	0
A_{1u}	1	1	1	1	1	1	-1	-1	-1
A_{2u}	1	1	1	1	-1	-1	-1	-1	1
E_u	2	2	-1	-1	0	0	-2	1	0
E'_g	2	-1	2	-1	-2	1	0	0	0
E'_u	2	-1	2	-1	2	-1	0	0	0
G'	4	-2	-2	1	0	0	0	0	0

Table A.4: Character table for group D''_{3d} .

the action of \mathcal{T} :

$$\begin{aligned}
\Sigma_i &\xrightarrow{\mathcal{T}} \Sigma_y \Sigma_i^* \Sigma_y = -\Sigma_i, \\
\Lambda_i &\xrightarrow{\mathcal{T}} \Lambda_y \Lambda_i^* \Lambda_y = -\Lambda_i,
\end{aligned} \tag{A.3}$$

and then the possible SOC terms are constructed from products of a spin matrix s_i with Σ_i or Λ_i .

A.2 D_{3d}

The point group of the bilayer graphene crystal is D_{3d} , which can be regarded as a direct product of the rhombohedral group D_3 and the inversion group C_i . Since D_{3d} and C_{6v} are isomorphic, the analysis carried out before can be straightforwardly applied. In particular, the character table for $D''_{3d} = D_{3d} + t_{a_1} \times D_{3d} + t_{a_2} \times D_{3d}$, shown in Tab. A.4, can be easily obtained from the one for C''_{6v} .

Now we must take into account that the π orbitals wave function in the tripled unit cell is represented by a 12-component vector, which can be reduced as $2A_{1g} + 2A_{2u} + E'_u + E'_g + G'$. A_{2g} and A_{1g} irreps correspond to the bonding and anti-bonding combinations of p_z orbitals at the original Γ point. E'_g and E'_u irreps correspond to the Bloch wave function at \mathbf{K}_{\pm} points associated, respectively, to the bonding and anti-bonding combinations of orbitals localized in the dimer sites. The Bloch wave function at \mathbf{K}_{\pm} associated to the non-dimer sites belong to the G' irrep, and constitute the low energy bands of the model as explained in the main text. Similarly to the case of C_{6v} , the 16 Hermitian operators acting on the low energy subspace can be

A_{1g}	A_{2g}	E_g	A_{1u}	A_{2u}	E_u	E'_g	E'_u	G'
\mathcal{I}	Σ_z	$\begin{pmatrix} \Lambda_z \Sigma_x \\ \Lambda_z \Sigma_y \end{pmatrix}$	Λ_z	$\Sigma_z \Lambda_z$	$\begin{pmatrix} \Sigma_x \\ \Sigma_y \end{pmatrix}$	$\begin{pmatrix} \Lambda_x \\ \Lambda_y \end{pmatrix}$	$\begin{pmatrix} \Sigma_z \Lambda_x \\ \Sigma_z \Lambda_y \end{pmatrix}$	$\begin{pmatrix} \Lambda_x \Sigma_y \\ -\Lambda_x \Sigma_x \\ \Lambda_y \Sigma_x \\ \Lambda_y \Sigma_y \end{pmatrix}$

Table A.5: Classification of the electronic operators (without spin) according to how they transform under the symmetry operations of D''_{3d}

$D_{3h} = D_3 \times \sigma_h$	E	$2C_3$	$3C'_2$	σ_h	$2S_3$	$3\sigma_v$
A'_1	1	1	1	1	1	1
A'_2	1	1	-1	1	1	-1
A''_1	1	1	1	-1	-1	-1
A''_2	1	1	-1	-1	-1	1
E'	2	-1	0	2	-1	0
E''	2	-1	0	-2	1	0

Table A.6: Character table of D_{3h} .

classified according to the irreps of D_{3d} taking into account the reduction:

$$G' \times G' \sim A_{1g} + A_{2g} + A_{1u} + A_{2u} + E_g + E_u + E'_g + E'_u + G'.$$

All the definitions are summarized in Tab. A.5.

A.3 D_{3h}

The point group of MX_2 monolayers is D_{3h} , which can be regarded as a direct product of the rhombohedral group D_3 and the mirror symmetry group σ_h . The character table is shown in Tab. A.6. As in the previous examples, we consider the tripled unit cell containing 3 M atoms and 6 X atoms. The group $D''_{3h} = D_{3h} + \mathbf{t}_{a_1} \times D_{3h} + \mathbf{t}_{a_2} \times D_{3h}$ contains 24 new elements and 6 additional conjugacy classes, which leads to 6 new 2-dimensional irreps (denoted by $E'_{1,2,3}$ and $E''_{1,2,3}$), the valley off-diagonal representations. The character table of D''_{3h} is shown in Tab. A.7.

In the main text, Tab. 2.3, the Bloch wave function at \mathbf{K}_{\pm} are classified according to the irreps of C_{3h} , the wave vector group at these points. In the tripled unit cell, the doublets formed by a certain combination of orbitals at one valley and the complex conjugated combination at the other belong to the valley off-diagonal representations

D''_{3h}	E	$2T$	σ_h	$2T\sigma_h$	$2C_3$	$2TC_3$	$2TC_3^2$	$2S_3$	$2TS_3$	$2TS_3^2$	$9TC'_2$	$9T\sigma_v$
A'_1	1	1	1	1	1	1	1	1	1	1	1	1
A'_2	1	1	1	1	1	1	1	1	1	1	-1	-1
A''_1	1	1	-1	-1	1	1	1	-1	-1	-1	1	-1
A''_2	1	1	-1	-1	1	1	1	-1	-1	-1	-1	1
E'	2	2	2	2	-1	-1	-1	-1	-1	-1	0	0
E''	2	2	-2	-2	-1	-1	-1	1	1	1	0	0
E'_1	2	-1	2	-1	2	-1	-1	2	-1	-1	0	0
E''_1	2	-1	-2	1	2	-1	-1	-2	1	1	0	0
E'_2	2	-1	2	-1	-1	2	-1	-1	2	-1	0	0
E''_2	2	-1	-2	1	-1	2	-1	1	-2	1	0	0
E'_3	2	-1	2	-1	-1	-1	2	-1	-1	2	0	0
E''_3	2	-1	-2	1	-1	-1	2	1	1	-2	0	0

 Table A.7: Character table of D''_{3h} .

of D''_{3h} according to the following rules (on the left irreps of C_{3h} , on the right irreps of D''_{3h}):

$$\begin{aligned}
 (A, A) &\sim E_1, \\
 (E, E^*) &\sim E_2, \\
 (E^*, E) &\sim E_3.
 \end{aligned}$$

The conduction band at these points is mostly made of $d_{3z^2-r^2}$ orbitals from M (E'_2 irrep), whereas the valence band is mostly made of $d_{x^2-y^2} \pm d_{xy}$ (E'_1 irrep). We may consider the space of 4-vectors $\sim (E'_2, E'_1)$ whose entries represent the projection of the Bloch wave function at conduction and valence states at \mathbf{K}_\pm points. We must consider the possible 16 hermitian matrices acting on this space, whose reduction in terms of irreps of D_{3h} is inferred from:

$$(E'_2, E'_1) \times (E'_2, E'_1) \sim 2A'_1 + 2A'_2 + 2E' + E'_1 + E'_2 + 2E'_3.$$

As before, this space of electronic operators can be constructed from two intercommuting Pauli algebras Σ_i, Λ_i . The definitions are summarized in Tab. A.8

Irrep	Operators
A'_1	$\mathcal{J}, \Lambda_z \Sigma_z$
A'_2	Σ_z, Λ_z
E'	$\begin{pmatrix} -\Lambda_z \Sigma_y \\ \Lambda_z \Sigma_x \end{pmatrix}, \begin{pmatrix} \Sigma_x \\ \Sigma_y \end{pmatrix}$
E'_1	$\begin{pmatrix} \Sigma_x \Lambda_y + \Sigma_y \Lambda_x \\ \Sigma_x \Lambda_x + \Sigma_y \Lambda_y \end{pmatrix}$
E'_2	$\begin{pmatrix} \Sigma_x \Lambda_y - \Sigma_y \Lambda_x \\ \Sigma_x \Lambda_x - \Sigma_y \Lambda_y \end{pmatrix}$
E'_3	$\begin{pmatrix} -\Sigma_z \Lambda_x \\ \Sigma_z \Lambda_y \end{pmatrix}, \begin{pmatrix} \Lambda_x \\ \Lambda_y \end{pmatrix}$

Table A.8: Definitions of the electronic operators in the two bands effective model at \mathbf{K}_\pm points.

B

Collision integral for scattering by phonons

The rate of change of $f_{\mathbf{k}}$ due to scattering, the so-called collision integral $\dot{f}_{\mathbf{k}}|_{\text{scatt}}$ appearing on the right hand side of the Boltzmann equation, Eq. (3.40), is the difference between the rate at which quasiparticles enter the state $|\mathbf{k}\rangle$ and the rate at which they leave it,

$$\dot{f}_{\mathbf{k}}|_{\text{scatt}} = \sum_{\mathbf{k}'} [f_{\mathbf{k}'}(1 - f_{\mathbf{k}})\mathcal{W}_{\mathbf{k}}^{\mathbf{k}'} - f_{\mathbf{k}}(1 - f_{\mathbf{k}'})\mathcal{W}_{\mathbf{k}}^{\mathbf{k}'}], \quad (\text{B.1})$$

where \mathcal{W}_i^f is the scattering probability between state $|i\rangle$ and $|f\rangle$. Here we use Fermi's golden rule, which reads

$$\mathcal{W}_i^f = \frac{2\pi}{\hbar} |\langle f | \mathcal{H}_{\text{int}} | i \rangle|^2 \delta(\mathcal{E}_f - \mathcal{E}_i), \quad (\text{B.2})$$

equivalent to rest upon the Born approximation for the differential scattering cross-section.

The crucial step to get $\dot{f}_{\mathbf{k}}|_{\text{scatt}}$ is finding the scattering probability for a quasi-particle in state $|\mathbf{k}\rangle$ to be scattered into state $|\mathbf{k}'\rangle$, i.e. $\mathcal{W}_{\mathbf{k}}^{\mathbf{k}'}$ (since the process is quasi-elastic

interband transitions are not allowed). The scattering mechanism is encoded in the interaction \mathcal{H}_{int} , which in the present case is given by H_{ep} in Eq. (3.38). It is readily seen that scattering occurs only through emission or absorption of one phonon or emission/absorption of two phonons. The initial and final states are thus tensorial products of the form $|i\rangle = |\mathbf{k}\rangle \otimes |n_{\mathbf{q}}\rangle$ or $|i\rangle = |\mathbf{k}\rangle \otimes |n_{\mathbf{q}}, n_{\mathbf{q}'}\rangle$, and $|f\rangle = |\mathbf{k}'\rangle \otimes |n_{\mathbf{q}} \pm 1\rangle$, $|f\rangle = |\mathbf{k}'\rangle \otimes |n_{\mathbf{q}} \pm 1, n_{\mathbf{q}'} \pm 1\rangle$ or $|f\rangle = |\mathbf{k}'\rangle \otimes |n_{\mathbf{q}} \pm 1, n_{\mathbf{q}'}^F \mp 1\rangle$, where $|n_{\mathbf{q}}\rangle$ and $|n_{\mathbf{q}}, n_{\mathbf{q}'}\rangle$ represent one and two phonon states in the occupation number representation,^[150] and the electron like quasiparticle state is written as $|\mathbf{k}\rangle = (e^{-i\theta_{\mathbf{k}}/2} a_{\mathbf{k}}^\dagger |0\rangle + e^{i\theta_{\mathbf{k}}/2} b_{\mathbf{k}}^\dagger |0\rangle) / \sqrt{2}$ in the case of monolayer, and with the substitution $\theta_{\mathbf{k}}/2 \rightarrow \theta_{\mathbf{k}}$ in the case of bilayer. Electron-hole symmetry guarantees that the result is the same for both electron and hole doping.

In order to obtain $|\langle f | H_{ep} | i \rangle|^2$, with $|i\rangle$ and $|f\rangle$ as given above, we take the following steps:

1. Terms of the form $V_1 V_2$, where V_1 stands for scalar potential and V_2 for gauge potential induced matrix elements in Eq. (3.39), are neglected. It is easy to show that such terms come proportional to oscillatory factors $e^{\pm i\theta_{\mathbf{k}}}$ or $e^{\pm i\theta_{\mathbf{k}'}}$ (in bilayer graphene $e^{\pm i2\theta_{\mathbf{k}}}$ or $e^{\pm i2\theta_{\mathbf{k}'}}$). These terms can safely be neglected in doing the summation over the direction of \mathbf{k} and \mathbf{k}' in the numerator of Eq. (3.53), keeping $\theta_{\mathbf{k},\mathbf{k}'}$ fixed. The resistivity is then the sum of two independent contributions, originating from scalar and gauge potentials, well in the spirit of Matthiessen's empirical rule.^[154]
2. The scalar potential contribution is proportional to the overlap of states belonging to the same band. For monolayer graphene,

$$\left| V_{1,\mathbf{q}}^v \frac{e^{i(\theta_{\mathbf{k}'} - \theta_{\mathbf{k}})/2}}{2} + V_{1,\mathbf{q}}^{v'} \frac{e^{-i(\theta_{\mathbf{k}'} - \theta_{\mathbf{k}})/2}}{2} \right|^2 = \left| V_{1,\mathbf{q}}^v \right|^2 \frac{1 + \cos \theta_{\mathbf{k},\mathbf{k}'}}{2}, \quad (\text{B.3})$$

whereas for bilayer,

$$\left| V_{1,\mathbf{q}}^v \frac{e^{i(\theta_{\mathbf{k}'} - \theta_{\mathbf{k}})}}{2} + V_{1,\mathbf{q}}^{v'} \frac{e^{-i(\theta_{\mathbf{k}'} - \theta_{\mathbf{k}})}}{2} \right|^2 = \left| V_{1,\mathbf{q}}^v \right|^2 \frac{1 + \cos 2\theta_{\mathbf{k},\mathbf{k}'}}{2}. \quad (\text{B.4})$$

The same manipulation holds for two phonon terms, with $V_{1,\mathbf{q}}^v \rightarrow V_{1,\mathbf{q},\mathbf{q}'}^F$.

3. For the gauge potential contribution there are oscillatory terms which, owing to the argument of point 1., can be neglected. For monolayer graphene,

$$\left| V_{2,\mathbf{q},\mathbf{k},\mathbf{k}'}^v \frac{e^{i(\theta_{\mathbf{k}'} + \theta_{\mathbf{k}})/2}}{2} + \left(V_{2,-\mathbf{q},\mathbf{k},\mathbf{k}'}^v \right)^* \frac{e^{-i(\theta_{\mathbf{k}'} + \theta_{\mathbf{k}})/2}}{2} \right|^2 \simeq \left| V_{2,\mathbf{q}}^v \right|^2, \quad (\text{B.5})$$

and for bilayer,

$$\left| V_{2,\mathbf{q},\mathbf{k},\mathbf{k}'}^v \frac{e^{i(\theta_{\mathbf{k}'}+\theta_{\mathbf{k}})}}{2} + \left(V_{2,-\mathbf{q},\mathbf{k},\mathbf{k}'}^v \right)^* \frac{e^{-i(\theta_{\mathbf{k}'}+\theta_{\mathbf{k}})}}{2} \right|^2 \simeq \left| \tilde{V}_{2,\mathbf{q}}^v \right|^2 \left(\frac{k^2}{2} + \frac{k'^2}{2} + kk' \cos \theta_{\mathbf{k},\mathbf{k}'} \right). \quad (\text{B.6})$$

A similar manipulation holds for two phonon terms, with $V_{2,\mathbf{q}}^v \rightarrow V_{2,\mathbf{q}}^F$.

Finally, summing over phonon momenta and doing the thermal average, we can write $\mathcal{W}_{\mathbf{k}}^{\mathbf{k}'}$ as follows. When scattering is via one phonon we have

$$\begin{aligned} \mathcal{W}_{\mathbf{k}}^{\mathbf{k}'} &= \frac{\pi}{\hbar} \sum_{\mathbf{q}} w_v(\mathbf{q}, \mathbf{k}, \mathbf{k}') n_{\mathbf{q}} \delta_{\mathbf{k}', \mathbf{k}+\mathbf{q}} \delta(\epsilon_{\mathbf{k}'} - \epsilon_{\mathbf{k}} - \hbar\omega_{\mathbf{q}}^v) + \\ &+ \frac{\pi}{\hbar} \sum_{\mathbf{q}} w_v(\mathbf{q}, \mathbf{k}, \mathbf{k}') (n_{\mathbf{q}} + 1) \delta_{\mathbf{k}', \mathbf{k}-\mathbf{q}} \delta(\epsilon_{\mathbf{k}'} - \epsilon_{\mathbf{k}} + \hbar\omega_{\mathbf{q}}^v), \end{aligned} \quad (\text{B.7})$$

where the first term is due to absorption and the second to emission of a single phonon. When scattering involves two phonons we obtain

$$\begin{aligned} \mathcal{W}_{\mathbf{k}}^{\mathbf{k}'} &= \frac{\pi}{\hbar} \sum_{\mathbf{q}, \mathbf{q}'} w_F(\mathbf{q}, \mathbf{q}', \mathbf{k}, \mathbf{k}') n_{\mathbf{q}} n_{\mathbf{q}'} \times \delta_{\mathbf{k}', \mathbf{k}+\mathbf{q}+\mathbf{q}'} \delta(\epsilon_{\mathbf{k}'} - \epsilon_{\mathbf{k}} - \hbar\omega_{\mathbf{q}}^F - \hbar\omega_{\mathbf{q}'}^F) + \\ &+ \frac{\pi}{\hbar} \sum_{\mathbf{q}, \mathbf{q}'} w_F(\mathbf{q}, \mathbf{q}', \mathbf{k}, \mathbf{k}') (n_{\mathbf{q}} + 1)(n_{\mathbf{q}'} + 1) \times \delta_{\mathbf{k}', \mathbf{k}-\mathbf{q}-\mathbf{q}'} \delta(\epsilon_{\mathbf{k}'} - \epsilon_{\mathbf{k}} + \hbar\omega_{\mathbf{q}}^F + \hbar\omega_{\mathbf{q}'}^F) + \\ &+ \frac{2\pi}{\hbar} \sum_{\mathbf{q}, \mathbf{q}'} w_F(\mathbf{q}, \mathbf{q}', \mathbf{k}, \mathbf{k}') (n_{\mathbf{q}} + 1) n_{\mathbf{q}'} \times \delta_{\mathbf{k}', \mathbf{k}-\mathbf{q}+\mathbf{q}'} \delta(\epsilon_{\mathbf{k}'} - \epsilon_{\mathbf{k}} + \hbar\omega_{\mathbf{q}}^F - \hbar\omega_{\mathbf{q}'}^F), \end{aligned} \quad (\text{B.8})$$

where the first term is due to absorption of two flexural phonons, the second to emission of two flexural phonons, and the last one comes from absorption of a single flexural phonon and emission of another one. The collision integral may finally be put in the form

$$\begin{aligned} \dot{f}_{\mathbf{k}} \Big|_{\text{scatt}} &= \frac{\pi}{\hbar} \sum_{\mathbf{k}'} \sum_{\mathbf{q}, \mathbf{v}} w_v(\mathbf{q}, \mathbf{k}, \mathbf{k}') \times \\ &\times \left\{ \left[f_{\mathbf{k}'}(1 - f_{\mathbf{k}}) n_{\mathbf{q}} - f_{\mathbf{k}}(1 - f_{\mathbf{k}'}) (n_{\mathbf{q}} + 1) \right] \delta_{\mathbf{k}, \mathbf{k}'+\mathbf{q}} \delta(\epsilon_{\mathbf{k}} - \epsilon_{\mathbf{k}'} - \hbar\omega_{\mathbf{q}}^v) \right. \\ &\left. + \left[f_{\mathbf{k}'}(1 - f_{\mathbf{k}}) (n_{\mathbf{q}} + 1) - f_{\mathbf{k}}(1 - f_{\mathbf{k}'}) n_{\mathbf{q}} \right] \delta_{\mathbf{k}, \mathbf{k}'-\mathbf{q}} \delta(\epsilon_{\mathbf{k}} - \epsilon_{\mathbf{k}'} + \hbar\omega_{\mathbf{q}}^v) \right\}, \end{aligned} \quad (\text{B.9})$$

for one phonon scattering processes, and

$$\begin{aligned}
 \dot{f}_{\mathbf{k}} \Big|_{\text{scatt}} = & \frac{\pi}{\hbar} \sum_{\mathbf{k}'} \sum_{\mathbf{q}, \mathbf{q}'} w_F(\mathbf{q}, \mathbf{q}', \mathbf{k}, \mathbf{k}') \times \\
 & \times \left\{ \left[f_{\mathbf{k}'}(1 - f_{\mathbf{k}})(n_{\mathbf{q}} + 1)(n_{\mathbf{q}'} + 1) - f_{\mathbf{k}}(1 - f_{\mathbf{k}'})(n_{\mathbf{q}} n_{\mathbf{q}'}) \right] \delta_{\mathbf{k}, \mathbf{k}' - \mathbf{q} - \mathbf{q}'} \delta(\varepsilon_{\mathbf{k}} - \varepsilon_{\mathbf{k}'} + \hbar\omega_{\mathbf{q}}^F + \hbar\omega_{\mathbf{q}'}^F) \right. \\
 & + \left[f_{\mathbf{k}'}(1 - f_{\mathbf{k}})(n_{\mathbf{q}} + 1)n_{\mathbf{q}'} - f_{\mathbf{k}}(1 - f_{\mathbf{k}'})(n_{\mathbf{q}}(n_{\mathbf{q}'} + 1)) \right] \delta_{\mathbf{k}, \mathbf{k}' - \mathbf{q} + \mathbf{q}'} \delta(\varepsilon_{\mathbf{k}} - \varepsilon_{\mathbf{k}'} + \hbar\omega_{\mathbf{q}}^F - \hbar\omega_{\mathbf{q}'}^F) \\
 & + \left[f_{\mathbf{k}'}(1 - f_{\mathbf{k}})n_{\mathbf{q}}n_{\mathbf{q}'} - f_{\mathbf{k}}(1 - f_{\mathbf{k}'})(n_{\mathbf{q}} + 1)(n_{\mathbf{q}'} + 1) \right] \delta_{\mathbf{k}, \mathbf{k}' + \mathbf{q} + \mathbf{q}'} \delta(\varepsilon_{\mathbf{k}} - \varepsilon_{\mathbf{k}'} - \hbar\omega_{\mathbf{q}}^F - \hbar\omega_{\mathbf{q}'}^F) \\
 & \left. + \left[f_{\mathbf{k}'}(1 - f_{\mathbf{k}})n_{\mathbf{q}}(n_{\mathbf{q}'} + 1) - f_{\mathbf{k}}(1 - f_{\mathbf{k}'})(n_{\mathbf{q}} + 1)n_{\mathbf{q}'} \right] \delta_{\mathbf{k}, \mathbf{k}' + \mathbf{q} - \mathbf{q}'} \delta(\varepsilon_{\mathbf{k}} - \varepsilon_{\mathbf{k}'} - \hbar\omega_{\mathbf{q}}^F + \hbar\omega_{\mathbf{q}'}^F) \right\}, \tag{B.10}
 \end{aligned}$$

for scattering through two flexural phonons.

Now we derive the linearized version of the collision integrals given in Eqs. (B.9) and (B.10). We start by expanding electron and phonon probability distributions around their equilibrium values,

$$f_{\mathbf{k}} = f_{\mathbf{k}}^{(0)} + \delta f_{\mathbf{k}}, \quad n_{\mathbf{q}} = n_{\mathbf{q}}^{(0)} + \delta n_{\mathbf{q}},$$

where the variations can be written as $\delta f_{\mathbf{k}} = -\frac{\partial f_{\mathbf{k}}^{(0)}}{\partial \varepsilon_{\mathbf{k}}} \varphi_{\mathbf{k}}$ [see Eq. (3.42)] and $\delta n_{\mathbf{q}} = -\frac{\partial n_{\mathbf{q}}^{(0)}}{\partial (\hbar\omega_{\mathbf{q}})} \chi_{\mathbf{q}}$. The linearized collision integral $\delta \dot{f}_{\mathbf{k}} \Big|_{\text{scatt}}$ is then obtained by expanding $\dot{f}_{\mathbf{k}} \Big|_{\text{scatt}}$ up to first order in the variations.^[154,286]

The one phonon scattering case follows closely the steps outlined in Ref. 286, and for the case of monolayer graphene it has been derived in Ref. 151. Since the difference between monolayer and bilayer amounts to a different kernel $w_v(\mathbf{q}, \mathbf{k}, \mathbf{k}')$ in Eqs. (B.9), which does not play any role in the linearization, we can directly apply the result of Ref.151 to the present case. In order to set notation for the more elaborated case of two phonon scattering, we outline the main steps of the derivation in the following.

We first note that at equilibrium detailed balance implies $\dot{f}_{\mathbf{k}}^{(0)} \Big|_{\text{scatt}} = 0$, from which we get the relation

$$f_{\mathbf{k}'}^{(0)}(1 - f_{\mathbf{k}}^{(0)})n_{\mathbf{q}}^{(0)} = f_{\mathbf{k}}^{(0)}(1 - f_{\mathbf{k}'}^{(0)})(n_{\mathbf{q}}^{(0)} + 1), \tag{B.11}$$

which can be easily verified by direct calculation.^[286] Therefore, in order to get the linearized collision integral it is enough to calculate the variation

$$\delta \left[f_{\mathbf{k}'}(1 - f_{\mathbf{k}})n_{\mathbf{q}} - f_{\mathbf{k}}(1 - f_{\mathbf{k}'})(n_{\mathbf{q}} + 1) \right]. \tag{B.12}$$

Note first that

$$\delta \left[f_{k'}(1-f_k)n_q - f_k(1-f_{k'})(n_q+1) \right] = (1-f_k^{(0)})(1-f_{k'}^{(0)})(n_q^{(0)}+1)\delta \left(\frac{f_{k'}}{1-f_{k'}} \frac{n_q}{n_q+1} - \frac{f_k}{1-f_k} \right). \quad (\text{B.13})$$

The variations appearing on the second line of Eq. (B.13) can be computed easily by noting that

$$\delta \left(\frac{f}{1-f} \right) = \frac{\delta f}{(1-f)^2} \quad \text{and} \quad \delta \left(\frac{n}{n+1} \right) = \frac{\delta n}{(n+1)^2}. \quad (\text{B.14})$$

At the same time we can rewrite δf_k and δn_q as

$$\delta f_k = f_k^{(0)}(1-f_k^{(0)}) \frac{\varphi_k}{k_B T}, \quad \delta n_q = n_q^{(0)}(n_q^{(0)}+1) \frac{\chi_q}{k_B T}. \quad (\text{B.15})$$

Using these expressions and the detailed balance condition it is straightforward to check that

$$\delta \left[f_{k'}(1-f_k)n_q - f_k(1-f_{k'})(n_q+1) \right] = \frac{1}{k_B T} f_k^{(0)}(1-f_{k'}^{(0)})(n_q^{(0)}+1) (\varphi_{k'} + \chi_q - \varphi_k). \quad (\text{B.16})$$

If we consider phonons at equilibrium by taking $\chi_q \approx 0$, so that $n_q \approx n_q^{(0)}$, valid at not too low temperatures,^[154] and also quasielastic scattering, with $\epsilon_k, \epsilon_{k'} \gg \hbar\omega_q$, then the linearized collision integral reads

$$\begin{aligned} \delta \dot{f}_k \Big|_{\text{scatt}} &= -\frac{2\pi}{\hbar} \sum_{k'} \sum_{\mathbf{q}, \nu} w_\nu(\mathbf{q}, \mathbf{k}, \mathbf{k}') \omega_q^\nu \times \\ &\times \frac{\partial n_q}{\partial \omega_q^\nu} \frac{\partial f_k^{(0)}}{\partial \epsilon_k} (\varphi_k - \varphi_{k'}) \delta_{\mathbf{k}, \mathbf{k}'+\mathbf{q}} \delta(\epsilon_k - \epsilon_{k'}), \end{aligned} \quad (\text{B.17})$$

so Eq. (B.17) can be put in the form of Eq. (3.43),

$$\dot{f}_k \Big|_{\text{scatt}} = - \sum_{k'} \mathcal{P}_{\mathbf{k}, k'} (\varphi_k - \varphi_{k'}), \quad (\text{B.18})$$

where $\mathcal{P}_{\mathbf{k}, k'}$ is given in Eq. (3.49).

Now we proceed with the linearization of the collision integral in Eq. (B.10), originating from scattering processes involving two flexural phonons. At equilibrium detailed

balance is guaranteed, $\dot{f}_{\mathbf{k}}^{(0)}|_{\text{scatt}} = 0$, and the following two relations hold,

$$\begin{aligned} \frac{f_{\mathbf{k}'}^{(0)}}{1 - f_{\mathbf{k}'}^{(0)}} &= \frac{f_{\mathbf{k}}^{(0)}}{1 - f_{\mathbf{k}}^{(0)}} \frac{n_{\mathbf{q}}^{(0)}}{n_{\mathbf{q}}^{(0)} + 1} \frac{n_{\mathbf{q}'}^{(0)}}{n_{\mathbf{q}'}^{(0)} + 1}, \\ \frac{f_{\mathbf{k}'}^{(0)}}{1 - f_{\mathbf{k}'}^{(0)}} \frac{n_{\mathbf{q}'}^{(0)}}{n_{\mathbf{q}'}^{(0)} + 1} &= \frac{f_{\mathbf{k}}^{(0)}}{1 - f_{\mathbf{k}}^{(0)}} \frac{n_{\mathbf{q}}^{(0)}}{n_{\mathbf{q}}^{(0)} + 1}. \end{aligned} \quad (\text{B.19})$$

In order to get the linearized collision integral it is easy to see that we only need the following two variations,

$$\delta \left[f_{\mathbf{k}'}(1 - f_{\mathbf{k}})(n_{\mathbf{q}} + 1)(n_{\mathbf{q}'} + 1) - f_{\mathbf{k}}(1 - f_{\mathbf{k}'}n_{\mathbf{q}}n_{\mathbf{q}'} \right], \quad (\text{B.20})$$

and

$$\delta \left[f_{\mathbf{k}'}(1 - f_{\mathbf{k}})(n_{\mathbf{q}} + 1)n_{\mathbf{q}'} - f_{\mathbf{k}}(1 - f_{\mathbf{k}'}n_{\mathbf{q}}(n_{\mathbf{q}'} + 1) \right], \quad (\text{B.21})$$

the other two possibilities being related with these ones by a minus sign and $\mathbf{k} \rightarrow \mathbf{k}'$. Note first that

$$\begin{aligned} &\delta \left[f_{\mathbf{k}'}(1 - f_{\mathbf{k}})(n_{\mathbf{q}} + 1)(n_{\mathbf{q}'} + 1) - f_{\mathbf{k}}(1 - f_{\mathbf{k}'}n_{\mathbf{q}}n_{\mathbf{q}'} \right] = \\ &(1 - f_{\mathbf{k}}^{(0)})(1 - f_{\mathbf{k}'}^{(0)})(n_{\mathbf{q}}^{(0)} + 1)(n_{\mathbf{q}'}^{(0)} + 1) \times \delta \left(\frac{f_{\mathbf{k}'}}{1 - f_{\mathbf{k}'}} - \frac{f_{\mathbf{k}}}{1 - f_{\mathbf{k}}} \frac{n_{\mathbf{q}}}{n_{\mathbf{q}} + 1} \frac{n_{\mathbf{q}'}}{n_{\mathbf{q}'} + 1} \right), \end{aligned} \quad (\text{B.22})$$

and

$$\begin{aligned} &\delta \left[f_{\mathbf{k}'}(1 - f_{\mathbf{k}})(n_{\mathbf{q}} + 1)n_{\mathbf{q}'} - f_{\mathbf{k}}(1 - f_{\mathbf{k}'}n_{\mathbf{q}}(n_{\mathbf{q}'} + 1) \right] = \\ &(1 - f_{\mathbf{k}}^{(0)})(1 - f_{\mathbf{k}'}^{(0)})(n_{\mathbf{q}}^{(0)} + 1)(n_{\mathbf{q}'}^{(0)} + 1) \times \delta \left(\frac{f_{\mathbf{k}'}}{1 - f_{\mathbf{k}'}} \frac{n_{\mathbf{q}'}}{n_{\mathbf{q}'} + 1} - \frac{f_{\mathbf{k}}}{1 - f_{\mathbf{k}}} \frac{n_{\mathbf{q}}}{n_{\mathbf{q}} + 1} \right). \end{aligned} \quad (\text{B.23})$$

The variations appearing on the second lines of Eqs. (B.22) and (B.23) can be computed easily by using Eq. (B.14). Then, we arrive at the variations

$$\delta \left[f_{\mathbf{k}'}(1 - f_{\mathbf{k}})(n_{\mathbf{q}} + 1)(n_{\mathbf{q}'} + 1) - f_{\mathbf{k}}(1 - f_{\mathbf{k}'}n_{\mathbf{q}}n_{\mathbf{q}'} \right] = \quad (\text{B.24})$$

$$(1 - f_{\mathbf{k}}^{(0)})f_{\mathbf{k}'}^{(0)}(n_{\mathbf{q}}^{(0)} + 1)(n_{\mathbf{q}'}^{(0)} + 1) \frac{(\varphi_{\mathbf{k}'} - \varphi_{\mathbf{k}} - \chi_{\mathbf{q}} - \chi_{\mathbf{q}'})}{k_B T}, \quad (\text{B.25})$$

and

$$\delta \left[f_{\mathbf{k}'}(1 - f_{\mathbf{k}})(n_{\mathbf{q}} + 1)n_{\mathbf{q}'} - f_{\mathbf{k}}(1 - f_{\mathbf{k}'}n_{\mathbf{q}}(n_{\mathbf{q}'} + 1) \right] = \quad (\text{B.26})$$

$$(1 - f_{\mathbf{k}}^{(0)})f_{\mathbf{k}'}^{(0)}(n_{\mathbf{q}}^{(0)} + 1)n_{\mathbf{q}'}^{(0)} \frac{(\varphi_{\mathbf{k}'} + \chi_{\mathbf{q}'} - \varphi_{\mathbf{k}} - \chi_{\mathbf{q}})}{k_B T}, \quad (\text{B.27})$$

where we used Eq. (B.15) and the detailed balance condition. It is convenient to express the quantity $(1 - f_{\mathbf{k}}^{(0)})f_{\mathbf{k}'}^{(0)}$ in terms of the difference $(f_{\mathbf{k}'}^{(0)} - f_{\mathbf{k}}^{(0)})$. For that we use the relation

$$(1 - f_{\mathbf{k}}^{(0)})f_{\mathbf{k}'}^{(0)} = \frac{f_{\mathbf{k}'}^{(0)} - f_{\mathbf{k}}^{(0)}}{1 - \exp[(\varepsilon_{\mathbf{k}'} - \varepsilon_{\mathbf{k}})/k_B T]}, \quad (\text{B.28})$$

which can be easily verified by direct calculation. For the case of Eq. (B.25), where $\varepsilon_{\mathbf{k}'} - \varepsilon_{\mathbf{k}} = \hbar\omega_{\mathbf{q}}^F + \hbar\omega_{\mathbf{q}'}^F$ holds, we have

$$\frac{1}{1 - \exp[(\varepsilon_{\mathbf{k}'} - \varepsilon_{\mathbf{k}})/k_B T]} = -\frac{n_{\mathbf{q}}^{(0)}n_{\mathbf{q}'}^{(0)}}{1 + n_{\mathbf{q}}^{(0)} + n_{\mathbf{q}'}^{(0)}}, \quad (\text{B.29})$$

while in the case of Eq. (B.27), where $\varepsilon_{\mathbf{k}'} - \varepsilon_{\mathbf{k}} = \hbar\omega_{\mathbf{q}}^F - \hbar\omega_{\mathbf{q}'}^F$, we get

$$\frac{1}{1 - \exp[(\varepsilon_{\mathbf{k}'} - \varepsilon_{\mathbf{k}})/k_B T]} = \frac{n_{\mathbf{q}}^{(0)}(1 + n_{\mathbf{q}'}^{(0)})}{n_{\mathbf{q}}^{(0)} - n_{\mathbf{q}'}^{(0)}}. \quad (\text{B.30})$$

The variations in Eqs. (B.22) and (B.23) may then be cast in the form

$$\delta [f_{\mathbf{k}'}(1 - f_{\mathbf{k}})(n_{\mathbf{q}} + 1)(n_{\mathbf{q}'} + 1) - f_{\mathbf{k}}(1 - f_{\mathbf{k}'})(n_{\mathbf{q}}n_{\mathbf{q}'})] = \quad (\text{B.31})$$

$$-(f_{\mathbf{k}'}^{(0)} - f_{\mathbf{k}}^{(0)}) \frac{\partial n_{\mathbf{q}}^{(0)}}{\partial(\hbar\omega_{\mathbf{q}}^F)} \frac{\partial n_{\mathbf{q}'}^{(0)}}{\partial(\hbar\omega_{\mathbf{q}'}^F)} \frac{k_B T (\varphi_{\mathbf{k}'} - \varphi_{\mathbf{k}} - \chi_{\mathbf{q}} - \chi_{\mathbf{q}'})}{1 + n_{\mathbf{q}} + n_{\mathbf{q}'}}}, \quad (\text{B.32})$$

and

$$\delta [f_{\mathbf{k}'}(1 - f_{\mathbf{k}})(n_{\mathbf{q}} + 1)n_{\mathbf{q}'} - f_{\mathbf{k}}(1 - f_{\mathbf{k}'})(n_{\mathbf{q}}n_{\mathbf{q}'} + 1)] = \quad (\text{B.33})$$

$$(f_{\mathbf{k}'}^{(0)} - f_{\mathbf{k}}^{(0)}) \frac{\partial n_{\mathbf{q}}^{(0)}}{\partial(\hbar\omega_{\mathbf{q}}^F)} \frac{\partial n_{\mathbf{q}'}^{(0)}}{\partial(\hbar\omega_{\mathbf{q}'}^F)} \frac{k_B T (\varphi_{\mathbf{k}'} + \chi_{\mathbf{q}'} - \varphi_{\mathbf{k}} - \chi_{\mathbf{q}})}{n_{\mathbf{q}} - n_{\mathbf{q}'}}}. \quad (\text{B.34})$$

Then we introduce the same approximations as before considering phonons to be in equilibrium, $\chi_{\mathbf{q}} \approx 0$, so that $n_{\mathbf{q}} \approx n_{\mathbf{q}}^{(0)}$, and assuming quasielastic scattering. The linearized collision integral then reads

$$\begin{aligned} \delta \dot{f}_{\mathbf{k}}|_{\text{scatt}} &= -\frac{2\pi}{\hbar^2} k_B T \frac{\partial f_{\mathbf{k}}}{\partial \varepsilon_{\mathbf{k}}} \sum_{\mathbf{k}'} (\varphi_{\mathbf{k}'} - \varphi_{\mathbf{k}}) \times \\ &\sum_{\mathbf{q}, \mathbf{q}'} w_F(\mathbf{q}, \mathbf{q}', \mathbf{k}, \mathbf{k}') \left(\frac{\omega_{\mathbf{q}}^F + \omega_{\mathbf{q}'}^F}{1 + n_{\mathbf{q}} + n_{\mathbf{q}'}} - \frac{\omega_{\mathbf{q}}^F - \omega_{\mathbf{q}'}^F}{n_{\mathbf{q}} - n_{\mathbf{q}'}} \right) \times \\ &\frac{\partial n_{\mathbf{q}}}{\partial \omega_{\mathbf{q}}^F} \frac{\partial n_{\mathbf{q}'}}{\partial \omega_{\mathbf{q}'}^F} \delta_{\mathbf{k}, \mathbf{k}'+\mathbf{q}+\mathbf{q}'} \delta(\varepsilon_{\mathbf{k}} - \varepsilon_{\mathbf{k}'}). \end{aligned} \quad (\text{B.35})$$

It can be written in the form of Eq. (B.18), with $\mathcal{A}_{\mathbf{k}, \mathbf{k}'}$ as given in Eq. (3.50).



Electronic structure of graphene commensurate with a Pb monolayer

In this appendix we examine the particular example of a rectangular Pb monolayer completely commensurate with graphene. In that case, which does not correspond with the experimental situation analyzed in Chapter 8, it is possible to perform analytical estimations of the strength of the potentials deduced from the reduced C_{2v} symmetry of the system.

We consider the situation depicted in Fig. C.1. The super-cell of the system is 4 times bigger than the original unit-cell of graphene. Our approach to the problem is the following: we add to the standard nearest-neighbors tight-binding model of graphene possible hoppings to Pb orbitals; then, we integrate out Pb orbitals, so we get an effective tight-binding model for graphene with additional hoppings within the 8-atoms unit cell as result these virtual processes; finally, we treat these new hoppings as perturbations to the original Hamiltonian, and we estimate its effect on the low energy spectrum by using second order perturbation theory.

The Hamiltonian of the system in first quantization notation can be written as the

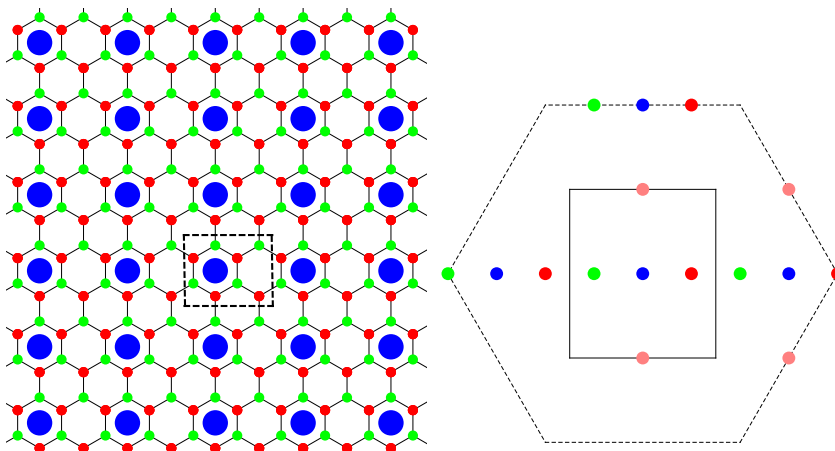


Figure C.1: Left: Real space lattice of graphene on an commensurate Pb monolayer. The unit cell of the system is highlighted within dashed lines. The blue circles represent the Pb atoms. Right: Original hexagonal BZ of graphene and the reduced BZ of graphene commensurate with Pb. The dots represent the folding of high symmetry points of the original BZ.

block matrix

$$\mathcal{H}_{G/Pb} = \begin{pmatrix} \mathcal{H}_G & V^\dagger \\ V & \mathcal{H}_{Pb} \end{pmatrix}, \quad (\text{C.1})$$

where V contains possible hoppings from graphene π orbitals to Pb orbitals. As mentioned before, we assume that \mathcal{H}_G is the nearest neighbors tight-binding Hamiltonian of graphene, where t is the hopping parameter. Following Ref.127, we assume a simplified Hamiltonian for the 4 outer-shell electrons of Pb in s , p_x , p_y and p_z orbitals. We introduce 3 parameters, ϵ_s , ϵ_p and Δ . The first two represent the on-site energies of s and p orbitals respectively, and Δ is the strength of the spin-orbit interaction in the $L \cdot S$ approximation. Finally, the possible hoppings from graphene π orbitals to Pb orbitals can be expressed in terms of 3 independent parameters, t_0 , t_z , and t_{in} , which parametrize the hoppings to s , p_z and $p_{x,y}$ orbitals of Pb respectively.

By projecting out the Pb orbitals by a Schrieffer-Wolf transformation^[75] we obtain an effective tight-binding Hamiltonian for graphene π orbitals,

$$\mathcal{H}_{eff} \approx \mathcal{H}_G - V^\dagger \mathcal{H}_{Pb}^{-1} V. \quad (\text{C.2})$$

The second term of this equation introduces the effective hoppings within the 8-atoms unit cell depicted in Fig. C.2. On the one hand, we have the spin-independent

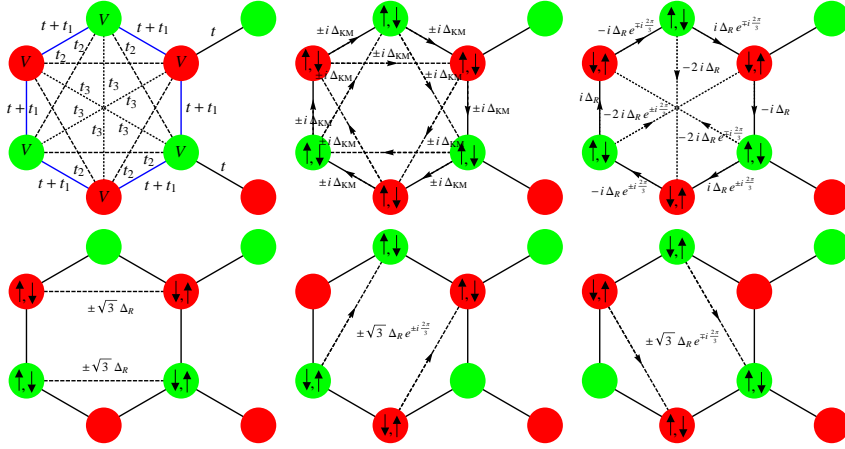


Figure C.2: New hopping terms within the 8 atoms unit cell generated after the integration of the Pb orbitals.

on-site and hopping energies,

$$\begin{aligned}
 V &= -\frac{t_{in}^2 + t_z^2}{\epsilon_p} - \frac{t_0^2}{\epsilon_s}, \\
 t_1 &= -\frac{t_{in}^2 + 2t_z^2}{2\epsilon_p} - \frac{t_0^2}{\epsilon_s}, \\
 t_2 &= \frac{t_{in}^2 - 2t_z^2}{2\epsilon_p} - \frac{t_0^2}{\epsilon_s}, \\
 t_3 &= \frac{t_{in}^2 - t_z^2}{\epsilon_p} - \frac{t_0^2}{\epsilon_s},
 \end{aligned} \tag{C.3}$$

and on the other hand, the spin-dependent hopping energies (up to first order in Δ),

$$\begin{aligned}
 \Delta_{KM} &= \frac{\sqrt{3}\Delta t^2}{4\epsilon_p^2}, \\
 \Delta_R &= \frac{\Delta t_{in} t_z}{2\epsilon_p^2}.
 \end{aligned} \tag{C.4}$$

From now on, we focus on the low energy description around the original \mathbf{K}_\pm . Note

that these new hoppings mediated by the Pb atoms couple Bloch states at \mathbf{K}_\pm points with modes at $\mathbf{K}_\pm \pm \mathbf{B}_1$, $\mathbf{K}_\pm \pm \mathbf{B}_2$ as result of the folding of the BZ, see Fig. C.1, where $\mathbf{B}_{1,2}$ are the reciprocal lattice vectors of the super-structure. If we treat these terms as weak perturbations to \mathcal{H}_G we can project out the modes by using the same perturbative scheme as before. If we do so and retain only the first order terms on Δ we obtain the SOC terms

$$\mathcal{H}_{SO} = \Delta_{int} \tau_z \sigma_z s_z + \Delta_0 \tau_z s_y + \Delta_1 (\tau_z \sigma_x s_y - \sigma_y s_x) + \Delta_2 (\tau_z \sigma_x s_y + \sigma_y s_x), \quad (\text{C.5})$$

with

$$\begin{aligned} \Delta_{int} &= \frac{3\sqrt{3}\Delta_{KM}}{4} \left(1 + \frac{5t_{in}^2}{2t\epsilon_p} \right), \\ \Delta_2 = \Delta_0 &= \frac{27t_{in}^2 \Delta_R}{32\epsilon_p t}, \\ \Delta_1 &= 0. \end{aligned} \quad (\text{C.6})$$

Note that the Hamiltonian of Eq. C.5 has the structure imposed by C_{2v} symmetry. Note also that $\Delta_1 = 0$ within this model due to the symmetry of the Pb orbitals considered in the calculation as it was pointed out in Ref. 127.

Bibliography

- [1] A. K. Geim and I. V. Grigorieva, *Van der Waals heterostructures*, Nature (London) **499**, 419 (2013). (see p. 3)
- [2] A. H. C. Neto, F. Guinea, N. M. R. Peres, K. S. Novoselov, and A. K. Geim, *The electronic properties of graphene*, Rev. Mod. Phys. **81**, 109 (2009). (see pp. 3 and 78)
- [3] K. S. Novoselov, A. K. Geim, S. V. Morozov, D. Jiang, Y. Zhang, S. V. Dubonos, I. V. Grigorieva, and A. A. Firsov, *Electric Field Effect in Atomically Thin Carbon Films*, Science **306**, 666 (2004). (see p. 3)
- [4] Jannik C. Meyer, A. K. Geim, M. I. Katsnelson, K. S. Novoselov, T. J. Booth, and S. Roth, *The structure of suspended graphene sheets*, Nature **446**, 60 (2006). (see p. 3)
- [5] E. McCann and M. Koshino, *The electronic properties of bilayer graphene*, Rep. Prog. Phys. **76**, 056503 (2013). (see p. 3)
- [6] Yi Zhang, Luyao Zhang, and Chongwu Zhon, *Review of chemical vapor deposition of graphene and related applications*, Acc. Chem. Res. **46**, 2329 (2013). (see p. 4)
- [7] P. Vogt, P. De Padova, C. Quaresima, J. Avila, E. Frantzeskakis, M. C. Asensio, A. Resta, B. Ealet, and G. Le Lay, *Silicene: Compelling Experimental Evidence for Graphenelike Two-Dimensional Silicon*, Phys. Rev. Lett. **108**, 155501 (2012). (see p. 4)
- [8] A. Fleurence, R. Friedlein, T. Ozaki, H. Kawai, Y. Wang, and Y. Yamada-Takamura, *Experimental Evidence for Epitaxial Silicene on Diboride Thin Films*, Phys. Rev. Lett. **108**, 245501 (2012). (see p. 4)
- [9] D. C. Elias, R. R. Nair, T. M. G. Mohiuddin, S. V. Morozov, P. Blake, M. P. Halsall, A. C. Ferrari, D. W. Boukhvalov, M. I. Katsnelson, A. K. Geim, and K. S. Novoselov, *Control of Graphene's Properties by Reversible Hydrogenation: Evidence for Graphane*, Science **323**, 610 (2009). (see p. 4)

- [10] E. Bianco, S. Butler, S. Jiang, O. D. Restrepo, W. Windl, and J. E. Goldberger, *Stability and Exfoliation of Germanane: A Germanium Graphane Analogue*, ACS Nano **7**, 4414 (2013). (see p. 4)
- [11] K. Watanabe, T. Taniguchi, and H. Kanda, *Direct-bandgap properties and evidence for ultraviolet lasing of hexagonal boron nitride single crystal*, Nat. Mater. **3**, 404 (2004). (see p. 4)
- [12] V. Zo'lyomi, N. D. Drummond, and V. I. Fal'ko, *Band structure and optical transitions in atomic layers of hexagonal gallium chalcogenides*, Phys. Rev. B **87**, 195403 (2013). (see p. 4)
- [13] Q. H. Wang, K. Kalantar-Zadeh, A. Kis, J. N. Coleman, and M. S. Strano, *Electronics and optoelectronics of two-dimensional transition metal dichalcogenides*, Nat. Nanotechnol. **7**, 699 (2012). (see pp. 4 and 26)
- [14] R. A. Gordon, D. Yang, E. D. Crozier, D. T. Jiang, and R. F. Frindt, *Structures of exfoliated single layers of WS₂, MoS₂, and MoSe₂ in aqueous suspension*, Phys. Rev. B **65**, 125407 (2002). (see p. 4)
- [15] A. H. Castro Neto, *Charge Density Wave, Superconductivity, and Anomalous Metallic Behavior in 2D Transition Metal Dichalcogenides*, Phys. Rev. Lett. **86**, 4382 (2001). (see p. 4)
- [16] W. Gerlach and O. Stern, *Das magnetische Moment des Silberatoms*, Zeitschrift für Physik **9**, 353 (1922). (see p. 4)
- [17] P. A. M. Dirac, *The Quantum Theory of the Electron*, Proceedings of the Royal Society of London, Series A **117**, 610 (1928). (see p. 5)
- [18] I. Zutic, J. Fabian, and S. D. Sarma, *Spintronics: Fundamentals and applications*, Rev. Mod. Phys. **76**, 323 (2004). (see pp. 6, 103, and 104)
- [19] D. Xiao, G.-B. Liu, W. Feng, X. Xu, and W. Yao, *Coupled Spin and Valley Physics in Monolayers of MoS₂ and Other Group-VI Dichalcogenides*, Phys. Rev. Lett. **108**, 196802 (2012). (see pp. 7, 32, 33, 46, and 47)
- [20] T. Cao, G. Wang, W. Han, H. Ye, C. Zhu, J. Shi, Q. Niu, P. Tan, E. Wang, B. Liu, and J. Feng, *Valley-selective circular dichroism of monolayer molybdenum disulphide*, Nat. Commun. **3**, 887 (2012). (see pp. 7 and 47)
- [21] K. F. Mak, K. He, J. Sahn, and T. F. Heinz, *Control of valley polarization in monolayer MoS₂ by optical helicity*, Nat. Nanotechnol. **7**, 494 (2012). (see pp. 7, 47, 114, and 122)

- [22] H. Zeng, J. Dai, W. Yao, D. Xiao, and X. Cui, *Valley polarization in MoS₂ monolayers by optical pumping*, Nat. Nanotechnol. **7**, 490 (2012). (see pp. 7 and 47)
- [23] Xiao-Gang Wen, *Quantum Field Theory of Many-Body Systems* (Oxford University Press, 2004). (see p. 7)
- [24] V. L. Ginzburg, and L. D. Landau, Zh. Eksp. Teor. Fiz. **20**, 1064 (1950). (see p. 7)
- [25] K. v. Klitzing, G. Dorda, and M. Pepper, *New Method for High-Accuracy Determination of the Fine-Structure Constant Based on Quantized Hall Resistance*, Phys. Rev. Lett. **45**, 494 (1980). (see p. 7)
- [26] D. C. Tsui, H. L. Stormer and A. C. Gossard, *Two-Dimensional Magnetotransport in the Extreme Quantum Limit*, Phys. Rev. Lett. **48**, 1559 (1982). (see p. 7)
- [27] X.-G. Wen, *Topological Orders in Rigid States*, Int. J. Mod. Phys. B **4**, 239 (1990). (see p. 7)
- [28] M. Nakahara, *Geometry, Topology and Physics* (Adam Hilger, Bristol, 1990). (see pp. 7 and 93)
- [29] E. Witten, *Topological quantum field theory*, Comm. Math. Phys. **117**, 353 (1988). (see p. 7)
- [30] M. V. Berry, *Quantal Phase Factors Accompanying Adiabatic Changes*, Proc. R. Soc. London Ser. A **392**, 45 (1984). (see p. 8)
- [31] Douglas R. Hofstadter, *Energy levels and wave functions of Bloch electrons in rational and irrational magnetic fields*, Phys. Rev. B **14**, 2239 (1976). (see p. 8)
- [32] R. Kubo, M. Toda, and N. Hashitsume, *Statistical Mechanics II* (Springer-Verlag, New York, 1985). (see p. 8)
- [33] D. J. Thouless, M. Kohmoto, M. P. Nightingale, and M. den Nijs, *Quantized Hall Conductance in a Two-Dimensional Periodic Potential*, Phys. Rev. Lett. **49**, 405 (1982). (see p. 8)
- [34] J. E. Avron, R. Seiler, and B. Simon, *Homotopy and Quantization in Condensed Matter Physics*, Phys. Rev. Lett. **51**, 51 (1983). (see p. 8)
- [35] B. Simon, *Holonomy, the Quantum Adiabatic Theorem, and Berry's Phase*, Phys. Rev. Lett. **51**, 2167 (1983). (see p. 8)
- [36] Q. Niu, D. J. Thouless, and Y. S. Wu, *Quantized Hall conductivity as a topological invariant*, Phys. Rev. B **31**, 3372 (1985). (see p. 8)

- [37] C. L. Kane and E. J. Mele, *Quantum Spin Hall Effect in Graphene*, Phys. Rev. Lett. **95**, 226801 (2005). (see pp. 9, 34, 38, 52, and 150)
- [38] G. E. Volovik and V. M. Yakovenko, *Fractional charge, spin and statistics of solitons in superfluid $^3\text{He-A}$ film*, J. Phys. Cond. Matt. **1**, 5263 (1989). (see p. 9)
- [39] C. Kane and E. J. Mele, \mathbb{Z}_2 topological order and the quantum spin Hall effect, Phys. Rev. Lett. **95**, 146802 (2005). (see pp. 9 and 52)
- [40] Liang Fu and C. L. Kane, *Time reversal polarization and a \mathbb{Z}_2 adiabatic spin pump*, Phys. Rev. B **74**, 195312 (2006). (see p. 9)
- [41] Liang Fu and C. L. Kane, *Topological insulators with inversion symmetry*, Phys. Rev. B **76**, 045302 (2007). (see p. 9)
- [42] Takahiro Fukui and Yasuhiro Hatsugai, *Quantum Spin Hall Effect in Three Dimensional Materials: Lattice Computation of \mathbb{Z}_2 Topological Invariants and Its Application to Bi and Sb*, J. Phys. Soc. Jpn. **76**, 053702 (2007). (see p. 9)
- [43] Takahiro Fukui, Takanori Fujiwara, and Yasuhiro Hatsugai, *Topological Meaning of \mathbb{Z}_2 Numbers in Time Reversal Invariant Systems*, J. Phys. Soc. Jpn. **77**, 123705 (2008). (see p. 9)
- [44] J. E. Moore and L. Balents, *Topological invariants of time-reversal-invariant band structures*, Phys. Rev. B **75**, 121306(R) (2007). (see p. 9)
- [45] Xiao-Liang Qi, Taylor L. Hughes, Shou-Cheng Zhang, *Topological field theory of time-reversal invariant insulators*, Phys. Rev. B **78**, 195424 (2008). (see p. 9)
- [46] Rahul Roy, *\mathbb{Z}_2 classification of quantum spin Hall systems: An approach using time-reversal invariance*, Phys. Rev. B **79**, 195321 (2009). (see p. 9)
- [47] Zhong Wang, Xiao-Liang Qi, and Shou-Cheng Zhang, *Equivalent topological invariants of topological insulators*, New J. Phys. **12**, 065007 (2010). (see p. 9)
- [48] Alexander Altland and Martin R. Zirnbauer, *Nonstandard symmetry classes in mesoscopic normal-superconducting hybrid structures*, Phys. Rev. B **55**, 1142 (1997). (see p. 9)
- [49] M. Z. Hasan and C. L. Kane *Colloquium: Topological insulators*, Rev. Mod. Phys. **82**, 3045 (2010). (see p. 9)
- [50] X.-L. Qi and S.-C. Zhang, *Topological insulators and superconductors*, Rev. Mod. Phys. **83**, 1057 (2011). (see p. 9)

-
- [51] R. Jackiw and C. Rebbi, *Solitons with fermion number one-half*, Phys. Rev. D **13**, 3398 (1976). (see p. 9)
- [52] W. P. Su, J. R. Schrieffer, and A. J. Heeger, *Solitons in Polyacetylene*, Phys. Rev. Lett. **42**, 1698 (1979). (see p. 9)
- [53] B. I. Halperin, *Quantized Hall conductance, current-carrying edge states, and the existence of extended states in a two-dimensional disordered potential*, Phys. Rev. B **25**, 2185 (1982). (see p. 9)
- [54] M. S. Dresselhaus, G. Dresselhaus, and A. Jorio, *Group Theory: Application to the Physics of Condensed Matter* (Springer, 2008). (see p. 13)
- [55] J. C. Slater and G. F. Koster, *Simplified LCAO Method for the Periodic Potential Problem*, Phys. Rev. **94**, 1498 (1954). (see pp. 13, 29, and 35)
- [56] Valeri N. Kotov, Bruno Uchoa, Vitor M. Pereira, F. Guinea, and A. H. Castro Neto, *Electron-Electron Interactions in Graphene: Current Status and Perspectives*, Rev. Mod. Phys. **84**, 1067 (2012). (see p. 13)
- [57] D. M. Basko, *Theory of resonant multiphonon Raman scattering in graphene*, Phys. Rev. B **78**, (2008). (see p. 15)
- [58] P. R. Wallace, *The Band Theory of Graphite*, Phys. Rev. **71**, 622 (1947). (see p. 16)
- [59] J. W. McClure, *Band Structure of Graphite and de Haas-van Alphen Effect*, Phys. Rev. **108**, 612 (1957). (see p. 16)
- [60] J. C. Slonczewski and P. R. Weiss, *Band Structure of Graphite*, Phys. Rev. **109**, 272 (1958). (see pp. 16 and 38)
- [61] J. P. Hobson and W. A. Nierenberg, *The Statistics of a Two-Dimensional, Hexagonal Net*, Phys. Rev. **89**, 662 (1953). (see p. 17)
- [62] S. Reich, J. Maultzsch, C. Thomsen, and P. Ordejón, *Tight-binding description of graphene*, Phys. Rev. B **66**, 035412 (2002). (see p. 17)
- [63] O. Klein, *Die Reflexion von Elektronen an einem Potentialsprung nach der relativistischen Dynamik von Dirac*, Z. Phys. **53**, 157 (1929). (see p. 18)
- [64] Tsuneya Ando, Takeshi Nakanishi, and Riichiro Saito, *Berry's Phase and Absence of Back Scattering in Carbon Nanotubes*, J. Phys. Soc. Jpn. **67**, 2857 (1998). (see p. 18)
- [65] Paul L. McEuen, Marc Bockrath, David H. Cobden, Young-Gui Yoon, and Steven G. Louie, *Disorder, Pseudospins, and Backscattering in Carbon Nanotubes*, Phys. Rev. Lett. **83**, 5098 (1999). (see p. 18)

- [66] M. I. Katsnelson, K. S. Novoselov, and A. K. Geim, *Chiral tunnelling and the Klein paradox in graphene*, Nat. Phys. **2**, 620 (2006). (see p. 18)
- [67] M. I. Katsnelson, *Graphene: carbon in two dimensions*, Mater. Today **10**, 20 (2007). (see pp. 18 and 22)
- [68] Hidekatsu Suzuura and Tsuneya Ando, *Crossover from Symplectic to Orthogonal Class in a Two-Dimensional Honeycomb Lattice*, Phys. Rev. Lett. **89**, 266603 (2002). (see p. 18)
- [69] E. McCann, K. Kechedzhi, Vladimir I. Fal'ko, H. Suzuura, T. Ando, and B. L. Altshuler, *Weak-Localization Magnetoresistance and Valley Symmetry in Graphene*, Phys. Rev. Lett. **97**, 146805 (2006). (see p. 18)
- [70] A. F. Morpurgo and F. Guinea, *Intervalley Scattering, Long-Range Disorder, and Effective Time-Reversal Symmetry Breaking in Graphene*, Phys. Rev. Lett. **97**, 196804 (2006). (see p. 18)
- [71] J. W. McClure, *Diamagnetism of Graphite*, Phys. Rev. **104**, 666 (1956). (see p. 19)
- [72] K. S. Novoselov, A. K. Geim, S. V. Morozov, D. Jiang, M. I. Katsnelson, I. V. Grigorieva, S. V. Dubonos, and A. A. Firsov, *Two-dimensional gas of massless Dirac fermions in graphene*, Nature **438**, 197 (2005). (see p. 19)
- [73] Yuanbo Zhang, Yan-Wen Tan, Horst L. Stormer, and Philip Kim, *Experimental observation of the quantum Hall effect and Berry's phase in graphene*, Nature **438**, 201 (2005). (see p. 19)
- [74] R. B. Laughlin, *Quantized Hall conductivity in two dimensions*, Phys. Rev. B **23**, 5632 (1981). (see p. 19)
- [75] J. R. Schrieffer and P. A. Wolf, *Relation between the Anderson and Kondo Hamiltonians*, Phys. Rev. **149**, 491 (1966). (see pp. 21, 37, 92, and 196)
- [76] Edward McCann and Vladimir I. Fal'ko, *Landau-Level Degeneracy and Quantum Hall Effect in a Graphite Bilayer*, Phys. Rev. Lett. **96**, 086805 (2006). (see pp. 21 and 22)
- [77] N. B. Brandt, S. M. Chudinov, and Y. G. Ponomarev, *Modern Problems in Condensed Matter Sciences* (North-Holland, Amsterdam, 1988). (see p. 22)
- [78] Edward McCann, *Asymmetry gap in the electronic band structure of bilayer graphene*, Phys. Rev. B **74**, 161403 (2006). (see p. 22)
- [79] Eduardo V. Castro, K. S. Novoselov, S. V. Morozov, N. M. R. Peres, J. M. B. Lopes dos Santos, Johan Nilsson, F. Guinea, A. K. Geim, and A. H. Castro Neto,

- Biased Bilayer Graphene: Semiconductor with a Gap Tunable by the Electric Field Effect*, Phys. Rev. Lett. **99**, 216802 (2007). (see p. 22)
- [80] K. Kechedzhi, Vladimir I. Fal'ko, E. McCann, and B. L. Altshuler, *Influence of Trigonal Warping on Interference Effects in Bilayer Graphene*, Phys. Rev. Lett. **98**, 176806 (2007). (see p. 22)
- [81] J. L. Mañes, F. Guinea and María A. H. Vozmediano, *Existence and topological stability of Fermi points in multilayered graphene*, Phys. Rev. B **75**, 155424 (2007). (see pp. 23 and 49)
- [82] F. Guinea, A. H. Castro Neto, and N. M. R. Peres, *Electronic states and Landau levels in graphene stacks*, Phys. Rev. B **73**, 245426 (2006). (see p. 25)
- [83] B. Partoens and F. M. Peeters, *From graphene to graphite: Electronic structure around the K point*, Phys. Rev. B **74**, 075404 (2006). (see p. 25)
- [84] J.A. Wilsona, F.J. Di Salvoa, and S. Mahajana, *Charge-density waves and superlattices in the metallic layered transition metal dichalcogenides*, Adv. Phys. **24**, 117 (1975). (see p. 26)
- [85] Kin Fai Mak, Changgu Lee, James Hone, Jie Shan, and Tony F. Heinz, *Atomically Thin MoS_2 : A New Direct-Gap Semiconductor*, Phys. Rev. Lett. **105**, 136805 (2010). (see p. 26)
- [86] Andrea Splendiani, Liang Sun, Yuanbo Zhang, Tianshu Li, Jonghwan Kim, Chi-Yung Chim, Giulia Galli, and Feng Wang, *Emerging Photoluminescence in Monolayer MoS_2* , Nano Lett. **10**, 1271 (2010). (see p. 26)
- [87] E. Cappelluti, R. Roldán, J. A. Silva-Guillén, P. Ordejón, and F. Guinea, *Tight-binding model and direct-gap/indirect-gap transition in single-layer and multi-layer MoS_2* , Phys. Rev. B **88**, 075409 (2013). (see pp. 30 and 32)
- [88] Gui-Bin Liu, Wen-Yu Shan, Yugui Yao, Wang Yao², and Di Xiao, *Three-band tight-binding model for monolayers of group-VIB transition metal dichalcogenides*, Phys. Rev. B **88**, 085433 (2013). (see p. 32)
- [89] Habib Rostami, Ali G. Moghaddam, and Reza Asgari, *Effective lattice Hamiltonian for monolayer MoS_2 : Tailoring electronic structure with perpendicular electric and magnetic fields*, Phys. Rev. B **88**, 085440 (2013). (see p. 32)
- [90] L. F. Mattheiss, *Band Structures of Transition-Metal-Dichalcogenide Layer Compounds*, Phys. Rev. B **8**, 3719 (1973). (see p. 32)
- [91] R. Coehoorn, C. Haas, J. Dijkstra, C. J. F. Flipse, R. A. de Groot, and A. Wold, *Electronic structure of MoSe_2 , MoS_2 , and WSe_2 . I. Band-structure calculations and photoelectron spectroscopy*, Phys. Rev. B **35**, 6195 (1987). (see p. 32)

- [92] A. Kuc, N. Zibouche, and T. Heine, *Influence of quantum confinement on the electronic structure of the transition metal sulfide TS_2* , Phys. Rev. B **83**, 245213 (2011). (see p. 32)
- [93] Z. Y. Zhu, Y. C. Cheng, and U. Schwingenschlogl, *Giant spin-orbit-induced spin splitting in two-dimensional transition-metal dichalcogenide semiconductors*, Phys. Rev. B **84**, 153402 (2011). (see pp. 32, 44, and 45)
- [94] Wanxiang Feng, Yugui Yao, Wenguang Zhu, Jinjian Zhou, Wang Yao, and Di Xiao, *Intrinsic spin Hall effect in monolayers of group-VI dichalcogenides: A first-principles study*, Phys. Rev. B **86**, 165108 (2012). (see pp. 32, 33, 44, and 45)
- [95] Andor Kormányos, Viktor Zólyomi, Neil D. Drummond, Péter Rakytá, Guido Burkard, and Vladimir I. Fal'ko, *Monolayer MoS_2 : Trigonal warping, the Γ valley, and spin-orbit coupling effects*, Phys. Rev. B **88**, 045416 (2013). (see pp. 32, 44, and 45)
- [96] Hai-Zhou Lu, Wang Yao, Di Xiao, and Shun-Qing Shen, *Intervalley Scattering and Localization Behaviors of Spin-Valley Coupled Dirac Fermions*, Phys. Rev. Lett. **110**, 016806 (2013). (see p. 32)
- [97] W. Kohn, J. M. Luttinger, *Quantum Theory of Electrical Transport Phenomena*, Phys. Rev. **108**, 590 (1957). (see p. 32)
- [98] Naoto Nagaosa, Jairo Sinova, Shigeki Onoda, A. H. MacDonald, and N. P. Ong, *Anomalous Hall effect*, Rev. Mod. Phys. **82**, 1539 (2010). (see p. 32)
- [99] Di Xiao, Ming-Che Chang, and Qian Niu, *Berry phase effects on electronic properties*, Rev. Mod. Phys. **82**, 1959 (2010). (see p. 32)
- [100] Wen-Yu Shan, Hai-Zhou Lu, and Di Xiao, *Spin Hall effect in spin-valley coupled monolayers of transition metal dichalcogenides*, Phys. Rev. B **88**, 125301 (2013). (see p. 33)
- [101] Edward McCann and Vladimir I. Fal'ko, *$z \rightarrow -z$ Symmetry of Spin-Orbit Coupling and Weak Localization in Graphene*, Phys. Rev. Lett. **108**, 166606 (2012). (see pp. 33 and 47)
- [102] Y. A. Bychkov and E. I. Rashba, *Oscillatory effects and the magnetic susceptibility of carriers in inversion layers*, J. Phys. C **17**, 6039 (1984). (see pp. 34 and 126)
- [103] Y. Yao, F. Ye, X.-L. Qi, S.-C. Zhang, and . Zhong Fang, *Spin-orbit gap of graphene: First-principles calculations*, Phys. Rev. B **75**, 041401(R) (2007). (see p. 35)
- [104] M. Gmitra, S. Konschuh, C. Ertler, C. Ambrosch-Draxl, and J. Fabian, *Band-structure topologies of graphene: Spin-orbit coupling effects from first principles*, Phys. Rev. B **80**, 235431 (2009). (see pp. 35, 38, and 100)

- [105] S. Abdelouahed, A. Ernst, J. Henk, I. V. Maznichenko, and I. Mertig, *Spin-split electronic states in graphene: Effects due to lattice deformation, Rashba effect, and adatoms by first principles*, Phys. Rev. B **82**, 125424 (2010). (see p. 35)
- [106] D. Huertas-Hernando, F. Guinea, and A. Brataas, *Spin-orbit coupling in curved graphene, fullerenes, nanotubes, and nanotube caps*, Phys. Rev. B **74**, 155426 (2006). (see pp. 35, 37, 92, 96, and 100)
- [107] H. Min, J. E. Hill, N. A. Sinitsyn, B. R. Sahu, L. Kleinman, and A. H. MacDonald, *Intrinsic and Rashba spin-orbit interactions in graphene sheets*, Phys. Rev. B **74**, 165310 (2006). (see pp. 35, 37, and 96)
- [108] S. Konschuh, M. Gmitra, and J. Fabian, *Tight-binding theory of the spin-orbit coupling in graphene*, Phys. Rev. B **82**, 245412 (2010). (see pp. 35, 37, 38, and 100)
- [109] M. Zarea and N. Sandler, *Electron-Electron and Spin-Orbit Interactions in Arm-chair Graphene Ribbons*, Phys. Rev. Lett. **99**, 256804 (2007). (see p. 35)
- [110] M. Zarea, C. Busser, and N. Sandler, *Unscreened Coulomb Interactions and the Quantum Spin Hall Phase in Neutral Zigzag Graphene Ribbons*, Phys. Rev. Lett. **101**, 196804 (2008). (see p. 35)
- [111] M. Zarea and N. Sandler, *Rashba spin-orbit interaction in graphene and zigzag nanoribbons*, Phys. Rev. B **79**, 165442 (2009). (see p. 35)
- [112] M. P. López-Sancho and M. C. Muñoz, *Intrinsic spin-orbit interactions in flat and curved graphene nanoribbons*, Phys. Rev. B **83**, 075406 (2011). (see p. 35)
- [113] H. Santos, M. C. Muñoz, M. P. López-Sancho, and L. Chico, *Interplay between symmetry and spin-orbit coupling on graphene nanoribbons*, Phys. Rev. B **87**, 235402 (2013). (see p. 35)
- [114] D. Tománek and S. G. Louie, *First-principles calculation of highly asymmetric structure in scanning-tunneling-microscopy images of graphite*, Phys. Rev. B **37**, 8327 (1988). (see p. 35)
- [115] D. Tománek and M. A. Schluter, *Growth regimes of carbon clusters*, Phys. Rev. Lett. **67**, 2331 (1991). (see p. 35)
- [116] J. Serrano, M. Cardona, and T. Ruf, *Spin-orbit splitting in diamond: excitons and acceptor related states*, Solid State Commun. **113**, 411 (2000). (see p. 37)

- [117] J. González, F. Guinea, and M. A. H. Vozmediano, *Non-Fermi liquid behaviour of electrons in the half-filled honeycomb lattice (A renormalization group approach)*, Nucl. Phys. B **424**, 595 (1994). (see p. 38)
- [118] D. T. Son, *Quantum critical point in graphene approached in the limit of infinitely strong Coulomb interaction*, Phys. Rev. B **75**, 235423 (2007). (see p. 38)
- [119] V. N. Kotov, B. Uchoa, and A. H. C. Neto, *1/N expansion in correlated graphene*, Phys. Rev. B **80**, 165424 (2009). (see p. 38)
- [120] F. de Juan, A. G. Grushin, and M. A. H. Vozmediano, *Renormalization of Coulomb interaction in graphene: Determining observable quantities*, Phys. Rev. B **82**, 125409 (2010). (see p. 38)
- [121] Igor F. Herbut, *Interactions and Phase Transitions on Graphene's Honeycomb Lattice*, Phys. Rev. Lett. **97**, 146401 (2006). (see p. 39)
- [122] F. Guinea, *Spin-orbit coupling in a graphene bilayer and in graphite*, New J. Phys. **12**, 083063 (2010). (see p. 41)
- [123] Ralph van Gelderen and C. Morais Smith, *Rashba and intrinsic spin-orbit interactions in biased bilayer graphene*, Phys. Rev. B **81**, 125435 (2010). (see p. 41)
- [124] Edward McCann and Mikito Koshino, *Spin-orbit coupling and broken spin degeneracy in multilayer graphene*, Phys. Rev. B **81**, 241409(R) (2010). (see pp. 41 and 42)
- [125] S. Konschuh, M. Gmitra, D. Kochan, and J. Fabian, *Theory of spin-orbit coupling in bilayer graphene*, Phys. Rev. B **85**, 115423 (2012). (see p. 41)
- [126] R. Roldán, M.P. López-Sancho, E. Cappelluti, J.A. Silva-Guillén, P. Ordejón, F. Guinea, *Effect of spin-orbit interaction in single-layer and multi-layer transition metal dichalcogenides: a tight-binding approach*, arXiv:1401.5009 [cond-mat.mes-hall]. (see p. 44)
- [127] Conan Weeks, Jun Hu, Jason Alicea, Marcel Franz, and Ruqian Wu, *Engineering a Robust Quantum Spin Hall State in Graphene via Adatom Deposition*, Phys. Rev. X **1**, 021001 (2011). (see pp. 47, 48, 196, and 198)
- [128] Jun Hu, Jason Alicea, Ruqian Wu, and Marcel Franz, *Giant Topological Insulator Gap in Graphene with 5d Adatoms*, Phys. Rev. Lett. **109**, 266801 (2012). (see p. 47)
- [129] A. H. Castro Neto and F. Guinea, *Impurity-Induced Spin-Orbit Coupling in Graphene*, Phys. Rev. Lett. **103**, 026804 (2009). (see pp. 47, 104, and 115)

- [130] Martin Gmitra, Denis Kochan, and Jaroslav Fabian, *Spin-Orbit Coupling in Hydrogenated Graphene*, Phys. Rev. Lett. **110**, 246602 (2013). (see pp. 47 and 120)
- [131] F. D. M. Haldane, *Model for a Quantum Hall Effect without Landau Levels: Condensed-Matter Realization of the "Parity Anomaly"*, Phys. Rev. Lett. **61**, 2015 (1988). (see pp. 49, 148, and 151)
- [132] R. Peierls, *Zur Theorie des Diamagnetismus von Leitungselektronen*, Z. Phys. **80**, 763 (1933). (see p. 50)
- [133] R. Jackiw, *Fractional charge and zero modes for planar systems in a magnetic field*, Phys. Rev. D **29**, 2375 (1984). (see p. 51)
- [134] Shinsei Ryu and Yasuhiro Hatsugai, *Topological Origin of Zero-Energy Edge States in Particle-Hole Symmetric Systems*, Phys. Rev. Lett. **89**, 077002 (2002). (see p. 51)
- [135] B. Andrei Bernevig and Shou-Cheng Zhang, *Quantum Spin Hall Effect*, Phys. Rev. Lett. **96**, 106802 (2006). (see pp. 52, 140, 144, 167, and 169)
- [136] B. Andrei Bernevig, Taylor L. Hughes, and Shou-Cheng Zhang, *Quantum Spin Hall Effect and Topological Phase Transition in HgTe Quantum Wells*, Science **314**, 1757 (2006). (see p. 52)
- [137] Markus Konig, Steffen Wiedmann, Christoph Brune, Andreas Roth, Hartmut Buhmann, Laurens W. Molenkamp¹, Xiao-Liang Qi, and Shou-Cheng Zhang, *Quantum Spin Hall Insulator State in HgTe Quantum Wells*, Science **318**, 766 (2007). (see pp. 52 and 145)
- [138] S. V. Morozov, K. S. Novoselov, M. I. Katsnelson, F. Schedin, D. C. Elias, J. A. Jaszczak, and A. K. Geim, *Giant Intrinsic Carrier Mobilities in Graphene and Its Bilayer*, Phys. Rev. Lett. **100**, 016602 (2008). (see pp. 55, 56, and 83)
- [139] Jian-Hao Chen, Chaun Jang, Shudong Xiao, Masa Ishigami, and Michael S. Fuhrer, *Intrinsic and extrinsic performance limits of graphene devices on SiO₂*, Nature Nanotech. **3**, 206 (2008). (see pp. 55, 74, and 83)
- [140] Xu Du, Ivan Skachko, Anthony Barker, and Eva Y. Andrei, *Approaching ballistic transport in suspended graphene*, Nature Nanotech. **3**, (2008). (see pp. 55 and 84)
- [141] K.I. Bolotin, K.J. Sikes, Z. Jiang, M. Klima, G. Fudenberg, J. Hone, P. Kim, H.L. Stormera, *Ultrahigh electron mobility in suspended graphene*, Solid State Commun. **146**, (2008). (see pp. 55 and 84)

- [142] L. D. Landau and E. M. Lifshitz, *Theory of Elasticity*, Vo. 7 of *Course of Theoretical Physics* (Pergamon Press, Oxford, 1959). (see pp. 55, 57, 59, and 135)
- [143] *Statistical Mechanics of Membranes and Surfaces*, edited by D. Nelson, T. Piran, and S. Weinberg (World Scientific, Singapore, 2004). (see pp. 55, 57, and 61)
- [144] M. I. Katsnelson and A. K. Geim, *Electron scattering on microscopic corrugations in graphene*, *Phil. Trans. R. Soc. A* **366**, 195 (2008). (see pp. 56 and 78)
- [145] P. M. Chaikin and T. C. Lubensky, *Principles of Condensed Matter Physics* (Cambridge University Press, 1995). (see pp. 57 and 59)
- [146] Joseph A. Aronovitz and T. C. Lubensky, *Fluctuations of Solid Membranes*, *Phys. Rev. Lett.* **60**, 2634 (1988). (see p. 59)
- [147] K. V. Zakharchenko, J. H. Los, M. I. Katsnelson, and A. Fasolino, *Phys. Rev. B* **81**, 235439 (2010). (see p. 63)
- [148] Hidekatsu Suzuura and Tsuneya Ando, *Phonons and electron-phonon scattering in carbon nanotubes*, *Phys. Rev. B* **65**, 235412 (2002). (see pp. 63 and 73)
- [149] A. Atland and B. Simons, *Condensed Matter Field Theory* (Cambridge University Press, Cambridge 2006). (see p. 65)
- [150] Eros Mariani and Felix von Oppen, *Flexural Phonons in Free-Standing Graphene*, *Phys. Rev. Lett.* **100**, 076801 (2008). (see pp. 56, 66, 71, 78, and 188)
- [151] Eros Mariani and Felix von Oppen, *Temperature-dependent resistivity of suspended graphene*, *Phys. Rev. B* **82**, 195403 (2010). (see pp. 66, 71, and 190)
- [152] M. Auslender and M. I. Katsnelson, *Generalized kinetic equations for charge carriers in graphene*, *Phys. Rev. B* **76**, 235425 (2007). (see p. 67)
- [153] E. Cappelluti and L. Benfatto, *Vertex renormalization in dc conductivity of doped chiral graphene*, *Phys. Rev. B* **79**, 035419 (2009). (see p. 67)
- [154] J. M. Ziman, *Electrons and Phonons: the theory of transport phenomena in solids* (Oxford University Press, London 1960). (see pp. 67, 68, 72, 188, 190, and 191)
- [155] V.Y. Irkhin and M.I. Katsnelson, *Temperature dependences of resistivity and magnetoresistivity for half-metallic ferromagnets*, *Eur. Phys. J. B* **30**, 481 (2002). (see p. 68)
- [156] E. H. Hwang and S. Das Sarma, *Acoustic phonon scattering limited carrier mobility in two-dimensional extrinsic graphene*, *Phys. Rev. B* **77**, 115449 (2008). (see pp. 71, 72, and 73)

- [157] T. Stauber, N. M. R. Peres, and F. Guinea, *Electronic transport in graphene: A semiclassical approach including midgap states*, Phys. Rev. B **76**, 205423 (2007). (see p. 71)
- [158] Seon-Myeong Choi, Seung-Hoon Jhi, and Young-Woo Son, *Effects of strain on electronic properties of graphene*, Phys. Rev. B **81**, 081407(R) (2010). (see pp. 64 and 74)
- [159] Dmitri K. Efetov and Philip Kim, *Controlling Electron-Phonon Interactions in Graphene at Ultrahigh Carrier Densities*, Phys. Rev. Lett. **105**, 256805 (2010). (see p. 74)
- [160] Hongki Min, E. H. Hwang, and S. Das Sarma, *Chirality-dependent phonon-limited resistivity in multiple layers of graphene*, Phys. Rev. B **83**, 161404(R) (2011). (see p. 74)
- [161] K. V. Zakharchenko, R. Roldán, A. Fasolino, and M. I. Katsnelson, *Self-consistent screening approximation for flexible membranes: Application to graphene*, Phys. Rev. B **82**, 125435 (2010). (see pp. 78 and 85)
- [162] S. V. Morozov, K. S. Novoselov, M. I. Katsnelson, F. Schedin, D. C. Elias, J. A. Jaszczak, and A. K. Geim, *Giant Intrinsic Carrier Mobilities in Graphene and Its Bilayer*, Phys. Rev. Lett. **100**, 016602 (2008). (see p. 78)
- [163] Rafael Roldán, Annalisa Fasolino, Kostyantyn V. Zakharchenko, and Mikhail I. Katsnelson, *Suppression of anharmonicities in crystalline membranes by external strain*, Phys. Rev. B **83**, 174104 (2011). (see pp. 85 and 86)
- [164] D. R. Nelson and L. Peliti, *Fluctuations in membranes with crystalline and hexatic order*, J. Physique **48**, 1085 (1987). (see pp. 85 and 87)
- [165] A. Fasolino, J. H. Los, and M. I. Katsnelson, *Intrinsic ripples in graphene*, Nat. Mater. **6**, 858 (2007). (see p. 88)
- [166] K. I. Bolotin, K. J. Sikes, J. Hone, H. L. Stormer, and P. Kim, *Temperature-Dependent Transport in Suspended Graphene*, Phys. Rev. Lett. **101**, 096802 (2008). (see pp. 55 and 88)
- [167] S. Fratini, D. Gosálbez-Martínez, P. Merodio Cámara, and J. Fernández-Rossier, *Anisotropic intrinsic spin relaxation in graphene due to flexural distortions*, Phys. Rev. B **88**, 115426 (2013). (see pp. 89 and 125)
- [168] Ion Garate, *Phonon-Induced Topological Transitions and Crossovers in Dirac Materials*, Phys. Rev. Lett. **110**, 046402 (2013). (see p. 89)
- [169] Tsuneya Ando, *Spin-Orbit Interaction in Carbon Nanotubes*, J. Phys. Soc. Jpn. **69**, 1757 (2000). (see p. 92)

- [170] N. D. Drummond, V. Zólyomi, and V. I. Fal'ko, *Electrically tunable band gap in silicene*, Phys. Rev. B **85**, 075423 (2012). (see p. 95)
- [171] M. F. Thorpe and D. Weaire, *Electronic Density of States of Amorphous Si and Ge*, Phys. Rev. Lett. **27**, 1581 (1971). (see p. 95)
- [172] F. Guinea, *Electron-phonon scattering in graphite intercalation compounds: a localised approach*, J. Phys. C: Solid State Phys. **14**, 3345 (1981). (see p. 95)
- [173] Ludger Wirtz and Ángel Rubio, *The phonon dispersion of graphite revisited*, Solid State Commun. **131**, 141 (2004). (see p. 97)
- [174] Jae-Seung Jeong, Jeongkyu Shin, and Hyun-Woo Lee, *Curvature-induced spin-orbit coupling and spin relaxation in a chemically clean single-layer graphene*, Phys. Rev. B **84**, 195457 (2011). (see p. 100)
- [175] Fang Liu, Pingbing Ming, and Ju Li, *Ab initio calculation of ideal strength and phonon instability of graphene under tension*, Phys. Rev. B **76**, 064120 (2007). (see p. 100)
- [176] Yu Zhang and Feng Liu, *Maximum asymmetry in strain induced mechanical instability of graphene: Compression versus tension*, Appl. Phys. Lett. **99**, 241908 (2011). (see p. 100)
- [177] P. L. de Andres, F. Guinea, and M. I. Katsnelson, *Density functional theory analysis of flexural modes, elastic constants, and corrugations in strained graphene*, Phys. Rev. B **86**, 245409 (2012). (see p. 100)
- [178] Nicolas Mounet and Nicola Marzari, *First-principles determination of the structural, vibrational and thermodynamic properties of diamond, graphite, and derivatives*, Phys. Rev. B **71**, 205214 (2005). (see p. 100)
- [179] Monica Pozzo, Dario Alfé, Paolo Lacovig, Philip Hofmann, Silvano Lizzit, and Alessandro Baraldi, *Thermal Expansion of Supported and Freestanding Graphene: Lattice Constant versus Interatomic Distance*, Phys. Rev. Lett. **106**, 135501 (2011). (see p. 100)
- [180] L.J. Karssemeijer and Annalisa Fasolino, *Phonons of graphene and graphitic materials derived from the empirical potential LCBOPII*, Surf. Sci. **605**, 1611 (2011). (see p. 100)
- [181] P. L. de Andres, F. Guinea, and M. I. Katsnelson, *Bending modes, anharmonic effects, and thermal expansion coefficient in single-layer and multilayer graphene*, Phys. Rev. B **86**, 144103 (2012). (see p. 100)
- [182] C. A. Marianetti and H. G. Yevick, *Failure Mechanisms of Graphene under Tension*, Phys. Rev. Lett. **105**, 245502 (2010). (see p. 100)

-
- [183] T. Mashoff, M. Pratzner, V. Geringer, T. J. Echtermeyer, M. C. Lemme, M. Liebmann, and M. Morgenstern, *Bistability and Oscillatory Motion of Natural Nanomembranes Appearing within Monolayer Graphene on Silicon Dioxide*, Nano Lett. **10**, 461 (2010). (see p. 100)
- [184] F. Bloch, *Nuclear Induction*, Phys. Rev. **70**, 460 (1946). (see p. 103)
- [185] H. C. Torrey, *Bloch Equations with Diffusion Terms*, Phys. Rev. **104**, 563 (1956). (see p. 103)
- [186] Jerome I. Kaplan, *Application of the Diffusion-Modified Bloch Equation to Electron Spin Resonance in Ordinary and Ferromagnetic Metals*, Phys. Rev. **115**, 575 (1959). (see p. 103)
- [187] Y. Zhou and M. W. Wu, *Electron spin relaxation in graphene from a microscopic approach: Role of electron-electron interaction*, Phys. Rev. B **82**, 085304 (2010). (see p. 104)
- [188] V. K. Dugaev, E. Ya. Sherman, and J. Barnás, *Spin dephasing and pumping in graphene due to random spin-orbit interaction*, Phys. Rev. B **83**, 085306 (2011). (see p. 104)
- [189] P. Zhang and M. W. Wu, *Electron spin diffusion and transport in graphene*, Phys. Rev. B **84** 045304, (2011). (see p. 104)
- [190] P. Zhang and M. W. Wu, *Electron spin relaxation in graphene with random Rashba field: comparison of the D'yakonov-Perel' and Elliot-Yafet-like mechanisms*, New J. Phys. **14**, 033015 (2012). (see p. 104)
- [191] Mathias Diez and Guido Burkard, *Bias-dependent D'yakonov-Perel' spin relaxation in bilayer graphene*, Phys. Rev. B **85**, 195412 (2012). (see p. 104)
- [192] L. Wang and M. W. Wu, *Intrinsic electron spin relaxation due to the D'yakonov-Perel' mechanism in monolayer MoS₂*, arXiv:1305.3361 [cond-mat.mes-hall] (2013). (see p. 104)
- [193] L. Wang and M. W. Wu, *Electron spin relaxation due to D'yakonov-Perel' and Elliot-Yafet mechanisms in monolayer MoS₂: Role of intravalley and intervalley processes*, arXiv:1312.6985 [cond-mat.mes-hall] (2013). (see p. 104)
- [194] Christian Ertler, Sergej Konschuh, Martin Gmitra, and Jaroslav Fabian, *Electron spin relaxation in graphene: The role of the substrate*, Phys. Rev. B **80**, 041405(R) (2009). (see p. 104)
- [195] Hazime Mori and Kyozi Kawasaki, *Theory of Dynamical Behaviors of Ferromagnetic Spins*, Prog. Theor. Phys. **27**, 529 (1962). (see pp. 104 and 107)

- [196] Hazime Mori and Kyozi Kawasaki, *Antiferromagnetic Resonance Absorption*, Prog. Theor. Phys. **28**, 971 (1962). (see pp. 104 and 107)
- [197] B. Dóra, F. Murányi, and F. Simon, *Electron spin dynamics and electron spin resonance in graphene*, Europhys. Lett. **92**, 17002 (2010). (see pp. 104 and 114)
- [198] Nikolaos Tombros, Csaba Jozsa, Mihaita Popinciuc, Harry T. Jonkman, and Bart J. van Wees, *Electronic spin transport and spin precession in single graphene layers at room temperature*, Nature **448**, 571 (2007). (see p. 104)
- [199] Bruno Dlubak, Marie-Blandine Martin, Cyrille Deranlot, Bernard Servet, Stephane Xavier, Richard Mattana, Mike Sprinkle, Claire Berger, Walt A. De Heer, Frederic Petroff, Abdelmadjid Anane, Pierre Seneor, and Albert Fert, *Highly efficient spin transport in epitaxial graphene on SiC*, Natur. Phys. **10**, 1038 (2012). (see p. 104)
- [200] Megumi Ohishi, Masashi Shiraishi, Ryo Nouchi, Takayuki Nozaki, Teruya Shinjo, and Yoshishige Suzuki, *Spin injection into a graphene thin film at room temperature*, Jpn. J. Appl. Phys. **46**, 605 (2007). (see p. 104)
- [201] Sungjae Cho, Yung-Fu Chen, and Michael S. Fuhrer, *Gate-tunable graphene spin valve*, Appl. Phys. Lett. **91**, 123105 (2007). (see p. 104)
- [202] C. Jozsa, M. Popinciuc, N. Tombros, H. T. Jonkman, and B. J. van Wees, *Electronic spin drift in graphene field-effect transistors*, Phys. Rev. Lett. **100**, 236603 (2008). (see p. 104)
- [203] Wei Han, K. Pi, W. Bao, K. M. McCreary, Yan Li, W. H. Wang, C. N. Lau, and R. K. Kawakami, *Electrical detection of spin precession in single layer graphene spin valves with transparent contacts*, Appl. Phys. Lett. **94**, 222109 (2009). (see p. 104)
- [204] Wei Han, W. H. Wang, K. Pi, K. M. McCreary, W. Bao, Yan Li, F. Miao, C. N. Lau, and R. K. Kawakami, *Electron-hole asymmetry of spin injection and transport in single-layer graphene*, Phys. Rev. Lett. **102**, 137205 (2009). (see p. 104)
- [205] C. Jozsa, T. Maassen, M. Popinciuc, P. J. Zomer, A. Veligura, H. T. Jonkman, and B. J. van Wees, *Linear scaling between momentum and spin scattering in graphene*, Phys. Rev. B **80**, 241403(R) (2009). (see p. 104)
- [206] C. Jozsa, M. Popinciuc, N. Tombros, H. T. Jonkman, and B. J. van Wees, *Controlling the efficiency of spin injection into 3 graphene by carrier drift*, Phys. rev. B **79**, 081402 (2009). (see p. 104)

- [207] Kazuya Muramoto, Masashi Shiraishi, Nobuhiko Mitoma, Takayuki Nozaki, Teruya Shinjo, and Yoshishige Suzuki, *Analysis of degradation in graphene-based spin valves*, Appl. Phys. Express **2**, 123004 (2009). (see p. 104)
- [208] M. Popinciuc, C. Jozsa, P. J. Zomer, N. Tombros, A. Veligura, H. T. Jonkman, and B. J. van Wees, *Electronic spin transport in graphene field-effect transistors*, Phys. Rev. B **80**, 214427 (2009). (see p. 104)
- [209] Masashi Shiraishi, Megumi Ohishi, Ryo Nouchi, Nobuhiko Mitoma, Takayuki Nozaki, Teruya Shinjo, and Yoshishige Suzuki, *Robustness of spin polarization in graphene-based spin valves*, Adv. Funct. Mater. **19**, 3711 (2009). (see p. 104)
- [210] Ahmet Avsar, Tsung-Yeh Yang, Sukang Bae, Jayakumar Balakrishnan, Frank Volmer, Manu Jaiswal, Zheng Yi, Syed Rizwan Ali, Gernot Guntherodt, Byung Hee Hong, Bernd Beschoten, and Barbaros Ozyilmaz, *Toward wafer scale fabrication of graphene based spin valve devices*, Nano Lett. **11**, 2363 (2011). (see p. 104)
- [211] Wei Han and R. K. Kawakami, *Spin relaxation in single-layer and bilayer graphene*, Phys. Rev. Lett. **107**, 047207 (2011). (see p. 104)
- [212] Sanghyun Jo, Dong-Keun Ki, Dongchan Jeong, Hu-Jong Lee, and Stefan Kettmann, *Spin relaxation properties in graphene due to its linear dispersion*, Phys. Rev. B **84**, 075453 (2011). (see p. 104)
- [213] T.-Y. Yang, J. Balakrishnan, F. Volmer, A. Avsar, M. Jaiswal, J. Sann, S. R. Ali, A. Pachoud, M. Zeng, M. Popinciuc, G. Guntherodt, B. Beschoten, and B. Ozyilmaz, *Observation of long spin-relaxation times in bilayer graphene at room temperature*, Phys. Rev. Lett. **107**, 047206 (2011). (see p. 104)
- [214] T. Maassen, F. K. Dejene, M. H. D. Guimaraes, C. Jozsa, and B. J. van Wees, *Comparison between charge and spin transport in few-layer graphene*, Phys. Rev. B **83**, 115410 (2011). (see p. 104)
- [215] Marcos H. D. Guimaraes, A. Veligura, P. J. Zomer, T. Maassen, I. J. Vera-Marun, N. Tombros, and B. J. van Wees, *Spin transport in high-quality suspended graphene devices*, Nano Lett. **12**, 3512 (2012). (see p. 104)
- [216] P. J. Zomer, M. H. D. Guimaraes, N. Tombros, and B. J. van Wees, *Long-distance spin transport in high-mobility graphene on hexagonal boron nitride*, Phys. Rev. B **86**, 161416 (2012). (see p. 104)
- [217] K. Pi, Wei Han, K. M. McCreary, A. G. Swartz, Yan Li, and R. K. Kawakami, *Manipulation of Spin Transport in Graphene by Surface Chemical Doping*, Phys. Rev. Lett. **104**, 187201 (2010). (see p. 104)

- [218] Wei Han, Jen-Ru Chen, Deqi Wang, Kathleen M. McCreary, Hua Wen, Adrian G. Swartz, Jing Shi, and Roland K. Kawakami, *Spin relaxation in single-layer graphene with tunable mobility*, Nano Lett. **12**, 3443 (2012). (see p. 104)
- [219] Adrian G. Swartz, Jen-Ru Chen, Kathleen M. McCreary, Patrick M. Odenthal, Wei Han, and Roland K. Kawakami, *Effect of in situ deposition of Mg adatoms on spin relaxation in graphene*, Phys. Rev. B **87**, 075455 (2013). (see p. 104)
- [220] M. Wojtaszek, I. J. Vera-Marun, T. Maassen, and B. J. van Wees, *Enhancement of spin relaxation time in hydrogenated graphene spin-valve devices*, Phys. Rev. B **87**, 081402(R) (2013). (see p. 104)
- [221] Kathleen M. McCreary, Adrian G. Swartz, Wei Han, Jaroslav Fabian, and Roland K. Kawakami, *Magnetic Moment Formation in Graphene Detected by Scattering of Pure Spin Currents*, Phys. Rev. Lett. **109**, 186604 (2012). (see pp. 104, 115, and 122)
- [222] R. J. Elliot, *Theory of the Effect of Spin-Orbit Coupling on Magnetic Resonance in Some Semiconductors*, Phys. Rev. **96**, 266 (1954). (see pp. 104 and 105)
- [223] Y. Yafet, *Solid State Physics* (Academic, New York, 1963). (see p. 104)
- [224] M. I. D'yakonov and V. I. Perel', *Spin relaxation of conduction electrons in noncentrosymmetric semiconductors*, Sov. Phys. Solid State **13**, 3023 (1971). (see p. 104)
- [225] M. I. D'yakonov, *Spin Physics in Semiconductors* (Springer, New York, 2008). (see pp. 104 and 114)
- [226] G. L. Bir, A. G. Aronov and G. E. Pikus, *Spin relaxation of electrons scattered by holes*, Zh. Eksp. Teor. Fiz **69**, 1382 (1975). (see pp. 104 and 105)
- [227] M. I. D'yakonov and V. I. Perel', *Optical Orientation in a System of Electrons and Lattice Nuclei in Semiconductors-Theory*, Zh. Eksp. Teor. Fiz **65**, 362 (1973). (see p. 104)
- [228] Pil Hun Song and K. W. Kim, *Spin relaxation of conduction electrons in bulk III-V semiconductors*, Phys. Rev. B **66**, 035207 (2002). (see p. 105)
- [229] J.-N. Chazalviel, *Spin relaxation of conduction electrons in n-type indium antimonide at low temperature*, Phys. Rev. B **11**, 1555 (1975). (see p. 105)
- [230] F. J. Jedema, M. S. Nijboer, A. T. Filip, and B. J. van Wees, *Spin injection and spin accumulation in all-metal mesoscopic spin valves*, Phys. Rev. B **67**, 085319 (2003). (see p. 105)

- [231] Jaroslav Fabian, Alex Matos-Abiague, Christian Ertler, Peter Stano, and Igor Zutic, *Semiconductor Spintronics*, Acta Physica Slovaca **57**, (2007). (see p. 106)
- [232] D. Huertas-Hernando, F. Guinea, and Arne Brataas, *Spin-Orbit-Mediated Spin Relaxation in Graphene*, Phys. Rev. Lett. **103**, 146801 (2009). (see p. 106)
- [233] Péter Boross, Balázs Dóra, Annamária Kiss, and Ferenc Simon, *A unified theory of spin-relaxation due to spin-orbit coupling in metals and semiconductors*, Sci. Rep. **3**, 3233 (2013). (see p. 107)
- [234] Masaki Oshikawa and Ian Affleck, *Electron spin resonance in $S = 1/2$ antiferromagnetic chains*, Phys. Rev. B **65**, 134410 (2002). (see p. 108)
- [235] B. Radisavljevic, A. Radenovic, J. Brivio, V. Giacometti, A. Kis, *Single-layer MoS_2 transistors*, Nat. Nanotechnol. **6**, 147 (2011). (see pp. xix, 113, 130, and 134)
- [236] Yijin Zhang, Jianting Ye, Yusuke Matsushashi, and Yoshihiro Iwasa, *Ambipolar MoS_2 Thin Flake Transistors*, Nano Lett. **12**, 1136 (2012). (see pp. xix, 113, 130, and 134)
- [237] Wenzhong Bao, Xinghan Cai, Dohun Kim, Karthik Sridhara, and Michael S. Fuhrer, *High mobility ambipolar MoS_2 field-effect transistors: Substrate and dielectric effects*, Appl. Phys. Lett. **102**, 042104 (2013). (see pp. xix, 113, 130, and 134)
- [238] D. Huertas-Hernando, F. Guinea, A. Brataas, *Spin relaxation times in disordered graphene*, Eur. Phys. J. Special Topics **148**, 177 (2007). (see p. 115)
- [239] Denis Kochan, Martin Gmitra, Jaroslav Fabian, *Spin relaxation mechanism in graphene: resonant scattering by magnetic impurities*, arXiv:1306.0230 [cond-mat.mes-hall]. (see p. 115)
- [240] Vitor M. Pereira, F. Guinea, J. M. B. Lopes dos Santos, N. M. R. Peres, and A. H. Castro Neto, *Disorder Induced Localized States in Graphene*, Phys. rev. Lett. **96**, 036801 (2006). (see p. 117)
- [241] A. R. Akhmerov and C. W. J. Beenakker, *Boundary conditions for Dirac fermions on a terminated honeycomb lattice*, Phys. Rev. B **77**, 085423 (2008). (see p. 119)
- [242] M. M. Ugeda, I. Brihuega, F. Guinea, and J. M. Gómez-Rodríguez, *Missing Atom as a Source of Carbon Magnetism*, Phys. Rev. Lett. **104**, 096804 (2010). (see p. 122)

- [243] P. Haase, S. Fuchs, T. Pruschke, H. Ochoa, and F. Guinea, *Magnetic moments and Kondo effect near vacancies and resonant scatterers in graphene*, Phys. Rev. B **83**, 241408(R) (2011). (see p. 122)
- [244] E. I. Rashba, *Theory of electrical spin injection: Tunnel contacts as a solution of the conductivity mismatch problem*, Phys. Rev. B **62**, R16267(R) (2000). (see p. 122)
- [245] Wei Han, K. Pi, K. M. McCreary, Yan Li, Jared J. I. Wong, A. G. Swartz, and R. K. Kawakami, *Tunneling Spin Injection into Single Layer Graphene*, Phys. Rev. Lett. **105**, 167202 (2010). (see p. 122)
- [246] B. Dlubak, P. Seneor, A. Anane, C. Barraud, C. Deranlot, D. Deneuve, B. Servet, R. Mattana, F. Petroff, and A. Fert, *Are Al₂O₃ and MgO tunnel barriers suitable for spin injection in graphene?*, Appl. Phys. Lett. **97**, 092502 (2010). (see p. 122)
- [247] B. Dlubak, M.-B. Martin, C. Deranlot, K. Bouzehouane, S. Fusil, R. Mattana, F. Petroff, A. Anane, P. Seneor, and A. Fert, *Homogeneous pinhole free 1 nm Al₂O₃ tunnel barriers on graphene*, Appl. Phys. Lett. **101**, 203104 (2012). (see p. 122)
- [248] Takehiro Yamaguchi, Satoru Masubuchi, Kazuyuki Iguchi, Rai Moriya, and Tomoki Machida, *Tunnel spin injection into graphene using Al₂O₃ barrier grown by atomic layer deposition on functionalized graphene surface*, J. Magn. Mater. **324**, 849 (2012). (see p. 122)
- [249] Mark S. Rudner, and Emmanuel I. Rashba, *Spin relaxation due to deflection coupling in nanotube quantum dots*, Phys. Rev. B **81**, 125426 (2010). (see p. 124)
- [250] Matthias Droth and Guido Burkard, *Electron spin relaxation in graphene nanoribbon quantum dots*, Phys. Rev. B **87**, 205432 (2013). (see p. 124)
- [251] Jorgen Rammer, *Quantum Transport Theory* (Westview Press, 2004). (see p. 125)
- [252] G. Dresselhaus, *Spin-Orbit Coupling Effects in Zinc Blende Structures*, Phys. Rev. **100**, 580 (1955). (see p. 126)
- [253] Jacopo Brivio, Duncan T. L. Alexander, and Andras Kis, *Ripples and Layers in Ultrathin MoS₂ Membranes*, Nano Lett. **11**, 5148 (2011). (see pp. xix, 130, and 134)
- [254] M M Benameur, B Radisavljevic, J S Héron, S Sahoo, H Berger, and A Kis, *Visibility of dichalcogenide nanolayers*, Nanotechnology **22**, 125706 (2011). (see p. 135)

- [255] A. Castellanos-Gómez, M. Poot, G. A. Steele, H. S. J. van der Zant, N. Agrait, and G. Rubio-Bollinger, *Elastic Properties of Freely Suspended MoS₂ Nanosheets*, *Adv. Mater.* **24**, 772 (2012). (see p. 135)
- [256] M. Lovell, M. Khonsari, and R. Marangoni, *A finite element analysis of the frictional forces between a cylindrical bearing element and MoS₂ coated and uncoated surfaces*, *Wear* **194**, 60 (1996). (see p. 135)
- [257] Bruno Amorim and Francisco Guinea, *Flexural mode of graphene on a substrate*, *Phys. Rev. B* **88**, 115418 (2013). (see p. 135)
- [258] M. A. Vozmediano, M. I. Katsnelson, and F. Guinea, *Gauge fields in graphene*, *Physics Reports* **496**, 109 (2010). (see pp. 139, 142, and 153)
- [259] F. Guinea, M. I. Katsnelson, and A. K. Geim, *Energy gaps and a zero-field quantum Hall effect in graphene by strain engineering*, *Nature Physics*, **6**, 30 (2010). (see pp. 139, 140, 144, 145, and 167)
- [260] N. Levy, S. A. Burke, K. L. Meaker, M. Panlasigui, A. Zettl, F. Guinea, A. H. Castro Neto, M. F. Crommie, *Strain-Induced Pseudo-Magnetic Fields Greater Than 300 Tesla in Graphene Nanobubbles*, *Science* **329**, 544 (2010). (see pp. 139, 140, 145, and 146)
- [261] J. Lu, A.H. Castro Neto, and K. P. Loh, *Transforming moiré blisters into geometric graphene nano-bubbles*, *Nature Comm.* **3**, 823 (2012). (see pp. 139, 140, 145, and 146)
- [262] T. Low, F. Guinea, and K. I. Katsnelson, *Gaps tunable by electrostatic gates in strained graphene*, *Phys. Rev. B* **83** 195436 (2011). (see p. 140)
- [263] R. C. Cooper, C. Lee, C. A. Marianetti, X. Wei, J. Hone, and J. W. Kysar, *Non-linear elastic behavior of two-dimensional molybdenum disulfide*, *Phys. Rev. B* **87**, 035423 (2013). (see p. 144)
- [264] Y. Aharonov and A. Casher, *Ground state of a spin-1/2 charged particle in a two-dimensional magnetic field*, *Phys. Rev. A* **19**, 2461 (1979). (see pp. 144 and 145)
- [265] M. Bander, *Fractional quantum Hall effect in nonuniform magnetic fields*, *Phys. Rev. B* **41**, 9028 (1990). (see p. 145)
- [266] M. Taillefumier, V. K. Dugaev, B. Canals, C. Lacroix, and P. Bruno, *Chiral two-dimensional electron gas in a periodic magnetic field: Persistent current and quantized anomalous Hall effect*, *Phys. Rev. B* **78**, 155330 (2008). (see p. 145)
- [267] I. Knez, R.-R. Du, G. Sullivan, *Evidence for Helical Edge Modes in Inverted InAs/GaSb Quantum Wells*, *Phys. Rev. Lett.* **107**, 136603 (2011) (see p. 145)

- [268] C. Xu and J. Moore, *Stability of the quantum spin Hall effect: Effects of interactions, disorder, and \mathbb{Z}_2 topology*, Phys. Rev. B **73** 045322 (2006). (see p. 146)
- [269] Congjun Wu, B. Andrei Bernevig, and Shou-Cheng Zhang, *Helical Liquid and the Edge of Quantum Spin Hall Systems*, Phys. Rev. Lett. **96**, 106401 (2006). (see p. 146)
- [270] R. Roldán, E. Cappelutti, and F. Guinea, *Interactions and superconductivity in heavily doped MoS_2* , Phys. Rev. B **88**, 054515 (2013). (see p. 146)
- [271] Atsuo Shitade, Hosho Katsura, Jan Kunes, Xiao-Liang Qi, Shou-Cheng Zhang, and Naoto Nagaosa, *Quantum Spin Hall Effect in a Transition Metal Oxide Na_2IrO_3* , Phys. Rev. Lett. **102**, 256403 (2009). (see p. 146)
- [272] J. R. Wallbank, A. A. Patel, M. Mucha-Kruczynski, A. K. Geim, and V. I. Fal'ko, *Generic miniband structure of graphene on a hexagonal substrate*, Phys. Rev. B **87**, 245408 (2013). (see p. 148)
- [273] I. Snyman, *Gapped state of a carbon monolayer in periodic magnetic and electric fields*, Phys. Rev. B **80**, 054303 (2009). (see p. 151)
- [274] Matthew Yankowitz, Jiamin Xue, Daniel Cormode, Javier D. Sanchez-Yamagishi, K. Watanabe, T. Taniguchi, Pablo Jarillo-Herrero, Philippe Jacquod, and Brian J. LeRoy, *Emergence of superlattice Dirac points in graphene on hexagonal boron nitride*, Nature Phys. **8**, 382 (2012). (see p. 151)
- [275] L. A. Ponomarenko, R. V. Gorbachev, G. L. Yu, D. C. Elias, R. Jalil, A. A. Patel, A. Mishchenko, A. S. Mayorov, C. R. Woods, J. R. Wallbank, M. Mucha-Kruczynski, B. A. Piot, M. Potemski, I. V. Grigorieva, K. S. Novoselov, F. Guinea, V. I. Fal'ko, and A. K. Geim, *Cloning of Dirac fermions in graphene superlattices*, Nature **497**, 594 (2013). (see p. 151)
- [276] C. R. Dean, L. Wang, P. Maher, C. Forsythe, F. Ghahari, Y. Gao, J. Katoch, M. Ishigami, P. Moon, M. Koshino, T. Taniguchi, K. Watanabe, K. L. Shepard, J. Hone, and P. Kim, *Hofstadter's butterfly and the fractal quantum Hall effect in moiré superlattices*, Nature **497**, 598 (2013). (see p. 151)
- [277] B. Hunt, J. D. Sanchez-Yamagishi, A. F. Young, M. Yankowitz, B. J. LeRoy, K. Watanabe, T. Taniguchi, P. Moon, M. Koshino, P. Jarillo-Herrero, R. C. Ashoori, *Massive Dirac Fermions and Hofstadter Butterfly in a van der Waals Heterostructure*, Science **340**, 1427 (2013). (see p. 151)
- [278] O. P. Sushkov, and A. H. Castro Neto, *Topological Insulating States in Laterally Patterned Ordinary Semiconductors*, Phys. Rev. Lett. **110**, 186601 (2013). (see p. 151)

- [279] J. Sun, H. A. Fertig, and L. Brey, *Effective Magnetic Fields in Graphene Superlattices*, Phys. Rev. Lett. **105**, 186501 (2010). (see p. 153)
- [280] S. Gopalakrishnan, P. Ghaemi, and S. Ryu, *Non-Abelian $SU(2)$ gauge fields through density wave order and strain in graphene*, Phys. Rev. B **86**, 081403 (2012). (see p. 153)
- [281] P. San-Jose, J. González, and F. Guinea, *Non-Abelian Gauge Potentials in Graphene Bilayers*, Phys. Rev. Lett. **108**, 216802 (2012). (see pp. 153 and 161)
- [282] J. R. Anderson and A. V. Gold, *Fermi Surface, Pseudopotential Coefficients, and Spin-Orbit in Lead*, Phys. Rev. **139**, 1459 (1965). (see pp. 154 and 169)
- [283] Alpha T. N'Diaye, Sebastian Bleikamp, Peter J. Feibelman, and Thomas Michely, *Two-Dimensional Ir Cluster Lattice on a Graphene Moiré on Ir(111)*, Phys. Rev. Lett. **97**, 215501 (2006). (see p. 154)
- [284] Alpha T. N'Diaye, Johann Coraux, Tim N Plasa, Carsten Busse and Thomas Michely, *Structure of epitaxial graphene on Ir(111)*, New J. Phys. **10**, 043033 (2008). (see p. 154)
- [285] Sara Barja, Manuela Garnica, Juan José Hinarejos, Amadeo L. Vázquez de Parga, Nazario Martín, and Rodolfo Miranda, *Self-organization of electron acceptor molecules on graphene*, Chem. Comm. **46**, 8198 (2010). (see p. 154)
- [286] L. D. Landau and E. M. Lifshitz, *Physical Kinetics* (Pergamon, Oxford, 1981). (see p. 190)

List of Publications

The research performed during the development of this thesis has led to the following publications:

1. *Limits on electron quality in suspended graphene due to flexural phonons.*
E. V. Castro, H. Ochoa, M. I. Katsnelson, R. V. Gorbachev, D. C. Elias, K. S. Novoselov, A. K. Geim, and F. Guinea,
Physical Review Letters **105**, 266601 (2010).
2. *Temperature-dependent resistivity in bilayer graphene due to flexural phonons.*
H. Ochoa, Eduardo V. Castro, M. I. Katsnelson, and F. Guinea,
Physical Review B **83**, 235416 (2011).
3. *Scattering by flexural phonons in suspended graphene under back gate induced strain.*
H. Ochoa, Eduardo V. Castro, M.I. Katsnelson, and F. Guinea,
Physica E **44**, 963 (2012).
4. *Elliot-Yafet mechanism in graphene.*
H. Ochoa, A. H. Castro Neto, and F. Guinea,
Physical Review Letters **108**, 206808 (2012).
5. *Spin-orbit coupling assisted by flexural phonons in graphene.*
H. Ochoa, A. H. Castro Neto, V. I. Fal'ko, and F. Guinea,
Physical Review B **86**, 245411 (2012).
6. *Spin-Orbit mediated spin relaxation in monolayer MoS₂.*
H. Ochoa and R. Roldán,
Physical Review B **87**, 245421 (2013).
7. *Spin memory and spin-lattice relaxation in two-dimensional hexagonal crystals.*
H. Ochoa, F. Guinea, and V. I. Fal'ko,
Physical Review B **88**, 195417 (2013).
8. *Quantum Spin Hall Effect in Strained Two-dimensional Crystals of Transition Metal Dichalcogenides.*
M. A. Cazalilla, H. Ochoa, and F. Guinea,
arXiv:1311.6650,
submitted to Physical Review Letters.
9. *Giant Spin-Orbit effect induces electron confinement in graphene on Pb islands.*
Fabián Calleja, Héctor Ochoa, Manuela Garnica, Sara Barja, Juan Jesús Navarro,

Andrés Black, Amadeo L. Vázquez de Parga, Francisco Guinea, and Rodolfo Miranda, in preparation

Other publications during this period:

- *Magnetic moments and Kondo effect near vacancies and resonant scatterers in graphene.*
P. Haase, S. Fuchs, T. Pruschke, H. Ochoa, and F. Guinea,
Physical Review B **83**, 241408(R) (2011).

